

DISSERTATION

ON THE ENVIRONMENTS AND DYNAMICS OF NOCTURNAL MESOSCALE CONVECTIVE SYSTEMS

Submitted by

Stacey Hitchcock

Department of Atmospheric Science

In partial fulfillment of the requirements

For the Degree of Doctor of Philosophy

Colorado State University

Fort Collins, Colorado

Fall 2018

Doctoral Committee:

Advisor: Russ S. Schumacher

David A. Randall

Susan C. van den Heever

Richard Eykholt

Copyright by Stacey Hitchcock 2018

All Rights Reserved

## ABSTRACT

### ON THE ENVIRONMENTS AND DYNAMICS OF NOCTURNAL MESOSCALE CONVECTIVE SYSTEMS

The 2015 Plains Elevated Convection at Night (PECAN) field campaign was motivated by unanswered questions about key processes in elevated mesoscale convective systems (MCSs) and the difficulty in accurately forecasting them. During the campaign, 15 MCS environments were sampled by an array of instruments including radiosondes launched by fixed and mobile sounding teams. Cluster analysis of observed vertical profiles established three primary pre-convective categories. Only one of these groups fits well with the common conceptual model of nocturnal MCS environments where  $\theta_e$  increases in an elevated layer with the onset of the low-level jet (LLJ). Post-convective soundings demonstrate substantial variability, but cold pools were observed in nearly every PECAN MCS case. However, stronger, deeper stable layers appear to lead to structures where the largest cooling is observed above the surface.

On 24-25 June 2015, a ‘bow-and-arrow’ MCS structure was observed in an environment with strong low-level stability. Previous work on the mechanisms that support the structure in the arrow region (also sometimes referred to as rearward off-boundary development or ROD) has relied on a combination of a surface cold pool and large scale ascent provided by the interaction of a LLJ with a baroclinic zone. A horizontally homogeneous simulation initialized with a near-storm pre-convective PECAN sounding from the 24-25 June 2015 produces nearly the same MCS structure in the absence of a surface cold pool. Instead, outflow takes on several different forms in different regions of the MCS. Ultimately, the ROD (or arrow) is most likely supported by gravity wave amplified by vertical wind shear over the same layer, and maintained by persistent downdrafts.

The success of both MCS initiation and development of ROD despite the strong stable layer and idealized horizontally homogeneous initial conditions suggests that the interactions between convective outflow and a stable layer in a sheared environment are important in both of these processes. Very few studies to date have explored these interactions, and even less in 3D. A series of 2D and 3D experiments were designed to explore 1) What happens when a downdraft impacts a stable layer with and without shear? 2) What low-level shear profiles support MCS development in an idealized simulation with strong stability and why? 3) What shear characteristics are favorable for ROD development? Results indicate that strong low level shear is critical for sustaining convection, that low-level shear may

be as important as stability in determining the effective inflow layer, and that upper level winds play a critical role in the development of ROD.

## ACKNOWLEDGMENTS

First and foremost, this work would not be possible without the support and encouragement of my advisor, Russ Schumacher. I am also grateful for the support and critical feedback from committee members Sue van den Heever, Dave Randall, and Richard Eykholt throughout this process. Insightful discussions with Kevin Haghi, Greg Herman, Erik Nielsen, Leah Grant, and Peter Marinescu sparked excitement and helped improve this work. Critical feedback from Matt Parker, Mike Coniglio, Conrad Zeiglar, and Greg Herman was invaluable; this is especially true of their comments on the work presented in Chapter 2. Numerous others have also given scientific feedback at the PECAN science, AMS Annual, AMS Mesoscale, AMS WAF-NWP, and (CSU) Storms Super Group meetings.

This research is supported by NSF grants AGS-1359727 and AGS-1359709. The mobile upsonde systems that collected the radiosonde data used in this article were supported by the NSF Award AGS-1359726. A NOAA/Office of Atmospheric Research (OAR)/Office of Weather and Air Quality (AWAQ) award provided all mobile sounding expendables used by the CSU and two NSSL sounding vehicles during PECAN. Thanks to Sean Waugh and NOAA/National Severe Storms Laboratory (NSSL) for configuring and maintaining the CSU and two NSSL mobile sounding vehicles. Computing resources were provided by NCAR. Thanks also to the technical and administrative staff at CSU for their support. A special thank you also goes to the many PECAN participants for their dedication to seeing the sunrise before bedtime for the sake of science.

I am grateful for the Colorado State University and University of Oklahoma communities, and in particular the CSU atmospheric science community, as well as the broader atmospheric science community (especially the American Meteorological Society) for the opportunities they have provided me over the years. I've also been lucky enough to have a remarkable set of academic and life mentors over the years including but not limited to: Russ Schumacher, Mike Coniglio, Sue van den Heever, Chuck Doswell, Kevin Kloesel, Lance Leslie, Patrick Marsh, Harold Brooks, Vicki Schaeffer, Beverly George, and Emily Bishop.

Finally, thank you to the friends and family who love me, encourage me, push me, feed me, and remind me to go have fun too. I am forever indebted to my family, especially my parents for their love and support.

## DEDICATION

*For my family, friends, teachers, and mentors that believe in and support me.*

## TABLE OF CONTENTS

ABSTRACT .....	ii
ACKNOWLEDGMENTS .....	iv
DEDICATION .....	v
LIST OF TABLES .....	viii
LIST OF FIGURES .....	ix
Chapter 1. Introduction .....	1
1.1 Motivation .....	1
1.2 Density currents, bores, and gravity waves (Oh my!) .....	2
1.3 Plains Elevated Convection at Night (PECAN) .....	3
1.4 Dissertation Goals .....	4
Chapter 2. Evolution of Pre- and Post-Convective Environmental Profiles from Mesoscale Convective Systems During PECAN .....	7
2.1 Introduction .....	7
2.2 Overview of Mesoscale Convective System Cases during PECAN .....	9
2.3 Methods .....	14
2.4 Cluster Analysis Results on Environment Soundings .....	16
2.5 Post Convection .....	30
2.6 Discussion and Summary .....	35
Chapter 3. Analysis of Back-Building Convection in Simulations with a Strong Low-Level Stable Layer .....	39
3.1 Methods .....	40
3.2 Results .....	44
3.3 Summary and Conclusions .....	76

Chapter 4. Sensitivity of Convective Outflow Characteristics to Modifications to Stability and Shear and Impacts on ROD . . . . .	78
4.1 Introduction . . . . .	78
4.2 Methods . . . . .	79
4.3 Results . . . . .	86
4.4 Summary of Results . . . . .	154
Chapter 5. Summary of Findings . . . . .	157
References . . . . .	163
Appendix A. . . . .	172
A1 PECAN Radiosonde Observations of MCS Environments . . . . .	172
A2 Principal Component Analysis . . . . .	175
A3 Shared Nearest Neighbors (SNN) Clustering . . . . .	177

LIST OF TABLES

Table 1.1 Surface characteristics of convectively generated propagation mechanisms . . . . . 3

Table 2.1 Selected cases, region of intensive observation, and platforms available in identified region. . . . . 10

Table 2.2 Sources of radiosonde data included in this study. . . . . 14

Table 2.3 Number of soundings clustered for each case in each cluster. An asterisk denotes that at least 25% of soundings from the given case were clustered. . . . . 18

Table 2.4 A simple summary of changes in virtual potential temperature  $\theta_v$ .  $\theta'_{vmax}$  is the magnitude of the largest observed average decrease in  $\theta_v$ .  $\theta'_{vmax}$  Hgt is the height at which  $\theta'_{vmax}$  occurred.  $\theta'_v$  Top is the minimum height in which the mean difference between  $\theta_v$  in pre- and post-convective soundings is no longer negative. If a second layer of  $-\theta_v$  of equal or larger magnitude exists above a shallow layer of weakly  $-\theta_v$ , the parenthetical number is the top of that second layer. . . . . 31

Table 3.1 Model Setup . . . . . 41

Table 4.1 Cold bubble drop sensitivity experiments. Variations in drop strength, drop height, and grid spacing. . . . . 82

Table 4.2 . . . . . 86

Table 4.3 . . . . . 142

LIST OF FIGURES

Fig. 2.1 0000 UTC Rapid Refresh (RAP) analysis for each case. 500 hPa heights (m; black contour), 850 hPa wind vectors where  $v > 10 \text{ m s}^{-1}$ , 850 hPa temperature ( $^{\circ}\text{C}$ ; color contours), and 850 hPa mixing ratios ( $\text{g kg}^{-1}$ ; green filled). Colored dots represent clusters in which soundings were grouped. Half shaded circles indicate  $< 25\%$  of soundings the case were in the cluster. . . . . 11

Fig. 2.2 Radar reflectivity from the NSSL Multi-Radar Multi-Sensor (MRMS) system (Zhang et al. 2016) of observed convection during each IOP and positions of mobile assets at (a) 0300 UTC 11 June (b) 0500 UTC 12 June (c) 0200 UTC 15 June (d) 0500 UTC 17 June (e) 0500 UTC 25 June (f) 0500 UTC 26 June (g) 0400 UTC 1 July (h) 0400 UTC 2 July (i) 0500 UTC 6 July (j) 0400 UTC 9 July (k) 0400 UTC 10 July (l) 0600 UTC 11 July (m) 0600 UTC 13 July (n) 0200 UTC 14 July (o) 0300 UTC 16 July. Colored dots represent case sounding clusters as in Figure 2.1. Open circle, square, and triangle symbols are used for MG, MP, and FP assets respectively. . . . . 13

Fig. 2.3 Mean (solid lines) and standard deviation (semi-transparent shading) of (a,d,g)  $\theta_e$  (K), (b,e,h)  $u$ , and  $v$  ( $\text{m s}^{-1}$ ) below 3 km for each case in each cluster. Dates of intensive observing periods (IOPs) are given by different colors. The number in parentheses in the lower left of (a,d,g) is the number of cases with more than 25% of pre-convective soundings clustered (Listed in Table 2.3). Cluster means given by the gray dashed line. Histograms in (c,f,i) show a distribution of launch times by hour for each cluster. . . . . 17

Fig. 2.4 Mean (solid lines) and standard deviation (semi-transparent shading)  $\theta_v$  (K) below 3 km for the (a) Potentially Neutral + Jet, (b) Potentially Neutral, and (c) Elevated Instability clusters. Dates of intensive observing periods (IOPs) are given by different colors. Cluster means are given by the gray dashed line. . . . . 18

Fig. 2.5 Violin plots of (a) MUCAPE ( $\text{J kg}^{-1}$ ), (b) MUCIN ( $\text{J kg}^{-1}$ ), (c) SBCAPE ( $\text{J kg}^{-1}$ ), (d) SBCIN ( $\text{J kg}^{-1}$ ), (e) MU parcel source (hPa above surface) f) precipitable water (PW; mm), (g) 0-6 km shear (knots), and (h) 0-1 km shear (knots) for each cluster. Plots indicate the distribution (shaded); min/max (blue horizontal lines at top and bottom of plot respectively), median (middle blue horizontal line), mean (magenta) of the set of

	soundings. The mean and median are equal if the magenta line is not visible. The green star is the variable value in the composite soundings. . . . .	21
Fig. 2.6	Skew-T log-P plots and hodographs (inset) of composites of the three clusters. Winds in $\text{m s}^{-1}$ . Shading in the hodograph changes at 1 km intervals from light to dark. . . . .	23
Fig. 2.7	Composite plots depicting 0000 UTC RAP analysis of the (a,b) potentially neutral + jet, (c,d) potentially neutral, and (e,f) elevated instability clusters. In (a,c,e): 500 hPa heights (m; black), 850 hPa wind speed (greyscale) and barbs ( $\text{m s}^{-1}$ ), 850 hPa temperature ( $^{\circ}\text{C}$ ; color contours), and 850 hPa temperature advection $>\sim 0.5 \text{ K hr}^{-1}$ (stippled with open circles). In (b,d,f): 250 mb winds $> 50$ knots (unfilled dark blue contour), 850 hPa wind speed (unfilled gray contours), 850 hPa wind barbs ( $\text{m s}^{-1}$ ), 850 hPa water vapor mixing ratio ( $\text{g kg}^{-1}$ ; green filled contours), and 850 hPa moisture advection $> 0.2 \text{ g kg}^{-1}$ per hour (stippled with open circles). . . . .	25
Fig. 2.8	Time-height diagrams of MG launches on (a,b) 16-17 June, (c,d) 11-12 June, (e,f) 12-13 July. (a,c,e) $\theta_e$ (filled contours; K) and meridional wind (unfilled contours; $\text{m s}^{-1}$ ). (b,d,f) $\theta_v$ (filled contours; K) and zonal wind (unfilled contours; $\text{m s}^{-1}$ ) . . . . .	28
Fig. 2.9	Average $\theta_v$ deficit (K) of post-convective soundings. Shading indicates $+/- 1\sigma$ . . . . .	30
Fig. 2.10	Scatter plot of the height of greatest observed cooling (from Table 2.4) and the a) strength (K) and b) depth (m) of the observed stable layer in pre-convective soundings. Individual markers are pie-charts that indicate the fraction of the pre-convective soundings with an identifiable low-level stable layer (shaded). Bars represent one standard deviation. . . . .	34
Fig. 3.1	Skew-T Log-P of the original 0428 UTC 25 June 2015 PECAN sounding (T in red, Td in green, wind barbs in gray), and the sounding used to initialize the homogeneous environment used in simulations (T in black, Td in blue, wind barbs in black). Thin lines on the inset hodograph are original sounding winds, thick lines are input sounding winds). . . . .	42
Fig. 3.2	Radar reflectivity at 0440 UTC on 25 June 2015 and location of the sounding in Fig. 3.1	43
Fig. 3.3	Simulated reflectivity every 30 minutes from 1.5 hours to 4 hours. Blue contours indicate $-0.5 \text{ K surface } \theta'$ . . . . .	45
Fig. 3.4	4 hour output of (a) Surface $\theta'_p$ (filled), 40 dBz reflectivity at lowest model level (unfilled black), $1 \text{ m s}^{-1}$ w at 0.5 km (gray unfilled), and surface wind vectors. (b) As in a, but	

	wind vectors and $\theta'_\rho$ in filled contours at 0.5 km. (c) $P'$ (filled), 40 dBz reflectivity at lowest model level (unfilled black), $1 \text{ m s}^{-1}$ w at 0.5 km (gray unfilled), and surface wind perturbation vectors. (d) As in c, but w in filled contours. . . . .	47
Fig. 3.5	Cross section through (a,b) A-A', (c,d) B-B', (e,f) C-C' after 4 hours. (a,c,e) $\theta'_\rho$ (K) in filled contours, w ( $\text{m s}^{-1}$ ) in unfilled black contours, $\pm 0.5$ and $1 \text{ Pa}$ $P'$ unfilled green contours, and wind vectors. (b,d,f) Wind perturbations ( $\text{m s}^{-1}$ in filled contours and vectors, $\theta$ (K) in unfilled blue contours, w ( $\text{m s}^{-1}$ ) in unfilled black contours, 80% passive tracer initialized in the lowest 1.5 km indicated by gold contours. Magnitude of w multiplied by 10 in plotted vectors for emphasis. Wind perturbations are vectors projected onto the plane of the cross section. . . . .	48
Fig. 3.6	Cross section through C-C' at 4 hours of $P'$ (hPa, filled), $w = \pm 1$ (unfilled black), $\theta'_{rho} = \pm 1$ K (unfilled green), and wind perturbations ( $\text{m s}^{-1}$ ). . . . .	50
Fig. 3.7	(a,d,g,f) $\theta'_\rho$ (K; filled), $1 \text{ m s}^{-1}$ w (gray), and wind perturbations from $t=0$ (vectors) at 0.5 km, 40 dBz reflectivity (black unfilled) and 80% passive tracer concentration at lowest model level. Green lines trace path of parcels that reach $5 \text{ m s}^{-1}$ in a small region of ROD updrafts. (b,e,h,k) Cross section through C-C' of $\theta'_\rho$ (filled), w (black unfilled), wind vectors. Green lines as in previous column. (c,f,i,l) Cross section of wind perturbations (filled), $\theta$ (blue unfilled), w (black unfilled), and 80% passive tracer. Gray lines now represent parcel paths. . . . .	52
Fig. 3.8	Change in parcel height since time $t=0$ for parcels that reach $5 \text{ m s}^{-1}$ in a region of ROD updrafts. Averages and standard deviations shown by initial parcel height for parcels originating between (a) 1 and 2 km, (b) 2 and 3 km, and (c) 3 and 4 km. . . . .	54
Fig. 3.9	3 km average cross section through C-C' (Fig. 3.4a) of CAPE ( $\text{J kg}^{-1}$ ; shaded) and $\Delta z_{lfc}$ (m; magenta unfilled) for parcels lifted from each level after 4 hours. Vertical velocity of $\pm 1 \text{ m s}^{-1}$ (black unfilled), $\theta_\rho = 298, 304 \text{ K}$ (blue unfilled), and passive tracer =80% plotted for reference. . . . .	56
Fig. 3.10	0.5 km $\theta'_\rho$ (K; filled), 0.5 km $w=1 \text{ m s}^{-1}$ (gray), and reflectivity of 40 dBz (black unfilled) after 1 hour of the 3D simulation described in section 3.1 and cross section locations . . . . .	60
Fig. 3.11	(a,b) Cross section through A-A' (Fig. 3.10) at 1 hour. The orange line is contour of 80% (think of the decrease below 1.5 km as 20% removal) of the passive tracer initialized below 1.5 km. (c,d) Results of a dry, 2D -10 K cold bubble drop initialized with the zonal	

	(u) wind profile after 15 minutes (2DX experiment). The orange line is the 10 % contour of passive tracer initialized in the cold bubble. (a,c) $\theta'_\rho$ (filled contours), $w = \pm 1 \text{ m s}^{-1}$ (open black contours), wind vectors. (b,d) wind perturbations from $t=0$ (filled contours and vectors) and $\theta$ (blue contours). . . . .	61
Fig. 3.12	(a,b) Cross section through D-D' (Fig. 3.10) after 1 hour. (c,d) Results of a dry, 2D -10 K cold bubble drop initialized with the meridional (v) wind profile after 15 minutes (2DY experiment). Panel contours and vectors identical to Fig. 3.11 . . . . .	62
Fig. 3.13	Top: An intrusion between two fluids generating a bore in a laboratory. From Rottman and Simpson (1989). Bottom: Two snapshots of a laboratory generated intrusion in a uniformly stratified fluid (Sutherland and Munroe 2014). . . . .	64
Fig. 3.14	Temperature profile through $x=137.75$ (the strongest warming) in Fig. 3.11c,d after 15 minutes (red) and the original temperature profile (black) on a Skew-T Log-P diagram. . . . .	66
Fig. 3.15	Horizontal vorticity ( $\eta * 10^3 \text{ s}^{-1}$ ) and Brunt-Vaisala frequency ( $N^2 \text{ s}^{-2}$ ) of 2D simulations with (a,b) u wind profile (c,d) v wind profile. $\theta$ , $w = \pm 1$ , and passive tracer =80% provided for reference. . . . .	69
Fig. 3.16	Schematic of wave amplification in an environment with shear reversal and shear vectors for key layers. A simplification of processes in the X-direction (u winds) is shown in (a), the Y-direction (v winds) is shown in (b) . . . . .	71
Fig. 3.17	a) Reflectivity (filled contours), 0.5 km $w = 1 \text{ m s}^{-1}$ (black unfilled) and wind vectors, surface $\theta' = -0.5 \text{ K}$ (blue unfilled) at a time shortly before the southwestern edge of the leading line gained a stronger southerly component of motion; b) The minimum height (m) where $5 \text{ m s}^{-1}$ updrafts are observed (colored contours) and 40 dBz reflectivity (black unfilled); c) A hovmöller of the minimum in x direction of the column minimum height of $1 \text{ m s}^{-1}$ updrafts in the box bounded by the magenta lines. Values in the y direction (km) are plotted as a function of time (s) d) as in c, but for $5 \text{ m s}^{-1}$ updrafts. The first dashed line in c,d marks the time of a, the second marks the time of b. . . . .	73
Fig. 3.18	Percentage of initial concentration of parcel tracer released below 500 m at initialization. (a) % at 5 km after 1 hour, (b) % at 5 km after 4 hours, cross sections through (c) A-A' after 1 hour, (d) A-A' after 4 hours, (e) A-A' after 2 hours, and (f) C-C' after 4 hours. Note that color shading is not linear. . . . .	75

Fig. 4.1	Real and idealized soundings . . . . .	81
Fig. 4.2	u (left) and v (right) wind profiles from the Elevated Instability composite sounding created in Chapter 2 (blue) and from the 0428 UTC 25 June 2015 sounding used in Chapter 3. . . . .	84
Fig. 4.3	Observed and smoothed winds from the 0428 UTC 25 June 2015 sounding, and a selection of experimental wind profiles described by Table 4.2. . . . .	85
Fig. 4.4	Comparison of cross section through the 3D moist warm bubble simulation after 1 hour and the dry 2D cold bubble after 15 minutes. (a,c) $\theta'_{rho}$ (K; filled) and +/- 0.5 and 1 hPa pressure perturbations (green contours), 80% contour of passive tracer placed below 1.5 km. (b,d) $\eta$ ( $\ast 10^{-3} s^{-1}$ ; filled) and $\theta$ (K, unfilled blue). $w = +/- 1 m s^{-1}$ (black unfilled) and 10% contour of passive tracer initialized in the cold bubble plotted for reference (orange unfilled). Winds (here perturbations) given by vectors, where w has been multiplied by 10 for visibility. . . . .	88
Fig. 4.5	U0V0 simulation with cold bubble strength variations. (a,c,e) $\theta'$ (K; filled) and +/- 0.5, 1 hpa pressure perturbations (green contours). (b,d,f) $\eta$ ( $\ast 10^{-3} s^{-1}$ ; filled) and $\theta$ (K, unfilled blue) 30 minutes after cold bubble release for (a,b) -10 K, (c,d) -16 K, and (e,f) -24 K warm bubble. $w = +/- 1 m s^{-1}$ (black unfilled) and passive tracer = 10% plotted for reference (orange unfilled). Winds (here perturbations) given by vectors, where w has been multiplied by 10 for visibility. . . . .	90
Fig. 4.6	As in Fig. 4.5, but for 2DX simulations. . . . .	93
Fig. 4.7	As in Fig. 4.5, but for 2DY simulations. . . . .	94
Fig. 4.8	No shear, 2DX, and 2DY experiments repeated with $dx=100$ m and stretched 50-100 m vertical grid ( $dx100dz50stretch$ experiments). (a,c,e) $\theta'$ (K; filled), +/- 0.5, 1 hpa pressure perturbations (green contours), 10% passive tracer concentration. (b,d,f) $\theta$ (K; filled). Wind vectors (with $w \ast 10$ ) shown in all plots. . . . .	96
Fig. 4.9	(a,b) Simulated reflectivity (dBz) and -0.5 K $\theta'$ (blue unfilled) and (c,d) total precipitation (mm) where the precipitation maximum indicated by the black star and accompanying text for (a,c) REAL run (from Chapter 3) after 4 hours and (b,c) CTRL run after 4 hours. . . . .	99
Fig. 4.10	(a) surface $\theta'_p$ (K; filled), simulated reflectivity > 40 dBz at lowest model level (black unfilled), 0.5 km vertical velocity of $1 m s^{-1}$ (gray unfilled), surface passive tracer = 80% (orange unfilled), and surface wind vectors; (b) 0.5 km vertical velocity ( $m s^{-1}$ ;	

- filled), simulated reflectivity > 40 dBz at lowest model level (black unfilled), 0.5 km passive tracer = 80% (orange unfilled), and 0.5 km wind vectors. (c) % of passive tracer initialized below 500 m lofted to 5 km (filled), 0.5 km vertical velocity of 1 m s<sup>-1</sup> (gray unfilled), simulated reflectivity > 40 dBz at lowest model level (black unfilled), and 5 km wind vectors; (d) The minimum height (m) where 5 m s<sup>-1</sup> updrafts are observed (colored contours) and 40 dBz reflectivity (black unfilled) . . . . . 101
- Fig. 4.11 Cross section through Fig. 4.10 (a,b) A-A', (c,d) B-B' after 4 hours through depth of the troposphere. (a,c)  $\theta'_\rho$  (K) in filled contours, w (m s<sup>-1</sup>) in unfilled black contours, +/-0.5 and 1 Pa P' unfilled green contours, and wind vectors. (b,d) Wind perturbations (m s<sup>-1</sup> in filled contours in the plane of the cross section,  $\theta$  (K) in unfilled blue contours, w (m s<sup>-1</sup>) in unfilled black contours, and 80% of passive tracer initialized below 1.5 km (orange). Magnitude of w multiplied by 10 in plotted vectors for emphasis. Approximations of shear vectors for more traditional layers, and for potentially relevant layers shown to the far left. Locations of shear reversal are indicated by dashed grey lines. . . . . 102
- Fig. 4.12 (a,c,g)  $\theta'_\rho$  (K; filled), 1 m s<sup>-1</sup> w (gray), and wind perturbations from t=0 (vectors) at 0.5 km, 40 dBz reflectivity (black unfilled) and 80% passive tracer concentration at lowest model level. Green lines trace path of parcels that reach 5 m s<sup>-1</sup> in a small region of ROD updrafts. (b,e,h) Cross section through B-B' of  $\theta'_\rho$  (filled), w (black unfilled), wind vectors. Green lines as in previous column. (c,f,i) Cross section of wind perturbations (filled),  $\theta$  (blue unfilled), w (black unfilled), and 80% passive tracer. Gray lines now represent parcel paths. . . . . 104
- Fig. 4.13 Simulated reflectivity (filled), -0.5 K surface  $\theta'$  (blue unfilled), and surface wind vectors for (a) U0V0 (b) U25V0 (c) UhookV0 (d) U0VLLJ (e) UhookVLLJ (f) UhookVjet2 (g) UujVLLJ (h) ULLJVuj (i) UujVuj (j) UujVjet2 (k) UujVjet3 and (l) CTRL runs after 2 hours. 106
- Fig. 4.14 Panels as in Fig. 4.13 but after 4 hours. . . . . 107
- Fig. 4.15 4 hour precipitation totals for (a) U0V0 (b) U25V0 (c) UhookV0 (d) U0VLLJ (e) UhookVLLJ (f) UhookVjet2 (g) UujVLLJ (h) ULLJVuj (i) UujVuj (j) UujVjet2 (k) UujVjet3 and (l) CTRL runs. . . . . 109
- Fig. 4.16 Time series of (a) Lowest observed height (m) of 1 m s<sup>-1</sup> updrafts averaged over the domain masked to include updrafts that begin only below 3 km, (b) as in (a) but for 5 m s<sup>-1</sup> updrafts, and (c) domain maximum updraft speeds (m s<sup>-1</sup>). . . . . 111

Fig. 4.17	Time series of (a) Lowest observed height (m) of $-1 \text{ m s}^{-1}$ downdrafts averaged over the domain masked to include downdrafts that extend below 3 km, (b) as in (a) but for $-2 \text{ m s}^{-1}$ downdrafts, and (c) maximum downdraft speeds (domain vertical velocity minimum; $\text{m s}^{-1}$ ). . . . .	112
Fig. 4.18	Panels as in Fig. 4.10 but for UhookVLLJ run. Note cross section locations are different due to different MCS motion, but the labeling of cross section direction/orientation is identical to Fig. 4.10. . . . .	115
Fig. 4.19	Cross section through Fig. 4.18 for UhookVLLJXC run. Panels as in Fig. 4.11. . . . .	116
Fig. 4.20	Parcel trajectories for ROD updrafts in the UhookVLLJ run. Panels as in Fig. 4.12. Cross sections at location B-B' consistent with cross section B-B' in figure 4.19 . . . . .	118
Fig. 4.21	Panels as in Fig. 4.10 but for UhookVjet2 run. Note cross section locations are different due to different MCS motion, but the labeling of cross section direction/orientation is identical to Fig. 4.10. . . . .	121
Fig. 4.22	Cross section through Fig. 4.21 for UhookVjet2 run. Panels as in Fig. 4.11. . . . .	122
Fig. 4.23	Parcel trajectories for ROD updrafts in UhookVjet2 run. Panels as in Fig. 4.12. Cross sections at location B-B' consistent with cross section B-B' in figure 4.22 . . . . .	124
Fig. 4.24	Panels as in Fig. 4.10 but for UujVjet3 run. Note cross section locations are different due to different MCS motion, but the labeling of cross section direction/orientation is identical to Fig. 4.10. . . . .	126
Fig. 4.25	Cross section through Fig. 4.24 for UujVjet3 run. Panels as in Fig. 4.11. . . . .	128
Fig. 4.26	Parcel trajectories for ROD updrafts in the UujVjet3 run. Panels as in Fig. 4.12. Cross sections at location B-B' consistent with cross section B-B' in figure 4.25 . . . . .	129
Fig. 4.27	Panels as in Fig. 4.10 but for UujVuj run. Note cross section locations are different due to different MCS motion, but the labeling of cross section direction/orientation is identical to Fig. 4.10. . . . .	132
Fig. 4.28	Cross section through Fig. 4.27 for UujVuj run. Panels as in Fig. 4.11. . . . .	134
Fig. 4.29	Parcel trajectories for box in wake region where discrete cells develop in the UujVuj run. Panels as in Fig. 4.12. Cross sections at location B-B' consistent with cross section B-B' in figure 4.28 . . . . .	135
Fig. 4.30	Parcel trajectories for box in wake region where discrete cells develop. Panels as in Fig. 4.12. Cross sections at location B-B' consistent with cross section B-B' in figure 4.28 . . . . .	136

Fig. 4.31	Curvature of the wind profile as a function of height (m) for waves approaching from a direction specified along the x-axis for (a) UujVuj run and (b) UujVjet3 run. . . . .	139
Fig. 4.32	Wind profiles for u modification experiments. . . . .	142
Fig. 4.33	Simulated reflectivity and -0.5 surface $\theta'$ after 4 hours for (a) U15V0, (b) U25V0, (c) U35V0, and (d) UhookV0 runs. . . . .	143
Fig. 4.34	W-E cross sections through convective cell at 1 hour. (a,c,e,g) $\theta'_p$ (K; filled). (b,d,f,h) horizontal vorticity ( $\ast 10^{-3} \text{ s}^{-1}$ ; filled), $\theta$ (blue unfilled). All plots show $w = \pm 1 \text{ (m s}^{-1}$ ; black unfilled), passive tracer = 80% (orange unfilled), and wind vectors for reference. . . . .	145
Fig. 4.35	Horizontal vorticity ( $\frac{du}{dz}$ ; $\text{s}^{-1}$ ) and curvature ( $\frac{d^2u}{dz^2}$ ; $\text{s}^{-2}$ ) in solid and dashed lines respectively for the four u modification experiments. Vorticity is computed for the environment orthogonal to the direction of motion. Curvature is computed for the same orthogonal plane, but *in the same direction as the direction of motion* and is multiplied by 100 to scale.) . . . . .	147
Fig. 4.36	As in Fig. 4.34 but after 1 hour. . . . .	149
Fig. 4.37	Passive tracer % of initial concentration after (a,c,e) 2 hours and (b,d,f) 4 hours for (a,b) U25V0, (c,d) U35V0, and (e,f) UhookV0 runs. . . . .	153
Fig. A1	All pre- and post- convective $\theta_e$ (K) and meridional wind ( $\text{m s}^{-1}$ ) profiles from MG teams for (a) 10-11 June (b) 11-12 June (c) 14-15 June (d) 16-17 June (e) 24-25 June (f) 25-26 June. Each hour is represented by a color family with 00xx UTC profiles in reds and 04xx UTC profiles in blues. *All MG profiles on 14-15 June observed post-convective regions. . . . .	173
Fig. A2	All pre- and post- convective $\theta_e$ (K) and meridional wind ( $\text{m s}^{-1}$ ) profiles from MG teams for (a) 30 June – 1 July (b) 1-2 July (c) 5-6 July (d) 8-9 July (e) 9-10 July (f) 10-11 July (g) 12-13 July (h) 13-14 July (i) 15-16 July. Each hour is represented by a color family with 00xx UTC profiles in reds and 04xx UTC profiles in blues. *All MG profiles on 10-11 July observed pre-convective environments. . . . .	174
Fig. A3	PC Loadings for (a) $\frac{d\theta_e}{dz}$ , (b) $\frac{du}{dz}$ , (c) $\frac{dv}{dz}$ . . . . .	176

## CHAPTER 1

### INTRODUCTION

A mesoscale convective system (MCS) is defined as a cluster of thunderstorms with a precipitation area that spans more than 100 km in one direction (e.g. Houze 2004). They can be organized as lines, bows, clusters, vortices, etc. and move quickly or slowly depending, in part, on their organization. MCSs frequently occur downstream from mountain ranges in several regions around the world, including the US Great Plains region. There, they are a common summertime occurrence, and the majority of their rainfall occurs after dark, making them an important contributor to the summertime nocturnal precipitation maximum (e.g. Kincer 1916; Wallace 1975; Maddox et al. 1980).

#### 1.1 MOTIVATION

In the US great plains region, these nighttime precipitation systems can provide critical rainfall for agriculture (Jirak et al. 2003). However, they can also be responsible for severe wind, hail, tornadoes (Houze et al. 1990), and in cases where convection trains or backbuilds over the same location, extreme rainfall and flash flooding (Schumacher and Johnson 2005).

With the rapid improvement in computing capabilities, model representation of deep convection and related processes has also improved (e.g. Done et al. 2004). However, there are still often errors in the timing, location, and precipitation amounts of nocturnal convection across a variety of scales (Davis et al. 2003; Clark et al. 2007). Plus, errors in moist convective forecasts tend to grow rapidly (Zhang et al. 2003), and can have impacts on everything from next day forecasts in the same region (e.g. Schumacher et al. 2013) to forecasts as far downstream as Europe (Rodwell et al. 2013).

In earlier studies (e.g. Davis et al. 2003; Trenberth et al. 2003; Clark et al. 2007; Surcel et al.; Kain et al. 2013; Pinto et al. 2015), the poor MCS forecast skill is attributed, in part, to the representation (or lack thereof) of nocturnal convection in convective parameterizations. These issues remain relevant for some operational models (e.g. Surcel et al.) and global climate models (Trenberth et al. 2003) while it remains impractical to run a convective permitting grid over the globe for extended periods of time. More recent work identifies errors in CI timing and location (Kain et al. 2013) as well as system duration and quantitative precipitation forecasts (QPF) (Pinto et al. 2015).

Improved understanding of MCS environments, maintenance/propagation processes, and environmental feedbacks can help to improve numerical representation of MCSs in climate and operational models, as well as human forecasts of MCSs and their associated hazards. More accurate forecasts can help to enhance public safety, and are particularly valuable to decision makers across a variety of public and private entities (e.g. aviation and the transportation sector, energy, emergency management, large event venues, outdoor recreation, water resource management, etc.) responsible for protection of life, property, and the environment.

## 1.2 DENSITY CURRENTS, BORES, AND GRAVITY WAVES (OH MY!)

One of the challenges of forecasting nocturnal convection, is limited knowledge of the interaction of convection with the nocturnal boundary layer. While some studies suggest that in a nocturnal environment convection that is primarily elevated or even decoupled from the surface (e.g. Moore et al. 2003; Corfidi et al. 2008), others have demonstrated that convection can continue to ingest remarkably stable boundary layer air (Davis et al. 2004; Parker 2008; French and Parker 2010; Billings and Parker 2012). Convective outflow characteristics and resulting propagation speeds are determined by the strength of convective downdrafts (e.g. Trier and Parsons 1993), strength and depth of the nocturnal stable layer (e.g. Parker 2008), the curvature (Rottman and Simpson 1989; Haghi et al. 2017) generated by vertical wind shear, the horizontal vorticity generated by vertical wind shear and whether it balances baroclinic generation of vorticity along the gradient at the edge of the convectively generated cold pool (Rotunno et al. 1988, hereafter, RKW), and the effective inflow layer - a layer where this RKW balance is optimal (e.g. French and Parker 2010). Each one of these factors, in turn, is determined by a number of other variables. For example, stability is influenced by cloud cover, near surface moisture, land and soil characteristics, terrain, and antecedent or nearby convection to name a few. Modifications of the nearby environment by the convection itself can also have positive or negative feedbacks.

A density current describes the flow of a relatively dense fluid in a lighter fluid (Markowski and Richardson 2010). Cold pools are a form of density current whose surface passage is marked by a decrease in temperature, an increase in pressure, and a wind shift. Recently, a number of studies have taken a significant interest in bores, and their potential to sustain or even initiate convection (Blake et al. 2017; Parsons et al. 2018) – so much so, that it was one of the main focus areas of the Plains Elevated Convection at Night (PECAN) field campaign (Geerts et al. 2017). Bores are generated by the intrusion

TABLE 1.1. Surface characteristics of convectively generated propagation mechanisms

	P	T	wind
Cold Pool	semi-permanent increase	Decrease	single wind shift
Non-Undular Bore	semi-permanent increase	no change or increase	single wind shift
Undular bore	semi-permanent increase with oscillations	no change or increase	oscillates with pressure
Solitary wave/ gravity wave	single oscillation	no change or increase	oscillates with pressure
Soliton	multiple oscillations decreasing in amplitude	no change or increase	oscillates with pressure

of convective outflow into a low-level stable layer, and are defined as the semi-permanent deepening of the inversion layer ahead of the density current. The surface passage of a bore is marked by a pronounced and sustained increase in surface pressure, an increase or no change in surface temperature, and a wind shift. When oscillations in pressure and wind (that still result in a net increase/shift) accompany the passage of a bore it is called 'undular' (i.e. with undulations). In order to generate a bore, there must be a low-level stable layer, and in order to sustain a bore the environment must be conducive to wave trapping. This will be discussed in greater detail in chapter 4, but for a more comprehensive background on the theory and a classifications of bores observed during the International H<sub>2</sub>O Campaign (IHOP2002 Weckwerth et al. 2004), see Haghi et al. (2017). A solitary wave is a type of gravity wave generated by the same mechanism as a bore. Similar surface characteristics are observed with its passage, but are not accompanied by a sustained pressure increase. A soliton refers to a packet of solitary waves (e.g. Koch et al. 2008). Finally, gravity waves can be generated by mechanisms other than a density current. Latent heating at or just below the inversion can also generate a gravity wave response capable of sustaining convection (e.g. Schumacher and Johnson 2008). Table 1.1 provides summary of the characteristics described above. Ultimately though, the interaction of convectively generated outflow and wave features under different wind shear conditions influence the convective organization and resulting propagation speed.

### 1.3 PLAINS ELEVATED CONVECTION AT NIGHT (PECAN)

The Plains Elevated Convection at Night field campaign was a large, multi-agency field project motivated by unanswered questions about nocturnal MCSs. The five primary focus areas of PECAN were on 1) nocturnal MCSs (structure, dynamics, microphysics, outflow production/character/transition, inflow layer, etc.), 2) nocturnal CI, 3) bores, 4) the nocturnal LLJ, 5) integration of PECAN observations

with numerical weather forecasts in an effort to aid in forecasting efforts. PECAN operated from 1 June - 15 July 2015 over a domain that originally stretched from northern Oklahoma through Nebraska and from eastern Colorado to western Missouri, but by the end of the project extended to South Dakota, Texas, Iowa, Minnesota, and Indiana. Additional details about PECAN, more specific to upsonde data collection from fixed and mobile platforms, will be discussed in Chapter 2, and a more detailed description of the PECAN goals, instrumentation, and deployments can be found in (Geerts et al. 2017).

While previous campaigns such as PRE-STORM (Cunning 1986), IHOP (Weckwerth et al. 2004), BAMEX (Davis et al. 2003), and MPEX (Weisman et al. 2015) have collected some observations relevant to these goals, PECAN was the first to explicitly focus on nocturnal CI and MCSs (Geerts et al. 2017).

#### 1.4 DISSERTATION GOALS

The overarching goals of this work are to improve 1) the understanding of nocturnal MCS environments and 2) the conditions and relevant processes that support MCS development and propagation in very stable nocturnal environments, with a specific focus on convection that develops behind the leading convective line and offset from the southwest outflow boundary. These more general goals will be addressed through a combination of observation analysis and modeling studies in three projects with a number of more specific research questions.

In Chapter 2, the rich upsonde observational dataset collected during PECAN will be used to expand the current understanding of what constitutes a ‘typical’ nocturnal MCS environment, and to present the first analysis on the most comprehensive upsonde dataset of nocturnal post-convective environments. Specifically, analysis is designed to answer the questions 1) What are the defining thermodynamic characteristics of the pre-convective nocturnal MCS environments sampled? 2) How do these observed MCS environments fit with the common conceptual model? and 3) What are the thermodynamic characteristics of post-convective environments sampled?

One particularly interesting case was observed during PECAN on 24-25 June 2015. As will be shown in Chapter 2, this case had the strongest and deepest observed stable layer with a 8 K  $\theta$  difference between the surface and the top of the stable layer<sup>1</sup>. at just over 800 m. This stands out from the vast majority of cases that had average stable layer strengths between 2 and 4 K over depths of 400-600 m. Additionally, on this day, the observations taken behind the convective outflow boundary, had an average  $\theta'_v$  of only -1.9 K and the largest decrease in  $\theta_v$  was observed in an elevated layer, around 700 m above the surface. The MCS observed on this day had both a forward-propagating leading line and a

---

<sup>1</sup>The top of the stable layer will be defined here as where the slope becomes steeper than moist adiabatic

region of back-building convection behind and offset from the leading line. In these ‘bow and arrow’ type MCSs (Keene and Schumacher 2013), the ‘arrow’ region of back-building convection removed from the leading line is sometimes called rearward off-boundary development (ROD; Peters and Schumacher 2014). In the ROD support mechanism identified in (Peters and Schumacher 2015a), parcels that encounter the edge of the leading southwest outflow boundary may not immediately be lifted to their level of free convection (LFC), but instead may continue to be lifted by a cold pool until they eventually reach their LFCs some distance behind the leading line. However, in the Peters and Schumacher (2015b) study, low-level stability was weaker than that in this PECAN case, and convection produced a cold pool, where the largest  $\theta'$  were generally observed at the surface. The strong stability and weak surface  $\theta'$  observed during the PECAN case and with ROD lead to the questions: 1) Is ROD possible in the absence of a surface cold pool? If so, how is it supported? 2) How might ROD actually begin in this case? These questions are addressed primarily through analysis of an horizontally homogeneous 3D simulation initialized with a pre-convective sounding taken shortly before the passage of the leading convective line. By removal of external forcing mechanisms, it becomes possible to isolate specific MCS-environment interactions that contribute to convective maintenance in this environment.

The success of idealized simulations to produce an MCS from a single warm bubble in Chapter 3, and the subsequent development of ROD convection suggest that something about the environment itself is conducive not only to the development of MCSs themselves, but also the highly nonlinear structure of the bow-and-arrow-type MCS. Additionally, dry 2D experiments where a cold bubble is dropped onto a stable layer have remarkable resemblance to cross sections through the moist 3D experiment. These results motivated a number of sensitivity experiments in two and three dimensions, with an emphasis on wind shear modifications, that are used in chapter 4 to address the questions 1) What is the resulting behavior when cold air impinges on a strong low-level stable layer, 2) How is this behavior modified by changes in stability and shear. These insights are then used to help understand 3) What vertical wind shear characteristics are supportive of a) an MCS b) ROD in an environment with strong low-level stability.

There are still many unanswered questions about MCS- environment interactions, especially in highly 3-dimensional MCSs. The environmental and dynamical changes that occur with the transition to a nocturnal environment, the heterogeneity of these changes within the convective region of a single case, and the variability of the nocturnal environment from case to case add additional layers of complexity. This work represents a contribution to a much larger effort to analyze and synthesize the data

collected during PECAN, and to apply insights gleaned to address known knowledge gaps, but also to ask new questions about nocturnal MCSs and their environments with the ultimate goal of improving their prediction.

## CHAPTER 2

### EVOLUTION OF PRE- AND POST-CONVECTIVE ENVIRONMENTAL PROFILES FROM MESOSCALE CONVECTIVE SYSTEMS DURING PECAN

#### 2.1 INTRODUCTION

Mesoscale convective systems (MCSs) play a critical role in the warm season nocturnal precipitation maximum over the United States Great Plains region (e.g. Wallace 1975; Maddox 1980; Fritsch et al. 1986; Carbone et al. 2002). These systems provide essential rainfall, but are often associated with severe weather (Jirak et al. 2003; Maddox 1980). Despite its frequency and importance, nocturnal convection is not particularly well forecast in numerical models (Davis et al. 2003; Clark et al. 2007; Johnson and Wang 2012; Johnson et al. 2013).

MCSs span a distance of  $\sim 100$  km or larger and can have a variety of organizational modes (Parker and Johnson 2000; Houze 2004; Schumacher and Johnson 2005). They are often associated with a mid-level shortwave trough, a baroclinic zone (such as a warm or stationary surface front in the US), a stable boundary layer, a low-level jet (LLJ), and the associated advection of warm, moist, high  $\theta_e$  air in an elevated layer (Maddox 1983; Trier and Parsons 1993; Augustine and Caracena 1994; Laing and Fritsch 2000; Moore et al. 2003; Peters and Schumacher 2014). Because of the nocturnal nature of many MCSs, the inflow layer is often thought to be primarily elevated (e.g. Moore et al. 2003; Corfidi et al. 2008; Geerts et al. 2017).

In a study of a nocturnal mesoscale convective complex (MCC) during PRE-STORM (Cunning 1986), large increases in  $\theta_e$  were observed in an elevated layer between 0200 and 0500 UTC (Trier and Parsons 1993). Changes were associated with the southward progression of a shallow surface front, and an increase in moisture advection in conjunction with the onset of the southerly nocturnal LLJ. These observations led to a schematic (Fig. 20 in Trier and Parsons 1993) of isentropic ascent of high  $\theta_e$  air associated with the LLJ over a quasi-stationary frontal zone. This has become a relatively common conceptual model for nocturnal MCS environments (e.g. Fritsch and Forbes 2001; Moore et al. 2003; Trier et al. 2006).

An increase in  $\theta_e$  can also lead to a large increase in potential instability over an elevated layer. Potential instability (convective instability) occurs when the equivalent potential temperature  $\theta_e$  of the environment decreases with height ( $\frac{d\theta_e}{dz} < 0$ ; Rossby 1932; Hewson 1937). This elevated instability serves as a critical source of inflow air to storms located on the cool side of a frontal boundary (Trier et al.

2006), or above a nocturnal stable layer (Parker 2008) and is related to layer lifting, a process considered critical in the development of nocturnal deep convection (Moncrieff 1992; Bryan and Fritsch 2000; Houze 2004; Alfaro and Coniglio 2018). In addition to the transport of warm, moist air, the LLJ can be a source of kinematic forcing that can make environments more favorable for MCS development (e.g. Trier and Parsons 1993; Augustine and Caracena 1994; Tuttle and Davis 2006; Trier et al. 2006).

Nocturnal convection is usually associated with a statically stable boundary layer (See Schultz et al. (2000) for an in-depth review of instabilities.) brought about by nocturnal cooling (e.g. Trier and Parsons 1993; Corfidi et al. 2008; Parker 2008; Geerts et al. 2017) or with MCS initiation on the cool side of a quasi-stationary or warm front (e.g. Maddox et al. 1978; Trier and Parsons 1993; Corfidi et al. 2008; Peters and Schumacher 2014). Past studies have suggested that depending on the strength of convective downdrafts (e.g. Trier and Parsons 1993; Marsham et al. 2010), the amount of low-level cooling (e.g. Parker 2008), and more recently the curvature of the wind shear (Haghi et al. 2017), that MCS outflow may manifest as surface cold pools (e.g. Trier et al. 2006; Parker 2008; Peters and Schumacher 2015a), bores (e.g. Crook 1988; Wilson and Roberts 2006; Haghi et al. 2017), gravity waves (Crook and Moncrieff 1988; Parker 2008; Schumacher 2009; Marsham et al. 2010) or other combinations of gravity waves and gravity currents (e.g. Raymond and Rotunno 1989; Haertel et al. 2001). There is additional evidence that with changing conditions, MCSs may also transition from one driving mechanism to another (Parker 2008; Trier et al. 2011). Despite previous understanding that in the presence of a stable layer, the primary inflow is decoupled from the surface, more recent work has shown that some MCSs may continue to ingest stable boundary layer air, even after significant cooling has occurred (Davis et al. 2004; Parker 2008; French and Parker 2008; Billings and Parker 2012). The interaction of convection with a stable boundary layer is not well understood, yet their relationship plays a key role in determining the propagation and maintenance of nocturnal MCSs.

A number of past field campaigns have used relatively closely-spaced, high-frequency radiosonde launches from fixed and mobile assets to learn about convection and convective environments in the Great Plains (e.g. PRE-STORM, Cunning (1986); BAMEX, Davis et al. (2004); VORTEX2, Wurman et al. (2012); MPEX, Weisman et al. (2015)). In a manner similar to the present study, Correia and Arritt (2008) used dropsonde observations from the Bow Echo and MCV Experiment (BAMEX) to construct composite soundings of seven distinct MCS sub-regions. Their study placed a greater emphasis on spatio-temporal variability than case-to-case variability, and had a notable focus on transition and stratiform regions. Their results note similar pre-convective environments to previously mentioned studies and

large thermodynamic variability in transition and stratiform regions below 0 ° C. Over the years, technological improvements have changed the definition of closely-spaced and high-frequency. This, combined with different sampling strategies, has improved our ability to observe smaller-scale changes in the convective environment.

During the 2015 Plains Elevated Convection at Night (PECAN) field experiment, a vast array of instruments were deployed by a multitude of research groups to observe nocturnal MCSs and their essential ingredients, in order to work towards improving the low predictive skill of their forecasts. PECAN was the first of its magnitude to explicitly focus on nocturnal environments (Geerts et al. 2017). During the campaign, missions or intensive observing periods (IOPs) were conducted to observe convective initiation (CI), bores, MCSs, and the LLJ. During each of these IOPs, numerous observations were collected from both fixed and mobile platforms. The work presented here focuses on documenting and analyzing the radiosonde observations collected in MCS environments from all platforms. For a more detailed description of PECAN goals, assets, and deployments see Geerts et al. (2017).

The goals of this paper are to address the questions: 1) What are the defining thermodynamic characteristics of the pre-convective nocturnal MCS environments sampled? 2) How do these observed MCS environments fit with the common conceptual model? 3) What are the thermodynamic characteristics of sampled post-convective environments? More specifically, how frequently are cold pools observed? How strong/deep/variable are they? This work applies a cluster analysis to the rich dataset of nocturnal MCS soundings collected during PECAN to explore the different pre-convective MCS environments observed. Next, temperature perturbations observed in post-convective regions are compared between cases, and related to pre-convective stability.

## 2.2 OVERVIEW OF MESOSCALE CONVECTIVE SYSTEM CASES DURING PECAN

Thirteen MCS cases and two bore cases from PECAN with observations of MCS environments were selected for this study. One MCS IOP and three aircraft-only MCS unofficial field operations ("UFOs") were not included in this study due to a missed deployment (storms developed north of the array and propagated north) and lack of radiosonde observations, respectively. A list of cases used<sup>1</sup> and the region where they were observed can be found in Table 2.1.

Figure 2.1 shows fields from the 0000 UTC Rapid Refresh (RAP) analysis (Benjamin et al. 2016) for each case. Cases are generally associated with a N-S temperature gradient, predominately westerly

---

<sup>1</sup>Nighttime events often begin on one day and end the next. To reduce confusion, cases are referred to using two days in the text, and by the second day in the figures. The first is the day an IOP/UFO was selected, teams deployed, and often when observations began. The second is when the majority of observations actually took place in UTC.

TABLE 2.1. Selected cases, region of intensive observation, and platforms available in identified region.

Date	Region	Available Platforms	Pre-Convective Soundings	Post-Convective Soundings
10-11 June	S.E. NE	MGs, FP3-FP6, MPs	8	14
11-12 June	S.W. KS	MGs, FP1-FP3, FP5, MPs	16	21
14-15 June	S.C. KS	MGs, FP1, FP2, FP6, MPs	11	7
16-17 June	S.W. NE	MGs, FP3-FP5, MPs	23	12
24-25 June	S.E. IA	MGs, MP3, MP4	18	8
25-26 June	N.E. KS	MGs, FP2-FP6, MPs	28	16
30 June - 1 July	N.W. MO	MGs, FP4, MPs	19	21
1-2 July	W. MO	MG1, MG2, MP1	7	2
5-6 July	SD	MGs, FP4, FP5, MPs	19	7
8-9 July	TX Panhandle	MGs	9	9
9-10 July	TX Panhandle	MGs, FP2	19	2
10-11 July	KS/NE border	MGs, FPs, MP2-MP4	39	0
12-13 July	S.E. MN	MGs, MP1	26	4
13-14 July	W. IN	MGs, MP1	5	6
15-16 July	S.E. NE	MGs, FP2-FP6, MPs	48	20
Total			295	149

upper-level flow, and 850-hPa<sup>2</sup> RAP-analyzed southerly winds in the target region. There are, however, differences in the orientation of the surface front and the 500-hPa heights, coverage of the 850-hPa southerly winds, and the existence of an upper-level wind maximum from case to case. Note that a 0000 UTC analysis may not provide an accurate depiction of the LLJ strength for a particular case, since the LLJ typically develops after sunset, which occurs around 0200 UTC over much of the Great Plains at this time of year. A more detailed analysis based on composites of observed MCS environments and a more detailed case analysis for representative cases are discussed in section 2.42.4.4.

<sup>2</sup>An 850-hPa analysis was selected because while it may be too high for an accurate depiction of the LLJ in some observed cases, a 925-hPa analysis is below ground in others.

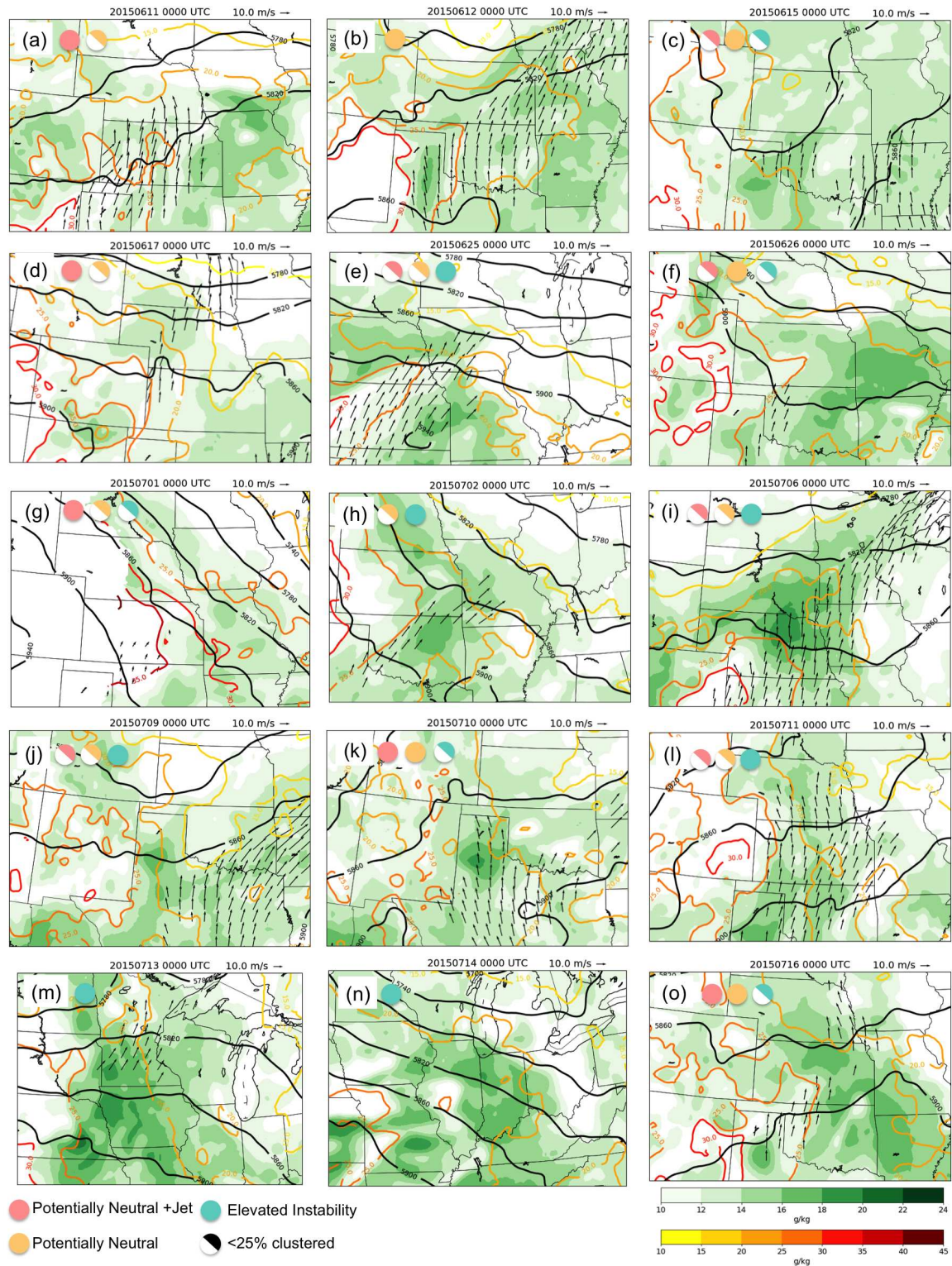


FIG. 2.1. 0000 UTC Rapid Refresh (RAP) analysis for each case. 500 hPa heights (m; black contour), 850 hPa wind vectors where  $v > 10 \text{ m s}^{-1}$ , 850 hPa temperature ( $^{\circ}\text{C}$ ; color contours), and 850 hPa mixing ratios ( $\text{g kg}^{-1}$ ; green filled). Colored dots represent clusters in which soundings were grouped. Half shaded circles indicate  $< 25\%$  of soundings the case were in the cluster.

IOPs sampled a range of MCS structures from a well-organized, progressive bow echo with a trailing stratiform region on 12-13 July in MN (Fig. 2.2m), to MCSs with quasi-stationary or training cells (Fig. 2.2e,j), and many more loosely organized cases with various structures such as those of 25-26 June and 15-16 July (Fig. 2.2f,o). In some cases, observations primarily captured weakly-organized early convection and upscale growth (e.g. Fig. 2.2d). In others, observations captured the weakening of a convective line, as convective cells transitioned to stratiform precipitation (e.g. Fig. 2.2k). In one case, 13-14 July, an MCS only formed to the south and east of the target location well after the IOP ended. It was still included here given the favorable MCS environment and forecast.

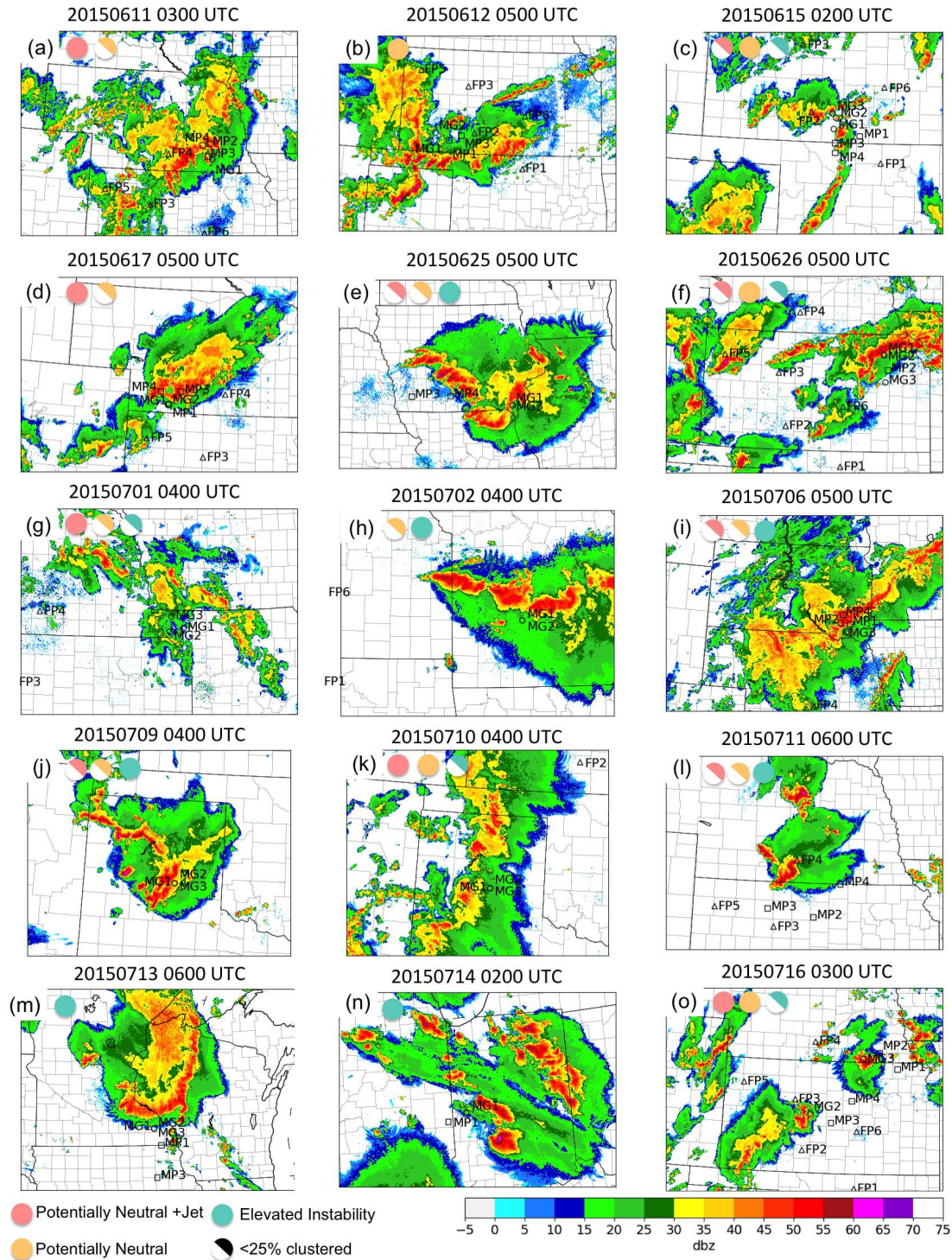


FIG. 2.2. Radar reflectivity from the NSSL Multi-Radar Multi-Sensor (MRMS) system (Zhang et al. 2016) of observed convection during each IOP and positions of mobile assets at (a) 0300 UTC 11 June (b) 0500 UTC 12 June (c) 0200 UTC 15 June (d) 0500 UTC 17 June (e) 0500 UTC 25 June (f) 0500 UTC 26 June (g) 0400 UTC 1 July (h) 0400 UTC 2 July (i) 0500 UTC 6 July (j) 0400 UTC 9 July (k) 0400 UTC 10 July (l) 0600 UTC 11 July (m) 0600 UTC 13 July (n) 0200 UTC 14 July (o) 0300 UTC 16 July. Colored dots represent case sounding clusters as in Figure 2.1. Open circle, square, and triangle symbols are used for MG, MP, and FP assets respectively.

TABLE 2.2. Sources of radiosonde data included in this study.

Platform	Location	Radiosonde Type	Citation
MGs	Mobile	Vaisala RS-92	Ziegler et al. (2016)
FP1	Lamont, OK	Vaisala RS-92	UCAR/NCAR - Earth Observing Laboratory. (2015a)
FP2	Greensburg, KS	iMet-1	Vermeesch (2016)
FP3	Ellis, KS	Vaisala RS-92	Clark (2016)
FP4	Minden, NE	Vaisala RS-92	UCAR/NCAR - Earth Observing Laboratory. (2016a)
FP5	Brewster, KS	Vaisala RS-92	UCAR/NCAR - Earth Observing Laboratory. (2016b)
FP6	Hesston, KS	Vaisala RS-92	Holdridge and Turner (2016)
MP1	Mobile	iMet-1	Klein et al. (2016)
MP2	Mobile	iMet-1	Knupp (2015)
MP3	Mobile	Vaisala RS-92	Wagner et al. (2016)
MP4	Mobile	Vaisala RS-92	UCAR/NCAR - Earth Observing Laboratory. (2016c)
		Lockheed	
NWS	Relevant	Martin LMS-6/ Vaisala RS-92	UCAR/NCAR - Earth Observing Laboratory. (2015b)

## 2.3 METHODS

### 2.3.1 Dataset

Radiosondes were launched from a number of fixed and mobile sites throughout PECAN. A list of those used in this work are given in Table 2.2. Radiosonde data was quality controlled (QC'd) by NCAR's Earth Observing Laboratory and post-processed by Aspen software (see <https://www.eol.ucar.edu/software/aspen>). The six fixed sites, referred to as fixed PECAN integrated sounding arrays (PISA; FPs), were located in Kansas, Nebraska, and Oklahoma. During MCS missions, these sites often launched radiosondes every three hours beginning at 0000 UTC. Sometimes, the FP sites did additional launches during the day to aid in forecasting efforts. The four mobile PISAs (MPs) also had the capability to launch soundings, and when they participated in MCS IOPs<sup>3</sup>, they typically launched radiosondes every 1-3 hours.

While MPs were stationary during the IOP, Mobile GPS radiosonde launch vehicles (MGs) were highly-mobile. The MGs' primary responsibility was to launch radiosondes with high-temporal/spatial frequency throughout the duration of the IOP. Two main sampling strategies were used for the MGs. In one, teams were staggered parallel to the convective line and would reposition after its passage to sample along-line spatial heterogeneities (as in 10-11 June); in the other, teams were co-located and did 'rapid-fire' launches at 15-20 minute intervals to sample the rapid temporal changes as the convection

<sup>3</sup>Toward the end of the project, there were some split missions, and some MCS IOPs took place outside of the originally defined PECAN domain. The MPs did not always accompany the MCS IOP but when they did, they provided valuable additional radiosonde data.

approached. The latter method tended to be preferred as the project progressed. Where appropriate, standard NWS soundings were used to supplement the data set. In the 15 MCS cases used (Table 2.1), a relatively large number of radiosondes sampled an MCS environment during at least one stage of its life cycle leading to a total of 295 pre-convective and 149 post-convective soundings. Additional details about PECAN radiosonde observations in MCS environments can be found in Appendix A.

### 2.3.2 Cluster Analysis

During early analysis, it became clear that potential (in)stability ( $\frac{d\theta_e}{dz}$ ) varied widely from case to case, but different cases appeared to have some common features at low levels. In order to objectively search for patterns to categorize the pre-convective soundings, a cluster analysis was used. The vertical gradient in equivalent potential temperature ( $\theta_e$ ) and both ground-relative wind components (u,v) were chosen as the variables used to identify clusters.  $\theta_e$  is a function of both temperature and moisture and as mentioned previously, its vertical gradient is related to the potential (in)stability of a layer. Changes in zonal and meridional wind components can be used to determine the location and existence of a nocturnal low-level wind maximum, and were included for this reason. Profiles of  $\theta_e$ , u, and v were interpolated to a 25 m vertical grid, and smoothed using a Gaussian smoother ( $\sigma = 100$  m, 50 m, 50 m respectively) to reduce noise but preserve structure. Soundings that did not reach 3 km in altitude were not included in this analysis, and analysis was only performed on the lowest 3 km of all remaining soundings. Changes in the selected variables with height ( $\frac{d\theta_e}{dz}$ ,  $\frac{du}{dz}$ , and  $\frac{dv}{dz}$ ) were computed and then standardized, using a global standard to maintain profile shape, so that they could be compared across cases. Principal component analysis (PCA) is commonly employed to reduce dimensionality in large datasets containing highly correlated variables (Herman and Schumacher 2018). PCA was applied here and three principal components were retained. Additional details about the PCA and related decisions can be found in Appendix B.

In order to focus on understanding differences within pre- and post- convective environments themselves, pre- and post- convective environments were first sorted manually based on the profiles of  $\theta_v$ ,  $\theta_e$ , wind, and the launch location relative to radar fine lines (where applicable). For the purposes of this analysis, a “pre-convective” sounding is one that was taken prior to the observation of a cold pool produced by the observed MCS at a particular location. Therefore, a “post-convective” sounding, for this purpose, is one that has been modified at low-levels by the outflow produced by the observed MCS. The number of pre- and post- convective soundings that made it to 3 km are listed in Table 2.1 by case.

Different clustering algorithms have different advantages and disadvantages. A number of different clustering techniques, including K-means (commonly used in geosciences), explored with various settings produced similar results. The method selected, Shared Nearest Neighbors (SNN; Ertöz et al. 2002), is able to produce clusters based on identification of nearest neighbors, but without forcing every single profile into a category, and is not limited by datasets with variations in density like many other methods. The clusters produced fit well with patterns identified qualitatively in  $\theta_e$  profiles. Since the clustering method itself is not the focus of this work, more specific details about it can be found in Appendix B.

Composite soundings for each cluster were generated using the technique described in Trier et al. (2000), where rather than truncating or extrapolating soundings to a common surface elevation, radiosonde data is interpolated to a normalized sigma ( $\sigma = \frac{p}{p_s}$ ) coordinate. Advantages of this method are its intention to preserve boundary layer structure and conserve the mean CAPE and CIN of the soundings used to create the composite. Levels are chosen such that  $\Delta\sigma = 0.01$  at lower levels and 0.02 aloft (Trier et al. 2000). The mean pressure at  $\sigma = 1$  for each cluster was used to compute the pressure at each sigma level in each cluster. The composites presented here were computed by taking a strict average of all soundings in each cluster, but compositing first on the mean of each case does not change results substantially.

#### 2.4 CLUSTER ANALYSIS RESULTS ON ENVIRONMENT SOUNDINGS

The cluster analysis sorted 252 of the 295 soundings into three distinct clusters. The first cluster, made up of 77 profiles from five primary cases (see Table 2.3 for individual cluster breakdowns), is approximately potentially neutral (constant  $\theta_e$  with height) in the lowest 2.5 km (Fig. 2.3a), and has evidence of a 10-20  $\text{m s}^{-1}$  low-level southerly wind maximum below 500 m (Fig. 2.3b). For this reason, this cluster will be referred to as ‘Potentially Neutral + Jet.’ This cluster also has a slight maximum in easterly winds in the lowest 250 m (Fig. 2.3b). Some of the clustered soundings, especially those from 15-16 July and 9-10 July, are even potentially unstable at low-levels. At the same time, some of the profiles, including the two cases just mentioned, have low-level static stability (Fig. 2.4a).

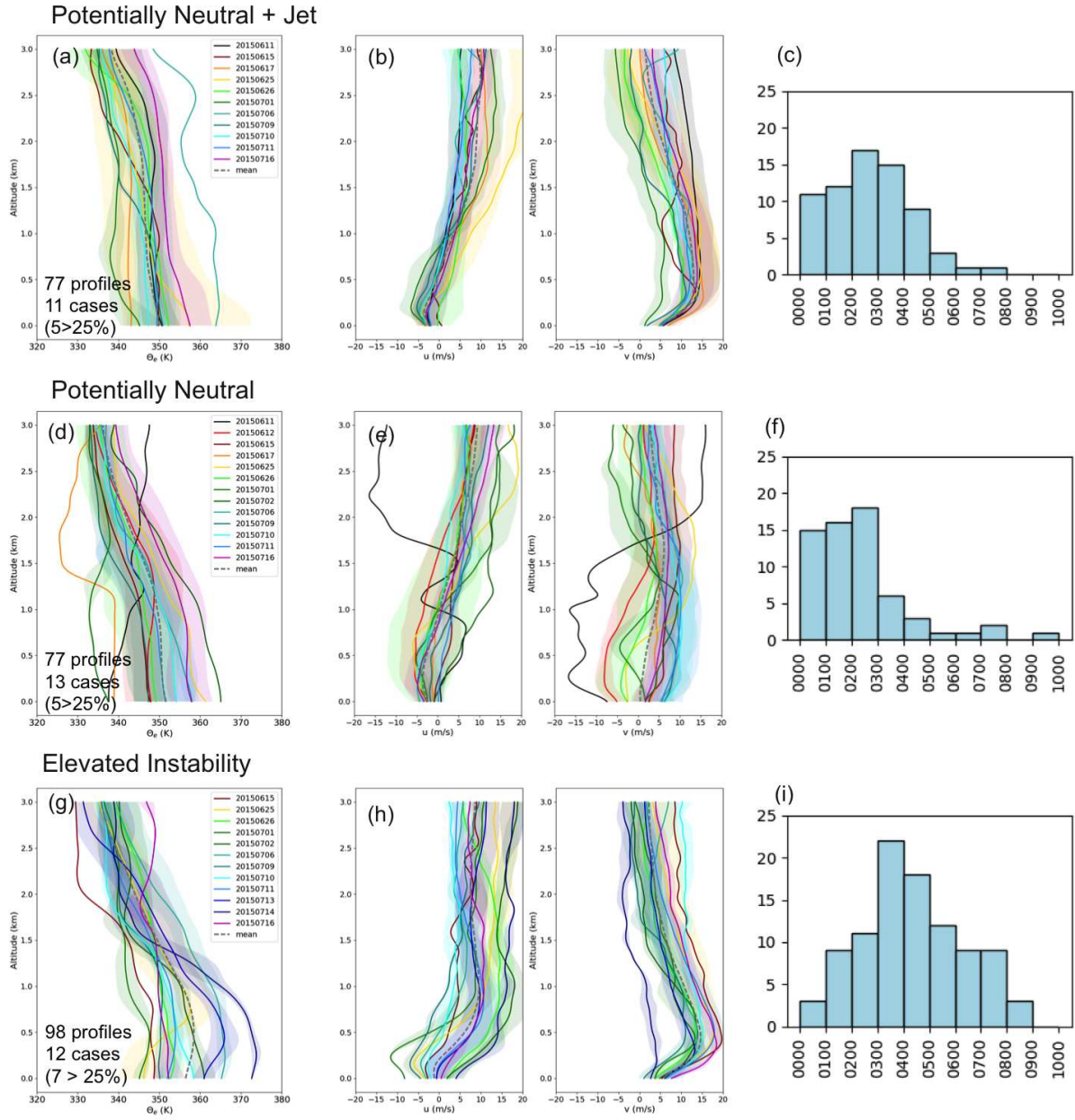


FIG. 2.3. Mean (solid lines) and standard deviation (semi-transparent shading) of (a,d,g)  $\theta_e$  (K), (b,e,h)  $u$ , and  $v$  ( $\text{m s}^{-1}$ ) below 3 km for each case in each cluster. Dates of intensive observing periods (IOPs) are given by different colors. The number in parentheses in the lower left of (a,d,g) is the number of cases with more than 25% of pre-convective soundings clustered (Listed in Table 2.3). Cluster means given by the gray dashed line. Histograms in (c,f,i) show a distribution of launch times by hour for each cluster.

TABLE 2.3. Number of soundings clustered for each case in each cluster. An asterisk denotes that at least 25% of soundings from the given case were clustered.

Date	Pre-Convective Soundings	Potentially Neutral + Jet	Potentially Neutral	Elevated Instability
10-11 June	8	7*	1	0
11-12 June	16	0	15*	0
14-15 June	11	1	9*	1
16-17 June	23	22*	1	0
24-25 June	18	4	1	7*
25-26 June	28	4	11*	4
30 June - 1 July	19	6*	2	2
1-2 July	7	0	1	6*
5-6 July	19	1	2	12*
8-9 July	9	2	2	5*
9-10 July	19	6*	7*	4
10-11 July	39	5	4	28*
12-13 July	26	0	0	25*
13-14 July	5	0	0	2*
15-16 July	48	19*	21*	2
Total	295	77	77	98

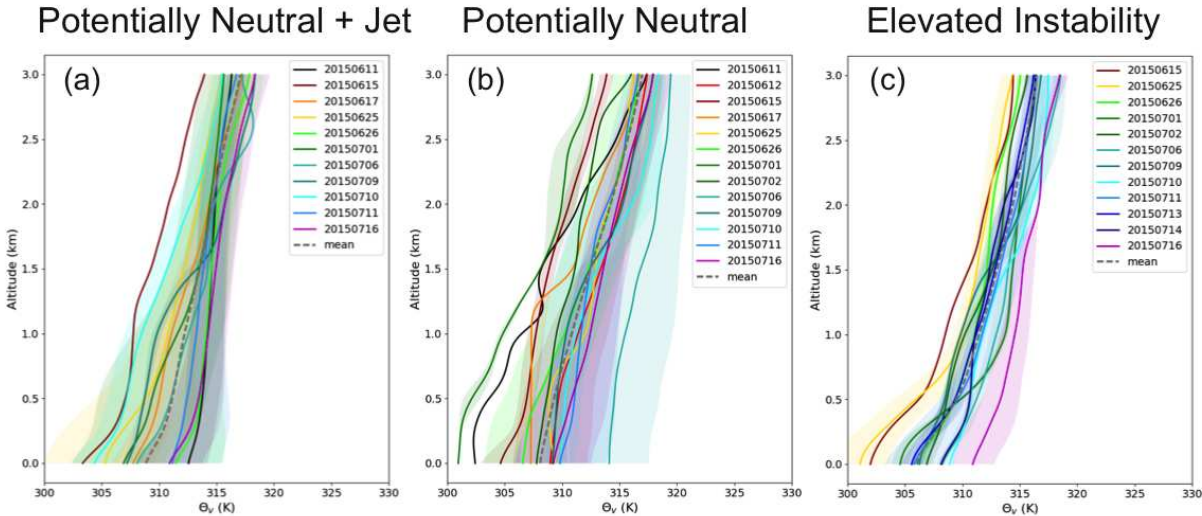


FIG. 2.4. Mean (solid lines) and standard deviation (semi-transparent shading)  $\theta_v$  (K) below 3 km for the (a) Potentially Neutral + Jet, (b) Potentially Neutral, and (c) Elevated Instability clusters. Dates of intensive observing periods (IOPs) are given by different colors. Cluster means are given by the gray dashed line.

The second cluster is made up of 79 profiles, primarily from 5 different cases (Fig. 2.3d, Table 2.3). This cluster is also potentially neutral at low levels, but becomes potentially unstable between 1 and 1.5 km (Fig. 2.3d). Unlike the previous cluster, most of the profiles in this cluster have little-to-no static

stability near the surface (Fig. 2.4b). Perhaps the greatest difference between this cluster and the first is that low-level winds are either considerably weaker southerlies, or even northerly (Fig. 2.3e). This cluster will be referred to as ‘Potentially Neutral’. This cluster also has a deeper layer with an easterly wind component.

The third cluster is made up of 98 profiles from 7 primary cases, most notably the 5-6 July, 10-11 July, and 12-13 July events (Fig. 2.3g). Five additional cases were represented in this cluster by < 25% of the case’s pre-convective soundings. The cluster name “Elevated Instability” was selected because 1) the most unstable parcel for profiles in this category is clearly elevated ( $\theta_e$  maximized above the surface) and 2) A deep region of potential instability can be found extending from the point of maximum  $\theta_e$ . This  $\theta_e$  maximum occurs at slightly different levels, between just below 0.5 km and 1 km, in the dominant cases. Below the elevated  $\theta_e$  maximum, the profiles are potentially stable, while above, they are potentially unstable. Note that just because the most unstable parcel in these environments is elevated, does not mean that the MCSs themselves are elevated. A few of the profiles have a slight easterly component near the surface that maximizes at or below 250 m (Fig. 2.3h). Above that, winds shift to more westerly just above 500 m. Some of the profiles do not have a near surface easterly component, and rather have nearly no zonal component (< 5 m s<sup>-1</sup> either direction; Fig. 2.3h). In this cluster, southerly winds increased between 10 and 15 m s<sup>-1</sup> over the lowest 500 m (Fig. 2.3h). The magnitude of southerly low level winds observed in this cluster are only slightly larger (on average) than those observed in the potentially neutral + jet cluster. This cluster also has a deeper and stronger layer of static stability than either of the other clusters (Fig. 2.4c).

Histograms of the launch times of clustered soundings indicate that soundings in the two potentially neutral clusters tended to be launched earlier in the evening than those in the elevated instability cluster (Fig. 2.3c,f). Admittedly, the potentially neutral cluster without the strong low-level wind maximum has more daytime-like environmental characteristics, and early soundings from many of the cases ended up in this category. However, a non-negligible number of soundings in the potentially neutral, no-jet cluster were launched well after dark, especially during the 11-12 June and 25-26 June cases. The vast majority of the soundings in the potentially neutral + jet cluster were still launched after sunset (~0200 UTC). The addition of a single case, 10-11 July, in which the primary MCS observations took place much later than the majority of other observed cases nearly doubles the number of launches after 0600 UTC in the elevated instability cluster. When the same cluster analysis was run on soundings launched after 0200 UTC, and even after 0400 UTC, the same basic clusters emerge.

### 2.4.1 *Distribution of Cluster Convective Parameters*

Violin plots of convective parameters computed from soundings that make up the clusters give an idea of the distribution of these parameters in the different environments identified. The elevated instability cluster has a larger distribution of, and on average more MUCAPE and a smaller distribution of, and less MUCIN than the two potentially neutral clusters (Fig. 2.5a,b). This fits well with the idea that the flux of high  $\theta_e$  air in an elevated layer contributes to destabilization aloft. The potentially neutral cluster with no jet generally had more MUCAPE and less MUCIN than its counterpart with a jet, which is most likely due to the lack of low-level (potential and static) stability and larger near surface  $\theta_e$  values. Distributions of surfaced-based (SB) CAPE and CIN were actually quite similar between clusters, with slightly larger values of SBCAPE and SBCIN observed in the elevated instability cluster (Fig. 2.5c,d). In general, MUCAPE is larger than SBCAPE in all three clusters, but MUCIN is also larger. In keeping with the elevated nature of the elevated instability cluster, the majority of the most unstable parcels are located above the surface, though the mean and median are only about 50 hPa above the surface (Fig. 2.5e). In the other two clusters, the mean difference between the surface pressure and most unstable parcel pressure is very small. In profiles that are nearly potentially neutral, the most-unstable parcel height is sensitive to small changes in  $\theta_e$  in the profile, which is likely the reason for their large range. Precipitable water had a narrower range and larger mean/median values in the elevated instability cluster; the high  $\theta_e$  values are associated with an influx of moisture in the inflow layer. 0-6 km bulk wind difference (hereafter referred to as shear<sup>4</sup>) didn't vary much from cluster to cluster, but the 0-1 km bulk wind difference was notably larger in the two clusters with elevated maxima in southerly low-level winds (potentially neutral + jet and elevated instability clusters), and largest in the elevated instability cluster.

---

<sup>4</sup>Note: Bulk wind difference is often used in lieu of wind shear to demonstrate changes in wind with height

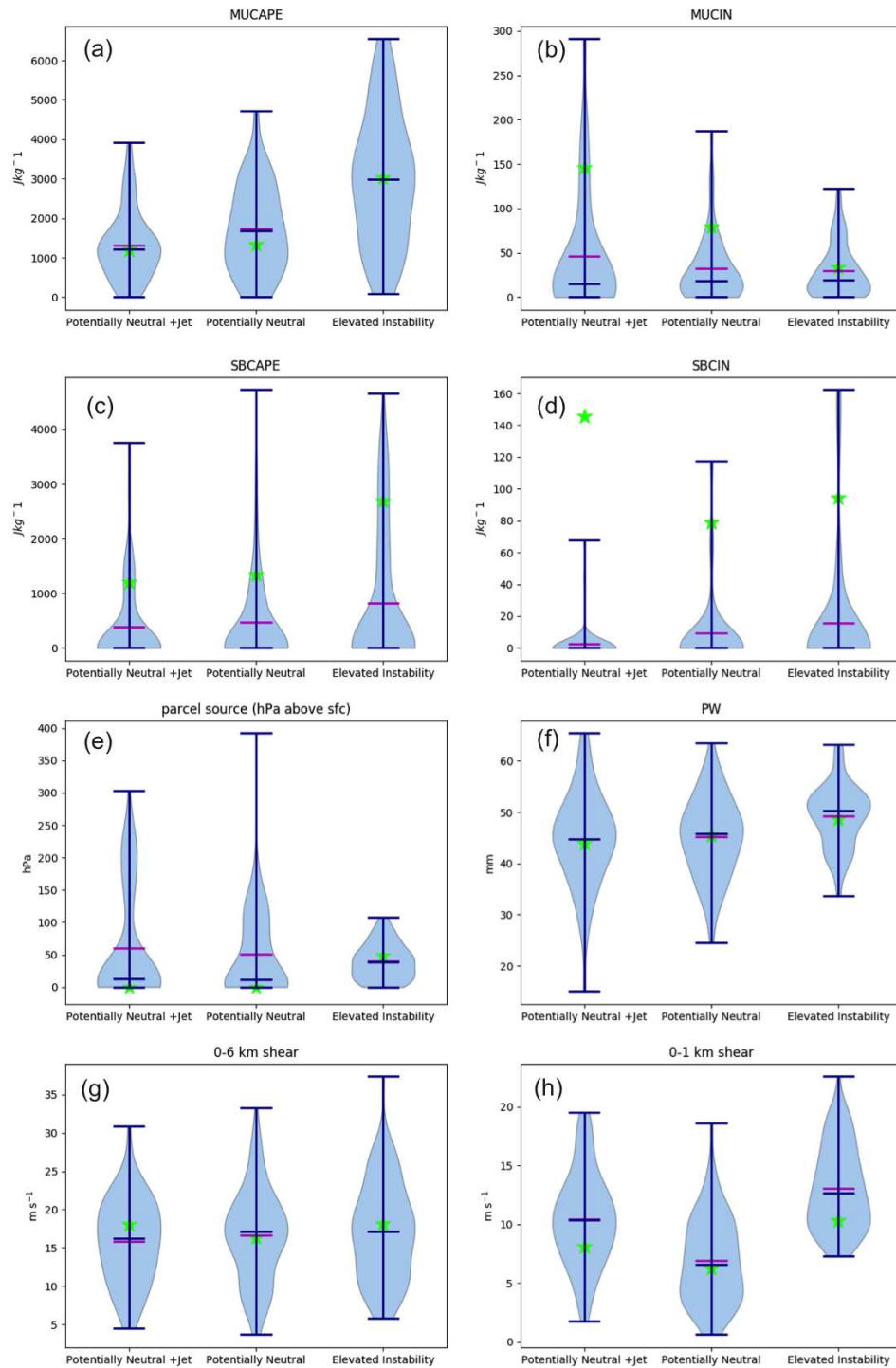


FIG. 2.5. Violin plots of (a) MUCAPE ( $\text{J kg}^{-1}$ ), (b) MUCIN ( $\text{J kg}^{-1}$ ), (c) SBCAPE ( $\text{J kg}^{-1}$ ), (d) SBCIN ( $\text{J kg}^{-1}$ ), (e) MU parcel source (hPa above surface), (f) precipitable water (PW; mm), (g) 0-6 km shear (knots), and (h) 0-1 km shear (knots) for each cluster. Plots indicate the distribution (shaded); min/max (blue horizontal lines at top and bottom of plot respectively), median (middle blue horizontal line), mean (magenta) of the set of soundings. The mean and median are equal if the magenta line is not visible. The green star is the variable value in the composite soundings.

### 2.4.2 Composite Soundings

The thermodynamic profiles at low-levels of both potentially neutral composites (Fig. 2.6) resemble the daytime convective boundary layer, but a very shallow inversion layer is present near the surface of the potentially neutral + jet composite (below about 275 m). As discussed in the cluster results, the potentially neutral + jet case has evidence of a low-level wind maximum of 10-15 m s<sup>-1</sup> out of the SSE. However, below 800 hPa this cluster was actually drier than both of the other clusters. The greatest RH is found around 700 hPa, around approximately the same level as  $\theta_e$  profiles in this cluster transition to potentially unstable. In the potentially neutral cluster without strong low level winds, the dew point decreases slowly with height at low levels, and the environment has more moisture over a greater depth than either of the other composites.

At low levels, the elevated instability cluster is nearly isothermal in temperature, and has the largest dew point of the clusters. There is an associated increase in low-level winds to just over 15 m s<sup>-1</sup> out of the southwest at about 500 m above the surface (Fig. 2.6). The winds are stronger over a deeper layer, and more westerly compared to the wind maximum in the potentially neutral + jet cluster. The major differences in temperature between the clusters are small, and occur almost entirely below 900 hPa. Differences in moisture and wind occur over slightly deeper layers, and are larger.

In two of the three clusters, very little stabilization occurred at low levels. When soundings from before 0200, 0300, or 0400 UTC are withheld in the creation of composite soundings (not shown), the primary changes are a very slight deepening of the inversion in the potentially neutral + jet cluster, and a moistening in the potentially neutral cluster, but the same fundamental characteristics remained.

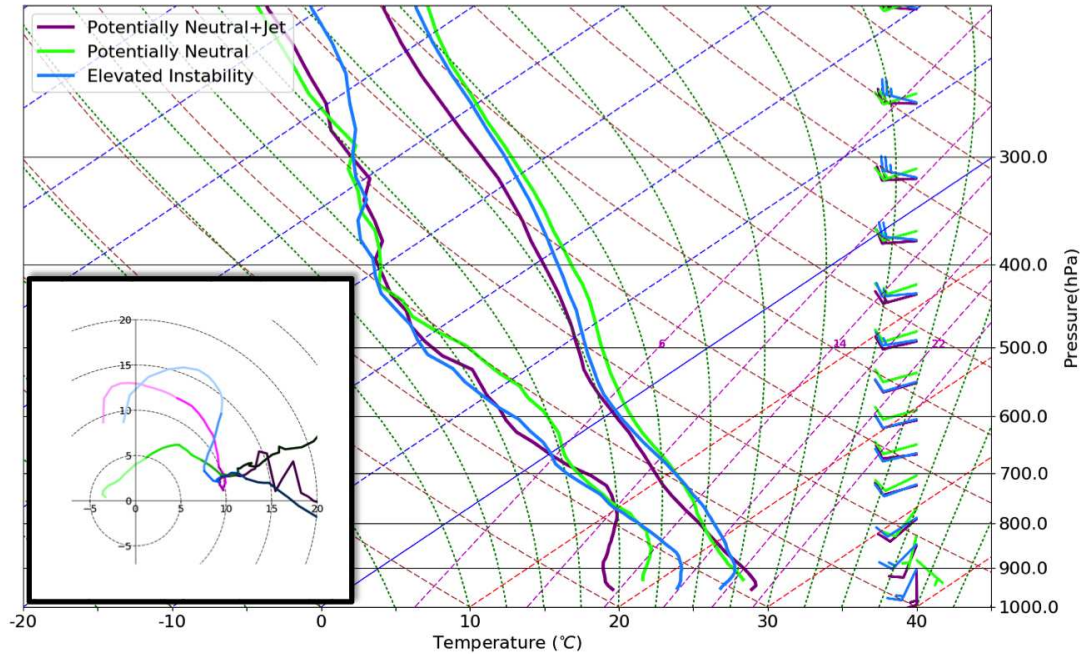


FIG. 2.6. Skew-T log-P plots and hodographs (inset) of composites of the three clusters. Winds in  $\text{m s}^{-1}$ . Shading in the hodograph changes at 1 km intervals from light to dark.

Convective parameters for the three clusters are plotted in Fig. 2.5. As desired, the compositing method conserves MUCAPE well, but the composite MUCIN, SBCAPE, and SBCIN all tend on the larger (in magnitude) tail of the highly skewed distributions. Precipitable water, 0-6 km shear, and 0-1 km shear are also relatively well conserved. Parcel source was near the median in all three clusters, and essentially at the surface in the two potentially neutral clusters.

#### 2.4.3 Composite Environments

0000 UTC RAP analyses were used to create composite environments associated with the clustered cases. Centroids were selected by computing the centroid of the soundings of each case in each cluster. Composites shown in Figure 2.7 include the cases represented by more than 25% of the soundings launched during that case in a given cluster. These are identified in Table 2.3 by asterisks, as well as in Figures 2.1 and 2.2 by solid shaded dots. In a qualitative comparison to composites that also included all cases, the differences were small. However, composites that do not include cases represented by a only a few clustered soundings are more likely to be representative of the environment under which the clustered conditions were observed.

In all three clusters, upper-level flow is generally zonal with a slight southerly (potentially neutral, no-jet) or northerly (elevated instability) component and the warmest air at 850 hPa is located in the west-southwest (Fig. 2.7a,c,e). Upper-level winds of greater than  $25 \text{ m s}^{-1}$  cover a broad area in the elevated instability composite, but are strongest only in the far north of the potentially neutral composites (Fig. 2.7b,d,f). A low-level wind maximum is present in all three clusters, but extends farther north in the potentially neutral + jet and elevated instability composites. Stronger 850-hPa winds cover a broader region in the elevated instability cluster, and southerly winds extend throughout nearly the entire region, where they begin to shift parallel to the isotherms in the northern portions of the potentially neutral composites. Consequently there are more regions of warm air advection associated with the interaction of the 850-hPa wind maximum and SW to NE temperature gradient (Fig. 2.7a,c,e). Additionally, there is more 850-hPa moisture in the elevated instability cluster (Fig. 2.7b,d,f) than either of the other clusters. This leads to greater spatial coverage of moisture advection by the low-level wind maximum consistent with the observed increases in  $\theta_e$  during elevated instability cases. In the potentially neutral cluster with a low-level wind maximum, the weak moisture gradient (or decreasing moisture to the south in places), leads to more sporadic moisture advection, and a composite that is generally consistent with observations of little change in  $\theta_e$  ahead of convection during potentially neutral cases (Fig. 2.7b). The potentially neutral cluster has more moisture and a more coherent region of moisture advection than the potentially neutral + jet cluster, consistent with the higher composite dew-points in Figure 2.6 (Fig. 2.7d). All three clusters have clear evidence of convergence of similar magnitudes at the left terminus of the low level wind maximum (not shown), but the strongest signal of advection of warm, moist air is in the elevated instability case.

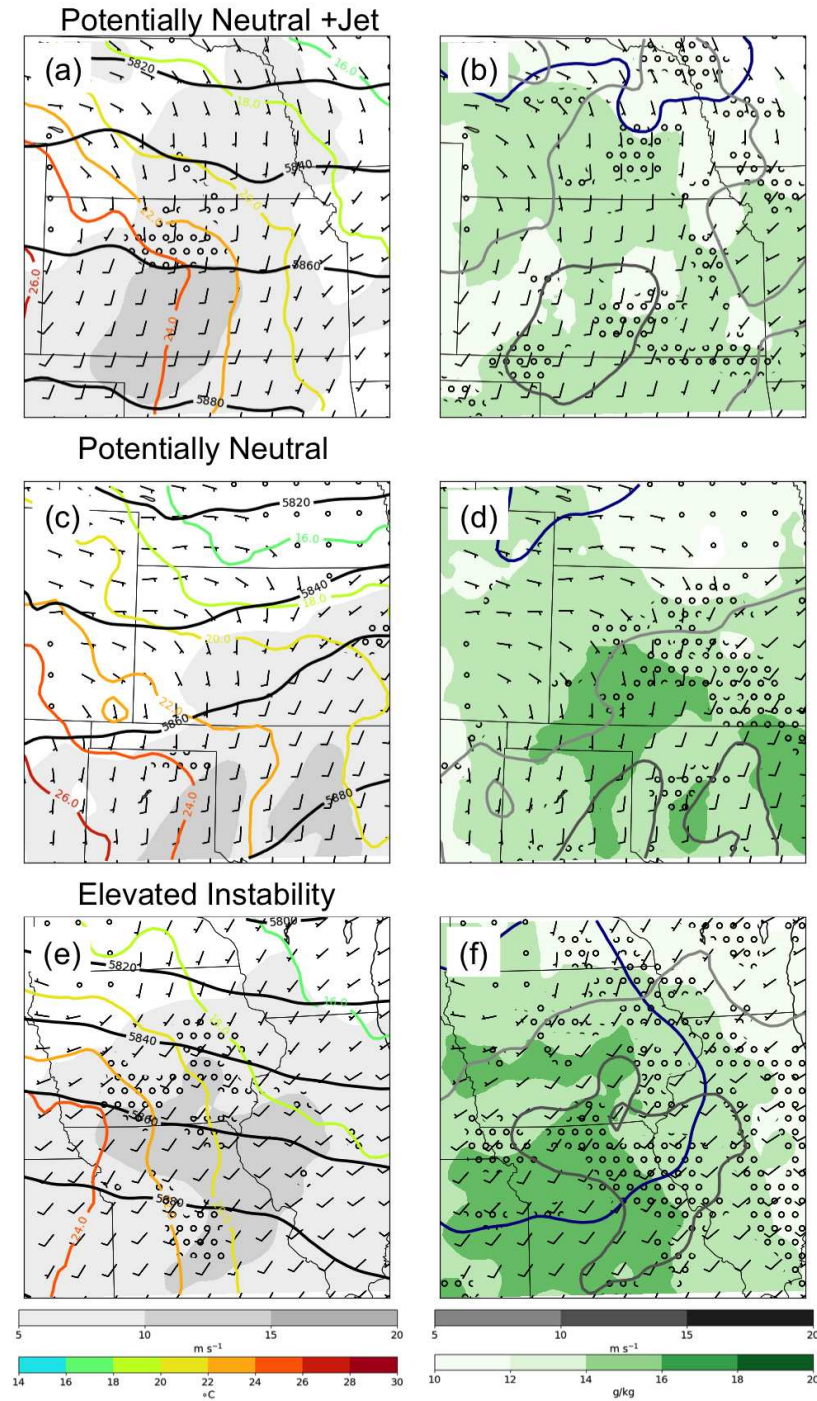


FIG. 2.7. Composite plots depicting 0000 UTC RAP analysis of the (a,b) potentially neutral + jet, (c,d) potentially neutral, and (e,f) elevated instability clusters. In (a,c,e): 500 hPa heights (m; black), 850 hPa wind speed (greyscale) and barbs ( $\text{m s}^{-1}$ ), 850 hPa temperature ( $^{\circ}\text{C}$ ; color contours), and 850 hPa temperature advection  $> \sim 0.5 \text{ K hr}^{-1}$  (stippled with open circles). In (b,d,f): 250 mb winds  $> 50$  knots (unfilled dark blue contour), 850 hPa wind speed (unfilled gray contours), 850 hPa wind barbs ( $\text{m s}^{-1}$ ), 850 hPa water vapor mixing ratio ( $\text{g kg}^{-1}$ ; green filled contours), and 850 hPa moisture advection  $> 0.2 \text{ g kg}^{-1}$  per hour (stippled with open circles).

Broadly speaking, the MCSs in the potentially neutral + jet cluster were slightly organized, weakly linear, and had large stratiform regions and a number of more discrete embedded cells (Fig. 2.2a,d,g,k,o). Cases in the potentially neutral, no-jet cluster also had some linear elements, in addition to more discrete cells (Fig. 2.2b,c,f,k,o). These no-jet cases also tended to have a number of soundings that were difficult to categorize as pre- or post-convective. In several cases, winds were northerly or calm, and observations were primarily taken between multiple regions of convection, but little-to-no stabilization had occurred at low levels (from any source). For example, the 11-12 June and 14-15 June cases, an initial, convective line formed along a boundary ahead of the mobile asset locations (Fig. 2.2b,c). In both cases, this convection moved east and dissipated as new, stronger, convection developed to the west of the target locations and was intercepted by mobile teams. With the exception of 13-14 July, when an MCS did not form until well after the end of the IOP (Fig. 2.2n), the elevated instability cases were more tightly organized (Fig. 2.1e,h,i,j,l,m) and several cases had bowing (Fig. 2.2m,i<sup>5</sup>), back-building (Fig. 2.2h) or regions of both (Fig. 2.2e,j,l). In all three clusters, the conditions were often cloudy at some level over an extended period before the passage of convection. Some cases in the elevated instability cluster did appear to have longer periods of clear conditions, and more high clouds. However, a deeper exploration of the relationship between high/low clouds and stabilization would be worthwhile, but it is beyond the scope of this paper.

#### 2.4.4 *Environment Evolution in Select Cases*

Composite analysis on cluster environments provides some general insight into different types of pre-convective environments observed during PECAN. However, it cannot capture the spatial and temporal variability that exists from case to case or even within a single case. To this end, the evolutions of environments from three cases, one from each of the major clusters, are examined in closer detail. The cases chosen each represent a large proportion of the soundings clustered in their respective categories and are as follows: 1) Potentially Neutral + Jet: 16-17 June 2015, 2) Potentially Neutral: 11-12 June 2015, and 3) Elevated Instability: 12-13 July 2015.

In order to visualize the temporal variability, soundings launched from MG locations were interpolated to a 100 m vertical grid and thermodynamic and kinematic fields were plotted as a function of height and launch time. Gaps in the analysis indicate missing data, where soundings did not reach 5 km (this was rather common for launches into convection). Ascent over the first 5 km usually occurs over the first ~20 minutes of a launch, and adjustments for launch duration would likely not impact

---

<sup>5</sup>Bowing in this case occurred about an hour before it reached the PECAN array

conclusions from this analysis. This method also assumes MGs were co-located throughout the duration of the IOP, and while they were not always exactly co-located on 16-17 June or 11-12 June cases, they were close enough to have sampled a similar evolution of the pre-convective environment.

On 16-17 June and 12-13 July, the gust front passages occurred around 0500 UTC and just before 0630 UTC respectively, and are clearly visible in a southerly to northerly wind shift and a near surface decrease in both  $\theta_e$  and  $\theta_v$  fields (Fig. 2.8a,b,e,f). General post-convective environments will be discussed in greater detail in Section 2.5, but it is interesting to note that while the initial gust front and northerly wind shift was observed around 0500 UTC on 17 June, deeper northerly winds and a more prominent decrease in  $\theta_v$  occurred about 30 minutes later (Fig. 2.8a,b). In both cases, an increase in low-level winds was observed between 0200 and 0300 UTC, over an elevated layer below 1 km (Fig. 2.8a,e). On 12-13 July, much like the common conceptual model,  $\theta_e$  increased over the same layer throughout the observing period (Fig. 2.8e). However, on 16-17 June, the  $\sim 3$  km deep layer of nearly constant  $\theta_e$  remained essentially unchanged until the passage of the gust front, despite the development of a low-level wind maximum where southerly wind speeds actually exceeded those observed on 12-13 July (Fig. 2.8a). In both cases, low-level zonal winds were weak, but a slightly larger easterly component was observed in the lowest 1 km on 16-17 June (Fig. 2.8b,f).

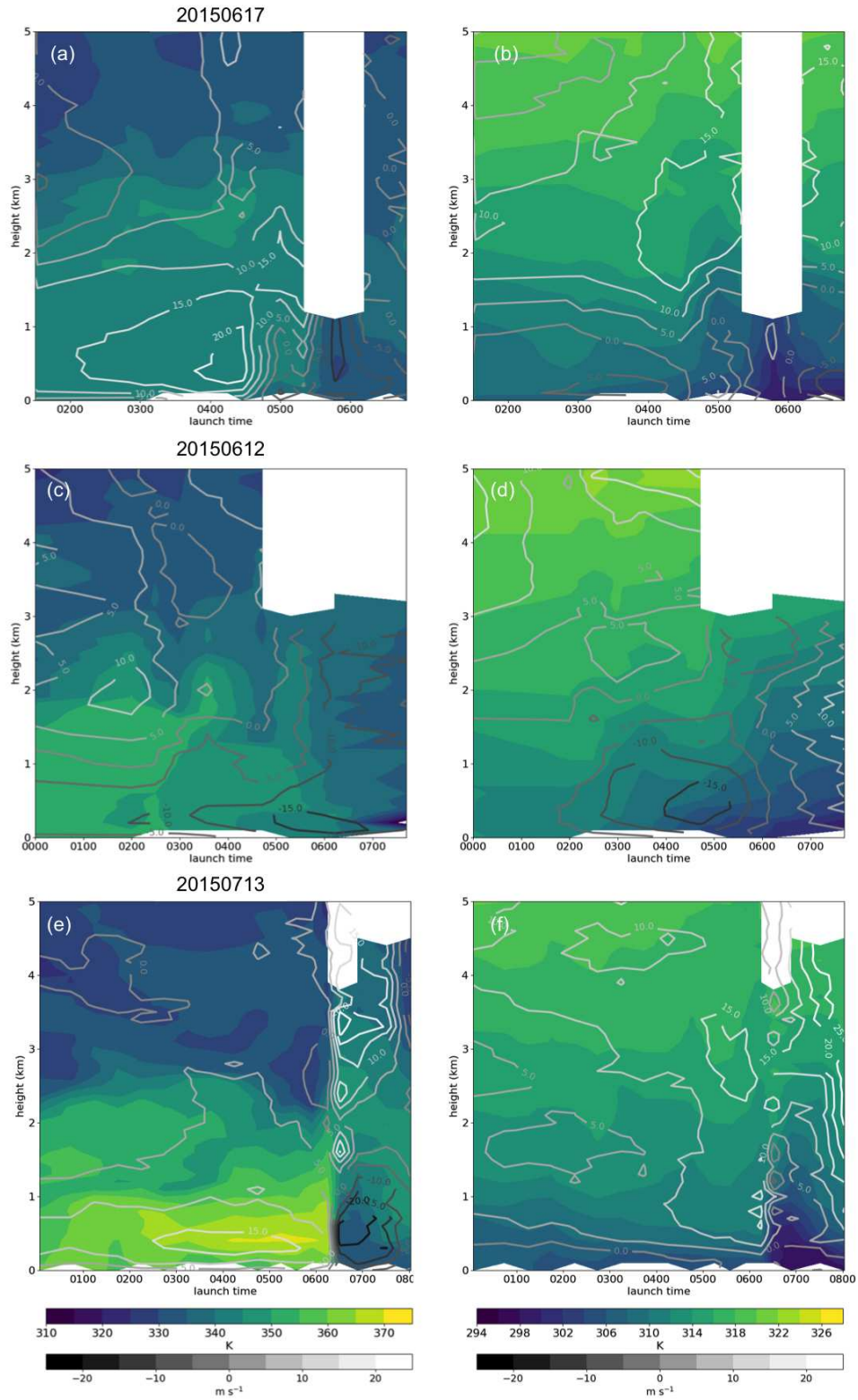


FIG. 2.8. Time-height diagrams of MG launches on (a,b) 16-17 June, (c,d) 11-12 June, (e,f) 12-13 July. (a,c,e)  $\theta_e$  (filled contours; K) and meridional wind (unfilled contours;  $\text{m s}^{-1}$ ). (b,d,f)  $\theta_v$  (filled contours; K) and zonal wind (unfilled contours;  $\text{m s}^{-1}$ )

Of the other elevated instability cases, the 24-25 June case (Fig. 2.2e; Described in greater detail in Peters et al. 2017) evolves most similarly to the 12-13 July case, destabilizing rapidly in an elevated layer. Other cases in this cluster do have an increase in  $\theta_e$  just above the surface, but evolve more slowly with time, and at times have a 1-2 km deep layer of nearly constant  $\theta_e$  resembling that of the other two clusters. Other potentially neutral + jet cases are generally quite similar to that of 16-17 June, and cases that are split between the two potentially neutral cases tend to resemble the potentially neutral cluster early, and transition to the potentially neutral + jet with the onset of the LLJ.

While the 11-12 June case has a 2 km deep layer of nearly constant  $\theta_e$ , it is distinctly different from 16-17 June because it lacks low-level southerly winds. On this day, mobile assets were located on the cool side of a shallow surface front in a region of northerly low-level winds (northerly winds below 1 km visible in Fig. 2.8c). Surface observations indicate that a southerly to northerly wind shift was accompanied by temperature changes of only 1-2 degrees Celsius across the boundary, and soundings on the cool side of the boundary indicate that cooling was over a very shallow layer. Although an initial line of convection initiated to the south and east of the mobile assets along this boundary, it moved southeast, and sounding observations did not appear to be influenced by convectively generated outflow until between 0330 and 0430 UTC when new convection initiated along the stronger thermal gradient associated with the front, and essentially on top of mobile assets. Even then, it is difficult to distinguish between convective outflow and changes associated with the front during this period. Around 0600 UTC, much more vigorous convection passed over the MGs, and is associated with a decrease in  $\theta_v$  over a deeper layer and a shift to westerly winds over the same layer.

In summary, in environments that resemble the elevated instability conceptual model,  $\theta_e$  evolves with time – sometimes quite rapidly. In environments with 2-3 km deep potentially neutral layers,  $\theta_e$  evolves slowly (if at all), even when a strong low level wind maximum develops. Furthermore,  $\theta_e$  on the cool side of a frontal boundary may not change much with time in the absence of convection, and may have little-to-no increase with height, even when there is some evidence of a low level wind maximum above the frontal boundary.

## 2.5 POST CONVECTION

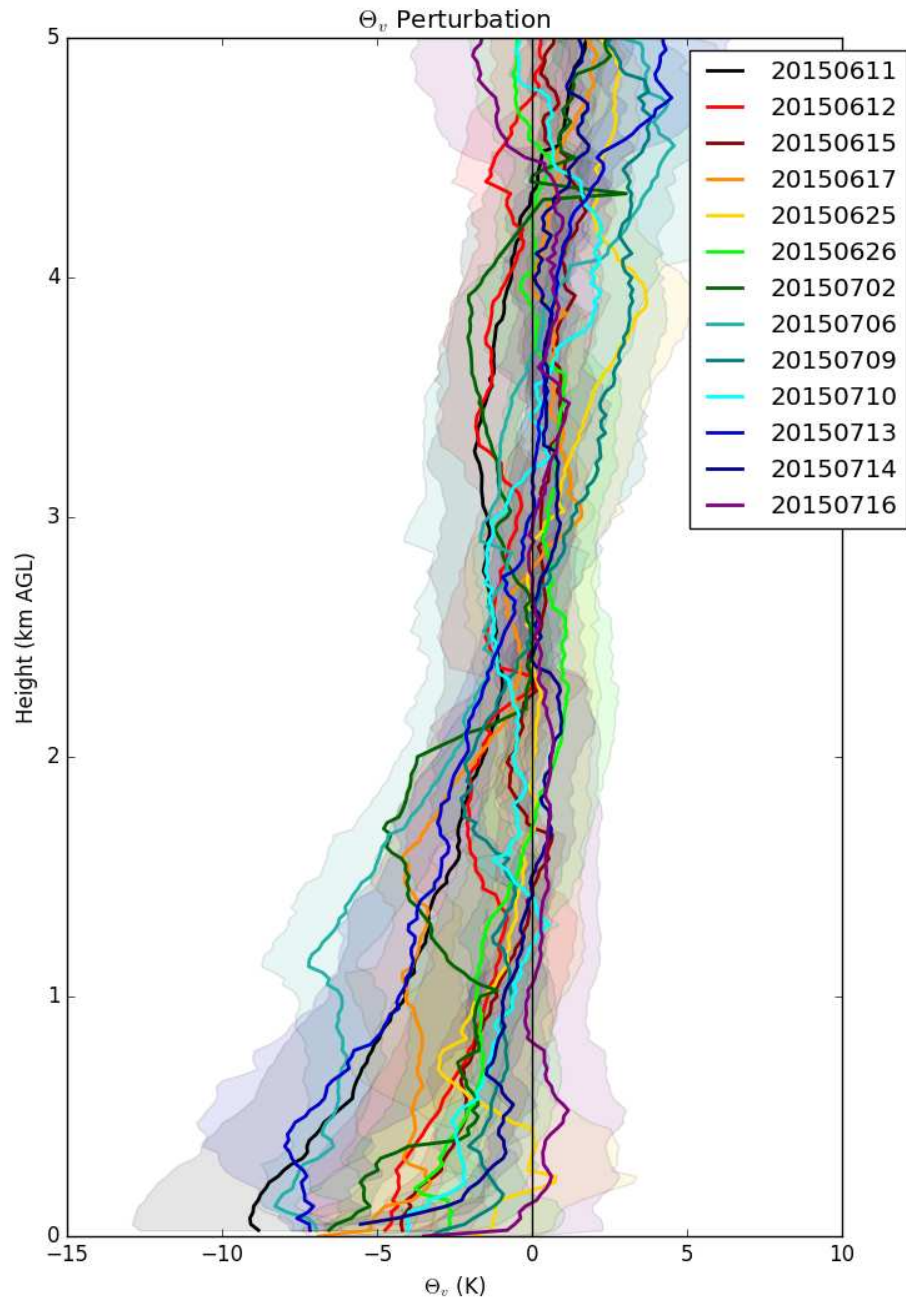


FIG. 2.9. Average  $\theta_v$  deficit (K) of post-convective soundings. Shading indicates  $\pm 1\sigma$ .

TABLE 2.4. A simple summary of changes in virtual potential temperature  $\theta_v$ .  $\theta'_{vmax}$  is the magnitude of the largest observed average decrease in  $\theta_v$ .  $\theta'_{vmax}$  Hgt is the height at which  $\theta'_{vmax}$  occurred.  $\theta'_v$  Top is the minimum height in which the mean difference between  $\theta_v$  in pre- and post-convective soundings is no longer negative. If a second layer of  $-\theta_v$  of equal or larger magnitude exists above a shallow layer of weakly  $-\theta_v$ , the parenthetical number is the top of that second layer.

Date	$\theta'_v$ sfc (K)	$\theta'_{vmax}$ (K)	$\theta'_{vmax}$ Hgt (m)	$\theta'_v$ Top (km)
10-11 June	<b>-8.82</b>	<b>-9.10</b>	50	<b>4.350</b>
11-12 June	-4.74	-4.74	0	2.275
14-15 June	-4.18	-4.22	25	1.400
16-17 June	-6.88	-6.88	0	2.800
24-25 June	<i>-1.90</i>	<i>-3.02</i>	<b>700</b>	0.200, (1.700)
25-26 June	-2.85	-3.77	200	1.725
1-2 July	-6.55	-6.55	0	2.400
5-6 July	-6.95	-8.29	100	3.675
8-9 July	-3.28	-3.28	0	2.500
9-10 July	-3.99	-4.01	50	1.200
12-13 July	-7.16	-7.98	350	3.000
13-14 July	-5.53	-5.53	0	1.375
15-16 July	-3.49	-3.49	0	<i>0.150</i>

Bold numbers highlight largest, deepest, or most elevated observed  $\theta_v$  deficits. Italicized numbers highlight smallest or shallowest  $\theta_v$  deficits.

Changes in virtual potential temperature ( $\theta_v$ ) from pre- to post- convective environments  $\theta'_v$  were computed to explore characteristics of post-convective environments observed during PECAN MCSs. A pre-convective sounding representative of the environment just before the passage of the MCS-produced density current was subjectively identified using  $\theta_e$ ,  $\theta_v$ , and wind profiles from all platforms as well as radar fine lines where appropriate. Soundings were interpolated to common vertical levels, and the mean  $\theta_v$  perturbation of the observed post-convective environment was computed for each case (Fig. 2.9). For this analysis, soundings that were ahead of the precipitation, but after the passage of a gust front were included to capture the full range of outflow characteristics. However, for this study, wave-like features were not considered in distinguishing outflow boundaries, in part due to the complexity of identifying them in several cases. 149 soundings were identified as post-convective and used in this analysis. A summary of the statistics for the post-convective soundings is shown in Table 2.4.

Despite the nocturnal nature of the MCSs observed, a cold pool was observed in nearly every case<sup>6</sup>. It is clear from Figure 2.9 that there is substantial variability in the depth and strength of the change

<sup>6</sup>On the 10-11 July, several soundings were launched before and after the passage of a bore, but none of them observed a density current which was likely present closer-to or behind the convective region.

in  $\theta_v$  from case to case (and even within a single case). Some cases, like 16-17 June have the greatest decrease in  $\theta_v$  at the surface, while several other cases, like 24-25 June have the greatest decrease in  $\theta_v$  above the surface. Still other cases, like 15-16 July, have almost no change in  $\theta_v$  with the passage of convection except in the lowest 150 meters. Table 2.4 highlights several extremes in observed changes in  $\theta_v$  seen in Figure 2.9. The largest mean decrease in  $\theta_v$  was -9.10 K, observed during the 10-11 June case, just above the surface. The 24-25 June, case observed only a -1.90 K  $\theta'_v$  at the surface over a very shallow layer. However, a mean  $\theta'_v$  of -3.02 K was observed at 700 m above the surface above a layer with little change (and even a slight increase) in  $\theta_v$ .

Six out of the 13 cases included in this analysis observed the largest decrease in  $\theta_v$  at the surface. Another three cases observed the largest decrease in  $\theta_v$  just above the surface, and four cases observed the largest decrease in  $\theta_v$  well above the surface. In these cases, the height of largest decrease in  $\theta_v$  ranged from 100 m to 700 m above the surface. The average depth of the observed  $-\theta'_v$  (a measure of cold pool depth) ranged from 150 m to 4.350 km between cases. The two deepest observed cold pools, on 10-11 June and 5-6 July, also had the greatest maximum change in  $\theta_v$  and two of the top three largest observed decreases in surface  $\theta_v$ . The shallowest layer of mean near surface  $-\theta'_v$  was observed on 15-16 July and not in conjunction with the smallest decrease in  $\theta_v$ . Rather, the smallest decrease in surface  $\theta_v$  observed occurred on 24-25 June, a day when the largest decrease in  $\theta_v$  occurred aloft. The average of the mean observed depth of  $-\theta'_v$  for the 13 PECAN cases with post-gust front observations is 2.08 km. The average observed change in  $\theta_v$  is -5.1 K at the surface and the average maximum change in  $\theta_v$  is -5.45 K.

In the literature it has been noted that in cases with strong low-level stable layers, convective downdrafts may not be strong enough to penetrate to the surface, and instead can produce gravity waves or bores (e.g. Trier and Parsons 1993; Carbone et al. 1990; Parker 2008). In these cases, convectively cooled outflow may mix out before it reaches the surface, but it likely cools the upper regions of the inversion layer. In some cases, a particularly strong downdraft may actually still reach the surface, even when a relatively strong stable layer is present. When this happens, the greatest cooling may still be seen aloft, where the layer of warm air at the top of the inversion is cooled more than the relatively cooler layer near the surface. One might expect then to find a relationship between the observed outflow-produced

cooling profile and characteristics of the stable layer. A comparison of the height of the greatest decrease in  $\theta_v$  to the strength and depth of the observed pre-convective stable layer<sup>7</sup> shows evidence of this (Fig. 2.10).

---

<sup>7</sup>The depth of the stable layer was taken as the height at which the lapse rate becomes greater than the moist adiabatic lapse rate. Stable layers that did not begin at the surface were not included. If shallow regions (< 100 m) of conditional instability existed between two stable layers, the top of the upper most stable layer was taken to be the depth. The stable layer strength is defined as the difference between  $\theta_v$  at the top of the inversion and the surface.

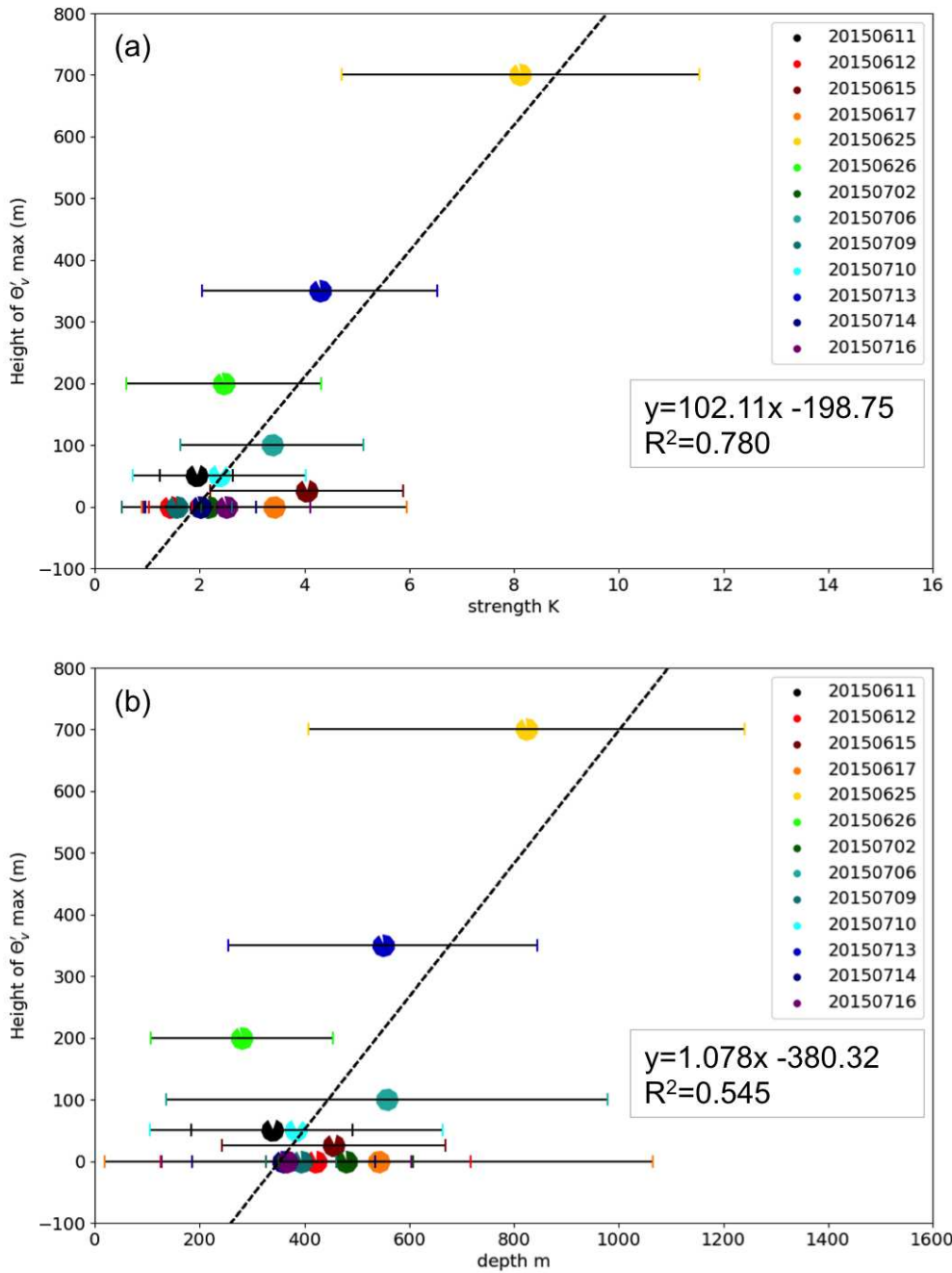


FIG. 2.10. Scatter plot of the height of greatest observed cooling (from Table 2.4) and the a) strength (K) and b) depth (m) of the observed stable layer in pre-convective soundings. Individual markers are pie-charts that indicate the fraction of the pre-convective soundings with an identifiable low-level stable layer (shaded). Bars represent one standard deviation.

A linear regression between the depth of the greatest  $\theta'_v$  and the stable layer properties of strength and depth indicates, at least to a first order approximation, that there is a relationship between them (Fig. 2.10). Stable layer strength (Fig. 2.10a) appears to have a stronger relationship to the depth of observed  $\theta'_v$  than stable layer depth (Fig. 2.10b) with  $R^2$  values of 0.780 and 0.545 respectively. Even though it is often thought that convectively cooled outflow may not reach the surface in the presence of a strong stable layer (Trier and Parsons 1993; Marsham et al. 2010, e.g.), it is not unusual to find a cold pool at the surface during an MCS in a stable low-level environment. That said, there is evidence that properties of the stable layer do modify the cold pool structure. Another possible explanation of this elevated maximum in cooling is that rather than a true cold pool, this is a "Type C" bore as described in Rottman and Simpson (1989), where the density current and bore move at the same speed, and a semi-permanent deepening of the inversion layer leads to a decrease in  $\theta'_v$  in an elevated layer. More data is needed in environments with strong and deep stable layers, and additional work is needed to explore these relationships further.

Other relationships between pre- and post-convective environments were explored, including: freezing layer depth and cold pool depth, stable layer strength/depth and cold pool depth, and stable layer strength/depth and cold pool intensity at the surface. No clear trends were seen in those relationships.

Given the results of the cluster analysis presented in earlier sections of the paper, it initially came as somewhat of a surprise that the majority of pre-convective soundings in every observed PECAN case did have a low-level stable layer (shown by the shaded fraction of the marker in Fig. 2.10). However, it is not unusual for low-level absolute stability and potential instability or neutrality to exist in the same layer. As noted by the bars marking 1 standard deviation, there is a large amount of variability in the strength, and especially the depth, of the average pre-convective stable layer (Fig. 2.10). A large number of variables can influence the stability at low levels including: moisture (in the air, vegetation, and soil), cloud cover, other convection, location relative to frontal boundary, and slope and strength of frontal boundary. A combination of these and other factors likely influenced environments observed during PECAN on any given night. This in-turn influences the relationship between observed MCSs and their environment.

## 2.6 DISCUSSION AND SUMMARY

Analysis of nearly 300 soundings launched in pre-convective MCS environments during PECAN resulted in identification of three distinct categories, 1) Potentially Neutral, (2) Potentially Neutral + Jet,

(3) Elevated Instability, of environments observed before the passage of the convective line. One category, 'elevated instability,' fits the Trier and Parsons (1993) conceptual model of nocturnal convection well. A near surface inversion is topped by a layer of high  $\theta_e$  air and potential instability that appears to increase in magnitude and deepen with time. A corresponding increase in low-level southerly winds was also seen, indicating the presence of a low-level jet. In this category, low-level winds generally maximized at a higher altitude, greater magnitude, and with a greater westerly component than in the potentially neutral category. However, the layer of southerly wind increases was below the layer of maximum  $\theta_e$  in both cases.

The second category, termed 'potentially neutral + jet', had only a weak near surface stable layer, and near constant  $\theta_e$  in the lowest 2.5 km. Profiles in this category did tend to be from slightly earlier in the IOP than the elevated instability category. However, the majority of profiles in this category still came from soundings launched after sunset ( $\sim 0200$  UTC). Low-level wind maxima in the potentially neutral category tended to occur closer to the surface, and had a stronger near-surface easterly component. Despite the nocturnal nature of these MCSs and evidence of an LLJ, around 30% PECAN MCS soundings fell into this category.

A third category, termed 'potentially neutral,' thermodynamically resembled the previous category at low levels. Soundings in this category were generally taken on the cool side of a frontal boundary or after a wind shift, and so had either very weak or even northerly surface winds. Again, despite being post-frontal and nocturnal, around 30% of soundings fell into this category. Combined with the other potentially neutral category, over half of the PECAN MCS soundings did not have a  $\theta_e$  maximum aloft.

Composite RAP analysis of the primary cases that make up the elevated instability cluster indicate stronger 850-hPa southerly winds, a large moisture content that tends to increase to the south, and consequently more moisture advection across a larger, more continuous region than composites of the potentially neutral clusters. The orientation of the temperature gradient relative to the low-level winds in the elevated instability cluster is also more favorable for warm air advection.

The strength and depth of observed stable layers have a large amount of variability both between cases and within individual cases. Stable layers are not present in every sounding from every case, but the majority of soundings launched in each case did have some identifiable near-surface stable layer.

Characteristics of the observed post-convective region are highly variable from case to case, and even within a single case, but nearly every case had evidence of a cold pool. Observed average  $\theta'_v$ 's ranged from nearly -10 K to less than -2 K and over depths from less than 150 m to over 4 km. Across

all cases, the average observed cold pool depth was just over 2 km, and the average observed change in  $\theta_v$  was 5-6 K. In some cases, the maximum  $\theta'_v$  was observed near the surface, but in over half of the cases with density current observations, the cooling was maximized above the surface. The existence of a relationship between the height where the most cooling occurred and stable layer characteristics implies that low-level stability can modulate cold pool structure.

The primary findings of this work can be summarized as follows:

- A large number of PECAN MCS cases did not have an elevated layer of high  $\theta_e$  air commonly associated with temperature and moisture advection by the low-level jet, despite evidence of at least a shallow southerly low-level wind maximum in many of the cases. These cases typically occurred earlier in the evening, but this profile can still exist well after dark. Critically, these cases had less moisture, less moisture advection, and less warm air advection than cases with  $\theta_e$  maximized above the surface.
- Just under 50% of the PECAN MCS cases (30% of soundings) fit into the classical conceptual model of an elevated  $\theta_e$  maximum.
- There is a large amount of observed variability in the strength and depth of observed near-surface stable layers prior to the onset of convection.
- All cases with observations after the passage of convection had evidence of some surface cooling, the degree and depth of which varied substantially.
- There is a relationship between the level at which cooling is maximized and characteristics of the nocturnal stable layer. This has implications on understanding the structure of cold pools produced by nocturnal storms.

In every case, the majority of soundings observed a near surface stable layer, but the large variability brings to light some important questions. What factors influence the development of low-level stability? In the case of nocturnal cooling: low-level moisture, cloud cover, cloud type, vegetation, terrain, and other features with high spatial heterogeneity all play a role in the development of the nocturnal stable layer. On the cool side of a frontal boundary, the depth of the stable layer is related to the distance from the edge of the front, the slope of the frontal boundary, and perhaps more localized features as well. As discussed previously, convectively produced cold pools act to increase the stability of low-levels (in fact, profiles that captured the passage of a cold pool prior to, or in the absence of convection looked remarkably similar to profiles whose low-levels had likely been cooled radiatively). How does

the development of a nocturnal stable layer vary spatially and temporally? Are there places that develop more consistent nocturnal stable layers than others? Does it take some regions longer to develop stable layers than others? Is the development of a low-level nocturnal stable layer influenced by any synoptic characteristics (other than front relative location)? Given the importance of understanding the interactions of MCSs with low-level stable layers, additional work into understanding the development of low-level stable layers (how/when/where) in the nocturnal atmosphere would be of significant value.

## CHAPTER 3

### **ANALYSIS OF BACK-BUILDING CONVECTION IN SIMULATIONS WITH A STRONG LOW-LEVEL STABLE LAYER**

Heavy rainfall can serve both as a valuable source of water, and a dangerous contributor to flash flooding around the world. Mesoscale convective systems (MCSs) are one of the major producers of heavy rainfall (Maddox et al. 1979; Maddox 1980). More specifically, since total precipitation is directly related to the rate and duration of rainfall (Doswell et al. 1996), MCSs that have convective elements that ‘train’, or back-build over the same location are particularly conducive to extreme precipitation (e.g. Chappell 1986; Schumacher and Johnson 2005). Training occurs where cells move parallel to the orientation of the convective line, resulting in repeated motion over the same location. In back-building convection, new cells repeatedly regenerate upstream, while mature cells decay downstream resulting in quasi-stationary behavior of the convective region (Schumacher and Johnson 2005).

Analysis of these heavy rainfall-producing MCS environments have led to several different methods of classification, but two distinct categories consistently emerge for events over the central Great Plains. In synoptic-type events, a strong mid-tropospheric trough and slow moving surface front lead to strong forcing for ascent in a region with southerly flow and associated moisture transport. During the warm season, isentropic ascent of warm, moist air transported by the nocturnal low level jet (LLJ) can lift an air to saturation on the cool side of a stationary or warm front (Schumacher 2017, and citations therein). In both cases, cloud layer winds can lead to cell motion parallel to the boundary and training/back-building.

Corfidi et al. (1996) developed a technique to forecast the instances of back-building or quasi-stationary convection using the mean cloud layer wind and the (negative of) the low level jet (LLJ). In a conceptual model in Corfidi (2003), quasi-stationary convection is thought to form along the portion of the outflow boundary parallel to the mean wind. Schumacher and Johnson (2008, 2009) and Schumacher (2009) explore the development and maintenance of back-building convection in MCSs in the absence of a surface front (Type 2 MCS; Fritsch and Forbes 2001). They found that back-building can be maintained by a latent-heating-forced gravity wave oriented approximately perpendicular to the inflow winds over the same layer. Other instances of back-building or training convection can form offset from a leading convective line. A ‘bow and arrow’ MCS (Keene and Schumacher 2013) has both a

forward-propagating leading line (the bow) and a region of convection that develops nearly perpendicular to the leading line some distance offset from the leading southwest outflow boundary. This ‘arrow’ portion of the convection is sometimes referred to as ‘rearward off-boundary development’ (ROD; Peters and Schumacher 2014) which more generally refers to convection that develops offset-from and behind a leading convective line (regardless of whether it bows or not). In these cases, back-building or TL/AS convection offset from a leading convective line is thought to be supported by a combination of external forcing for ascent due to the interaction of the low level jet and the quasi-stationary surface front and lifting through gradual ascent over the leading edge of a cold pool boundary associated with the forward propagating convective line (Keene and Schumacher 2013; Peters and Schumacher 2016).

Additionally, thus far, work on training convection has not distinguished between daytime and nighttime cases, so composite environments used have had only a weak stable layer (e.g. Fig. 9 in Peters and Schumacher 2015b). During PECAN, some cases had very strong stable layers, and observed stability varied substantially from case to case and even within individual cases (Chapter 2). Some studies have posed that the relative strength of the low level stable layer may impact the ability of a convective storm’s downdrafts to reach the surface (Raymond and Rotunno 1989; Trier and Parsons 1993; Haertel et al. 2001; Parker 2008; Marsham et al. 2010). However, despite observed stability, several other studies have found that some MCSs may continue to draw inflow from the near-surface layer, even after significant cooling has occurred (Davis et al. 2004; Parker 2008; French and Parker 2008; Billings and Parker 2012). These studies suggest that nocturnal convection may actually not be as decoupled from the boundary layer as previously thought. In an environment with a stable boundary layer, characteristics of the stable layer, windshear, and convective downdrafts influence the character of the MCS outflow (e.g. cold pool, bore, gravity wave). What would happen in the case of Peters and Schumacher (2016) if the low level stability was so strong that a cold pool was not produced? Are there still cases where its possible to have ROD in the absence of a low level cold pool, supported by another mechanism?

### 3.1 METHODS

Cloud Model 1 (CM1; Bryan and Fritsch 2002) version 19.1 was run on a 1170x1120x60 grid point domain with 500 m horizontal grid spacing and a stretched vertical grid from 100 m to 500 m at the 18 km model top. The domain was set to translate to the east at  $10.5 \text{ m s}^{-1}$  and to north at  $4.5 \text{ m s}^{-1}$ . Sixth order positive definite advection was used with sixth order monotonic diffusion. The Klemp-Wilhelmson time-splitting, vertically implicit pressure solver (Klemp and Wilhelmson 1978) and a 1

TABLE 3.1. Model Setup

Setting	
Initiation	1K $\theta'$ at 1.4 km, hrad=1.4 km, vrad=10 km
Domain	1170x1120x60
dx, dz	500 m, Stretched: 100-500 m
dt	1 s
Advection	6th order positive definite
Diffusion	6th order monotonic
Subgrid Turbulence	TKE
Pressure-Solver	Klemp-Wilhelmson time-splitting, vertically implicit
Microphysics	Morrison
LBCs	Open radiative, Durran and Klemp (1983)
Model top	18 km with Rayleigh damping
Model bottom	free slip
Other	No Coriolis

second time step were used. Open radiative lateral boundary conditions were used to allow fast moving gravity waves created during initiation to escape the domain. Rayleigh damping was applied near the model top, and a free slip condition was applied at the surface. This simulation uses Morrison microphysics (Morrison et al. 2005), and no Coriolis force. The Deardorff (1980) scheme was used for sub-grid scale turbulence. A summary of model set-up details can be found in Table 3.1

The sounding selected to initialize the environment was taken by a mobile team at 0428 UTC 25 June 2015 during the Plains Elevated Convection at Night Experiment (PECAN; Fig. 3.1). The sounding was launched about 30 minutes before convection passed over the launch location. On that night, remnants from an earlier cold pool contributed to a particularly deep stable layer;  $\theta$  increased 8.6 K over the lowest 721 m. The observed convection this day had both a forward-propagating leading line and a region of ROD (Fig. 3.2).

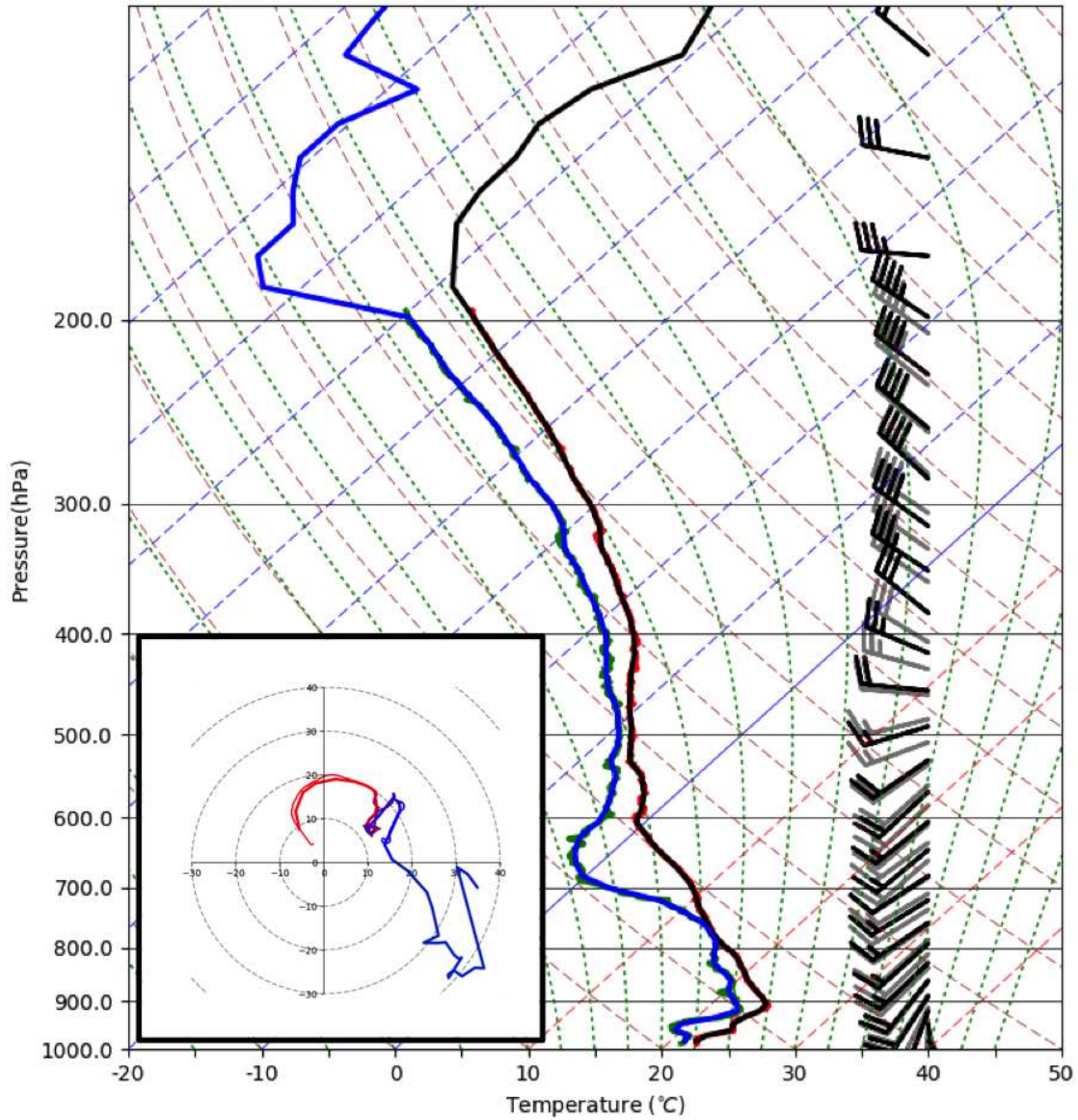


FIG. 3.1. Skew-T Log-P of the original 0428 UTC 25 June 2015 PECAN sounding (T in red, Td in green, wind barbs in gray), and the sounding used to initialize the homogeneous environment used in simulations (T in black, Td in blue, wind barbs in black). Thin lines on the inset hodograph are original sounding winds, thick lines are input sounding winds).

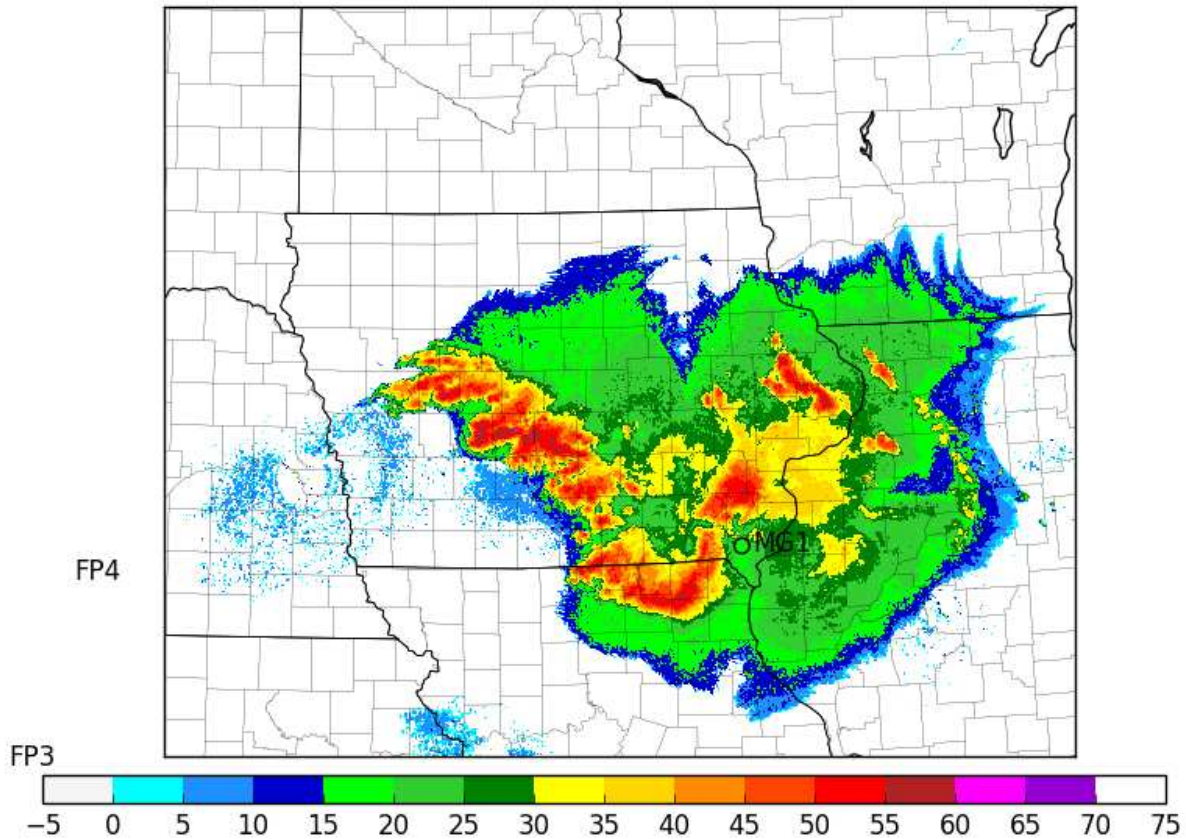


FIG. 3.2. Radar reflectivity at 0440 UTC on 25 June 2015 and location of the sounding in Fig. 3.1

This sounding did not quite reach the 18 km model top, so upper levels from the closest sounding that did were used. Weak smoothing was applied to all fields in order to reduce noise, but efforts were made to ensure that the the actual profiles were not modified artificially. Minor adjustments were necessary to reduce the gradient of wind with height at two points, one above and below the low level wind maximum. A combination of large gradients in wind and very low stability can lead to low Richardson numbers and Kelvin-Helmholtz instabilities ( $Ri < 0.25$ ). While these instabilities often exist in the real atmosphere, they are not desirable in initial conditions of a horizontally homogeneous simulation (Coffer and Parker 2015), and led to rapid overturning. Unlike soundings often used in these types of simulations, the sounding used was sufficiently moist though a very deep layer so no moisture modifications (e.g. Peters and Schumacher 2015b), or forced large scale lifting (Crook and Moncrieff 1988; Loftus et al. 2008; Schumacher 2009) was needed to initiate convection. Instead, a single, 1 K warm

bubble with a 10 km horizontal and 1 km vertical radius was all that was necessary to initiate convection in this environment.

Passive tracers were placed in the lowest 500 m at the start of the simulation in order to help identify near stable air lifted by updrafts. Passive tracers were also placed in the layer below 1.5 km in order to help identify convective outflow air with the idea that the replacement of the near surface air mass by convective outflow would lead to the removal of passive tracer. Further justification for this decision will be discussed in the presentation of 2D cold bubble simulations used to understand downdraft stable layer interactions. Additionally, forward parcel trajectories were initialized in approximately the southwestern 2/3 of the domain below 4 km with a vertical spacing of 250 m and a horizontal spacing of 1 km. In this case, the top of the stable layer was located around 800 m, so tracers and parcels placed below 500 m should adequately represent the near surface environment since any parcel from below 500 m would most certainly be associated with very stable air in this case (Plus, ~500 m has also been used to represent the near surface in other frequently referenced studies, such as Parker (2008)).

### 3.2 RESULTS

Despite the strong low-level stable layer, the horizontally homogeneous initial conditions, and simple warm bubble initialization, this environment was able to develop a mature MCS. The simulated MCS has a forward propagating leading line, a region of back-building convection along the southwestern portion of the leading line, and back-building convection in a region offset from the leading southwest outflow boundary (Fig. 3.3). The rest of the analysis will aim to 1) Explore the interaction between convective outflow and this environment and 2) Understand what supports ROD in the simulated MCS given the absence of a cold pool. A few other interesting features of this simulation will also be discussed.

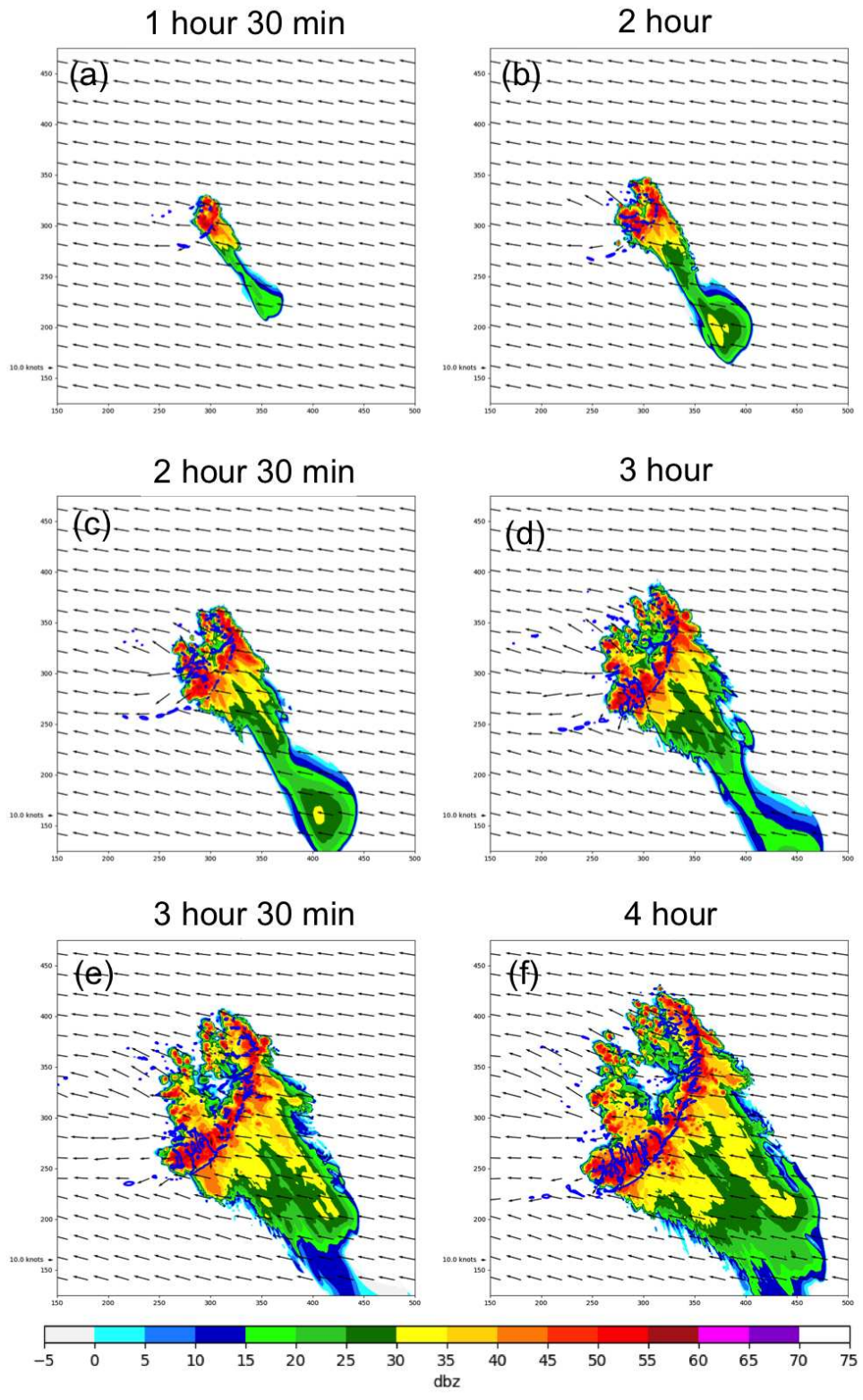


FIG. 3.3. Simulated reflectivity every 30 minutes from 1.5 hours to 4 hours. Blue contours indicate  $-0.5$  K surface  $\theta'$ .

### 3.2.1 Simulation Overview

Precipitation begins about 30 minutes after the start of the simulation, and the developing cell displays supercell-like characteristics ( $UH > 180 \text{ m}^2 \text{ s}^{-2}$  for at least 20 minutes; Naylor et al. (2012)) much like early convection observed on the day of the input sounding (Peters et al. 2017). Interestingly, early updrafts tend to be north and west of the highest reflectivity (not shown), and the initial cell moves towards the northeast. After about 1.5 hours, new cells begin to develop along the southwestern portion of an apparent outflow boundary, distinguishable by the narrow band of  $-0.5 \text{ K}$  surface  $\theta'$  in (Fig. 3.3a), as convection in the leading line begins to take on a more southeastward propagation. However, the generally sparse coverage of  $-0.5 \text{ K}$  surface  $\theta$  deficits suggests that there was no cold pool present. The leading line continues to propagate towards the southeast throughout the duration of the simulation, while new convection develops in the wake region nearly perpendicular to, and offset from the leading line. After 4 hours, only a small coherent region is enclosed by  $-0.5 \text{ K}$  contours (Fig. 3.3f).

#### 3.2.1.1 UPDRAFT MAINTENANCE ALONG THE LEADING LINE IN THE MATURE MCS

One of perhaps the most striking things about this simulation, is that not only does convection not produce a traditional cold pool, but there is a positive  $\theta'_\rho$  at the surface over most of the domain, even once the MCS has matured, 4 hours into the simulation (Fig. 3.4a). Rather, the greatest cooling observed in this simulation occurs in an elevated layer (Fig. 3.4b and 3.5a,c,e). The greatest decrease in  $\theta_\rho$  is observed around 650 m above the ground, which agrees remarkably well with the observations of the post-convective environment on the day of the sounding used to initialize the simulation (See Chapter 2, Table 4). While there is an impressive amount of surface warming, some  $\theta_\rho$  deficits do exist right at the edge of the gust front boundary and under the heaviest precipitation in the south (Fig. 3.4a). Negative pressure perturbations are seen ahead of convection and in the wake region, and positive perturbations accompany the passage of convection. Along the southwest outflow boundary, coincident oscillations in pressure and vertical velocity are indications of the presence of an undular bore or soliton which will be discussed in greater detail below.

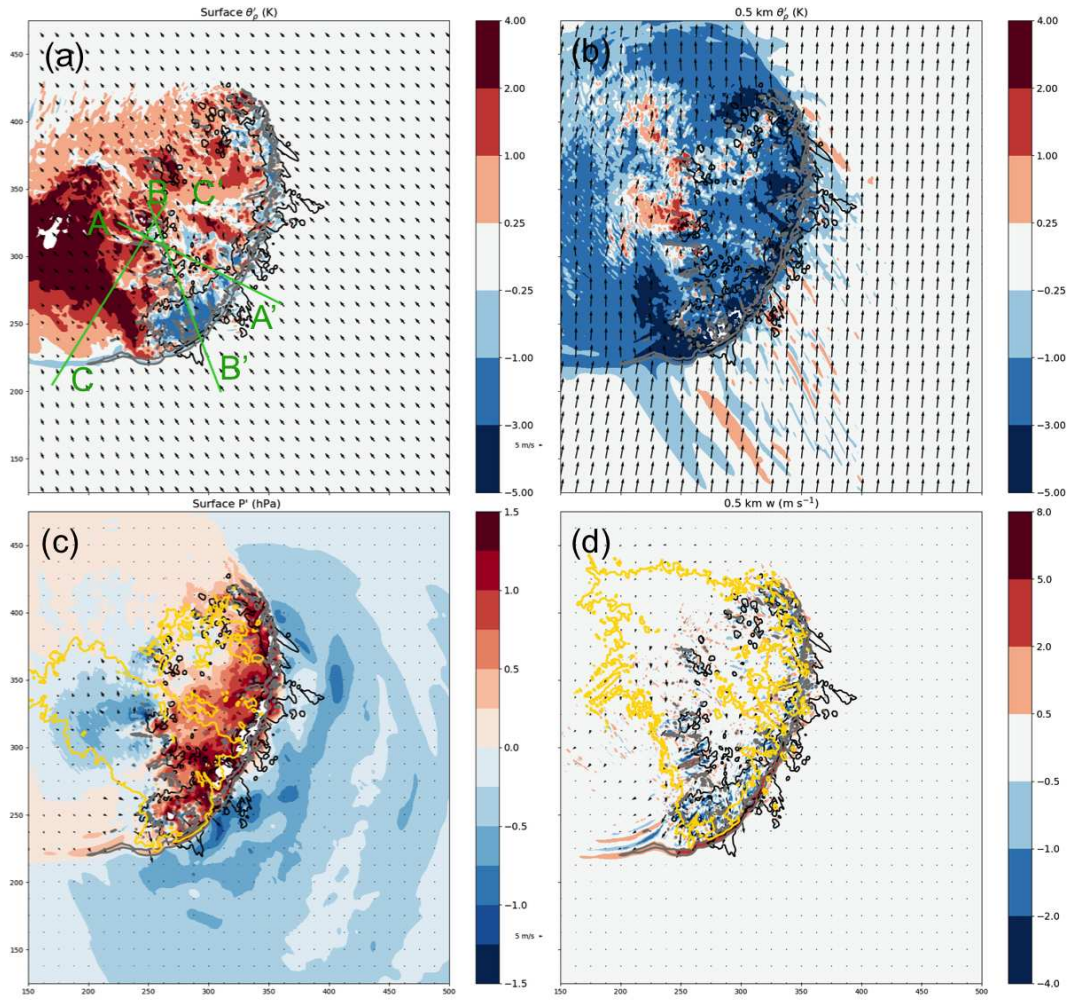


FIG. 3.4. 4 hour output of (a) Surface  $\theta'_\rho$  (filled), 40 dBz reflectivity at lowest model level (unfilled black),  $1 \text{ m s}^{-1}$   $w$  at 0.5 km (gray unfilled), and surface wind vectors. (b) As in a, but wind vectors and  $\theta'_\rho$  in filled contours at 0.5 km. (c)  $P'$  (filled), 40 dBz reflectivity at lowest model level (unfilled black),  $1 \text{ m s}^{-1}$   $w$  at 0.5 km (gray unfilled), and surface wind perturbation vectors. (d) As in c, but  $w$  in filled contours.

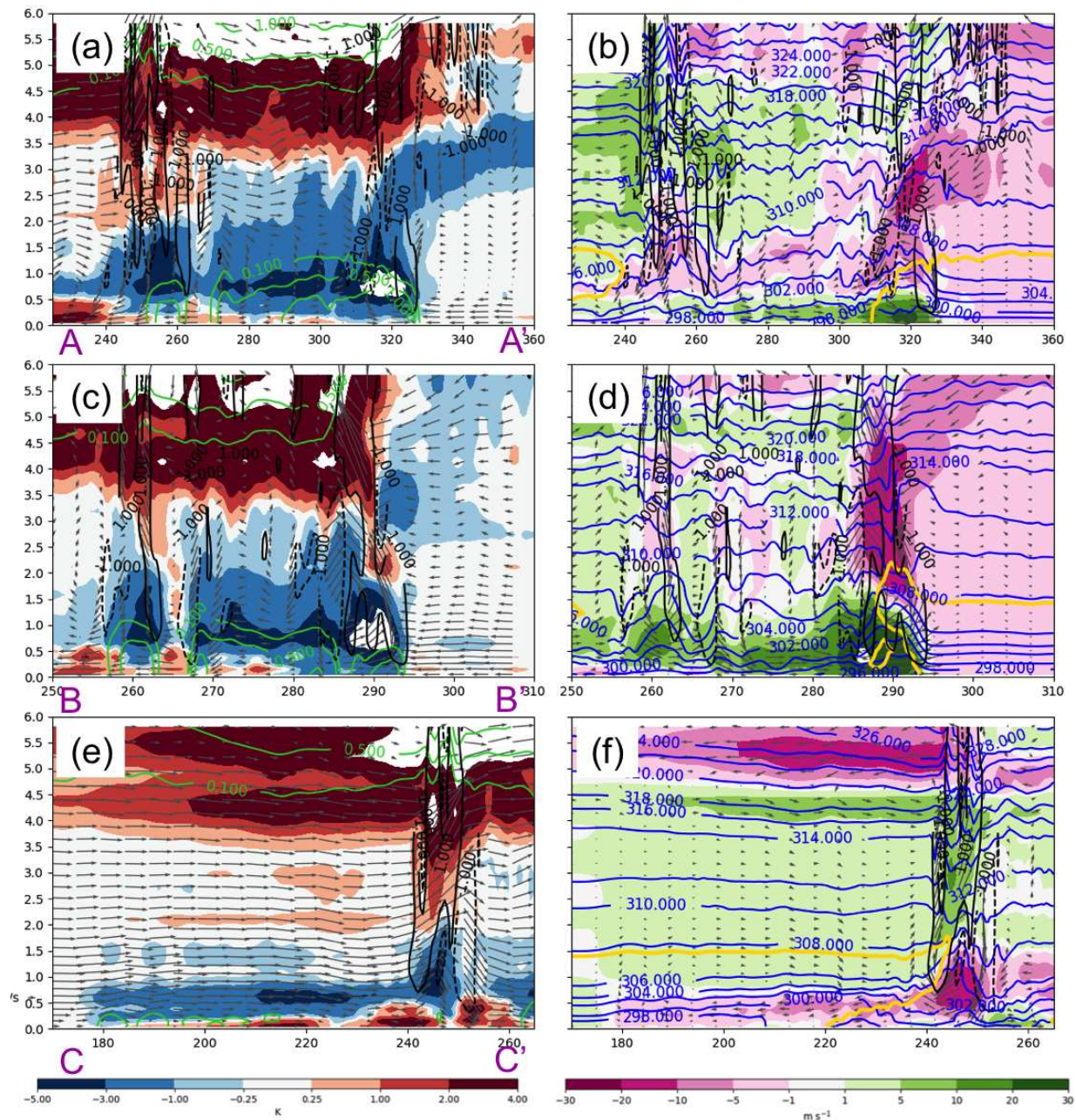


FIG. 3.5. Cross section through (a,b) A-A', (c,d) B-B', (e,f) C-C' after 4 hours. (a,c,e)  $\theta'_p$  (K) in filled contours,  $w$  ( $\text{m s}^{-1}$ ) in unfilled black contours,  $\pm 0.5$  and 1 Pa  $P'$  unfilled green contours, and wind vectors. (b,d,f) Wind perturbations ( $\text{m s}^{-1}$  in filled contours and vectors,  $\theta$  (K) in unfilled blue contours,  $w$  ( $\text{m s}^{-1}$ ) in unfilled black contours, 80% passive tracer initialized in the lowest 1.5 km indicated by gold contours. Magnitude of  $w$  multiplied by 10 in plotted vectors for emphasis. Wind perturbations are vectors projected onto the plane of the cross section.

Cross sections through different regions of the convection (identified by lines in figure 3.4a) show the vertical distributions of  $\theta'_\rho$ , and confirm that after four hours the greatest cooling is observed in an elevated layer, and very little, if any cooling occurs near the surface (Fig. 3.5a,c,e). In cross sections through the portion of convection with a strong eastward component (A-A'), the largest elevated  $\theta_\rho$  deficits were greater than 5 K. With the passage of the gust front, the 298 K isentrope at the lowest levels increases in height, but returns to its starting height shortly thereafter. At the same time, coincident increases in pressure and the 'semi-permanent' increase in the height of 302-306 K isentropes in cross sections A-A' (Fig. 3.5a,b) suggest that in this portion of the storm, the outflow takes on the characteristics of a wave-like bore much like those observed in Parker (2008); French and Parker (2008). It may be possible to use passive tracer removal as a proxy for identifying convective outflow air in locations where  $\theta'_\rho$  and wind perturbations are not intuitive (additional justification for this will be provided in future sections). The presence of more than 80% of the passive tracer below 1.5 km at the location of the wave/bore feature further supports the wave-like bore characterization. Since air flows through a wave, it is expected that tracer would still be present in the location of a wave in the absence of other convective processes (i.e. in a relatively undisturbed region). In Fig. 3.5b, tracer is only really removed right at the site of the downdraft and in the more turbulent region nearly 20 km behind the updraft at this location.

In cross section B-B' through the southwest portion of the leading line under the heaviest precipitation, a slight oscillation and semi-permanent increase in pressure coincident with a  $\theta$  deficit in an elevated layer (due to the semi-permanent increase in the height of the 300-308 K isentropes) suggests the presence of a bore (Fig. 3.5c,d). Unlike the northern portion of the leading line, here the presence of a 296 K isentrope and a  $\theta$  deficit at the surface suggest the presence of a \*very\* shallow density current at this location. Tracer removal shows a feature that nearly resembles a density current head just ahead of the 296 K line, and what appears to be lifting throughout the entire layer (Fig. 3.5d).

Further to the southwest, away from the precipitation, coincident oscillations in wind, pressure, and  $\theta_\rho$  perturbation can be seen in association with the clear oscillations in vertical velocity (Figure 3.4d). In the cross section through this region (C-C'; Fig. 3.5e,f), pressure oscillations are small ( $\sim 1$  Pa), but they do lead to a weak semi-permanent increase in pressure ahead of the convective outflow (Fig. 3.6). This, plus a shallow elevated layer is cooled 1 K, indicating a slight increase in the height of

the isentropes, and winds that oscillate weakly but then decrease in a layer that begins at the surface and ends just below the top of the layer of elevated cooling are characteristic of a weak undular bore<sup>1</sup>.

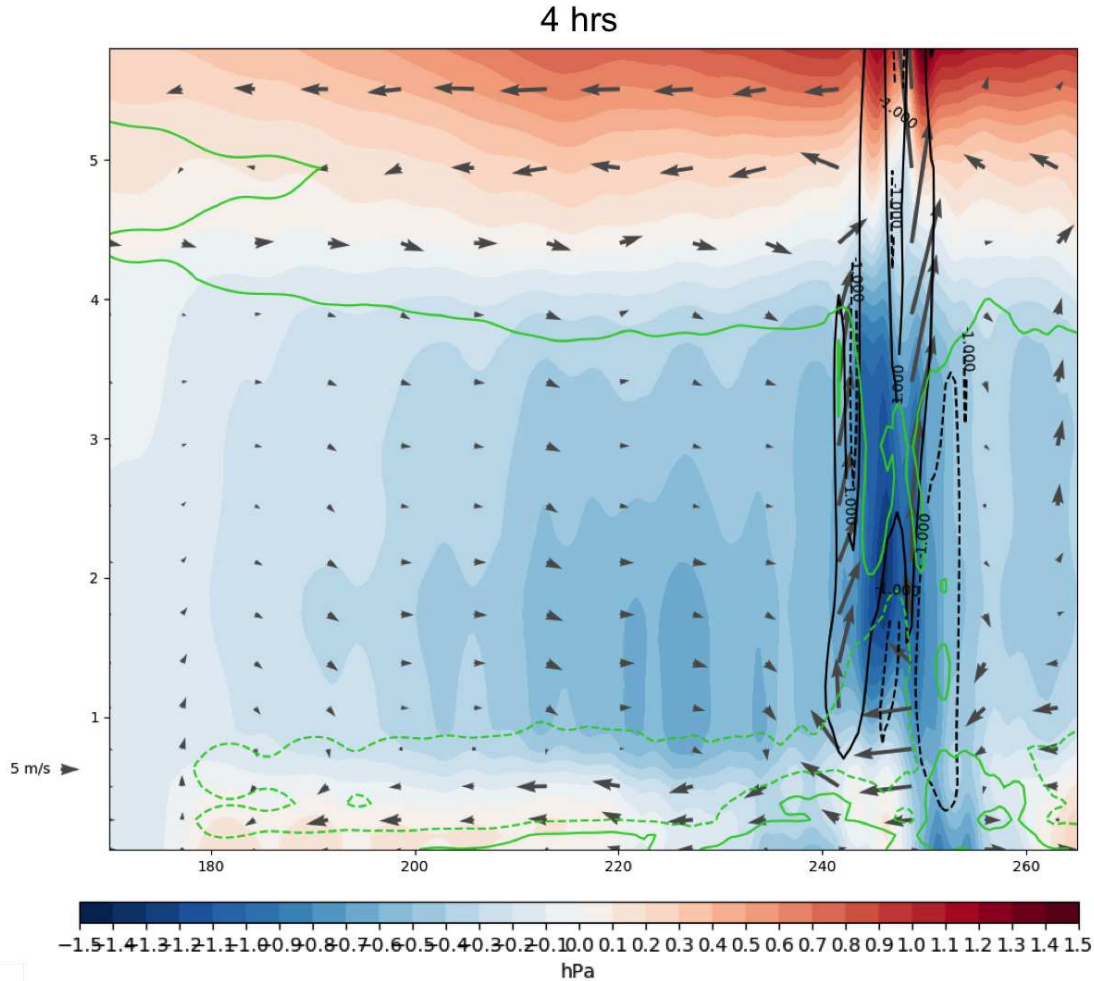


FIG. 3.6. Cross section through C-C' at 4 hours of  $P'$  (hPa, filled),  $w = \pm 1$  (unfilled black),  $\theta'_{rho} = \pm 1$  K (unfilled green), and wind perturbations ( $\text{m s}^{-1}$ ).

### 3.2.2 Rearward Off-boundary Development

Given the lack of a surface cold pool, it is of particular interest to explore the processes that might contribute to the ROD in this case. 1,880,000 passive parcels were placed in the southern western 2/3 (~ left of  $x=390$ , below  $y=390$ ). Parcels were initiated every 250 m between  $z=50$  m and  $z=4.05$  km. A sample of parcels that reached a vertical velocity of  $5 \text{ m s}^{-1}$  in a small region of the ROD convection

<sup>1</sup>If oscillations in  $P'$ ,  $\theta'$ , and winds did not result in a permanent change (albeit small), they would be considered a soliton.

(identified by the box in Fig. 3.7j) at 4 hours are assumed to have made it into ROD updrafts at this time. Figure 3.7 shows the path of these parcels in one hour chunks ( $t-45$  through  $t+15$  minutes) beginning at 2.5 hours, shortly before the parcels with the lowest starting altitude reach the SW outflow boundary. All three cross sections discussed in the previous section also intersect updrafts in the region of ROD. However, cross section C-C' most closely follows the trajectory of parcels that enter these updrafts, is displayed in figure 3.7, and will be the focus of much of the ROD discussion that follows.

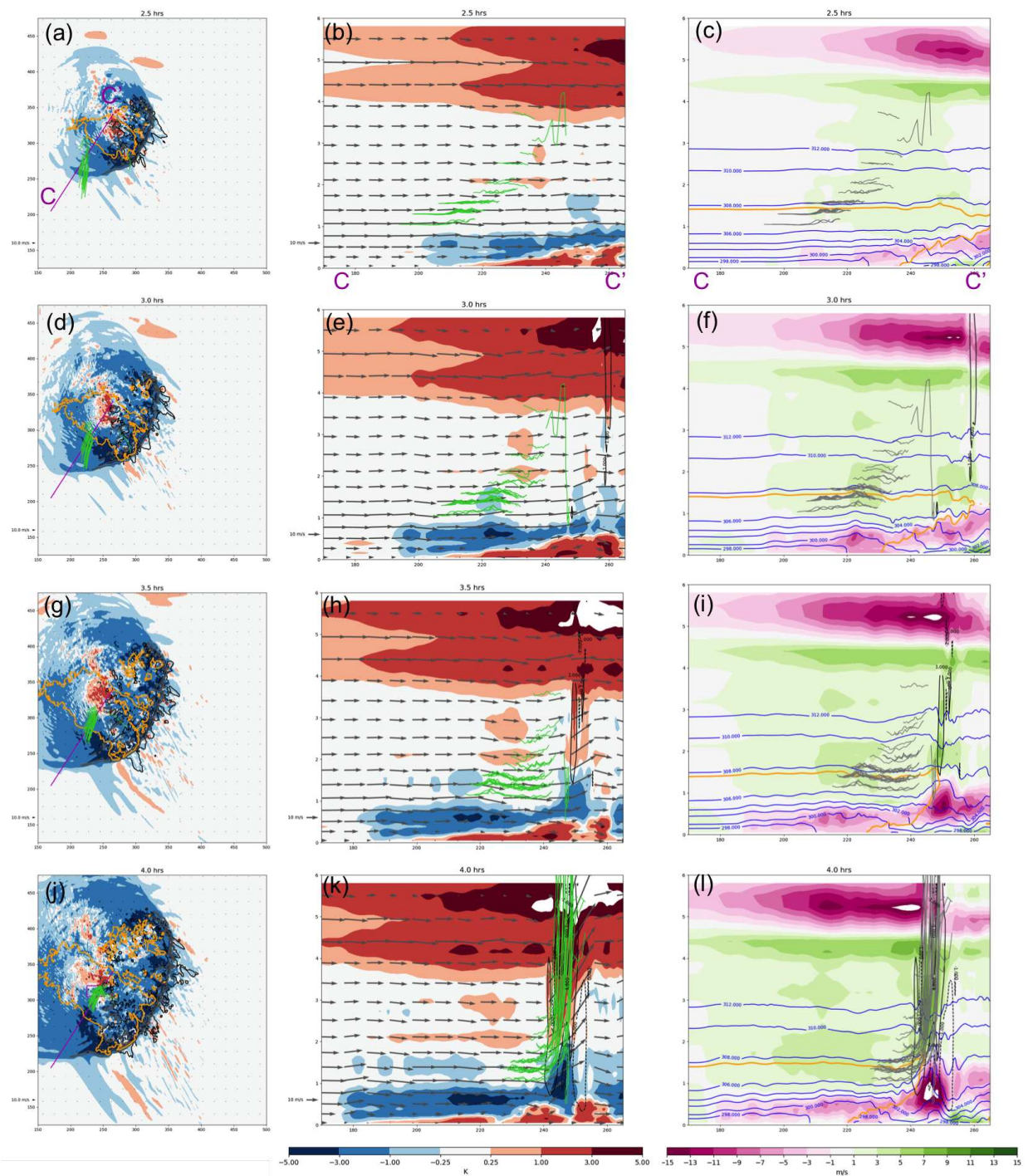


FIG. 3.7. (a,d,g,f)  $\theta'_\rho$  (K; filled),  $1 \text{ m s}^{-1}$   $w$  (gray), and wind perturbations from  $t=0$  (vectors) at 0.5 km, 40 dBZ reflectivity (black unfilled) and 80% passive tracer concentration at lowest model level. Green lines trace path of parcels that reach  $5 \text{ m s}^{-1}$  in a small region of ROD updrafts. (b,e,h,k) Cross section through C-C' of  $\theta'_\rho$  (filled),  $w$  (black unfilled), wind vectors. Green lines as in previous column. (c,f,i,l) Cross section of wind perturbations (filled),  $\theta$  (blue unfilled),  $w$  (black unfilled), and 80% passive tracer. Gray lines now represent parcel paths.

Parcels that reach ROD updrafts in this region come primarily from southwest of the MCS. Parcels encounter the shallow undular bore at a  $90^\circ$  angle while they are traveling almost due north (Fig. 3.7a), but then quickly curve to a more southwesterly trajectory. In a time series of parcel trajectories projected onto a cross section taken approximately tangent the parcel paths, it's clear that parcels that reach ROD updrafts almost entirely come from the above 1 km (Fig. 3.7). The few parcels that come from below 1 km all begin east of the convection and interact with the leading line before reaching the region of ROD. Here, only one of these near surface parcels is shown, but its path does not align with the cross section shown. Much like the parcels discussed in Peters and Schumacher (2015a), parcels gradually ascend over about 30 km after the passage of the leading edge of the southwest outflow boundary. Initially, they experience brief periods of ascent and descent with the passage of the waves at the leading edge of the boundary, but then ascend more smoothly, reaching a peak height around  $x=225$  (in the cross sections). Unlike the parcels lifted over the cold pool in (Peters and Schumacher 2015a), after a more gradual initial ascent, parcels experience a rather rapid ascent and then actually descend before reaching the updrafts in the ROD region. In fact, parcels that begin between 1-2 km essentially return to their starting height before being lifted into the ROD updraft (Fig. 3.8a). For the same parcels as plotted in figure 3.7, figure 3.8 shows the mean and standard deviation difference between the height of the parcel and its starting height ( $\Delta z$ ) as a function of time. Parcels that begin between 2-4 km actually descend between a few hundred meters and 3 km before entering the updraft (Fig. 3.8b,c). So instead of a gradual ascent lifting parcels to their level of free convection behind the southwest outflow boundary, the ascent is much more dramatic, and occurs closer to the convection.

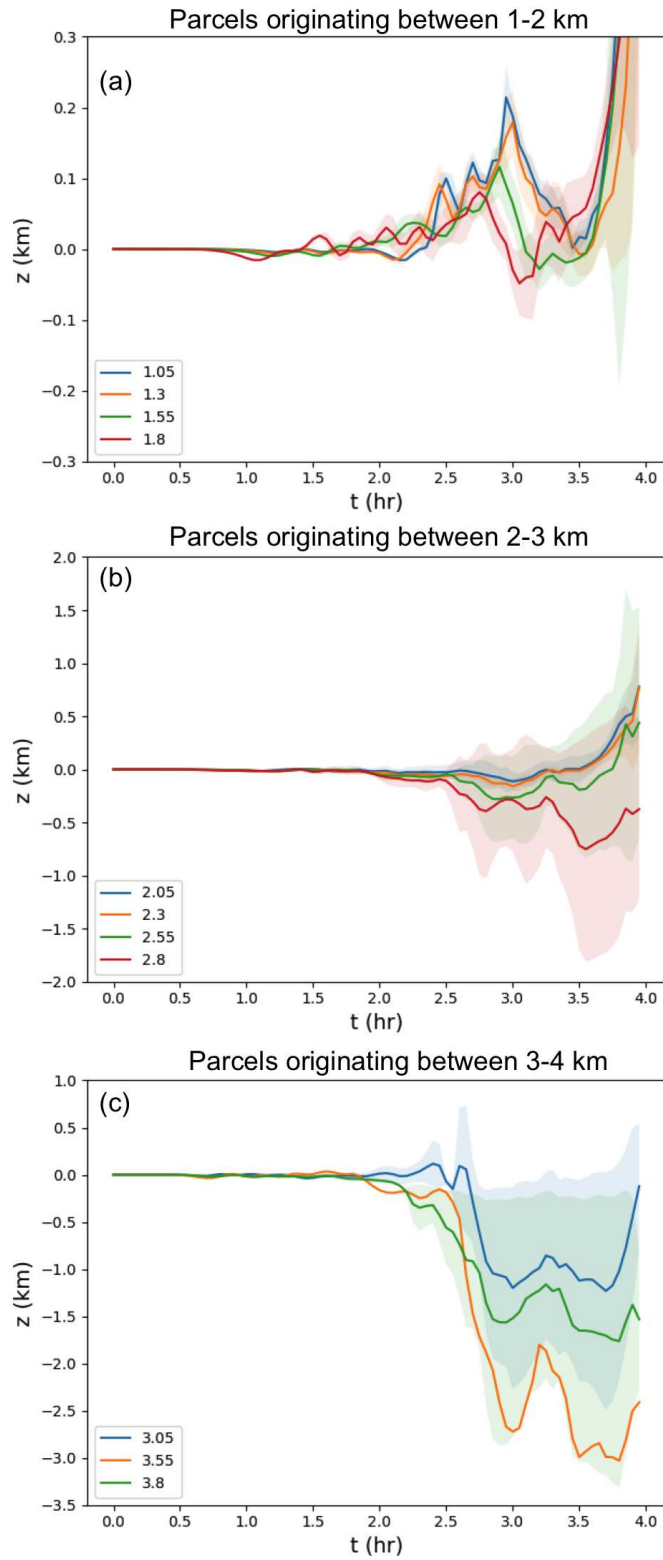


FIG. 3.8. Change in parcel height since time  $t=0$  for parcels that reach  $5 \text{ m s}^{-1}$  in a region of ROD updrafts. Averages and standard deviations shown by initial parcel height for parcels originating between (a) 1 and 2 km, (b) 2 and 3 km, and (c) 3 and 4 km.

In this environment, shallow layer of parcels located just below 2 km only needed to be lifted 10 m to reach their level of free convection (LFC; not shown). At the time shown in Figure 3.9, it appears that the bore initially reduces the distance parcels in the 1-1.5 km layer need to travel to reach their LFCs to  $< 10m$ . The depth of the layer of parcels with a small  $\Delta z_{lfc}$  briefly increases coincident with where the greatest elevated  $\theta$  deficit begins, however the layer of small  $\Delta z_{lfc}$  is completely removed as air descends behind the bore ahead of the updrafts.  $\Delta z_{lfc}$  only appears to be reduced again in the few kilometers ahead of the ROD updraft in association with an increase in the height of the  $\theta$  surfaces. In other words, the region of descent that follows the crest of the bore actually has a restablizing effect before parcels reach ROD updrafts. Curiously, in approximately the same location where the layer of parcels with  $\Delta z_{lfc} = 10$  m was removed corresponds to both a perturbation in the 298 K isentrope, as well as both a reduction of CAPE to below  $50 \text{ J kg}^{-1}$  and the removal of more than 20% of passive tracer initialized in the layer below 1.5 km.

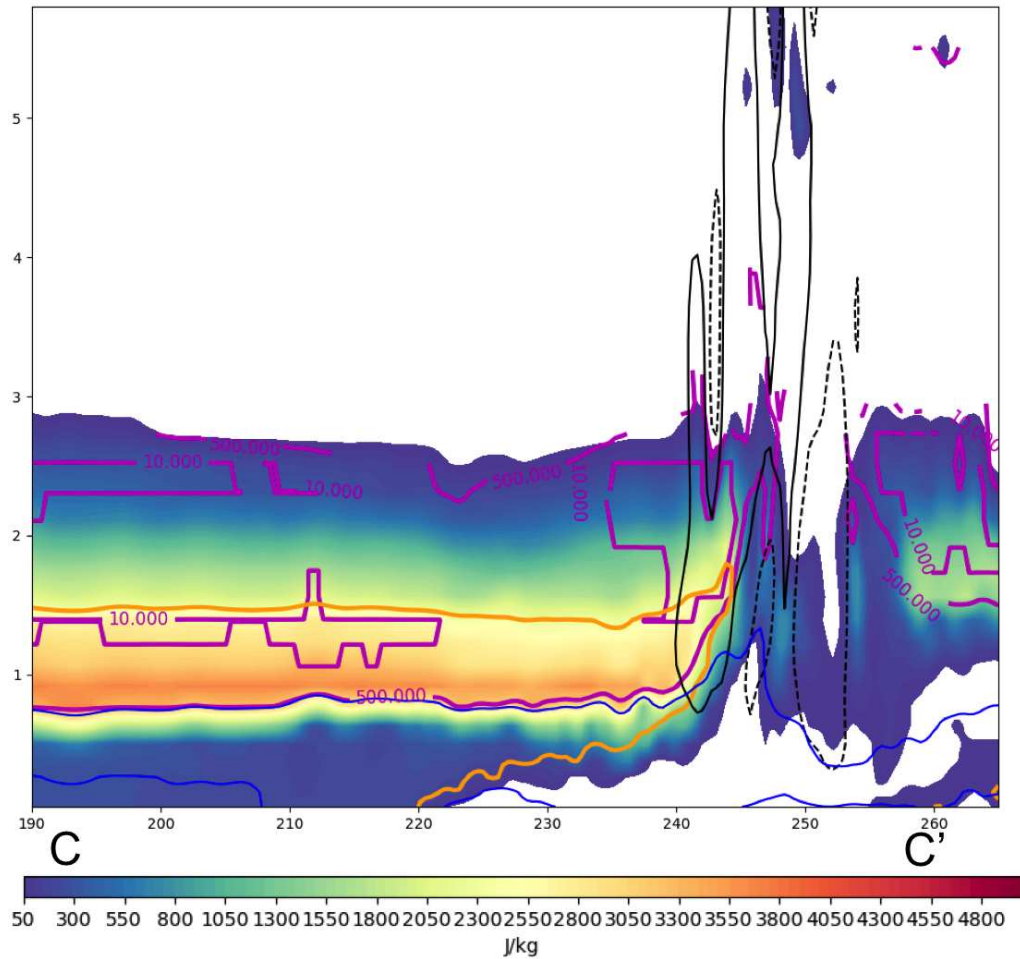


FIG. 3.9. 3 km average cross section through C-C' (Fig. 3.4a) of CAPE ( $\text{J kg}^{-1}$ ; shaded) and  $\Delta z_{LFC}$  (m; magenta unfilled) for parcels lifted from each level after 4 hours. Vertical velocity of  $\pm 1 \text{ m s}^{-1}$  (black unfilled),  $\theta_p = 298, 304 \text{ K}$  (blue unfilled), and passive tracer = 80% plotted for reference.

In another recent application of (Peters and Schumacher 2015a) to a case with a stronger bore at the leading southwest outflow boundary, the bore was found to lift parcels in a similar manner, reducing their CIN (and  $\Delta z_{LFC}$ ) more permanently before they were lifted to their LFC by the density current some distance behind the bore (Blake et al. 2017). Unlike Peters and Schumacher (2015a) and Blake et al. (2017) parcels that encounter this initial outflow boundary in the far southwest do not experience permanent lifting by the leading outflow. Instead, we propose that in this case, ROD parcels are lifted by a strong gravity wave that remains near its source in the layer where shear acts to amplify the wave

like those discussed in (Schmidt and Cotton 1989; Parker 2008; Schumacher et al. 2009; French and Parker 2008). Additional support may be provided by the convective outflow itself, in the form of an intrusion (discussed further below).

At the location of the updrafts, isentropes have a wave-like vertical displacement (and corresponding  $\theta'_\rho$  couplet) with up- and downdrafts corresponding to the upward and downward branches of the wave. The exact motion of convection is difficult to determine because of a combination of the grid translation and its very slow progression. But, given its nearly stationary appearance (with slight northward or southward trends depending on output time), its estimated motion is about 4.5 m/s to the north initially (the grid translation speed and direction), but later in the simulation slowly progresses towards the south. Studies have used a strong in-phase relationship between pressure and wind perturbations in the direction of wave motion ( $P'\bar{U}' > 0$ ) in identification of gravity waves (e.g. Bosart and Cussen Jr 1973; Koch and Golus 1988). Hereafter,  $\bar{U}'$  will be used to refer to wind perturbations in the direction of wave motion. Wind perturbations relative to the wave's northward motion between 0.5 and 1.5 km are negative, and the same layer has a negative pressure perturbation suggesting the in-phase oscillation of  $\bar{U}'P'$ . Waves generated below  $\sim 0.5$  km on the south side of the convection typically propagate south (discussed further in the following section), so here positive pressure perturbations and negative wind perturbations (positive in the direction of the wave motion) lead to in-phase variations in  $\bar{U}'$  and  $P'$  in this layer (Fig. 3.6). Parcels below 1 km (and even below 800 m) that come from the east either pass under or through the waves at lower levels and the majority are not lifted sufficiently to reach their LFCs<sup>2</sup> (not shown). Above  $\sim 0.5$  km, the waves that remain closely tied to the convection move north, so here a negative pressure perturbation and negative wind perturbation (relative to the direction of motion) also give an impedance ( $P'\bar{U}' > 0$ ). The vast majority of parcels that approach from the southwest above 1 km are lifted sufficiently to reach their LFCs and so do not pass through the wave.

If a strong gravity wave located in an elevated layer behind the convection is in fact doing the lifting, there are still several unanswered questions. Unlike the Blake et al. (2017) study, there is no surface cold pool in the region of the ROD updrafts, that in their study generate the perturbation aloft responsible for the final ascent. Furthermore, while the apparent MCS outflow boundary at the leading edge (i.e. at the gust front) extends a great distance away from the MCS, the only evidence of a density current

---

<sup>2</sup>Interestingly, surface parcels that do reach updrafts in the ROD region were first lifted by the bore at the leading line, but didn't reach their LFCs. Instead, they were lifted to some elevated level, where they could successfully be lifted by ROD updrafts. Generally, this occurred significantly less frequently than other processes described so far.

is in a small region confined to the southernmost portion of the storm. Yet, there must be downdrafts throughout the MCS, so what happens to the actual air associated with the convective downdrafts? The behavior of convective downdraft air that reaches the boundary layer is more complex, influenced by strong wind shear that changes direction with height and strong near surface stability. At the same time, what supports the wave in the region of ROD? Why is the wave only largely amplified in a layer from just above 500 m to 1.5 km, while the bore that propagates out ahead is primarily in the layer below 800 m? In the following section, dry 2D simulations were used to help answer these questions, and to more generally improve understanding of the interaction of convective outflow with a strong stable layer in sheared conditions.

### 3.2.3 2D Cold Bubble Experiments

Dry, 2D simulations were initialized by placing a  $-10\text{ K } \theta'$  cold bubble, with a vertical radius of 1 km and a horizontal radius of 10 km, 1.5 km above the surface. Two different 2D simulations were run: one with the zonal wind component (hereafter referred to as 2DX), and one with the meridional wind component (hereafter referred to as 2DY). Both simulations had the same thermodynamic profile as well as vertical and horizontal grid spacing as the original simulation. In these 2D simulations, it was possible to initialize passive parcels in the cold bubble in order to track the mass of the hypothetical downdraft as it interacts with the boundary layer. In the original 3D simulations, it's significantly more difficult to trace downdraft air in this way. Instead, tracer was placed in the lowest 1.5 km under the preface that since a density current transports mass, it should also replace mass. In other words, removal of tracer may act as a proxy for identifying convective outflow that does not present in typical cold-pool fashion. Though there are more processes that may contribute to the removal of tracer in the 3D simulation, test comparisons between 80% contour (20% removal) of tracer below 1.5 km and 10% contour of tracer initialized in the cold bubble were nearly identical (not shown).

The evolution of thermodynamic and wind fields strongly resembled those observed in cross sections (Fig. 3.10) through the moist 3D simulation (Figures 3.11 and 3.12). In cross sections with a primarily zonal component (A-A' in 3.10)<sup>3</sup> and 2DX, there is a large warm perturbation under the site of existing (or the initial) downdraft and a cool perturbation aloft. Passive tracer (presence or removal) co-located with the warm perturbation suggests that a non-negligible portion of the convective downdraft reaches the surface (Fig. 3.11). Over time, the passive tracer contour moves approximately with the warm perturbation towards west (left). Some of this cooling aloft in the warm bubble simulation

---

<sup>3</sup>Note: A-A' is actually the same cross section location showed previously at a time later in the simulation.

is an adiabatic response to lifting beneath the updraft, similar to the processes described in Schmidt and Cotton (1990) and Schumacher (2009) (Fig. 3.11a), but similar cooling exists in an elevated layer in the 2D simulation in the absence of strong, sustained updrafts (no moisture; Fig. 3.11c). Negative perturbations are generally maximized slightly east and west of the downdraft in association with the gravity waves generated on either side of it as it perturbed the stable layer (Fig. 3.11). In-phase wind and pressure perturbations ( $P'$ ) can be seen in both eastern waves, and the 2D western wave. In the 3D simulation, the western wave already has very small amplitude (and consequently small  $P'$  and  $\bar{U}'$ , that are in phase but just don't really show up well here).

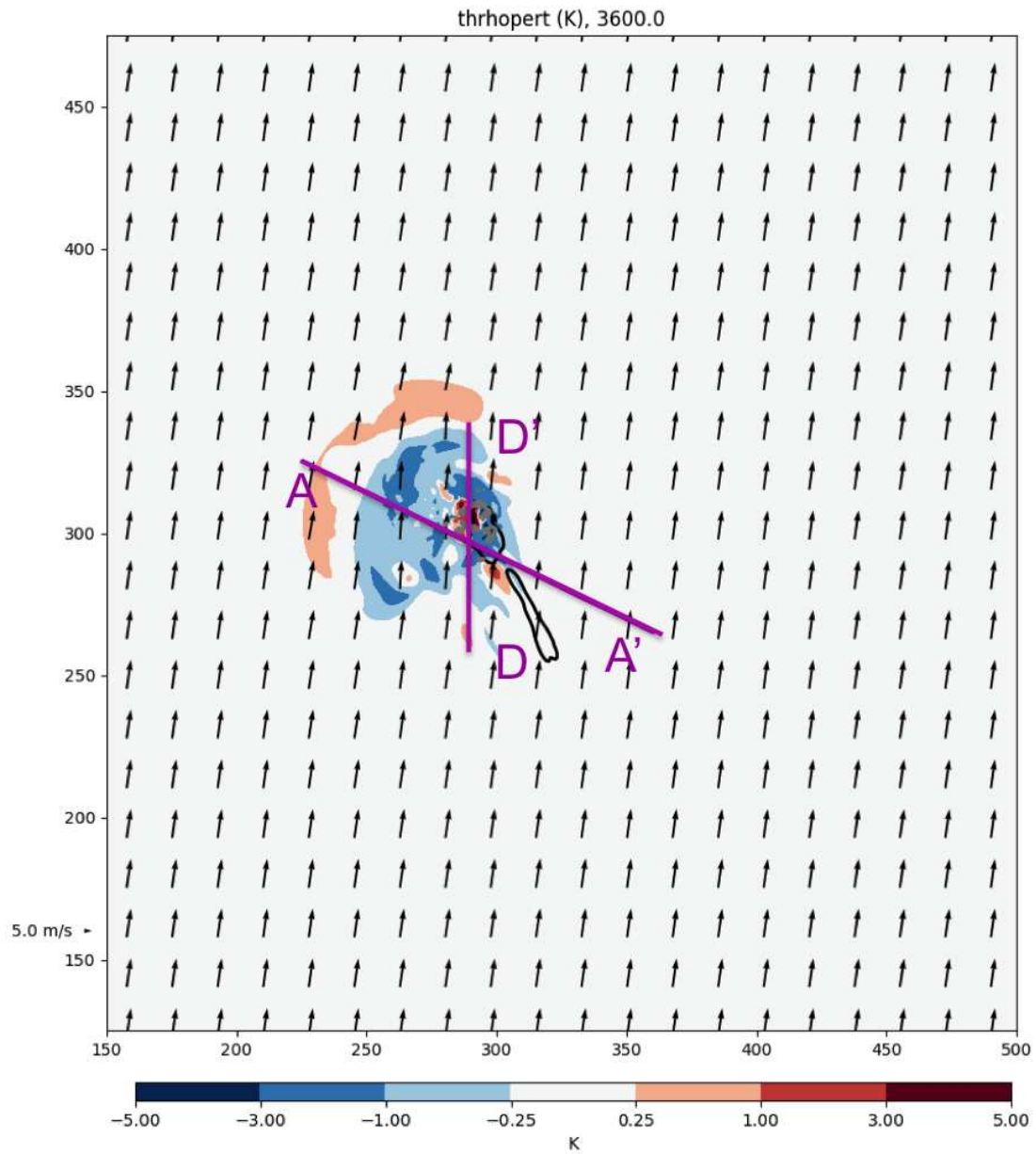


FIG. 3.10. 0.5 km  $\theta'_\rho$  (K; filled), 0.5 km  $w=1$  m s<sup>-1</sup> (gray), and reflectivity of 40 dBz (black unfilled) after 1 hour of the 3D simulation described in section 3.1 and cross section locations

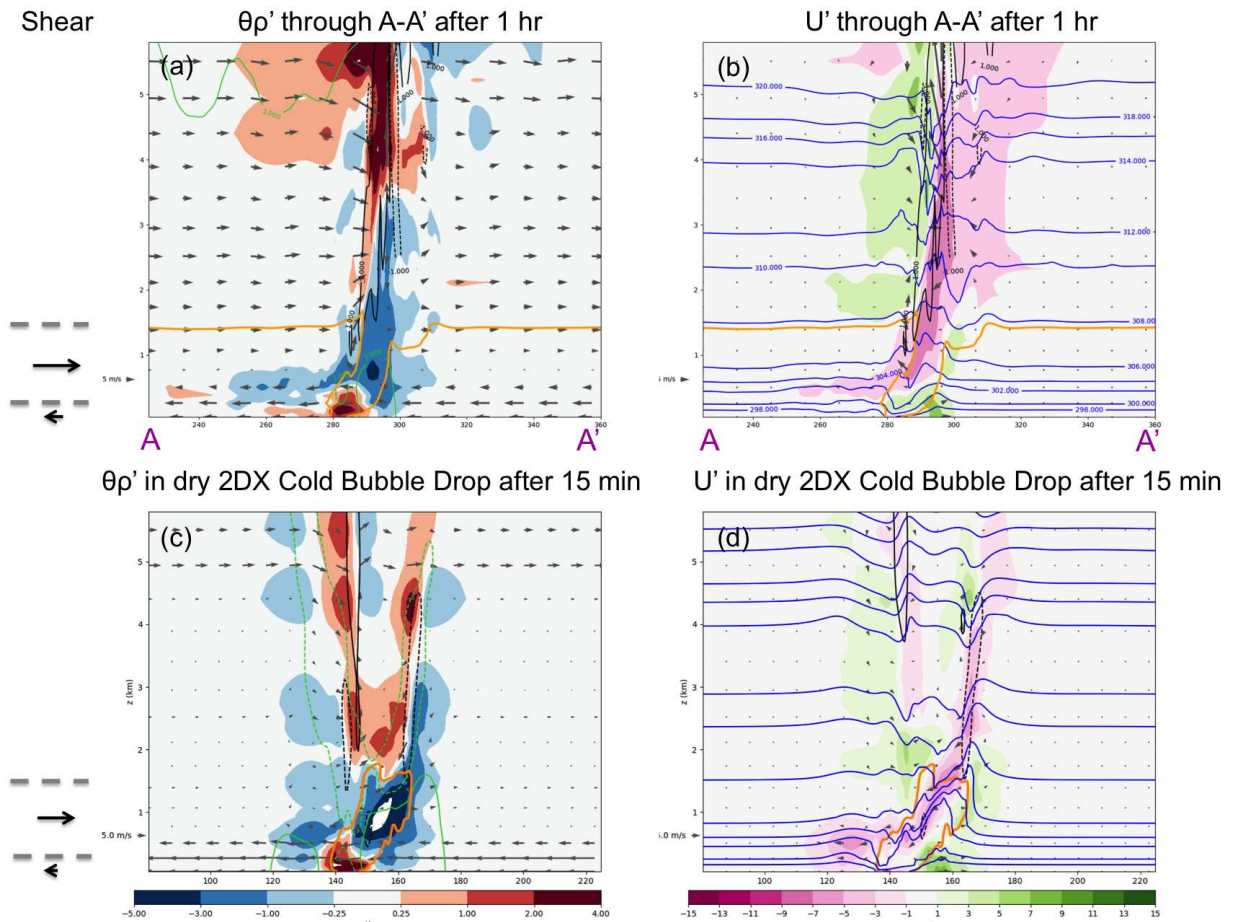


FIG. 3.11. (a,b) Cross section through A-A' (Fig. 3.10) at 1 hour. The orange line is contour of 80% (think of the decrease below 1.5 km as 20% removal) of the passive tracer initialized below 1.5 km. (c,d) Results of a dry, 2D -10 K cold bubble drop initialized with the zonal (u) wind profile after 15 minutes (2DX experiment). The orange line is the 10 % contour of passive tracer initialized in the cold bubble. (a,c)  $\theta_p'$  (filled contours),  $w = \pm 1 \text{ m s}^{-1}$  (open black contours), wind vectors. (b,d) wind perturbations from  $t=0$  (filled contours and vectors) and  $\theta$  (blue contours).

Shear

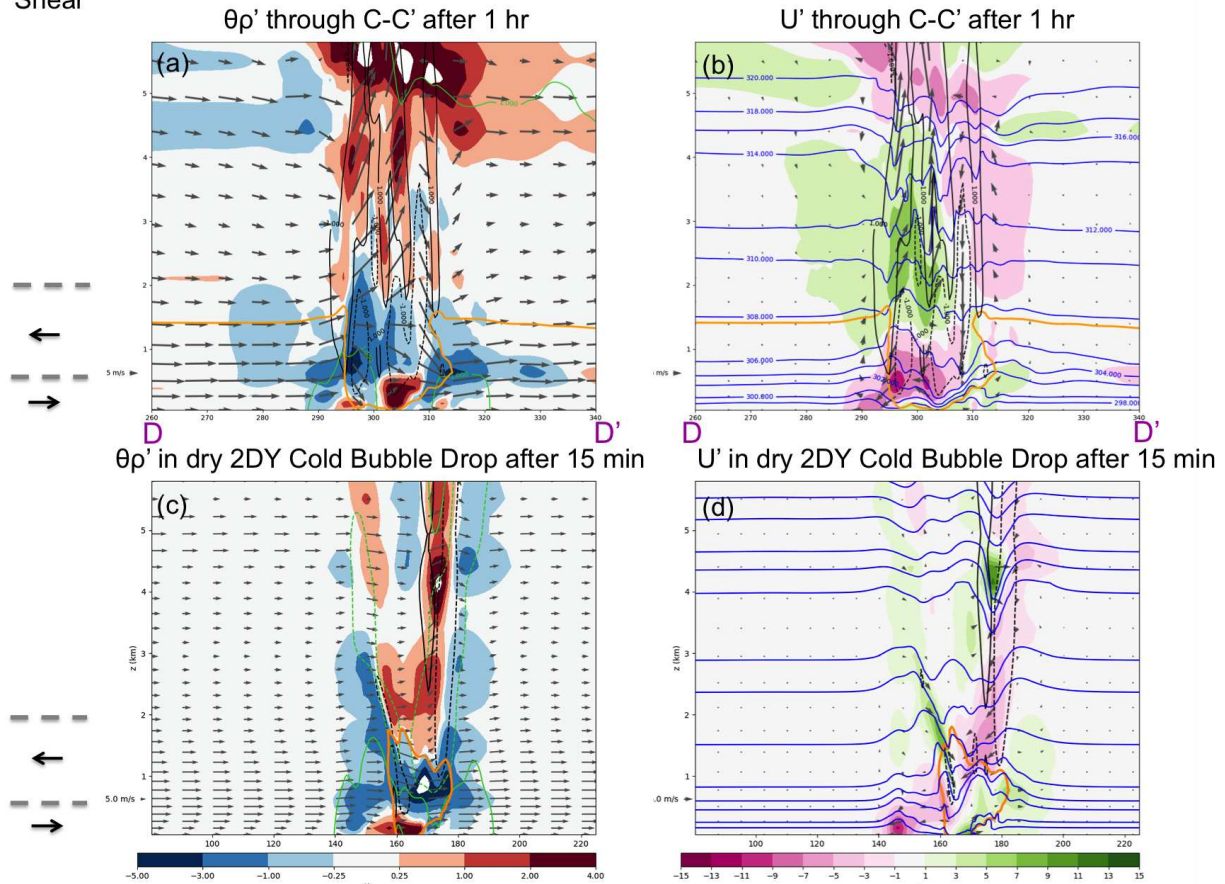


FIG. 3.12. (a,b) Cross section through D-D' (Fig. 3.10) after 1 hour. (c,d) Results of a dry, 2D -10 K cold bubble drop initialized with the meridional ( $v$ ) wind profile after 15 minutes (2DY experiment). Panel contours and vectors identical to Fig. 3.11

As in the 2DX experiments, 2DY cold bubble experiments and meridional cross sections through the 3D experiment (Fig. 3.10 D-D') have a near surface positive  $\theta'_p$  and negative  $\theta'_p$  in an elevated layer corresponding to a combination of the downdraft itself and the generation of gravity waves in either direction (Fig. 3.12). The greatest  $\theta_p$  deficit is more elevated and extends over a deeper layer to the south (left) than to the north (right) in the 3D cross section. The 2D cross section is slightly different; the largest  $\theta_p$  deficit is near the center, with deeper perturbations extending to the left and right. With this wind profile, to the south, it appears that the tracer has not spread any further than the initial southern boundary. Instead, some has reached the surface, and some remains above the inversion. Once again, passive tracer presence/removal at the surface lines up well with regions of warming. To the north, a large number of parcels are transported north (downstream) in a layer between 0.5 and 1 km, approximately with the strongest winds.

### 3.2.3.1 INTRUSIONS

In the above results, regions of cooling over warming suggests an increase in distance between isentropes in an elevated layer (which can be seen in actual isentrope contours in Figs. 3.11 and 3.12b,d ). This co-located with the presence/removal of passive tracer bears resemblance to something called an intrusion. In an instance with two fluid layers, an intrusion occurs when a fluid has a density less than that of the bottom layer, but greater than that of the top layer. In this scenario, an intrusion then travels along the interface, with a density between the densities of the layers (Figure 3.13a from Rottman and Simpson (1989)). In the present simulation, the fluid is stratified, but given the strong low level stability, it is reasonable to expect that downdrafts (especially early in the simulation) may actually be less dense than a layer near the surface, and so when they encounter that layer begin to spread out on top of it, generating waves ahead of, above and below it. Similar to density currents that reach the surface, intrusions can generate gravity waves and bores. The intrusion explanation is not perfect - there are places where downdraft air reaches the surface and travels along it but is actually warmer than the air it replaced (i.e. it could not be a density current). However, observed characteristics presented above suggest that it is at least one part of the puzzle.

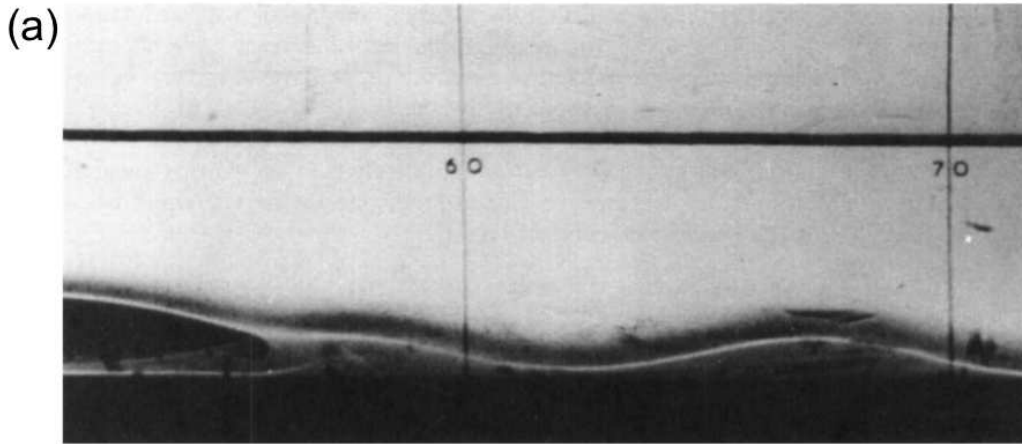


Figure 11. A photograph of an intrusion generating an undular bore on the interface between two fluids of different densities in the laboratory.

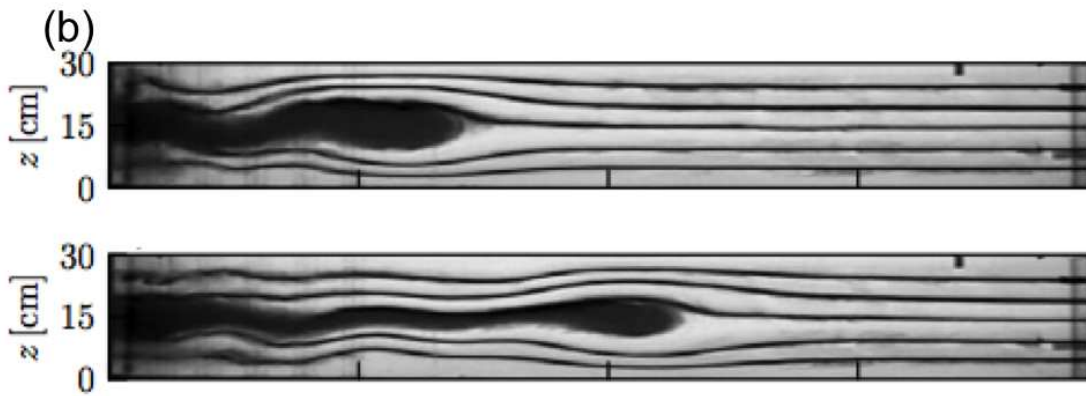


FIG. 3.13. Top: An intrusion between two fluids generating a bore in a laboratory. From Rottman and Simpson (1989). Bottom: Two snapshots of a laboratory generated intrusion in a uniformly stratified fluid (Sutherland and Munroe 2014).

An important difference between the intrusion described here and existing studies of intrusions, is that existing studies are done in stagnant flow (i.e. no wind shear) (e.g. Sutherland et al. 2004; Flynn and Sutherland 2004; Flynn and Linden 2006; Sutherland and Munroe 2014). Unlike a cold pool, it would be unphysical for an intrusion to flow upshear. So instead, when convective outflow less dense than air near the surface reaches a layer of equivalent density, the 'intrusion' is really more of an advection of outflow air by the wind. In the upstream environment, the wind prevents the intrusion from spreading out in the layer generating something like a barrier.

### 3.2.3.2 SURFACE WARMING

Let's return to the warm perturbation at the surface. Theoretically, an intrusion also effectively widens a layer between two  $\theta$  surfaces. By doing so, as it moves it will force some fluid to descend,

effectively bending the isentropes down and generating a warm perturbation. This is more clear in the example intrusion in figure 3.13b. However, there are several other possible reasons for the observed warming, any of which may occur at different times in different regions relative to the convection. In both simulations passive tracer (presence or removal) suggests that a non-negligible portion of the convective downdraft reaches the surface. One mechanism is simply that the air in the inversion region is potentially warmer than the air at the surface, so when a downdraft penetrates that layer, it brings some of that inversion layer air down to the surface. The downdraft air itself may also be potentially warmer than the air near the surface, such that when it descends the surface is warmed. Another mechanism that occurs more commonly in the wake region is the descent of air in unsaturated downdrafts that warms adiabatically as it descends. This is more commonly understood as the mechanism that leads a wake low through an associated hydrostatic reduction of surface pressure (Like that of Fig. 3.4c). However, an unsaturated downdraft would still encounter the low level stable layer, so multiple mechanisms may be at play.

At the location of the greatest observed  $+\theta'$ , the surface warms and the inversion layer is cooled, but the greatest observed warming is in a layer above the surface (Fig. 3.14). This effectively lowers the layer of conditional instability and the height of the inversion. The cooling at the top of the inversion actually leads to a weaker, but deeper second inversion layer. Despite this, the outflow can not be considered a density current here, since it is less dense than the air it is replacing! Once it reaches this level, since it is relatively cooler than inversion air above it, the outflow appears to just travel with the mean wind.

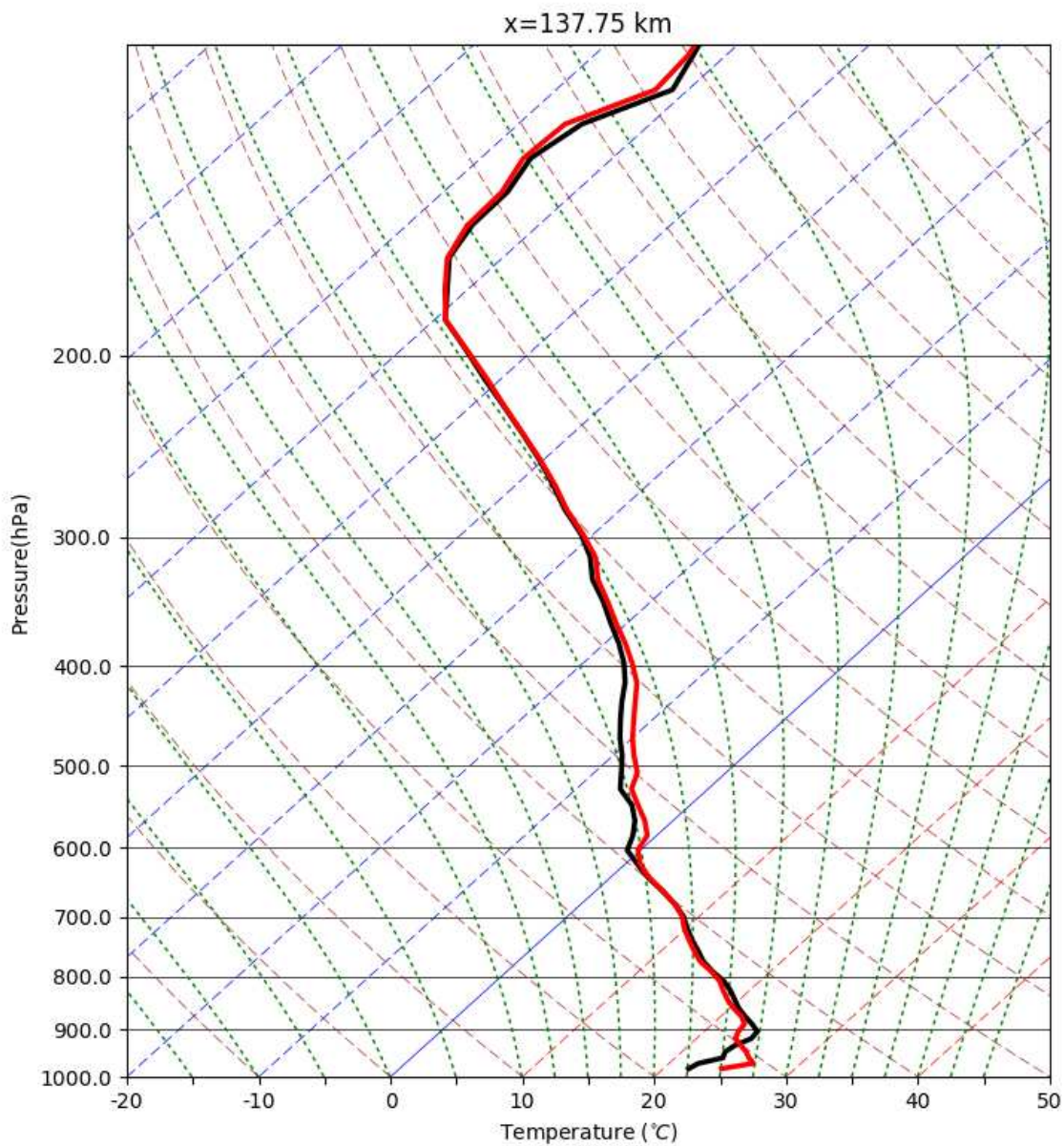


FIG. 3.14. Temperature profile through  $x=137.75$  (the strongest warming) in Fig. 3.11c,d after 15 minutes (red) and the original temperature profile (black) on a Skew-T Log-P diagram.

In the real atmosphere, and simulations with heterogeneous initial conditions, this sort of MCS often develops in an environment with a synoptic scale N-S temperature gradient that typically progresses with time and has a cooling effect in this same region. Nocturnal environments also tend to

cool with time, and though the amount of cooling depends on a number of variables, this would also likely have a cooling effect on the region. Thus, this warming may not be as strong or as obvious in a more realistic environment.

### 3.2.3.3 WIND SHEAR AND WAVE AMPLIFICATION

Schmidt and Cotton (1989) demonstrate that vertical wind shear acts to modulate the amplitude of low-level gravity waves. Critically, they show that stronger shear results in a higher amplitude wave on the downshear side. In their 2D simulations with a stable boundary layer, this wave amplification was instrumental to lifting parcels to their LFCs. French and Parker (2010) applies this in a layer sense (i.e. for an effective inflow layer), where the shear in the layer where the waves exist is responsible for the amplitude modulation. A similar approach may help to explain the support of the wave in the region of ROD.

In the  $u$  wind profile, the shear reversal with height occurs around 250 m (approximated by a dashed line to the left of panels in Fig. 3.11). In the 2DX experiments, greater  $-\theta'_\rho$ 's are observed downshear (southeast) in a slightly elevated layer (Fig. 3.11a,c), consistent with amplified waves in the downshear direction in that layer (Fig. 3.11b,d). While the waves look slightly different, largest amplification occurs between about 500 m and 2 km in both simulations (Fig. 3.11b,d). Waves are also more vertically aligned in the 3D simulation. At later times, it becomes clear that the downshear (eastern) wave remains closely tied to the convection, while the western wave propagates away from the convection and toward the west.

In the  $v$  wind profile, the shear reversal with height occurs around 500 m (approximated by a dashed line to the left of panels in Fig. 3.12). Wave amplification above 500 m is larger on the downshear (southern) side in the 3D simulations (Fig. 3.12a,b), in part due to the existence of an updraft at this time. However, in the 2D simulation large waves are initially generated above 500 m in both directions (even slightly deeper upshear) and the upshear wave (Located around  $x=175$  km in Fig. 3.12d) remains deep throughout the simulation (Fig. 3.12c,d). In this case, the upshear wave is located above a layer where significant spreading of isentropes and passive tracer throughout much of the simulation suggests the presence of an intrusion (Fig. 3.12d between  $x\sim 160-180$ ). The downshear wave above 500 m generally remains near the site of the initial perturbation to the south (around  $x=160$  km in Fig. 3.12d). In both 2D and 3D simulations, a wave below 500 m races to the south ( $\sim x=290$  km in Fig. 3.12a,b and  $\sim x=145$  km in Fig. 3.12c,d). In the sub-500 m layer, this corresponds to the the upshear direction. In the 2DY experiment, the stacking of waves to the north (Fig. 3.12d around  $x\sim 175$ ) and favorable shear

for amplification of the wave below 500 m may also contribute to the deeper amplification of the waves above 500 m even though they are upshear at that location.

#### 3.2.3.4 A CONSIDERATION OF VORTICITY

Since intrusions have similar properties to density currents and gravity waves are really packets of vorticity it seems reasonable to consider a vorticity framework akin to RKW theory for the 2D simulations described above as suggested by Schmidt and Cotton (1990) and French and Parker (2010). However, the intrusion is far from a typical density current, and complex shear/stable layer interactions generate a number of waves with different behaviors. An example is provided using 2D simulations. Horizontal vorticity ( $\eta = \frac{du}{dz} - \frac{dw}{dx}$ ) is plotted in Figure 3.15a,c. In 2DX, negative vorticity is co-located with the  $\theta$  gradient to the east around 1 km. Coupled with positive vorticity due to wind shear in the layer, this may contribute an additional upward vertical velocity component (Fig. 3.15). However, at the location of the surface warming on the west side where generation of negative vorticity along the gradient might be expected, there is very strong positive vorticity. In this case, it appears that the 'down-draft' helped to advect strong positive horizontal vorticity from an elevated layer to the surface. This as well as plots of Brunt Väisälä Frequency, which show the layer of strong stability which was originally elevated nearly at the surface (Fig. 3.15b) support earlier suggestions that warm air from the top of the inversion is mixed down to the surface may be valid<sup>4</sup>. In the y-direction, horizontal vorticity generated by the v wind component is much stronger (and positive) near the surface, and weaker and negative aloft. The cold bubble drop generates large amounts of negative vorticity in the upshear direction (to the north) and a strong vorticity couplet upshear that looks a bit like wave breaking (Fig. 3.15c) above ~500 m. Chapter 4 will investigate some of the vorticity concepts mentioned here in greater depth in more simplified experiments. Similar to the 2DX simulation, in 2DY experiments, the layer of strongest stability has been lowered in the region highlighted by passive tracer, indicating the transport of inversion air towards the surface. In summary, there may still be some value to considering horizontal vorticity in the generation of upward motion in environments with no cold pool, but a number of additional factors must be considered. As (Schmidt and Cotton 1989) mentioned, it would be worthwhile to explore the possibility of an RKW-like balance, but an in-depth exploration of this application is a task which goes beyond the scope of this work.

---

<sup>4</sup>It is also interesting to note that high stability air appears to be lifted over the waves coincident with the top of the passive tracer.

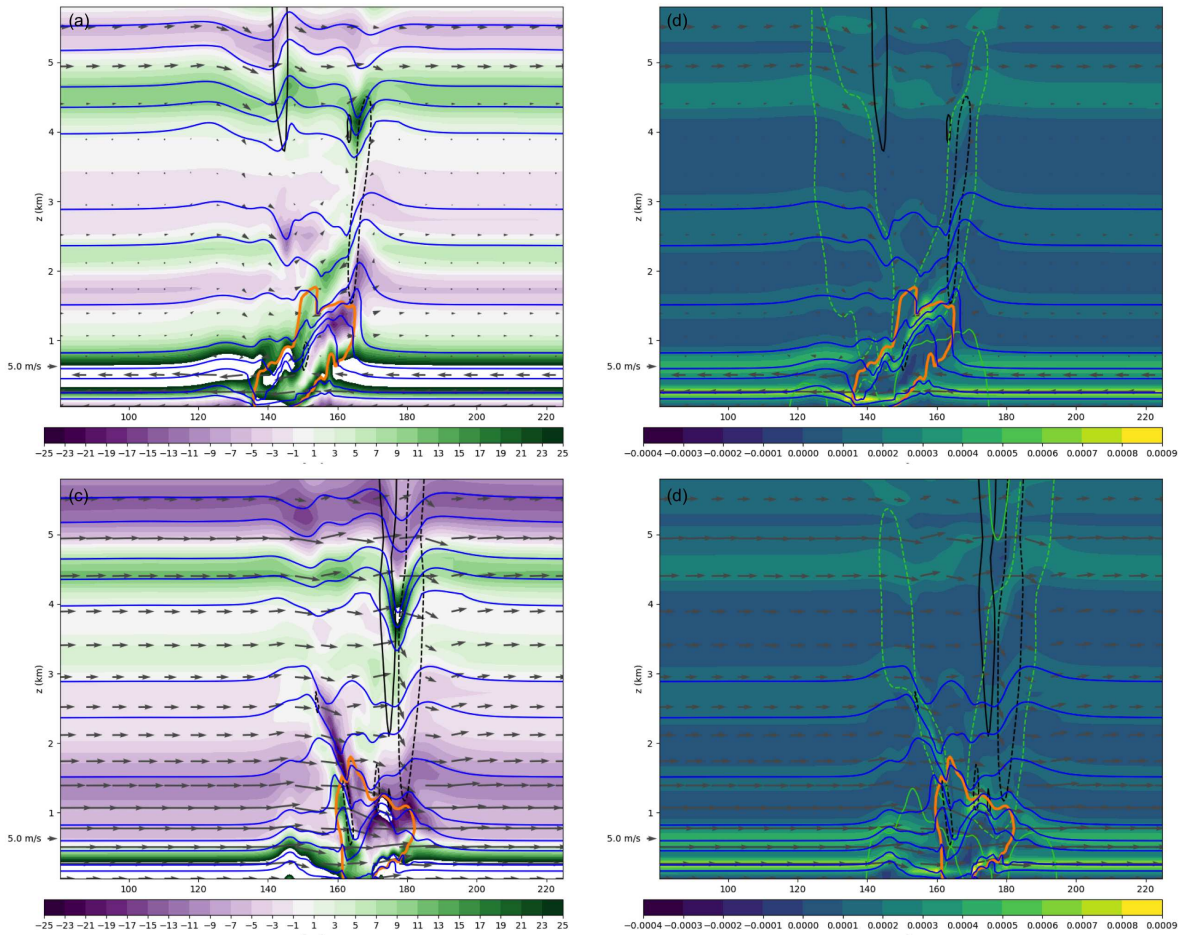


FIG. 3.15. Horizontal vorticity ( $\eta \cdot 10^3 \text{ s}^{-1}$ ) and Brunt-Vaisala frequency ( $N^2 \text{ s}^{-2}$ ) of 2D simulations with (a,b) u wind profile (c,d) v wind profile.  $\theta$ ,  $w = \pm 1$ , and passive tracer = 80% provided for reference.

### 3.2.3.5 SUMMARY OF PROCESSES

In summary, downdrafts that impede on a stable layer generate a number of waves during their descent. Downdrafts that are potentially warmer than the surface may overshoot their equilibrium layer, and warm the surface upon reaching it. Some downdraft air may also spread out in a layer of equivalent density, effectively spreading isentropes around it. Waves generated by downdrafts tend to be amplified upshear in a layer sense. The relevant shear layer may be somewhat dependent on the vertical organization of waves. While not detailed here, the primary processes seen in the control run are also present in sensitivity runs with varied microphysics as well as a run that includes Coriolis.

While shear and vorticity are absolutely related, based on the discussion in the previous section, a layered approach to the shear-amplification framework used in (Schmidt and Cotton 1989) is perhaps

the most consistent way to explain rising motion here. A conceptual schematic is presented in figure 3.16 for u and v wind profiles separately, and the layers of shear with different signs and the often used 0-1 km shear layer identified in both. In the x-direction, at upper levels the down-shear (eastern) wave is amplified. In this case, the low-level waves to the east remain relatively tied to their source. In the y-direction, particularly in the 3D simulation, the down-shear waves were amplified above and below  $\sim 500$  m, which means that southern waves were amplified above 500 m and northern waves below. Below 500 m, the southern (up-shear) wave is trapped, and moves away from its source. The down-shear wave remains tied to the convection and initially amplifies and then dampens as the upper-level upshear wave moves away from its source. In the 3D simulation, the upper-level downshear (southern) wave remains tied to its source, and is amplified as its reinforced by persistent downdrafts, but in the 2D simulation, the apparent wave breaking rapidly reduces the amplitude without the reinforcement from more persistent downdrafts.

If the processes that support ROD convection can be considered similar to those in meridional cross sections through the 3D simulation at during earlier times and somewhat similar to those in the 2DY simulations, then it is possible to apply the Y-direction schematic to help explain ROD convection. The bore along the southwest outflow boundary is like the wave that rapidly propagates to the south, and the ROD convection is supported by the 0.5 -1.5 km wave amplified and kept near the convection by wind shear in the same layer. Once convection has been initiated in this region, waves may also be amplified in response to the updrafts, and through the deepening of a layer between two isentropes by convective outflow that behaves as an intrusion.

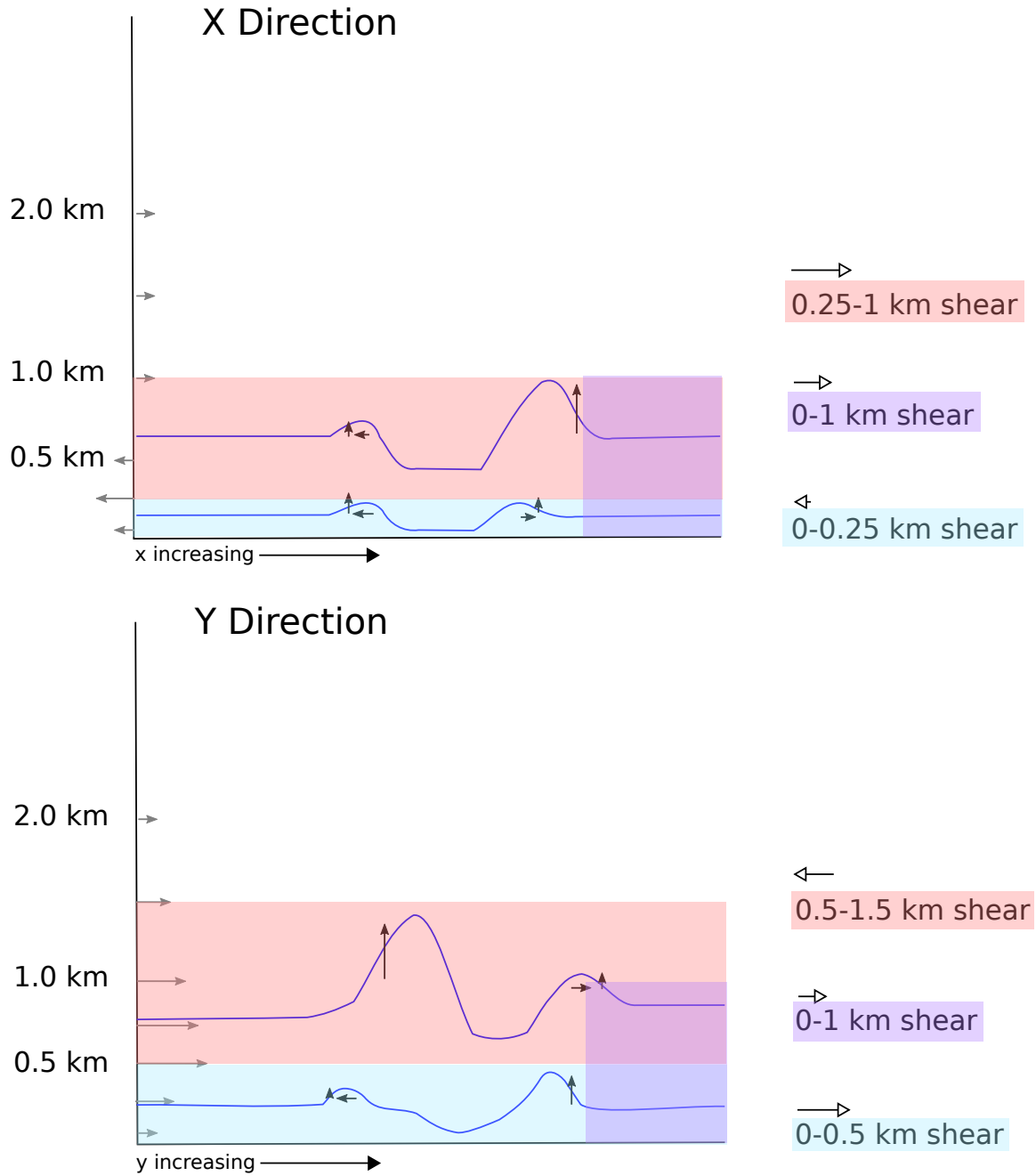


FIG. 3.16. Schematic of wave amplification in an environment with shear reversal and shear vectors for key layers. A simplification of processes in the X-direction ( $u$  winds) is shown in (a), the Y-direction ( $v$  winds) is shown in (b)

### 3.2.4 *Elevated?*

Several studies, notably Parker (2008), French and Parker (2008), and Billings and Parker (2012), have begun a discussion of whether nocturnal convection is truly elevated - decoupled from the stable layer - or not. In order to examine this in a new way, figure 3.17 was constructed to address the question of what vertical level(s) the updrafts originate in the present simulation. In panels b, c, and d of figure 3.17, the shaded field represents the lowest height of observed 1 or 5 m s<sup>-1</sup> vertical velocities at each point in the domain. Figure 3.17b displays the lowest observed height of 5 m s<sup>-1</sup> vertical velocities in a subset of the domain that includes the MCS just after 2 hours. In figure 3.17d, the minimum of the field shown in figure 3.17b taken in the x direction in the region bounded by the magenta vertical lines in figure 3.17b is shown. Figure 3.17c is identical to figure 3.17d, but for 1 m s<sup>-1</sup> updrafts. These boundaries were used to allow for a comparison between the southern edge of the leading line and the convection in region of ROD. Without this box, minimum heights of leading line updrafts would likely dominate.

In the first 2.5 hours, ascent rates below 1 km are greater than 1 m s<sup>-1</sup> at some point in the x direction in the 25 km bounded portion, over nearly the entire near-storm region (Fig. 3.17c). In figure 3.17c, the far northern updrafts correspond to the far northern portion of the convective line that bows slightly back into the bounding box at several times. Just after the first hour of the simulation, an initial southward propagating outflow boundary begins to generate 1 m s<sup>-1</sup> ascent rates below 250 m. As described above, shortly after this time, convection slowed its northerly progression, and began to push south as new cells generated along and strengthened the southern outflow boundary. This was just beginning at the time shown in Fig. 3.17a (marked by the first dashed line in 3.17 c,d). This southward progression is accompanied by even stronger near-surface ascent rates of 5 m s<sup>-1</sup>, even below 250 m in some places (Fig. 3.17d). At the time denoted by the second dashed line in figure 3.17d (where 5 m s<sup>-1</sup> were observed below 250 m at some point in the bounded region), figure 3.17b shows that 5 m s<sup>-1</sup> ascent rates were observed near the surface in several locations along the leading line, and between 1.5 and 4 km in the region of ROD. A break in low level 5 m s<sup>-1</sup> updrafts exists between the southward and eastward propagating segments, and it is not clear why. However, tests of other thresholds indicates that only 1 m s<sup>-1</sup> updrafts are relatively continuous across this region. In figure 3.17b the first (from the ground up) instance of 5 m s<sup>-1</sup> vertical velocities are observed closer to the surface along southern and eastern portions of the leading line than along the northern portion of the leading line.

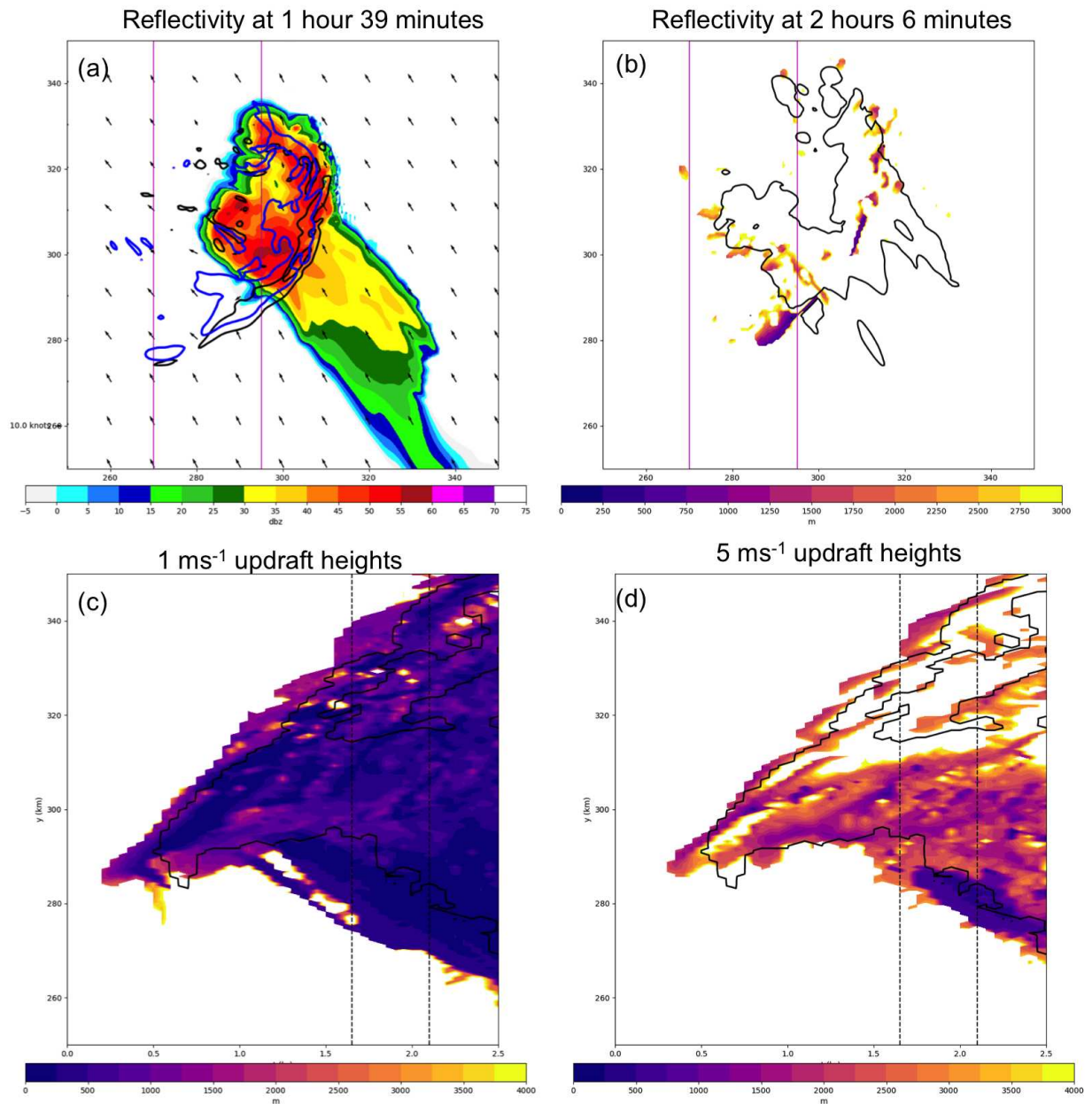


FIG. 3.17. a) Reflectivity (filled contours),  $0.5 \text{ km } w = 1 \text{ m s}^{-1}$  (black unfilled) and wind vectors, surface  $\theta' = -0.5 \text{ K}$  (blue unfilled) at a time shortly before the southwestern edge of the leading line gained a stronger southerly component of motion; b) The minimum height (m) where  $5 \text{ m s}^{-1}$  updrafts are observed (colored contours) and  $40 \text{ dBZ}$  reflectivity (black unfilled); c) A hovmöller of the minimum in  $x$  direction of the column minimum height of  $1 \text{ m s}^{-1}$  updrafts in the box bounded by the magenta lines. Values in the  $y$  direction (km) are plotted as a function of time (s) d) as in c, but for  $5 \text{ m s}^{-1}$  updrafts. The first dashed line in c,d marks the time of a, the second marks the time of b.

As in Parker (2008), French and Parker (2010), and Billings and Parker (2012), passive tracer was placed in the lowest 500 m. Since the stable layer in the input sounding was nearly 800 m deep, tracer lofted from below 500 m should be associated with stable air. One hour after initiation, none of the passive tracer has been lifted to 5 km (3.18a,c). This corresponds to primarily elevated inflow after the initial warm bubble release. 2 hours into the simulation, updrafts have become strong enough to at least lift some of the tracer a considerable distance (3.18e). At this point, downdrafts have reached the stable layer and generated waves. After 4 hours, the MCS has matured substantially, and 10-25% of tracer parcels placed in the lowest 500 m have been lofted to 5 km over a relatively large region in the southern half of the leading line (3.18b). In some places, percentages exceed 50%. This along with the previous analysis indicates that updrafts along the leading line may become more surface based with time; vertical velocities are observed closer to the surface along the southern outflow boundary as it begins to surge southward, and more near-surface tracer is lofted by the leading line over time. This fits with the findings of Parker (2008); French and Parker (2008); Billings and Parker (2012) and other recent works that suggest that even in strongly stable environments, perhaps some portion of the convective inflow still draws from the near surface environment.

In the northern portion of the leading line only 2% of parcels cover a broad area at 5 km, but smaller regions of >10% exist. This suggests, that even in this environment with horizontally homogeneous initial conditions, in addition to differences in updraft base height, there is some heterogeneity in the strength of low level updrafts. In other words, the interaction of the convection with the stable layer is likely not the same everywhere within an MCS, even along the same outflow boundary. These differences may be tied to the strength of convective downdrafts and the character of the outflow. In most of the ROD region, fewer than 2% of parcels make it to 5 km, indicating that convection in this region is basically completely elevated (3.18f). A comparison of a 3km average cross section through ROD and leading line updrafts emphasizes that more near surface tracers are lofted by the leading line, while < 2% of near surface tracers even make it above 3 km in the region of ROD (3.18d). This supports the suggestion of figure 3.17 panels b and d, that  $5 \text{ m s}^{-1}$  updrafts in the region of ROD are more elevated than updrafts along the leading line. In fact, figures 3.18 and 3.17d argue that at least the southern and eastern portions of the leading line are still very coupled to the surface. The idea that the forward-propagating portion of the MCS is more effective at lifting near-surface parcels than other parts of the MCS is consistent with findings of Schumacher (2015) where back-building regions of the simulated MCS ingested less near-surface air than the forward propagating portion of the MCS.

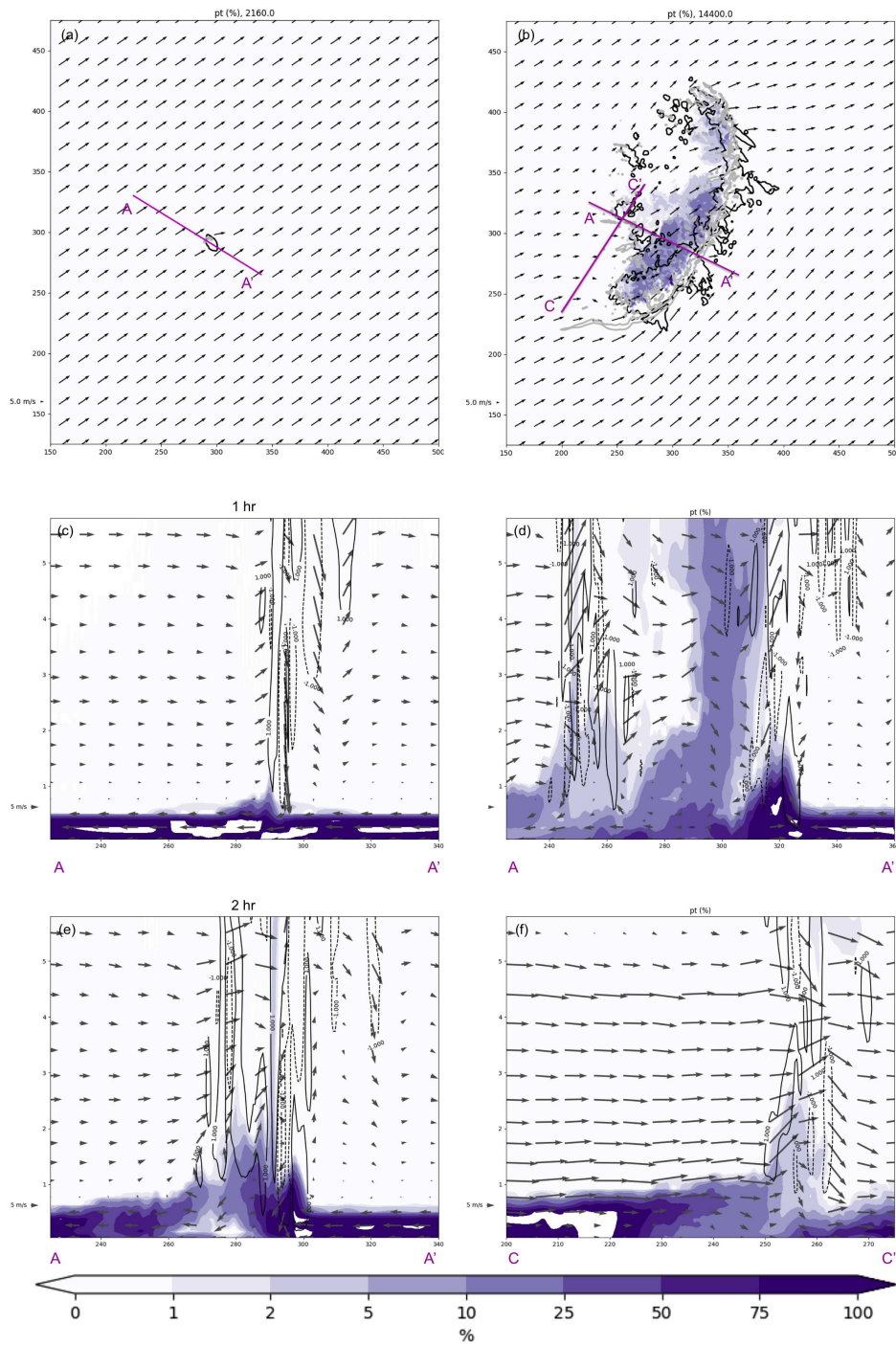


FIG. 3.18. Percentage of initial concentration of parcel tracer released below 500 m at initialization. (a) % at 5 km after 1 hour, (b) % at 5 km after 4 hours, cross sections through (c) A-A' after 1 hour, (d) A-A' after 4 hours, (e) A-A' after 2 hours, and (f) C-C' after 4 hours. Note that color shading is not linear.

### 3.3 SUMMARY AND CONCLUSIONS

In this work, a sounding launched as part of the PECAN field campaign on the 24-25 June 2015 was used as the environment in a idealized simulation with horizontally homogeneous initial conditions. This simulation was unique for several reasons: 1) The initial environment had a very strong low-level stable layer, different from previous studies focused on understanding ROD, 2) A simple warm bubble was sufficient to initiate not just a single cell, but a cell that was able to grow upscale into an MCS that had remarkable resemblance to the observed MCS. While some studies have focused on the spatial heterogeneity of the background environment (baroclinic zone, LLJ exit region, etc.) as important for the initiation and upscale growth of MCSs (e.g. Trier and Parsons 1993; Augustine and Caracena 1994; Tuttle and Davis 2006; Trier et al. 2006) and in the development of ROD (Keene and Schumacher 2013) this simulation has no external forcing for ascent in the background environment. Though external forcing likely played a role in the development of convection observed on the day of the environmental sounding, the homogeneous idealized setting provides an opportunity to explore other processes that might also support MCS development and ROD.

A summary of the major findings are as follows:

- The greatest observed  $\theta$  deficits are above the surface, similar the 25 June 2015 case that motivated this study and several other PECAN cases discussed in Chapter 2.
- Despite the strong stable layer, downdrafts still reach the surface, especially near the site of the downdraft, but their effect is a warm perturbation due to a variety of possible reasons. This may not necessarily manifest as strongly in heterogeneous simulations or in the real environment where other processes act simultaneously to cool the surface.
- Dropping a cold bubble in dry, 2D simulations with wind environments from the  $u$  and  $v$  wind components produces thermodynamic and kinematic effects that strongly resemble cross sections through moist 3D simulations.
- Downdraft air that is potentially warmer than the near-surface air may reach a layer of similar density and then spread out as an intrusion, which behaves a bit like an elevated cold pool, but in the downwind direction. However, the effect of shear may help the intrusion create a barrier on the upwind side.
- More intuitively, regardless of the motion of the outflow itself, the impact of a downdraft on a strong stable layer generates a variety of wave structures amplified on the downshear side with some layer dependency.

- In this case, ROD updrafts are most likely supported by a wave structure that is amplified and tied to the convection due to the wind shear in the effective inflow layer.
- ROD updrafts are nearly completely elevated. However, parcels experience descent (nearly returning to their initial heights) before being lifted into the updraft by something other than the bore tied at the edge of the leading line.
- Different regions of the same MCS, and even along the same outflow boundary may draw inflow from different layers depending on the interaction of outflow generated (waves/bores/etc.) and environmental wind shear.
- Even in an environment with the strongest observed stability during the PECAN field campaign, at least some portion of the convection rapidly became surface-based, with  $5 \text{ m s}^{-1}$  updrafts observed below 250 m and 50 m parcels lofted by updrafts. This further supports the growing body of evidence that nocturnal storms may not actually be decoupled from the stable boundary layer.

Even in an idealized environment, its clear that the interaction of an MCS with a strong low-level stable layer in a sheared environment is complex. MCS outflow is very non-linear, and results in a number of different wave structures that interact with wind shear relevant layers. In this case, ROD is supported by the amplification of a wave by the vertical wind shear between approximately 0.5 and 1.5 km. ROD is also likely reinforced by the convection itself (similar to early stages of the simulation), where updrafts enhance cooling below them and downdrafts lead to warming where they impinge on relatively cooler air below. There is still clearly much more work to be done to understand all of the relevant processes. Chapter 4 will focus on trying to unravel some of the intricacies of the balance between wind-shear and gravity waves, and what exactly about the wind shear profile makes MCS and ROD development possible.

## CHAPTER 4

### **SENSITIVITY OF CONVECTIVE OUTFLOW CHARACTERISTICS TO MODIFICATIONS TO STABILITY AND SHEAR AND IMPACTS ON ROD**

#### 4.1 INTRODUCTION

Studies of convective outflow – stable layer interactions have explored the instantaneous response to low-level cooling in different simple 2D environments (e.g. Raymond and Rotunno 1989; Haertel et al. 2001), 2D gravity wave–convection relationships in various wind shear conditions (Schmidt and Cotton 1990), gradual modification of stability or shear when vigorous convection is already ongoing (Parker 2008; French and Parker 2010), 3D gravity wave support of a back-building MCS (Schumacher 2009), and what happens when ongoing convection runs head first into a different air mass with much stronger stability (Lombardo and Kading 2018). Several of these studies, as well as Trier and Parsons (1993) and Marsham et al. (2010) have hypothesized about the inability of downdrafts to penetrate to the surface in environments with strong low-level stability. A number of the aforementioned stability studies (most notably Parker 2008, French and Parker 2010, and Billings and Parker 2012), as well as work discussed in previous chapters have begun to suggest that even in environments with strongly stable boundary layers, convection can actually continue to draw large amounts of inflow air from the near surface layer.

One of the more similar studies to those studies presented here, (Schmidt and Cotton 1990), used a warm bubble to initialize 2D simulations with a stable boundary layer in environments with no shear, weak shear, and strong shear. They found that deep-tropospheric gravity waves were capable of supporting convective updrafts, and that waves experience a Doppler shift and change in magnitude in the presence of wind shear. In particular, the downshear waves at low levels were amplified and suspected to be critical in lifting low-level air parcels to their level of free convection (LFC). They also express concern that their results can be traced back to the initial perturbation, and the displacement of isentropic surfaces generated by the initial heating near the top of the stable layer Schmidt and Cotton (1990). The work presented here explores a different mechanism for wave generation in 2D, and expands warm bubble experiments to 3D with more complex shear profiles.

In an environment with a low-level cold pool, (Rotunno et al. 1988) suggests that the optimal state (i.e. most upright updrafts, where convection is most likely to realize full CAPE) is reached when the integrated vorticity flux due to low-level wind shear is balanced by the baroclinic vorticity generation

due to a cold pool. The majority of 2D and 3D simulations presented in previous chapters either have no evidence of a cold pool, or only have cold pools in regions of strong convective precipitation. However, many waves are generated in the stable layer in all simulations. Since gravity waves are essentially packets of vorticity, and their motion is a result of vorticity flux, it is reasonable to consider the Schmidt and Cotton (1990) suggestion that a similar balance may exist for gravity waves in shear.

Both stability and shear in the nocturnal boundary layers observed during PECAN MCS cases had a large amount of variability (Chapter 2). In Chapter 3, horizontally homogeneous simulations initiated with a single warm bubble and a sounding from the environment with the strongest, deepest stable layer, and strong low-level wind shear led to the development of a highly 3-dimensional ‘bow-and-arrow’ MCS (Keene and Schumacher 2013). The MCS development from a single warm bubble, and the presence of rearward off-boundary development (ROD; Peters and Schumacher 2014) in the absence of both external forcing for ascent in the broader environment and a cold pool suggest that something inherent about the environment is supportive of MCS development and ROD. Given that ROD seems able to develop without previously studied mechanisms, and in a variety of low-level thermodynamic environments, perhaps something about the wind shear or specific combinations of stability and shear make this possible?

The primary goals of this Chapter are to address the questions 1) What is the resulting behavior when a ‘cold’ downdraft impinges on a strong low-level stable layer under sheared and unsheared conditions? 2) In strongly stable boundary layer, what vertical wind shear characteristics are supportive of a) an MCS b) ROD and why?

## 4.2 METHODS

The methods used here were designed to try to isolate individual components of the environment from the sounding used to initialize the base state of the simulation studied at length in Chapter 3 in order to better understand how they impact the characteristics of simulated MCSs and their convective outflow. This is made more challenging by the strong relationship between different components of the nocturnal environment.

Dry 2D simulations are used to diagnose relevant processes involved when downdrafts, represented as the cool perturbation, reach a strong low-level stable layer without the complexities of convection. Experiments that varied the strength of the cold bubble were used as a proxy for stable layer variation experiments with the assumption that the relative magnitude difference between the cold

bubble and the stable layer strength is more important than the true magnitude.<sup>1</sup> Wind modification experiments explore the changes to the interaction between the descending cool air and the stable layer that occur in different wind shear environments. Moist 3D simulations explore how convection develops in the different environments, and how the modifications influence the processes that maintain the MCS.

The sounding used for this set of experiments is an idealized sounding based on the 0428 UTC 25 June 2015 sounding used in Chapter 3. This case had the strongest and deepest stable layer observed during PECAN MCS cases (Chapter 2) and produced a ‘bow-and-arrow’ MCS with both a forward-propagating leading line and back-building along in a region offset from the leading southwest outflow boundary (Peters et al. 2017). To get the idealized sounding, data above 2 km were interpolated to a 200 m grid and below 2 km were interpolated to a 50 m grid. Then a 1 km (5 sigma) Gaussian smoother was applied to wind fields in the 600 to 150 mb layer and the full profile of temperature, dew point, and winds were smoothed using a 125-500m (2.5 sigma), 200-400 (2 sigma), and 200-400 (2 sigma) Gaussian smoother respectively. Finally, the temperature in the layer that extends from the surface to top of the inversion was replaced by a segment with a constant lapse rate that can be specified using the desired strength ( $d\theta$ ) and depth ( $dz$ ) of the layer<sup>2</sup>. In other words

$$\theta(z) = \theta_{inv} - \frac{d\theta}{dz} dz \quad (4.1)$$

Below the 600-700 hPa dry layer, RH is simply set to 90%, which is approximately the average RH for that layer. Finally, the modified temperature and moisture profiles are lightly smoothed again using 50-200 m (1 sigma) and 37.5-50 m (.75 sigma) respectively to remove any sharp changes at the intersection of the two segments without large additional modifications. Profiles were re-interpolated to a 50 m vertical grid spacing to insure that input soundings have higher vertical resolution than all of the experimental simulations.

---

<sup>1</sup>Originally planned experiments included a number of actual stable layer modifications. However, the modification of stability requires the modification of moisture, either so that that convection can be initiated or so that RH is not greater than 100% at initiation. At the same time, a reduction of stability in a strongly sheared environment can lead to low Richardson numbers ( $< .25$ ), and while Kelvin Helmholtz instabilities can and often do exist in the real atmosphere, in an environment with homogeneous initial conditions, they lead to an immediate overturning of the layer and are not realistic. Opposing goals of maintaining a true ‘control’ variable and maintaining a physically sensible environment make modification of the stable layer in this particular sounding especially challenging.

<sup>2</sup>This was originally done in anticipation of stable layer modification experiments, which may still be performed in the future.

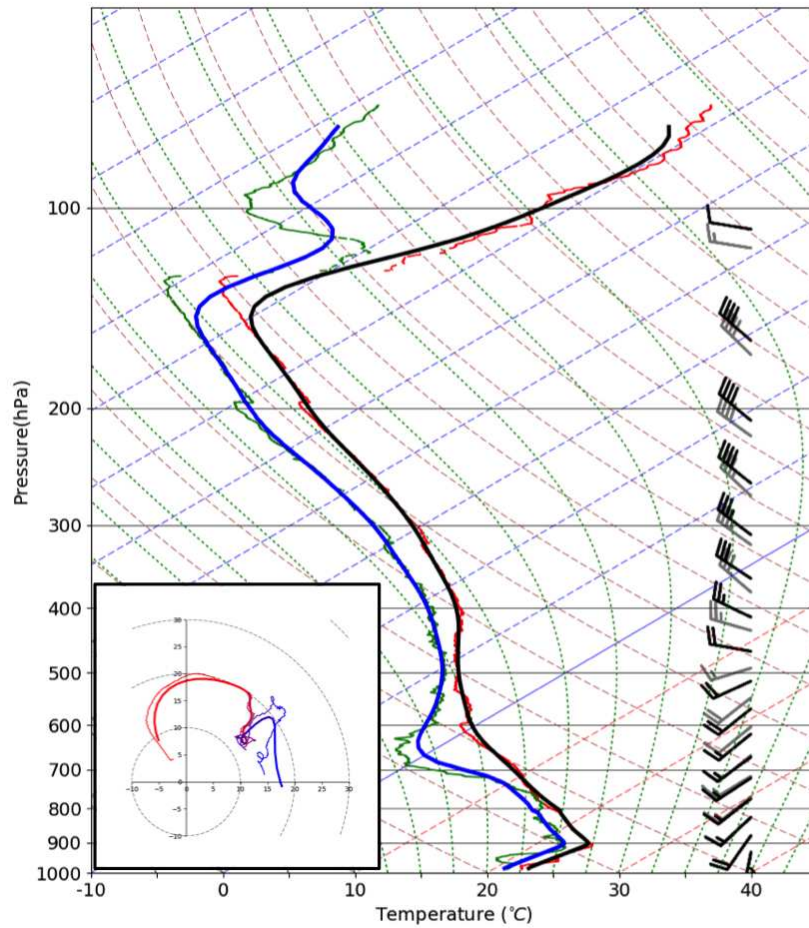


FIG. 4.1. Skew-T Log-P diagram of the 0428 UTC 25 June, 2015 sounding and an idealized version of it. The real sounding T, Td, and winds are represented by thin red lines, thin green lines, and gray barbs respectively. The idealized sounding T, Td, and winds are represented by black barbs. An inset hodograph also displays the real winds (thin line) and smoothed winds (thick line).

#### 4.2.1 2D Control Simulations

The 2D control simulation is initialized in a dry, horizontally homogeneous 612x60 grid point domain with 500 m horizontal grid spacing and a stretched vertical grid that has 100 m spacing near the surface and 500 m spacing aloft. Lateral boundary conditions are open-radiative, a free slip condition was applied at the surface, and a Rayleigh damping layer was applied near the 18 km model top. Sixth order positive definite advection was used with sixth order monotonic diffusion. The Klemp-Wilhelmson time-splitting, vertically implicit pressure solver (Klemp and Wilhelmson 1978) and a 1 second time step were used. The Deardorff (1980) turbulent kinetic energy scheme was used as the sub-grid scale turbulence.

TABLE 4.1. Cold bubble drop sensitivity experiments. Variations in drop strength, drop height, and grid spacing.

Run	dx	dz	Cold Bubble Strength (K)	Cold Bubble Center (km)
4KCPdrop	500 m	stretched 100-500 m	-4 K	2 km
10KCPdrop (CTRL)	500 m	stretched 100-500 m	-10 K	2 km
16KCPdrop	500 m	stretched 100-500 m	-16 K	2 km
24KCPdrop	500 m	stretched 100-500 m	-24 K	2 km
10KCPdrop1.5	500 m	stretched 100-500 m	-10 K	1.5 km
dz100	500 m	dz=100 m	-10 K	2 km
dz50stretch	500 m	stretched 50-250 m	-10 K	2 km
dx1000	1000 m	stretched 100-500 m	-10 K	2 km
dx250	250 m	stretched 100-500 m	-10 K	2 km
dx100	100 m	stretched 100-500 m	-10 K	2 km
dx100dz50stretch	100 m	stretched 50-250 m	-10 K	2 km

The simulation was initialized with a -10 K cold bubble with a horizontal radius of 10 km and a vertical radius of 1 km centered at 2 km above the surface, or about 1.2 km above the top of the inversion. Most observed downdrafts will certainly not have -10 K perturbations aloft, but many convective downdrafts are more persistent (i.e. they will not just happen once). As discussed in the previous Chapter, -10 K simulations had characteristics that resembled those produced by convective outflow in a similar environment remarkably well. Because of its 1 km radius, the cold bubble used in Chapter 3 actually applied artificial cooling to the top of the inversion layer. While the results between simulations with a 1.5 km center and a 2 km center are very similar, the sensitivity experiments explored here use a bubble with a 2 km center so that all of the initial cooling is applied above the top of the inversion.

Passive tracers were initialized in the same location as the cold bubble in order to help track the density current. Additional parcels were initialized in a layer below 1.5 km, with the idea that when a different air mass (i.e. a downdraft) penetrates the layer of parcels, the reduction of parcels should be another way to identify that air-mass. This becomes useful in 3D simulations where parcels can not easily be placed in downdrafts.

Before proceeding to modifications of stability and shear, the sensitivity of the simulation setup to the strength, horizontal and vertical radius (not shown), and depth of the center of the cold bubble were tested. Additional experiments varied the horizontal and vertical grid spacing (including using uniform vertical spacing) (Table 4.1).

#### 4.2.2 3D Control Simulation

The 3D control simulation is set up similar to the 2D control, and identically to the simulation discussed in Chapter 3. The domain is 1170x1170x60 grid points with the same vertical and horizontal grid spacing as the 2D control simulations, and a 1 second time step was used. In the 3D simulations, moisture is turned on. Simulations are initialized with a 1 K warm bubble centered at 1.4 km above the surface and with a horizontal radius of 10 km, and a vertical radius of 1.4 km. Passive parcels are initialized below 500 m in order to identify near surface parcels lofted by updrafts and below 1.5 km in order to assist in identification of outflow air (as in 2D simulations). Forward parcel trajectories were initialized in approximately the southwestern 2/3 of the domain below 4 km with a vertical spacing of 250 m and a horizontal spacing of 1 km.

#### 4.2.3 Shear Modifications

Shear modification experiments were set up identically to the control run, and only the wind shear profile was modified. The shear modification experiments were designed with two primary intents. The first, to understand how low-level wind shear impacts how outflow interacts with the stable layer. The second, was to isolate the individual components of the wind profile, specifically those that make this environment different from the elevated  $\theta_e$  composite environment in Chapter 2 (Fig. 4.2). CM1 simulations that use the composite elevated instability environment develop a bowing MCS, but no ROD. Differences in wind shear between the two profiles may provide clues as to the processes that support ROD.

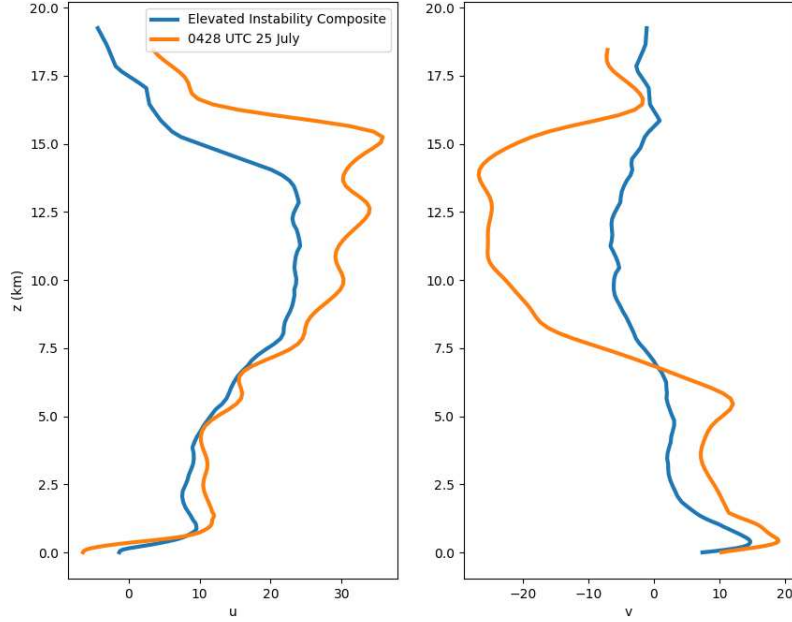


FIG. 4.2.  $u$  (left) and  $v$  (right) wind profiles from the Elevated Instability composite sounding created in Chapter 2 (blue) and from the 0428 UTC 25 June 2015 sounding used in Chapter 3.

Different combinations of three functions were used to generate analytical  $u$  and  $v$  profiles used in the experiments (listed in Table 4.2). The zonal wind profiles are generally built using a combination of a slightly modified equation 4 in Weisman and Klemp (1982) (WK82)

$$u_{WK82} = U_s \tanh(z/Z_s) - C \quad (4.2)$$

where  $C$  is a constant used to modify the profile in order to maintain an upper-level wind speed of  $10 \text{ m s}^{-1}$  and a simple Gaussian modified from (Peters and Schumacher 2015b)

$$M(z) = \begin{cases} A \exp\left[-\frac{(z_{ref}-z)^2}{\sigma^2}\right], & \text{if } (z_{ref}-z)^2 \leq z_{co}^2 \\ 0, & \text{if } (z_{ref}-z)^2 > z_{co}^2 \end{cases} \quad (4.3)$$

In equation 4.3 above,  $z_{ref}$  is the height of largest amplitude,  $z_{co}$  is the maximum vertical distance from  $z_{ref}$  where winds were modified,  $A$  is the amplitude, and  $\sigma$  controls the rate of amplitude decrease as the vertical distance from  $z_{ref}$  increases. Meridional wind profiles were made up of a combination of equation 4.3 and a third equation that accounts for skewness was introduced in order to maintain

resemblance to the LLJ in the real sounding. The skewed probability density function ( $M_{skew}$ ) was computed using the Python `skewnorm.pdf` function, with the parameters defined above and the addition of a skewness parameter ( $\alpha$ ). A list of experiments with the combinations of equations used to compute  $u$  and  $v$  and their respective  $z_{ref}$ ,  $z_{co}$ ,  $\sigma$ ,  $A$ , and  $\alpha$  parameters are given in Table 4.2. After initial analysis, four additional experiments were added to explore the sensitivity of the MCS development to specific low-level  $u$  characteristics. Those experiments are detailed in Table 4.3. A selection of resulting profiles (that visualize all possible combinations without plotting all profiles) are shown in figure 4.3.

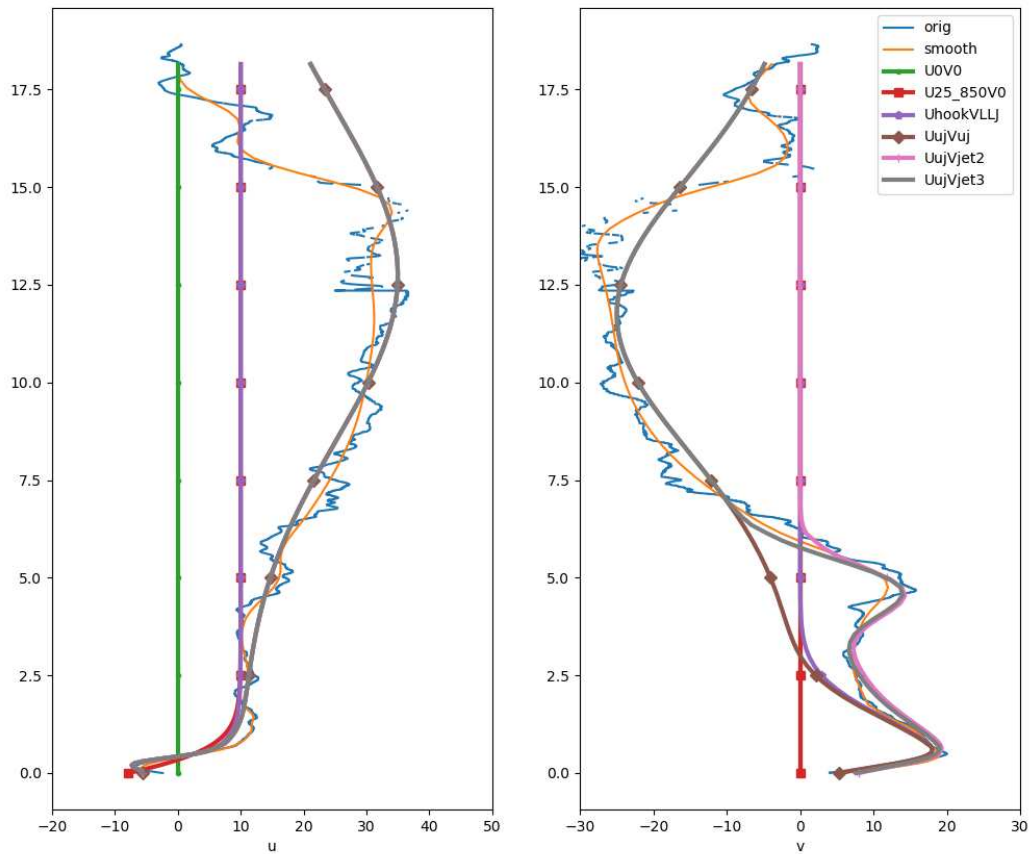


FIG. 4.3. Observed and smoothed winds from the 0428 UTC 25 June 2015 sounding, and a selection of experimental wind profiles described by Table 4.2.

TABLE 4.2

Run	Description	Equations	Parameters
CTRL	CTRL sounding shown in Fig. 4.1	N/A	
U0V0	No Wind	$u=0, v=0$	N/A
U25V0	Moderate unidirectional wind shear below 850 m	$u = u_{WK82}$	$U_s=25, Z_s=850, C=15$
UhookV0	u component of LLJ only - strong curvature ('hook')	$u = u_{WK82} - M1$	$u_{WK82}$ : $U_s=20, Z_s=0.85, C=10$ M1: $zref1=0.5, zco1=1.0, \sigma1=0.2, A1=8$
U0VLLJ	v component of LLJ only	$v=M1_{skew}$	$M1_{skew}$ : $zref1=0.4, zco1=6.0, \sigma1=1.2, a1=5, A1=25$
UhookVLLJ	LLJ only (both u and v)	$u = u_{WK82} - M1$ $v=K+M1_{skew}$	u as in UhookV0 v as in U0VLLJ
UhookVjet2	LLJ and 5 km v wind max	$u = u_{WK82} - M1$ $v = M1_{skew} + M2 + M3$	u as in UhookV0 $M1_{skew1}$ : $zref1=0.4, zco1=6.0, \sigma1=1.0, a1=4, A1=20$ M2: $zref2=4.9, zco2=5.0, \sigma2=0.9, A2=12$ M3: $zref3=2.3, zco3=4.0, \sigma3=2.3, A3=8$
UujVLLJ	upper-level jet in u LLJ only in v	$u = u_{WK82} - M1 + M2$ $v=K+M1_{skew}$	$u_{WK82}$ and M1 as in UhookV0 M2: $zref2=13.0, zco2=12.0, \sigma2=6.0, A2=25$
ULLJVuj	upper-level jet in v no 5 km v wind max LLJ only in u	$u = u_{WK82} - M1$ $v = M1_{skew} - M2$	$M1_{skew}$ as in U0VLLJ M2: $zref2=12.0, zco2=11.0, \sigma2=5.0, A2=25$
UujVuj	upper-level jet in u and v; no 5 km v wind max	$u = u_{WK82} - M1 + M2$ $v = M1_{skew} - M2$	u as in UujVLLJ v as in ULLJVuj
UujVjet2	upper-level jet in u v as in UhookVjet2	$u = u_{WK82} - M1 + M2$ $v = M1_{skew} + M2 + M3$	u as in UujVLLJ v as in UhookVjet2
UujVjet3	Analytical u,v most like CTRL run	$u = u_{WK82} - M1 + M2$ $v = M1_{skew} + M2 + M3 - M4$	u as in UujVLLJ $M1_{skew}$ as in UhookVjet2 M2: $zref2=5.0, zco2=7.0, \sigma2=1.0, A2=15$ M3: $zref3=2.4, zco3=4.0, \sigma3=2.3, A3=8$ M4: $zref4=12.0, zco4=11.0, \sigma4=5.0, A4=25$

### 4.3 RESULTS

There are slight differences in the bubble drop height and minor differences in the control sounding between results discussed below and the 2D experiments discussed in Chapter 3. However, as in

Chapter 3, the 2D simulation with u and v wind profiles (2DX and 2DY respectively) strongly resemble cross sections along the x and y direction in the 3D CTRL simulation.

One of the concerns presented by Schmidt and Cotton (1990) is the strong relationship between waves produced and the initial warm bubble. Given the different initial wave generation mechanism between warm bubble and cold bubble experiments, a brief comparison between early stages of 2D cold bubble simulations with no wind and a 3D warm bubble simulation with no wind is worthwhile. Cross sections in figure 4.4 are shown at different times because in the warm bubble simulation a downdraft has to be produced by convection. Despite differences at upper levels due to latent heating in the warm bubble simulation, the general thermodynamic structure observed at low levels is relatively consistent between the two runs (Fig. 4.4). There are elevated cool perturbations associated with gravity waves and warming at the surface. Passive tracer is removed in warm bubble simulations in a region that resembles the region where passive tracer initialized in the cold bubble is present. Vorticity is notably different between the simulations, but this is in part a function of how quickly the cold bubble simulation evolves compared to the warm bubble simulation. At later times in the warm bubble simulation, the vorticity near the surface changes sign and more closely resembles the vorticity of the cold bubble simulation (though by then, waves have moved well away from their point of initiation). This sign change in surface vorticity is discussed in greater detail in the following section.

## Warm Bubble Cross Section after 1 hour

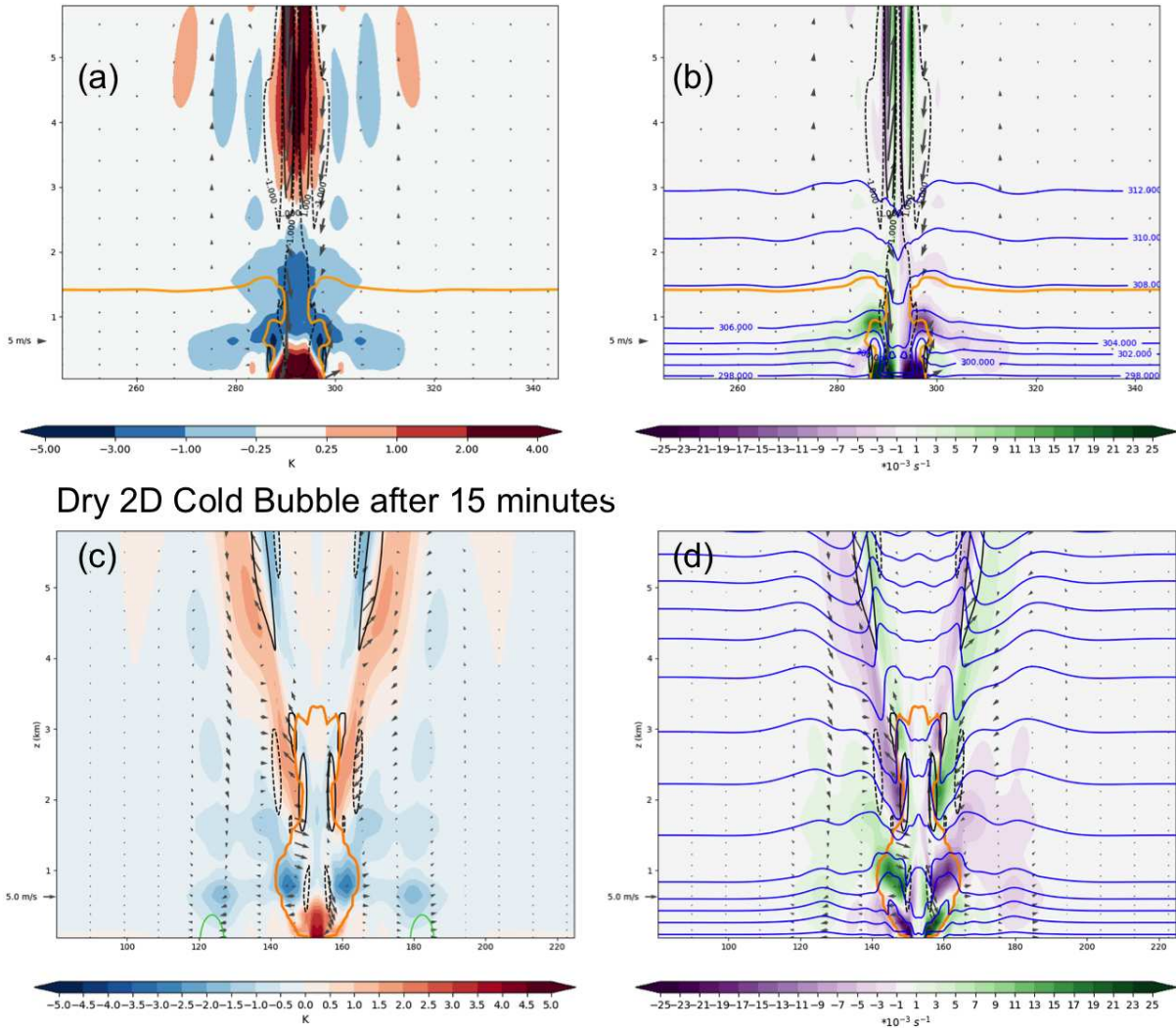


FIG. 4.4. Comparison of cross section through the 3D moist warm bubble simulation after 1 hour and the dry 2D cold bubble after 15 minutes. (a,c)  $\theta'_{rho}$  (K; filled) and  $\pm 0.5$  and 1 hPa pressure perturbations (green contours), 80% contour of passive tracer placed below 1.5 km. (b,d)  $\eta$  ( $\times 10^{-3} \text{ s}^{-1}$ ; filled) and  $\theta$  (K, unfilled blue).  $w = \pm 1 \text{ m s}^{-1}$  (black unfilled) and 10% contour of passive tracer initialized in the cold bubble plotted for reference (orange unfilled). Winds (here perturbations) given by vectors, where  $w$  has been multiplied by 10 for visibility.

### 4.3.1 2D Simulation Results

#### 4.3.1.1 SENSITIVITY TO COLD BUBBLE STRENGTH

The strength of the cold bubble was tested in experiments with no wind, and with  $u$  and  $v$  wind profiles from the control simulations (2DX and 2DY). The strength of the cold bubble was incrementally

decreased by 2 K until passive tracer did not appear to spread out in a layer below 1 km, and incrementally increased by 2 K until a cold pool finally reached the surface when the initial perturbation was -24 K (!). A selection of these experiments with a focus on larger perturbations are displayed in figure 4.5. In the -4 K simulation (not shown) waves like those in the CTRL run are generated, but are much weaker in magnitude and tracer did not spread out in a layer below 1 km; in fact, it did not appear to spread out anywhere (not shown). Note that the passive tracer displayed will nearly always have some concentration that remains at the location of the initial bubble. This is because the tracer was initialized with the same concentration everywhere where a  $-\theta'$  was applied, but the  $-\theta'$  was initialized with decreasing magnitude away from the center of the bubble. So, in some locations the tracer was initialized in a location with only a very small  $-\theta'$  relative to its surroundings.

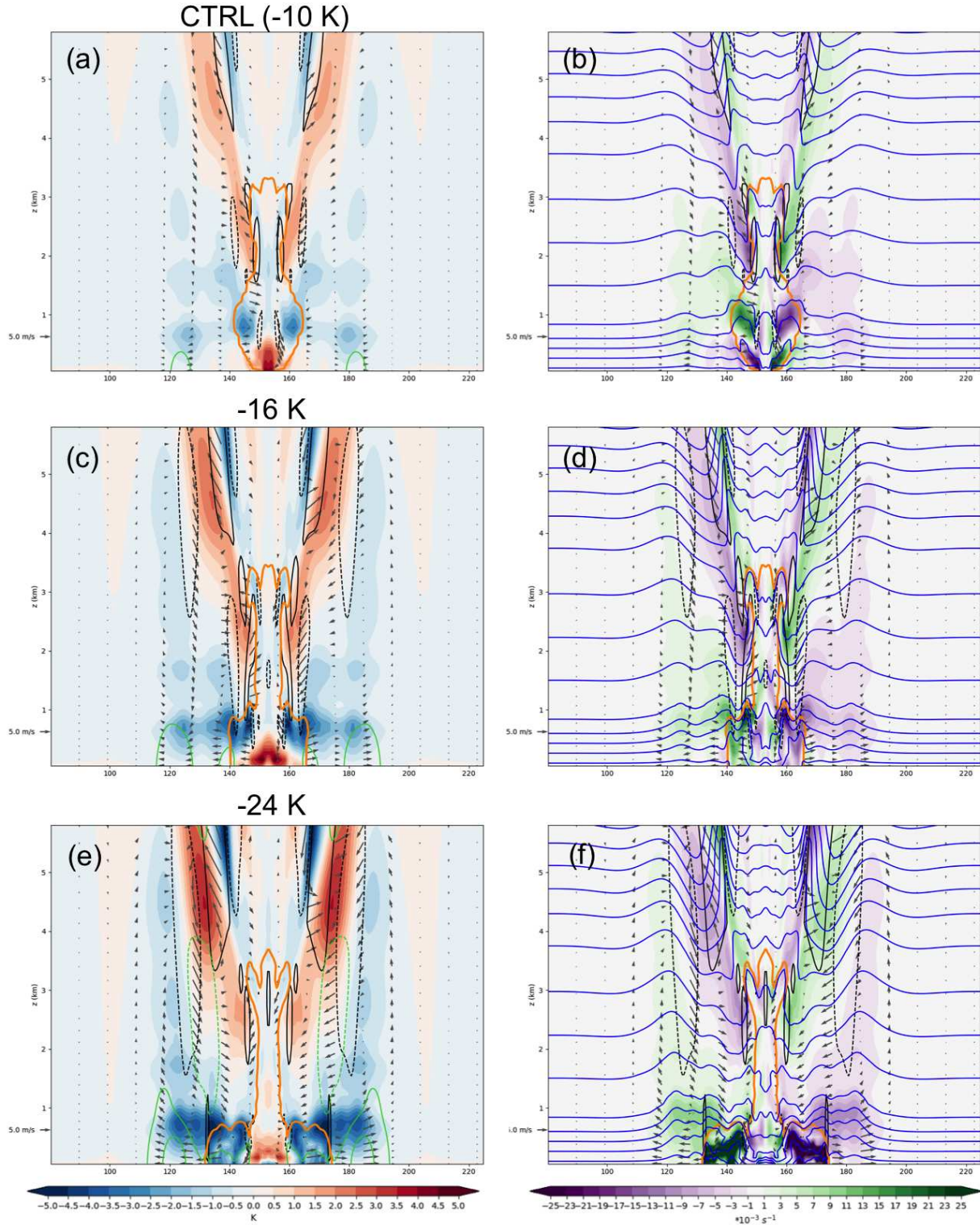


FIG. 4.5. UOV0 simulation with cold bubble strength variations. (a,c,e)  $\theta'$  (K; filled) and  $\pm 0.5, 1$  hpa pressure perturbations (green contours). (b,d,f)  $\eta$  ( $\times 10^{-3} \text{ s}^{-1}$ ; filled) and  $\theta$  (K, unfilled blue) 30 minutes after cold bubble release for (a,b) -10 K, (c,d) -16 K, and (e,f) -24 K warm bubble.  $w = \pm 1 \text{ m s}^{-1}$  (black unfilled) and passive tracer = 10% plotted for reference (orange unfilled). Winds (here perturbations) given by vectors, where  $w$  has been multiplied by 10 for visibility.

In all three simulations, a warm perturbation is produced near the surface under the site of the cold bubble drop, and an elevated cool perturbation associated with gravity waves propagates away from the drop location, but only in the -24 K simulation is cooling actually observed at the surface (Fig. 4.5). In the -24 K bubble experiments, strong negative vorticity to the right and positive vorticity to the left is generated baroclinically (Fig. 4.5f). This is something like a splash. While the negative perturbation at the surface is small, it remains throughout the simulation as it moves away from the drop location, as does the region of associated vorticity. An undular bore is generated ahead of and above the cold pool, but waves extend deep into the troposphere. While in the absence of wind shear this might suggest a weak or 'leaky wave-duct' (e.g. Haghi et al. 2017), the 2DX and 2DY experiments with the same bubble strength also had deep waves.

The addition of wind shear leads to structures that generally resemble those discussed in chapter 3. In both 2DX and 2DY runs, there is a notable warm perturbation at the surface co-located with passive tracer associated with the initial cold bubble (Figs. 4.6a,c and 4.7a,c ). This indicates that a non-negligible portion of the convective downdraft reaches the surface, but with a warming effect. As in the no shear experiments, only the -24 K bubble leads to a cold pool at the surface in both 2DX and 2DY experiments (Figs. 4.6e and 4.7e). In all three runs of both 2DX and 2DY experiments, the greatest cooling is observed in an elevated layer. In the 2DX simulations, the largest perturbations are observed in the downshear direction, consistent with downshear wave amplification discussed by Schmidt and Cotton (1990). In the 2DY simulations, the largest amplification is observed upshear. However, the strong amplification may also be due to the presence of an intrusion that acts to widen the layer between two isentropes. It is also worth noting, that both larger amplitude perturbations are also simply downwind. As described in Chapter 3, an intrusion occurs where a fluid travels between two layers with a density between the density of the two layers Rottman and Simpson (1989). It was also noted, that most intrusion literature is based on a still environment, and in the presence of strong wind shear, an intrusion may just flow in the layer with the wind. In the 2DY experiments, all three cold bubble strengths lead to the generation of a bore. The degree to which isentropes are permanently lifted (how quickly they return to their starting height) and depth of lifting, appear to be modulated by the strength of the cold bubble.

In summary, as many previous studies have noted, as a 'downdraft' (cold bubble) collides with a strong stable layer, it produces a number of waves that can extend deep into the troposphere (especially in the absence of sufficient trapping mechanism). In this simple dry set-up, it takes a very strong

perturbation to generate any sort of near surface cooling in an environment with a stable layer this strong. The 3D moist simulation with this thermodynamic profile did not have a cold pool early in the simulation, and only produced one under the heaviest precipitation. Since most downdrafts (at least simulated ones) are not that strong, moist (and 3D) processes must be important for generating cooling near the surface in that case. Despite this strong stability, there was some cooling near the surface in the real case, though the greatest  $\theta'$  was still observed aloft (See Table 4 Chapter 2). Even when a very strong temperature perturbation was used, a positive  $\theta'$  was observed at the surface below the site of the 'downdraft'. The descent of the downdraft also generates wind perturbations, the strength of which depend on the strength of the bubble. Vorticity is generated by the thermodynamic gradient and induced shear perturbations. The addition of vertical wind shear from u and v components of the control wind profile lead to structures that resembled those discussed in Chapter 3, including surface warming, elevated cooling, and wave amplification downshear in the 2DX and upshear in 2DY experiments where upshear waves in the 2DY run may be tied to the development of an intrusion downstream (here this is also upshear)

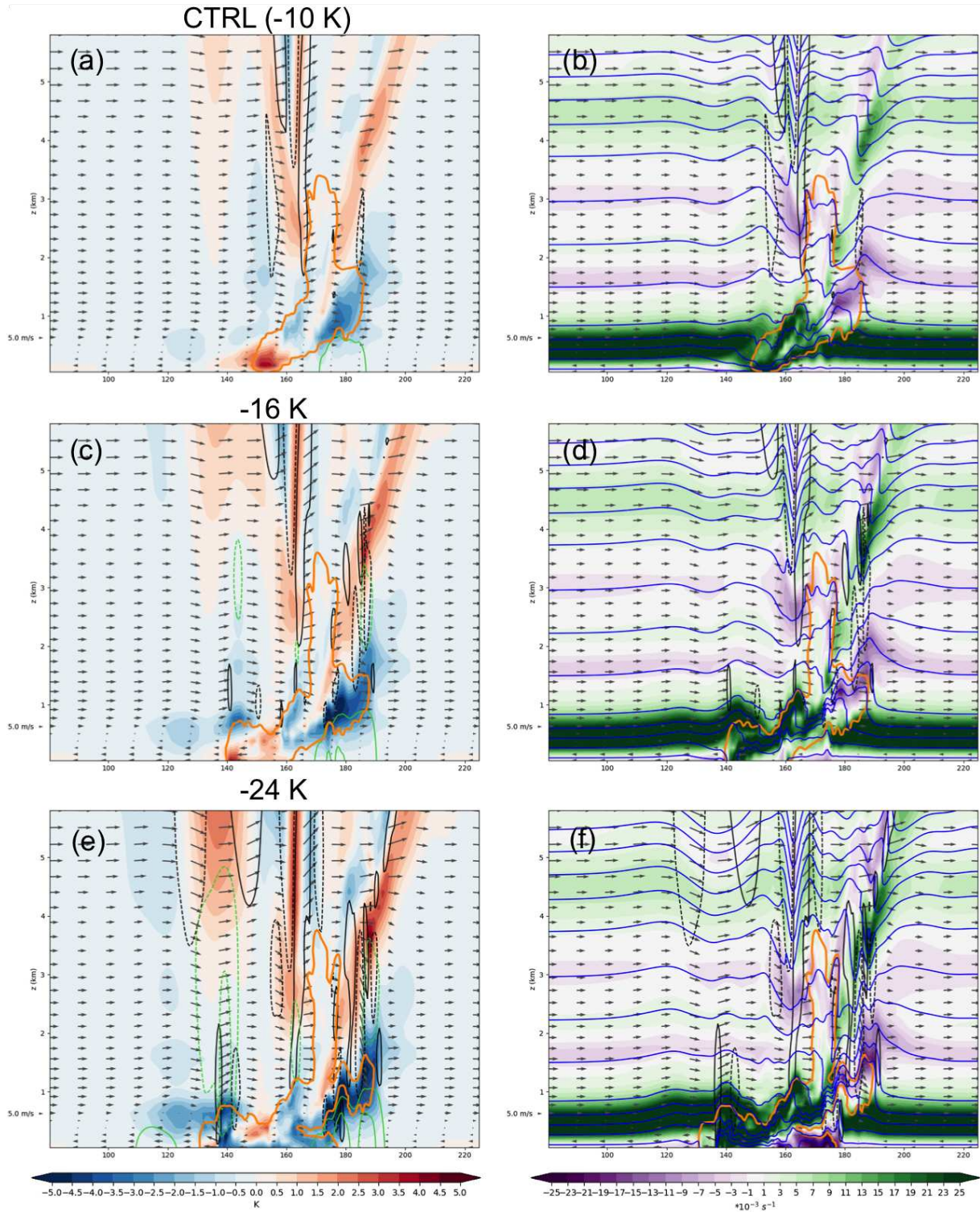


FIG. 4.6. As in Fig. 4.5, but for 2DX simulations.

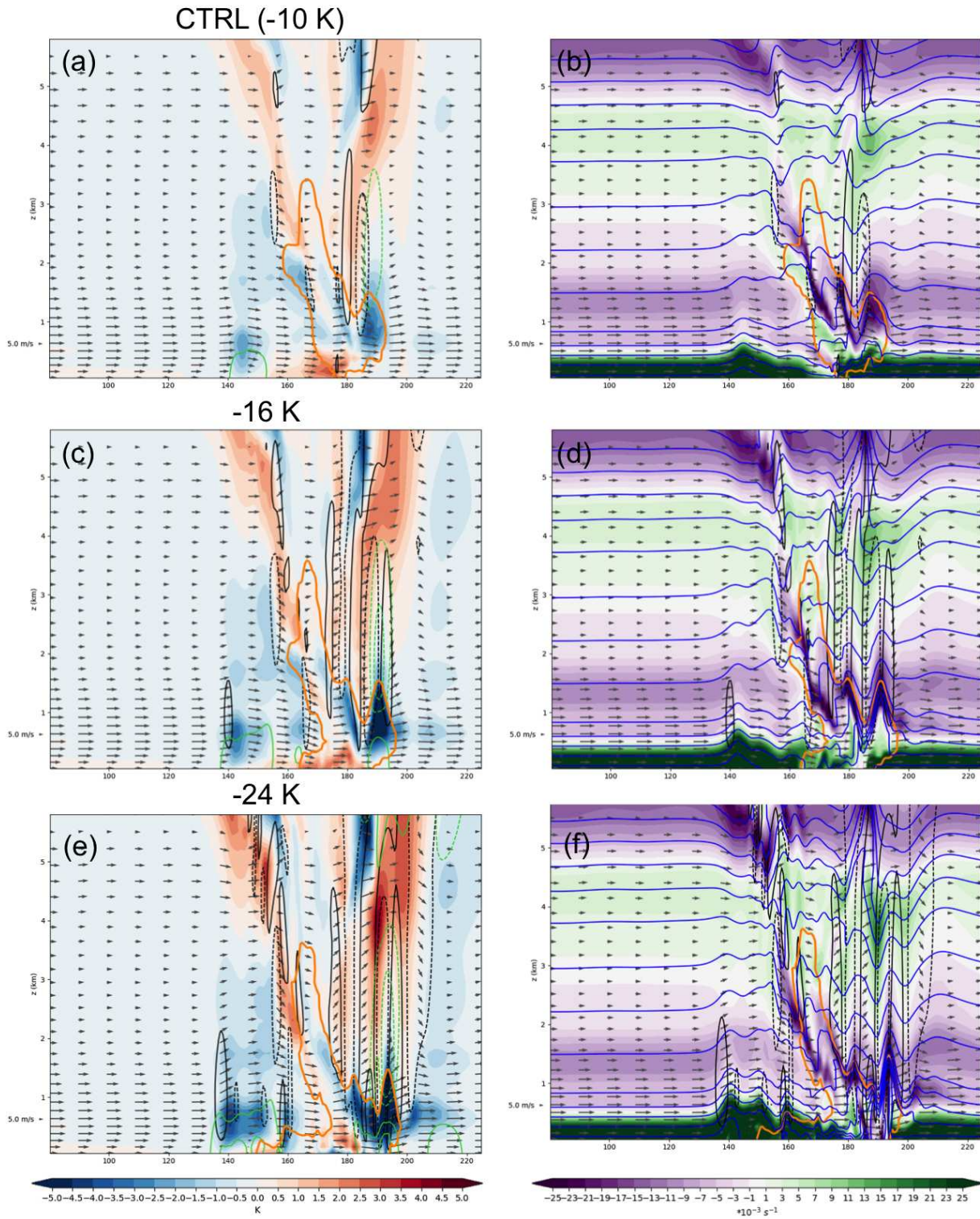


FIG. 4.7. As in Fig. 4.5, but for 2DY simulations.

#### 4.3.1.2 SENSITIVITY TO GRID SPACING

Several additional experiments were performed to explore the consistency in representation of convective outflow and subsequent waves at higher resolution. For brevity, only the dx100dz50stretch is discussed at length here. This simulation has the highest resolution tested, and generally produces the same features observed in the CTRL runs. In the simulation with no shear, a positive  $\theta'$  is observed below the site of the initial downdraft, and gravity waves are produced with largest amplitude near the top of the stable layer, but extend well above it.  $\pm 1 \text{ m s}^{-1}$  updrafts and downdrafts are more numerous and generally narrower in width. The passive tracer shows evidence of greater mixing between 1 and 2 km.

### No Shear

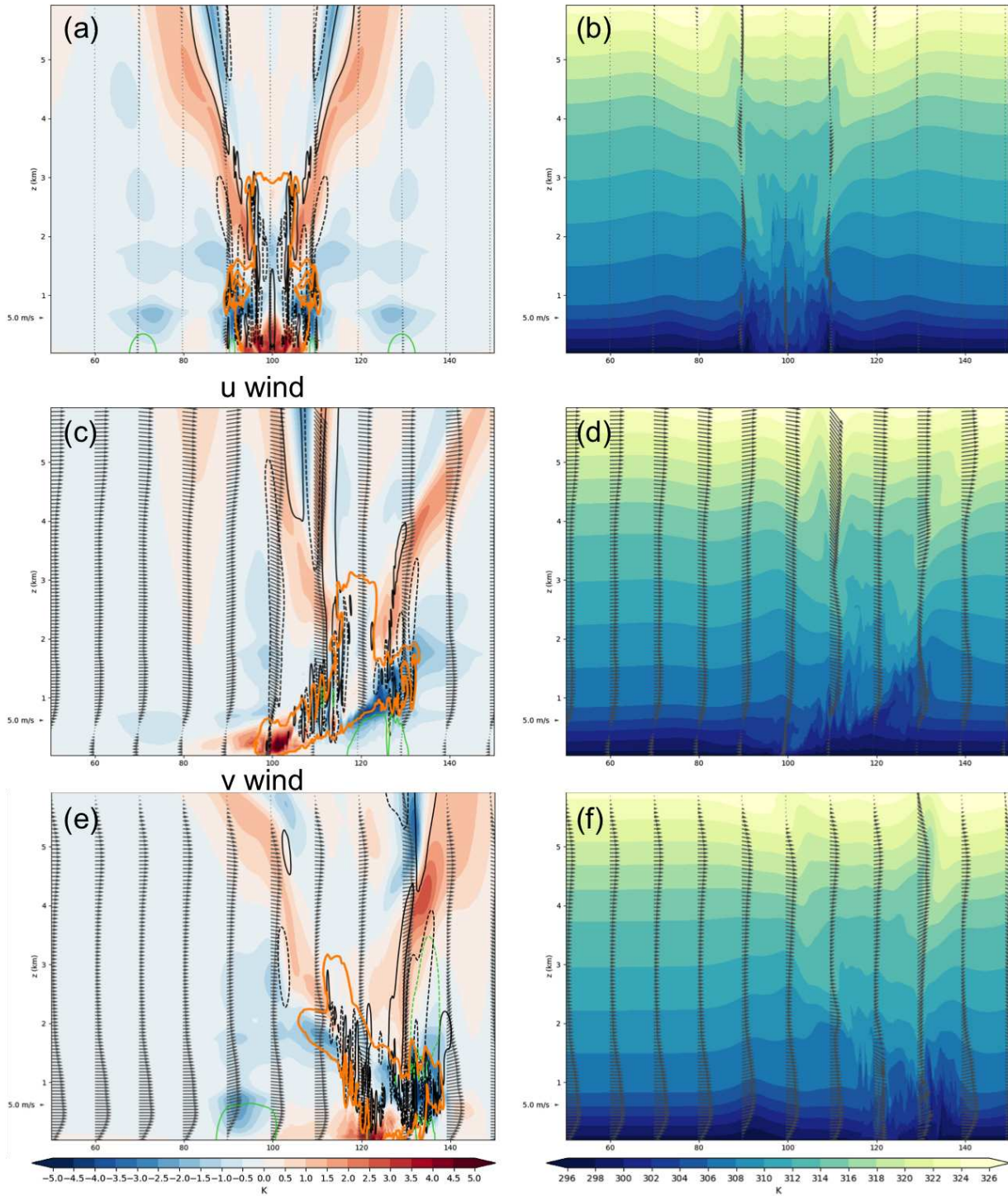


FIG. 4.8. No shear, 2DX, and 2DY experiments repeated with  $dx=100$  m and stretched 50-100 m vertical grid ( $dx100dz50stretch$  experiments). (a,c,e)  $\theta'$  (K; filled),  $\pm 0.5$ , 1 hpa pressure perturbations (green contours), 10% passive tracer concentration. (b,d,f)  $\theta$  (K; filled). Wind vectors (with  $w * 10$ ) shown in all plots.

In the run with higher resolution and u winds, a similar pattern of surface warming and elevated waves to the 2DXCTRL simulation is produced, but the magnitudes of observed perturbations ( $\theta$ , P, wind, w) is larger in the dx100dz50stretchX run. In the 2DXCTRL simulation, passive tracer concentration and spreading of isentropes suggested the presence of an intrusion in a layer just above the surface. In the dx100dz50stretch run, a ‘comma head’ much like something found at the leading edge of a density current is observed at several times in the layer just above the surface and  $\sim 800$  m. Above this breaking wave, gravity waves extend deep into the troposphere with decreasing amplitude. Behind it, several higher frequency waves line up with narrow updrafts and downdrafts and evidence of greater tracer mixing at the top of what remains of the initial downdraft air. As in the 2DXCTRL simulation, waves are amplified in the downshear region between 900 m and 2 km, but there is also some evidence of wave breaking in this layer.

In the run with the v wind profile (dx100dz50stretchY), shear is stronger below 500 m than above and reverses in height around 500 m. As in lower resolution simulations, low-level waves are more amplified to the north (right). Waves are relatively vertically stacked and decrease in amplitude from about 1.5 km to 4 km. To the south, low-level waves (and the leaked upper-level waves) quickly propagated upshear, but stronger waves between 1 and 2.5 km remain closer to the initial downdraft location. Similar to the dx100dz50stretchX run, a number of higher frequency waves are produced near the site of the downdraft that generate vertical velocities of  $\pm 1$  m s<sup>-1</sup>. Interestingly,  $\theta$  and pressure perturbations are actually smaller in the dx100dz50stretchY run than in the 2DYCTRL run on the right (north) and in the low-level wave that moves quickly to the left (south), but the positive surface  $\theta'$  and left negative  $\theta'$  aloft have larger amplitudes.

While the general wave structures, particularly of larger wave length/amplitude waves are represented, one of the primary losses from lower resolution that should be considered in the interpretation of 3D results below, is an apparent modification in wave amplitude — in particular, a reduction in amplitude on the downshear side. Additionally, higher frequency waves that may be generated along the interface of the convective outflow and stable layer are also lost.

### 4.3.2 3D Simulation Results

#### 4.3.2.1 CONTROL SIMULATION (CTRL)

The sounding used to initialize the control simulation is not exactly the same as the sounding used to initiate the simulation discussed at great length in Chapter 3 (but is identical to the 2D experiments

presented in the previous section). Most notably, a function was used at low levels to identify the stable layer, RH was set to a constant value in this layer, and a number of measures were taken to significantly smooth all variables. This means that the two-tiered inversion structure and near surface dry layer present in the original sounding are removed, the strength of the southwesterly wind maximum is weaker (Fig. 4.1), and the low-level layer of strong curvature (the ‘hook’) in the u profile is less defined.

On the whole, the control simulation (CTRL) here evolves much like the simulation described in Chapter 3 (which will be referred to as REAL here for its practically unmodified initialization sounding). There are a few differences that are worth noting. The MCS in the REAL simulation covers a larger area, the leading edge is further south, and the ROD has greater coverage and appears more organized earlier in the simulation (Fig. 4.9a,b). After 4 hours, total precipitation in the REAL run has greater coverage, and REAL precipitation maximum is 108.931 mm while the CTRL simulation precipitation maximum is only 65.9175 mm (Fig. 4.9c,d). However, after 5 hours, the CTRL simulation precipitation maximum is 102.969 mm, the precipitation coverage is broader, the MCS is more similar in size, and the ROD is more organized (not shown). This suggests overall slower development of the MCS in the CTRL run than in the REAL run.

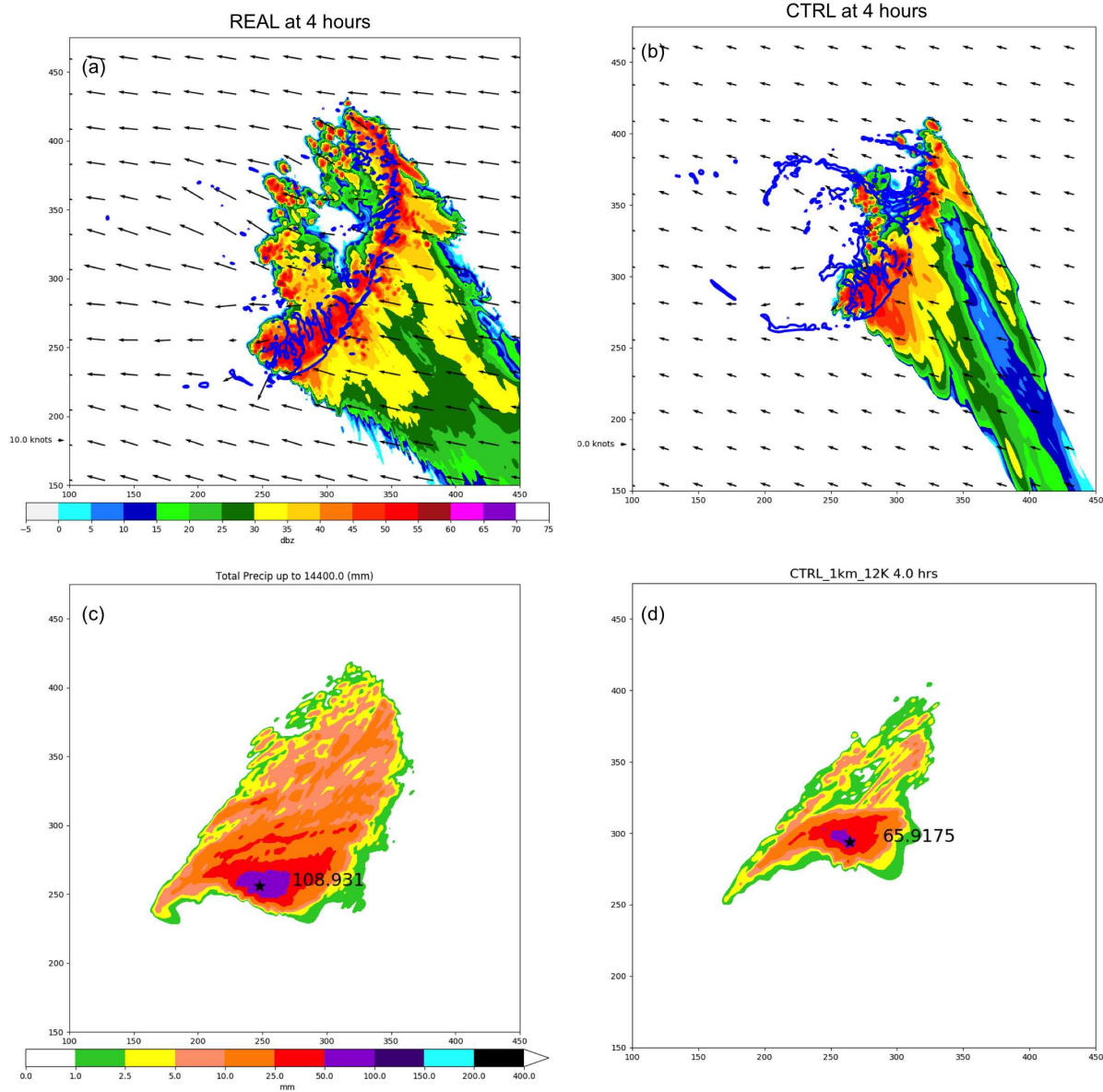


FIG. 4.9. (a,b) Simulated reflectivity (dBZ) and  $-0.5 \text{ K } \theta'$  (blue unfilled) and (c,d) total precipitation (mm) where the precipitation maximum indicated by the black star and accompanying text for (a,c) REAL run (from Chapter 3) after 4 hours and (b,c) CTRL run after 4 hours.

Despite these differences, the processes that support the convection appear to be generally consistent. Much like in the REAL simulation, a surface cold pool is only present in the far southern portion of the MCS under the heaviest precipitation (Fig. 4.10a), a number of oscillations in vertical velocity can be seen at the far SW boundary (Fig. 4.10b), and more near-surface tracer initialized in the lowest 500 m was lifted to 5 km in the southern portion of the leading line than in northern or ROD regions

(Fig. 4.10c). While not shown for the REAL run at this time,  $5 \text{ m s}^{-1}$  updrafts are more coherent in the southernmost portion of the MCS, and generally begin between 0.25 and 1 km in the CTRL run. In the northern portion and ROD region  $5 \text{ m s}^{-1}$  updrafts almost entirely begin above 1.5 km (Fig. 4.10c).

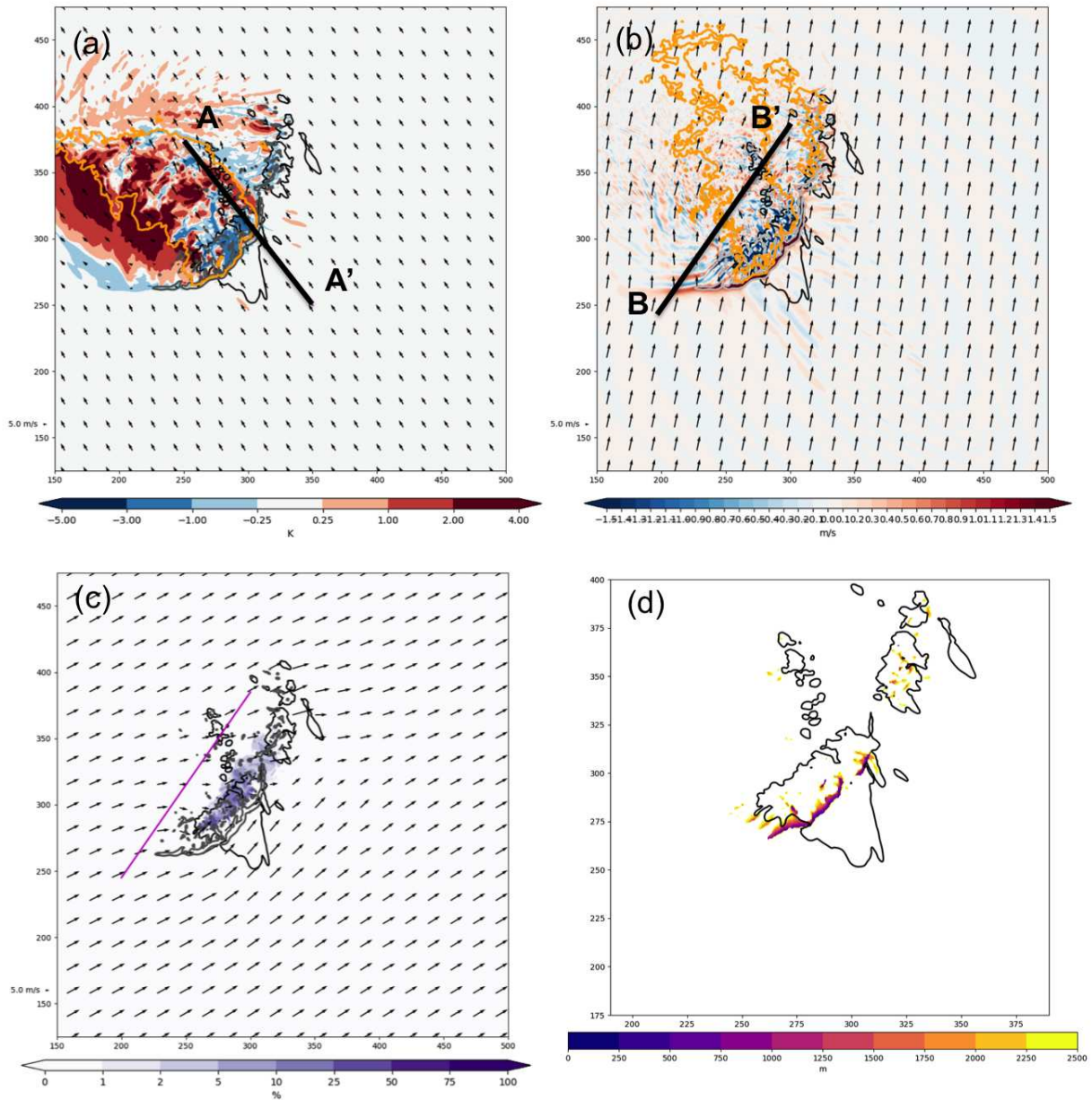


FIG. 4.10. (a) surface  $\theta'_p$  (K; filled), simulated reflectivity  $> 40$  dBz at lowest model level (black unfilled), 0.5 km vertical velocity of  $1 \text{ m s}^{-1}$  (gray unfilled), surface passive tracer = 80% (orange unfilled), and surface wind vectors; (b) 0.5 km vertical velocity ( $\text{m s}^{-1}$ ; filled), simulated reflectivity  $> 40$  dBz at lowest model level (black unfilled), 0.5 km passive tracer = 80% (orange unfilled), and 0.5 km wind vectors. (c) % of passive tracer initialized below 500 m lofted to 5 km (filled), 0.5 km vertical velocity of  $1 \text{ m s}^{-1}$  (gray unfilled), simulated reflectivity  $> 40$  dBz at lowest model level (black unfilled), and 5 km wind vectors; (d) The minimum height (m) where  $5 \text{ m s}^{-1}$  updrafts are observed (colored contours) and 40 dBz reflectivity (black unfilled)

As in the REAL run, a gravity wave initially supports the leading line, transitions to a wave-like bore, and eventually a density-current-driven bore in the region of heaviest precipitation. In the cross section A-A' through Fig. 4.10 shown in Fig.4.11, there is evidence of weak surface cooling some distance behind the first upward perturbation in isentropes, suggesting the generation of a bore by a weak density current (Fig. 4.11a,b). The presence of 1.5 km passive tracer behind the initial perturbation, but removal at low levels just ahead of the surface cooling further support this. However isentropes return nearly to their starting heights behind the region of surface cooling.

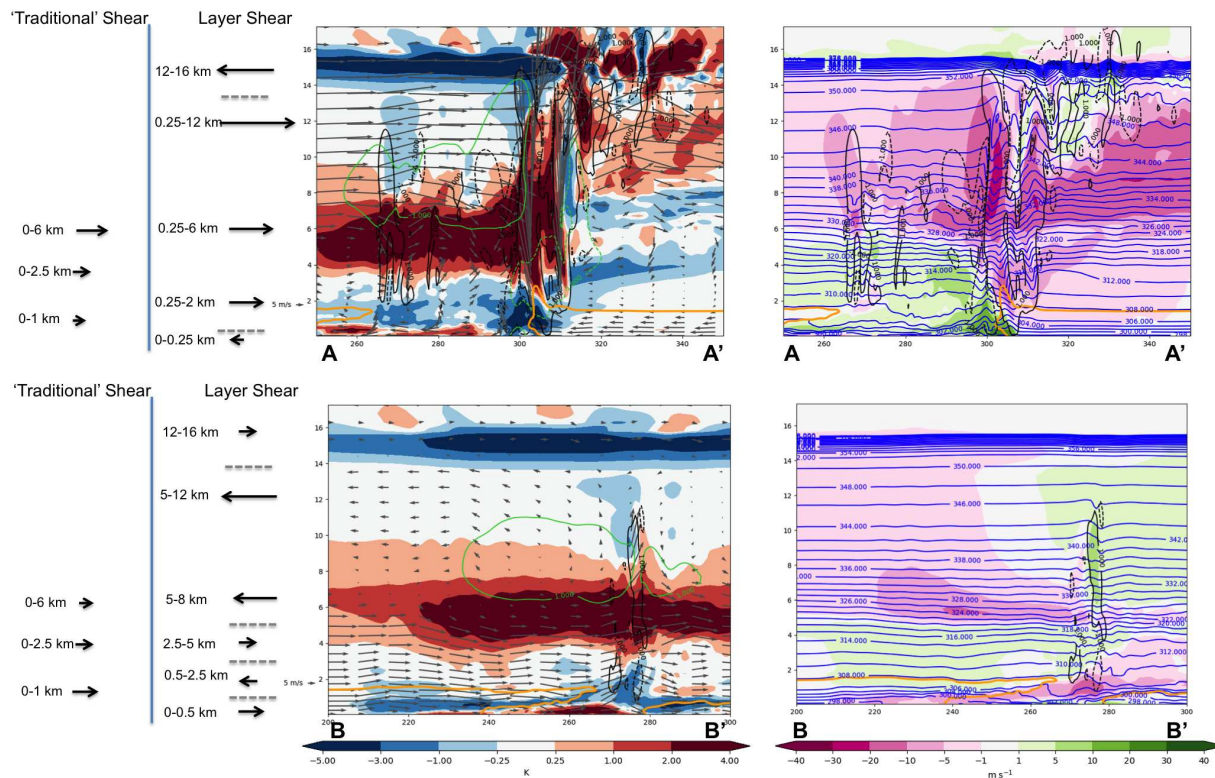


FIG. 4.11. Cross section through Fig. 4.10 (a,b) A-A', (c,d) B-B' after 4 hours through depth of the troposphere. (a,c)  $\theta'_\rho$  (K) in filled contours,  $w$  ( $\text{m s}^{-1}$ ) in unfilled black contours,  $\pm 0.5$  and  $1 \text{ Pa}$   $P'$  unfilled green contours, and wind vectors. (b,d) Wind perturbations ( $\text{m s}^{-1}$  in filled contours in the plane of the cross section,  $\theta$  (K) in unfilled blue contours,  $w$  ( $\text{m s}^{-1}$ ) in unfilled black contours, and 80% of passive tracer initialized below 1.5 km (orange). Magnitude of  $w$  multiplied by 10 in plotted vectors for emphasis. Approximations of shear vectors for more traditional layers, and for potentially relevant layers shown to the far left. Locations of shear reversal are indicated by dashed grey lines.

Because different regions of the MCS move at different speeds (and sometimes in different directions), and because this changes from run to run it is impractical to identify the storm relative wind field

for each region for each run. Though a translating domain was used, plotted winds are either projected onto the cross section from the full wind field (as in the vectors plotted in Fig. 4.11a,c) or perturbations from the initial time ( $U'$ ; shaded regions of Fig. 4.11b,d). The combination of these fields can be used to identify features like the rear-inflow jet (RIJ) or front-to-rear flow (FTRF) often associated with MCS organization. While the focus of Chapter 3 was primarily on low-level processes, it is advantageous to consider processes that extend deeper into the troposphere given the exploration of deep wind shear profiles (this is also why cross sections in Fig.4.11 and equivalent figures that follow extend through 16 km).

In this run, updrafts are nearly vertical along the leading line. There is some mid-level warming associated with latent heat release west of the leading line over the region of relatively cooler air behind the leading line (though this is not associated with a surface cold pool). In the layer between mid-level warming and weak low-level cooling, there is a weak positive wind perturbation (and weak westerly flow wind vectors) indicative of rear inflow. Negative wind perturbations in the inflow region and to the west of updrafts might suggest a weak FTRF, but upper-level winds are very strong westerly, and likely would be even if a  $\sim 15 \text{ m s}^{-1}$  storm motion is taken into account. As this is a MCS with leading stratiform, the larger circulation ahead of the leading line fittingly resembles the overturning circulation discussed by Parker and Johnson (2004c,a,b).

In the region of ROD, updrafts appear to be supported by waves between 1 and 2 km as in the REAL run. Described in Chapter 3, these waves lie in a layer where downshear amplification and the Doppler effect in that layer could help to explain the amplitude of the waves and their quasi-stationary behavior (Fig.4.11c,d). Additional support may still be provided by the intrusion of downdraft air itself into the layer below, as evidenced by the spreading of isentropes, and reduction of passive tracer in the layer below 1.5 km (Fig.4.11c,d).

Like the simulation described in Chapter 3, trajectory analysis shows that parcels that reach  $5 \text{ m s}^{-1}$  in the region of ROD primarily come from the southwest in the 1-2 km layer (Fig. 4.12). Parcels are nearly perpendicular to the SW gust front boundary when they reach it, but quickly take on a more southwesterly trajectory. They experience brief ascent and then descent over the bore at the southwest boundary, and a more dramatic ascent when they encounter the 1-2 km wave in the ROD region.

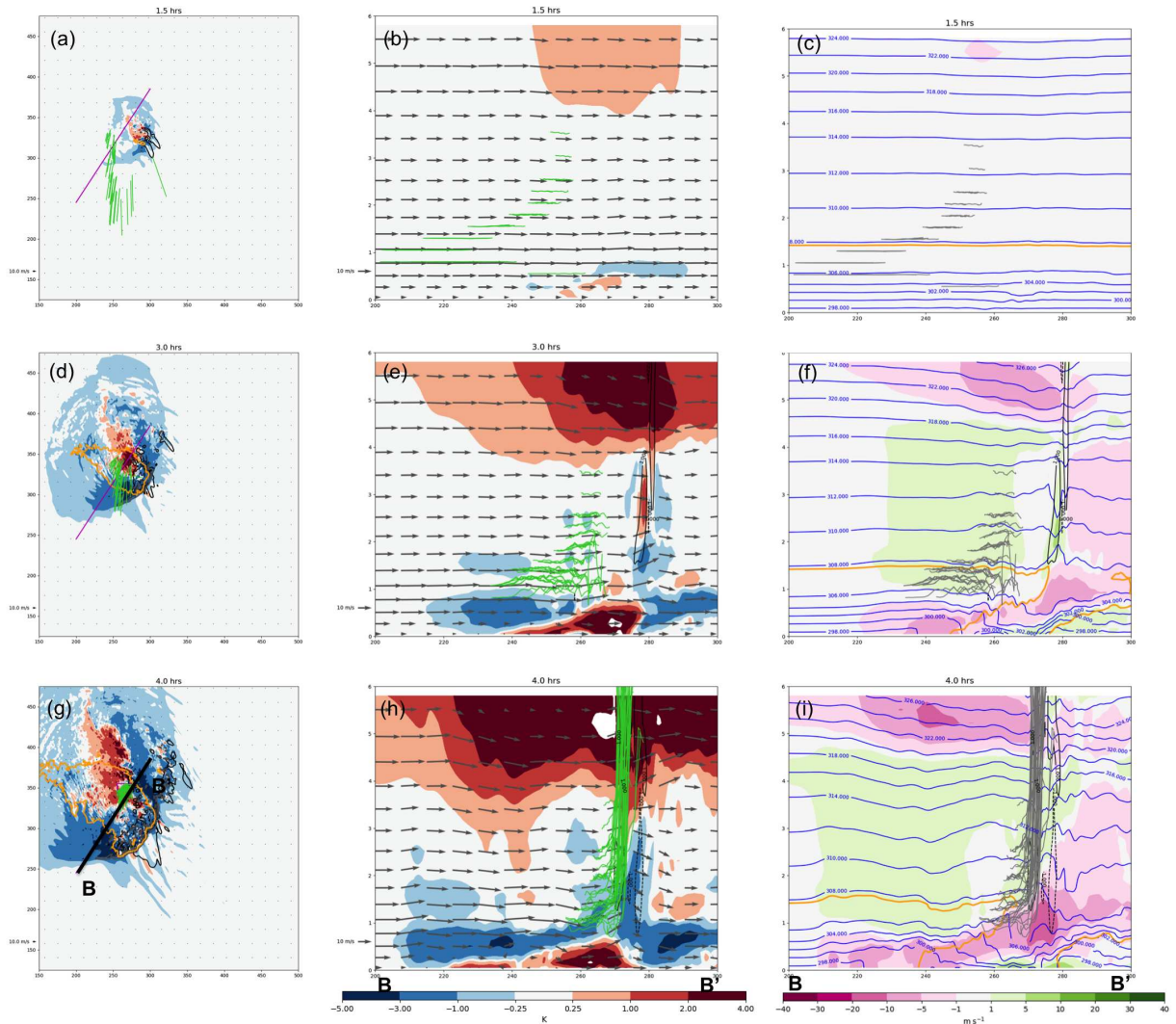


FIG. 4.12. (a,c,g)  $\theta'_\rho$  (K; filled),  $1 \text{ m s}^{-1}$  w (gray), and wind perturbations from  $t=0$  (vectors) at 0.5 km, 40 dBZ reflectivity (black unfilled) and 80% passive tracer concentration at lowest model level. Green lines trace path of parcels that reach  $5 \text{ m s}^{-1}$  in a small region of ROD updrafts. (b,e,h) Cross section through B-B' of  $\theta'_\rho$  (filled), w (black unfilled), wind vectors. Green lines as in previous column. (c,f,i) Cross section of wind perturbations (filled),  $\theta$  (blue unfilled), w (black unfilled), and 80% passive tracer. Gray lines now represent parcel paths.

#### 4.3.2.2 EXPERIMENTS OVERVIEW

Initial sensitivity experiments were designed primarily to test if any of the clear differences between the 0428 UTC 25 June 2015 wind profile used in Chapter 3 and the composite wind profile from the elevated instability cluster computed in Chapter 2 are critical to the development of ROD. Specifically, the strong LLJ, the presence of a  $5 \text{ km}$  southerly wind maximum, and the strong northerly upper-level jet. The idea was to begin with the most basic requirements for sustained convection (low-level wind

shear), and iteratively build up to a profile that closely resembles the CTRL simulation using combinations of equations shown in Table 4.2 for an analytical representation. Additional experiments were added to explore other sensitivities and test the robustness of results. This subsection provides an overview of the experiments with major low-level or upper-level wind modifications. For brevity, a selection of experiments that explore the major features highlighted above (UhookVLLJ, UhookVjet2, and UujVuj respectively) are explored in addition to the experiment with the most analytical wind profile most similar to the CTRL run (UujVjet3) in detail in the following sections.

All experiments described in Table 4.2 except the no wind experiment (U0V0) produce sustained convection, but the resulting MCS organization is unsurprisingly related to the wind profile chosen. Interestingly, the coverage of  $\theta$  deficits at the surface varies substantially from case to case (Figs. 4.13, 4.14). After 2 hours, nearly all cases with wind in both  $u$  and  $v$  have two narrow bands (with different orientations) of  $-0.5 \text{ K } \theta'$  at the surface, suggesting the presence of a low-level gravity wave (Fig. 4.13). In UujVuj, the northern band was broken up after 1.5 hours. After 4 hours,  $-0.5 \text{ K}$  contours suggest that convection has successfully generated a cold pool in the U25V0, UhookVLLJ, and UhookVjet2 runs over nearly the entire MCS region (Fig. 4.14b,e,f). The remaining simulations, except U0VLLJ have coherent region where a cold pool has reached the surface (like in the southern most precipitation region of the CTRL run), but the location and strength of perturbation (not shown) differs between runs (Fig. 4.14). In U0VLLJ, only warming is observed at the surface until after 5 hours, except where a broad southward moving wave extends well ahead of the heaviest precipitation. Of the experiments, the structure of U0VLLJ is most unrealistic. Since convection continues to grow in all simulations, by the end of the run (shortly after 5 hours), every simulation has a coherent region of  $-0.5 \text{ K}$  surface  $\theta'$ , but in the simulations with upper-level winds this coherent region does not extend over the entire MCS. This means that in an environment with a very stable near surface layer, wind shear plays a role in determining when and where a cold pool might form. Perhaps this is a reflection of the feedbacks between the storm and its environment? Amplification of downshear waves may act to modify the layer lifted and consequently the available energy of inflow parcels. Since characteristics of the inflow layer impact the strength of the convection, this may lead to more penetrative downdrafts. More penetrative downdrafts could act to deepen waves, which consequently modifies the relevant shear layer. This process could repeat until the MCS reaches a quasi-steady state.

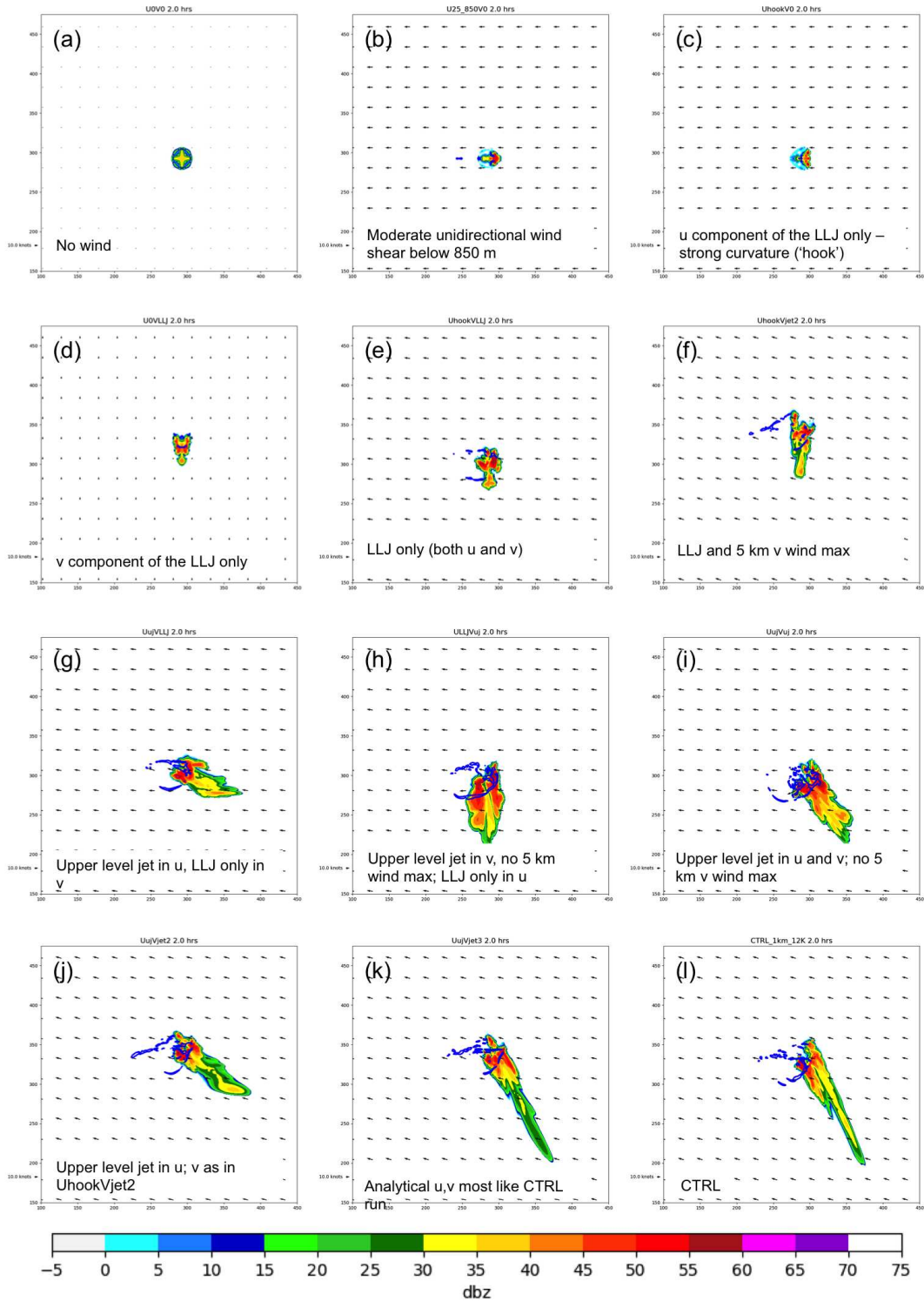


FIG. 4.13. Simulated reflectivity (filled),  $-0.5 \text{ K}$  surface  $\theta'$  (blue unfilled), and surface wind vectors for (a) U0V0 (b) U25V0 (c) UhookV0 (d) U0VLLJ (e) UhookVLLJ (f) UhookVjet2 (g) UujVLLJ (h) ULLJVuj (i) UujVuj (j) UujVjet2 (k) UujVjet3 and (l) CTRL runs after 2 hours.

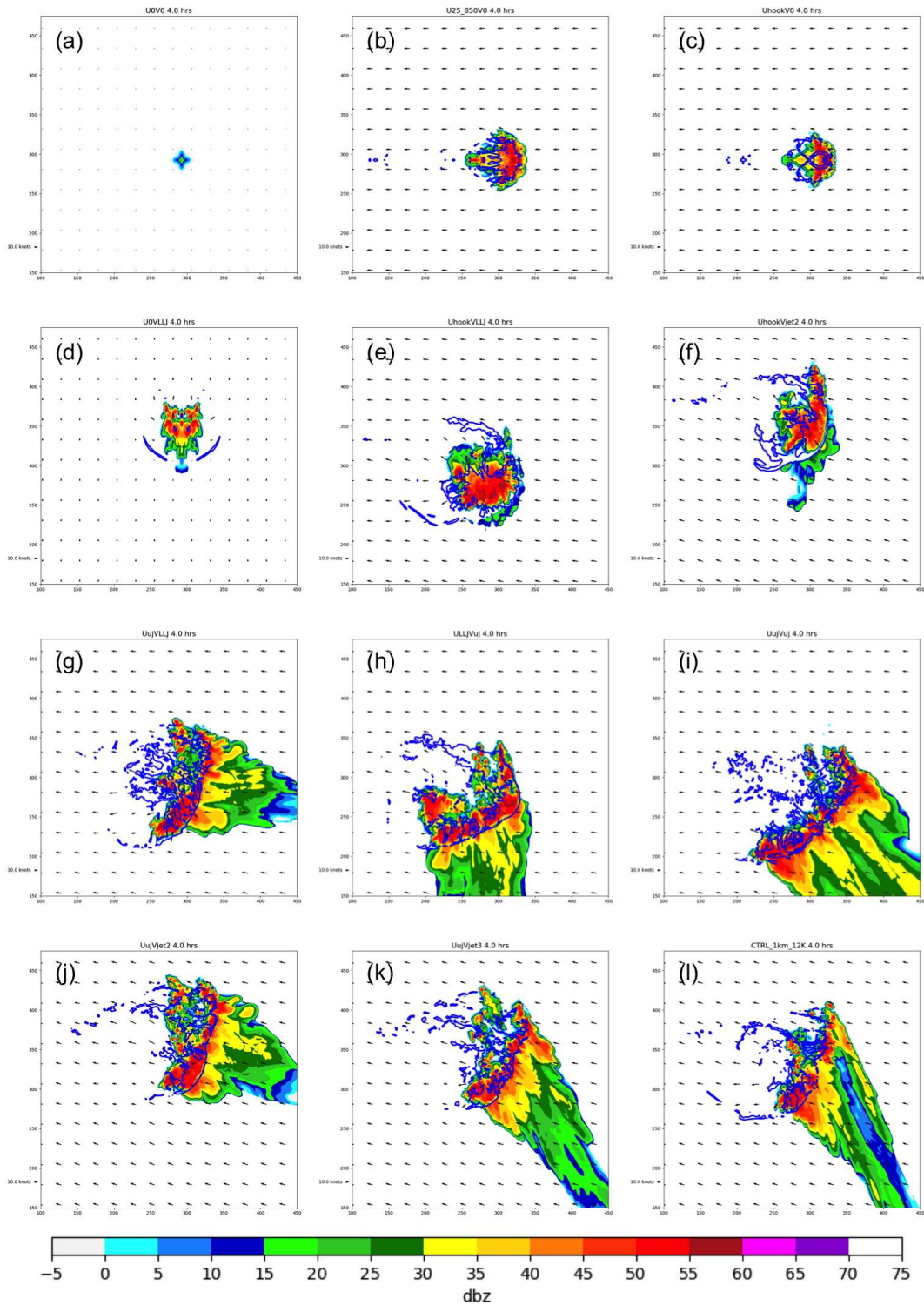


FIG. 4.14. Panels as in Fig. 4.13 but after 4 hours.

After 4 hours, the u only modification experiments (U25V0 and Uhook) had by far the lowest precipitation totals, likely due to their rapid propagation speeds throughout the simulation and no direction change (Fig. 4.15). Nearly every run with a 3D LLJ (with the exception of UhookVjet2) had precipitation totals of nearly 70 mm or more. Two of the four largest totals were the UujVjet2 (77.5949 mm) and UujVjet3 (88.8291 mm) experiments which had a strong, but nearly quasi-stationary southwest portion of the line and ROD (Fig. 4.15j,k); After 5 hours, these totals soared to around 140 mm (not shown). U0VLLJ also had very high precipitation totals (68.5482 mm), most likely due to stalling and eventual reversal of motion of convective cells as they intensified (Fig. 4.15d). The strong northerly jet experiments with no 5 km wind maximum (ULLJVuj and UujVuj) and 3d LLJ only experiment (UhookVLLJ) tended to have the most widespread heavy precipitation (based on coverage of the 50 mm contour), and ULLJVuj had both widespread heavy precipitation and a > 100mm maximum (Fig. 4.15e,h,i).

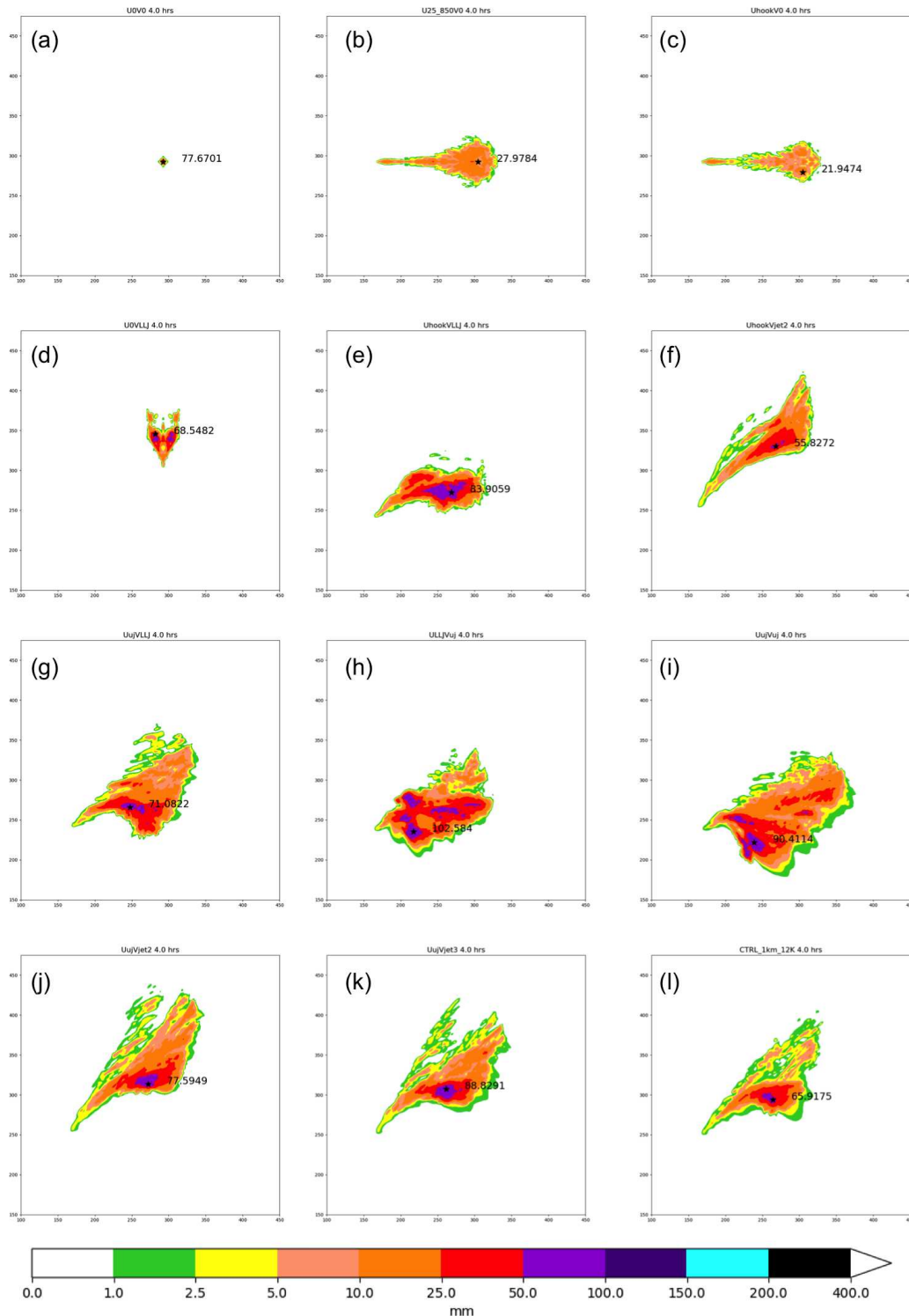


FIG. 4.15. 4 hour precipitation totals for (a) U0V0 (b) U25V0 (c) UhookV0 (d) U0VLLJ (e) UhookVLLJ (f) UhookVjet2 (g) UujVLLJ (h) ULLJVuj (i) UujVuj (j) UujVjet2 (k) UujVjet3 and (l) CTRL runs.

Wind shear through the depth of the profile also influences the mean updraft and downdraft characteristics as well as their trends over time (Figs. 4.16 and 4.17). In figure 4.16, the lowest observed height of 'x'  $\text{m s}^{-1}$  updrafts is used as a proxy for identifying updraft bases and are domain averages of the quantity shown in Fig. 4.10d. Downdraft statistics shown in 4.17 are similar, but for downdrafts. In both figures, only updrafts and downdrafts with minimum heights below 3 km are considered in order to focus on those that might contribute to the maintenance of convection. Average  $1 \text{ m s}^{-1}$  updraft bases rapidly lower in the first hour of the simulations (Fig. 4.16a) as convection initiates and produces downdrafts that also rapidly reach lower altitudes in the first hour (Fig. 4.16a,b). After the first hour, most of the runs have  $1 \text{ m s}^{-1}$  updraft bases between 1 and 1.5 km, with no clear trend in differences between runs (Fig. 4.16a). In all runs,  $5 \text{ m s}^{-1}$  updraft bases have a decreasing trend through the first 3 hours (with oscillations), but eventually become more consistent. At the same time, maximum updraft speeds generally increase in the first 3 hours, and then become more consistent.

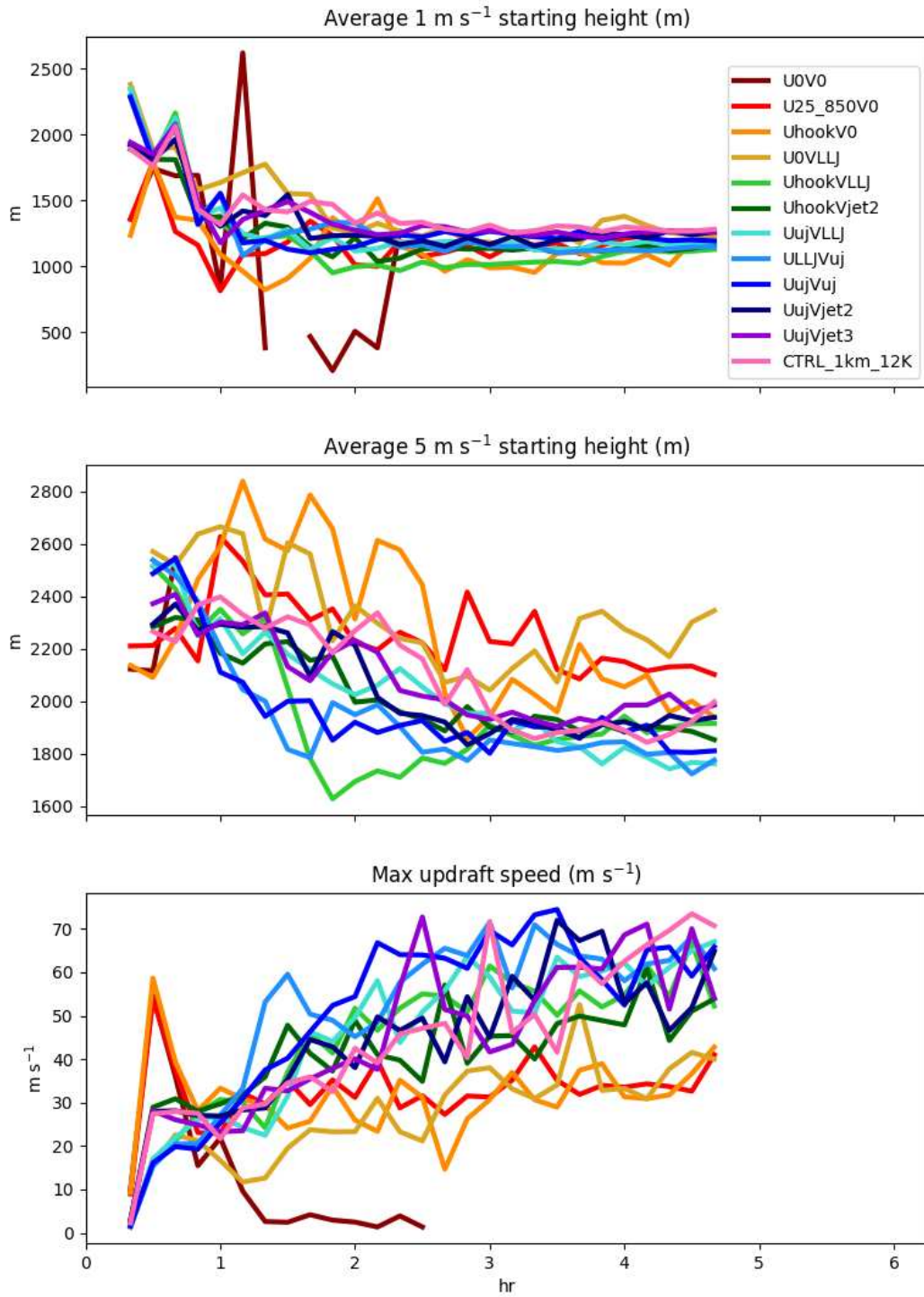


FIG. 4.16. Time series of (a) Lowest observed height (m) of 1 m s<sup>-1</sup> updrafts averaged over the domain masked to include updrafts that begin only below 3 km, (b) as in (a) but for 5 m s<sup>-1</sup> updrafts, and (c) domain maximum updraft speeds (m s<sup>-1</sup>).

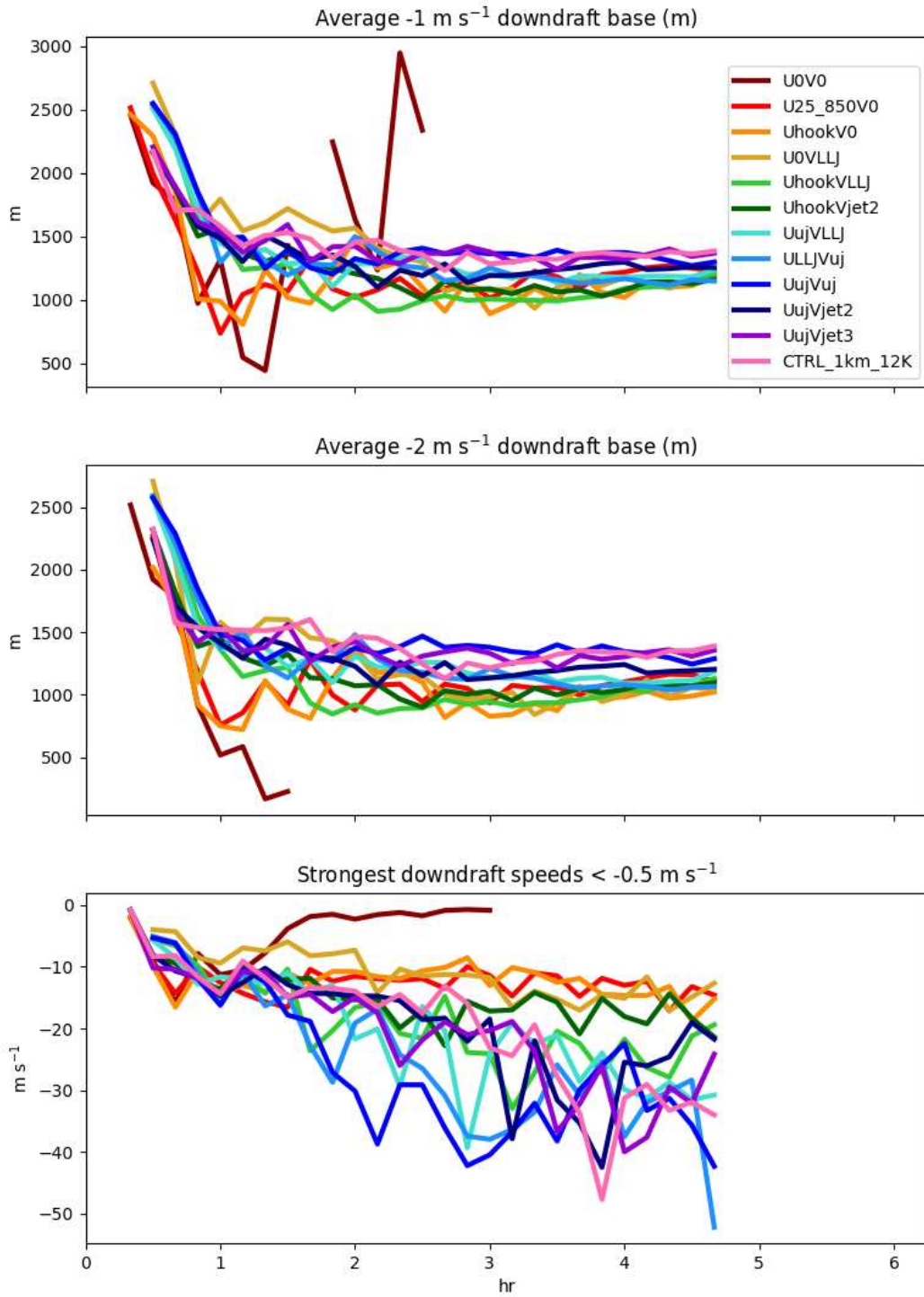


FIG. 4.17. Time series of (a) Lowest observed height (m) of  $-1 \text{ m s}^{-1}$  downdrafts averaged over the domain masked to include downdrafts that extend below 3 km, (b) as in (a) but for  $-2 \text{ m s}^{-1}$  downdrafts, and (c) maximum downdraft speeds (domain vertical velocity minimum;  $\text{m s}^{-1}$ ).

There is some distinction between 3 different groups of runs in the average height of  $5 \text{ m s}^{-1}$  updraft bases and maximum updraft speeds. Low-level wind experiments with wind modification in only one direction actually saw an increase in the height of  $5 \text{ m s}^{-1}$  updrafts in the first hour, followed by several oscillations (consistent with qualitative observations of pulsing of convection in these runs; not shown), and end with  $5 \text{ m s}^{-1}$  updrafts at higher altitudes than other runs (Fig. 4.16a). These same runs also consistently had the weakest maximum updrafts after the first hour (Fig. 4.16c). Both cases with the strong northerly upper-level jet but no 5 km wind maximum (ULLJVuj, UujVuj) had lower altitude observations of  $5 \text{ m s}^{-1}$  updrafts than other simulations in the first 3 hours, and consistently stronger updrafts throughout most of the run duration (Fig. 4.16b,c). In the remaining runs (with the exception of UhookVLLJ)  $5 \text{ m s}^{-1}$  updraft bases descend more slowly than ULLJVuj and UujVuj, but more rapidly than the experiments with only one component of the LLJ. In these same runs, maximum updraft speeds also generally lie between the previously described groups. In UhookVLLJ, where only the LLJ was represented in 3D, the average height of  $5 \text{ m s}^{-1}$  updraft bases decreased rapidly until shortly before 2 hours (and most notably in a 30 minute window surrounding 1.5 hrs), but then gradually increased to a more consistent height around 3 hours. In this case, while the strongest updrafts were nearest to the surface during a portion of the simulation, the maximum updrafts were not strongest.

There is a divide between cases with upper-level jets, and cases without in average downdraft heights (Fig. 4.17a,b). Runs with the 3D LLJ have consistently stronger downdrafts than those without, and runs with a component of the upper-level jet generally have stronger maximum downdrafts than those without suggesting the possible influence of a rear-inflow jet (RIJ). The addition of the 5 km wind maximum appears to lead to weaker downdrafts in the first 3 hours. However, later downdrafts in runs with both upper-level winds and 5 km wind maximum are comparable to other runs with upper-level winds. Interestingly, runs with the strongest downdrafts actually have higher -1 and -2  $\text{m s}^{-1}$  bases. This may be that downdrafts are somehow unable to extend as close to the surface in these cases, but more likely suggests more widespread weak descent in these runs.

Wind shear at both low levels and upper levels impact MCS organization, outflow characteristics, precipitation totals, updraft and downdraft speeds, downdraft coverage, and the height of observed updraft bases (e.g. how elevated they are). In this thermodynamic environment, the addition of a strong upper-level jet generally led to the strongest updrafts and downdrafts. On the other hand, the addition of the 5 km wind maximum in the  $v$  profile appears to lead to weaker updrafts and downdrafts as well as higher updraft and downdraft bases compared to the most similar runs without the 5 km wind

maximum regardless of the rest of the profile. At the same time, runs with the 5 km wind maximum and an upper-level jet had the highest precipitation maximums (even higher than the CTRL run).

#### 4.3.2.3 LLJ ONLY (UHOOKVLLJ)

The 3D LLJ simulation (UhookVLLJ) uses a wind profile that represents both  $u$  and  $v$  components of the observed LLJ, but has no vertical wind shear in layers that begin above about 2.5 km (purple profile in Fig. 4.3). The resulting MCS has stronger bowing than the other simulations, and in the absence of upper-level winds, a heavy region of stratiform precipitation forms to the northwest as the MCS propagates southeast (Fig. 4.14e). ROD does occur to the northwest of the leading line, beginning shortly before 3 hours into the simulation, and ROD cells merge with the leading line shortly after 4 hours (not shown). Even as strong convective cells form along the southwestern edge of the leading line, they remain offset from the gust front boundary throughout the rest of the simulation. This run had the 4th highest precipitation maximum and one of the broadest regions of coverage of  $> 50$  mm contour (Fig. 4.15e).

Of the runs tested, UhookVLLJ had the largest surface cold pool, with the largest observed surface  $\theta_p$  deficits ( $> 3$  K). A region of  $\theta_p$  increases was still observed downstream of convection (Fig. 4.18a). Consistent with this, passive tracer initialized below 1.5 km was reduced everywhere along (and behind) the leading line (Fig. 4.18a). Large concentrations of passive tracer initialized below 500 m are present in the same region as the heavy precipitation (Fig. 4.18c).  $5 \text{ m s}^{-1}$  updraft bases are nearest to the surface on the eastern edge of the gust front, and primarily elevated (and not along the gust front) on the southern edge of the line, while  $1 \text{ m s}^{-1}$  updrafts extend along the entire gust front (Fig. 4.18d). In other words, the leading edge of the gust front is generating at least  $5 \text{ m s}^{-1}$  updrafts along its leading edge, which at this time is the eastern portion of the convection. After 5 hours, the leading edge of the gust front associated with the  $5 \text{ m s}^{-1}$  has shifted to the southeast (not shown). The region of convection to the northwest merges with the leading line as this southeastern shift in the gust front lifting occurs, but cells along the southwest portion of the leading line offset from the leading gust front remain primarily elevated (updrafts above 1 km).

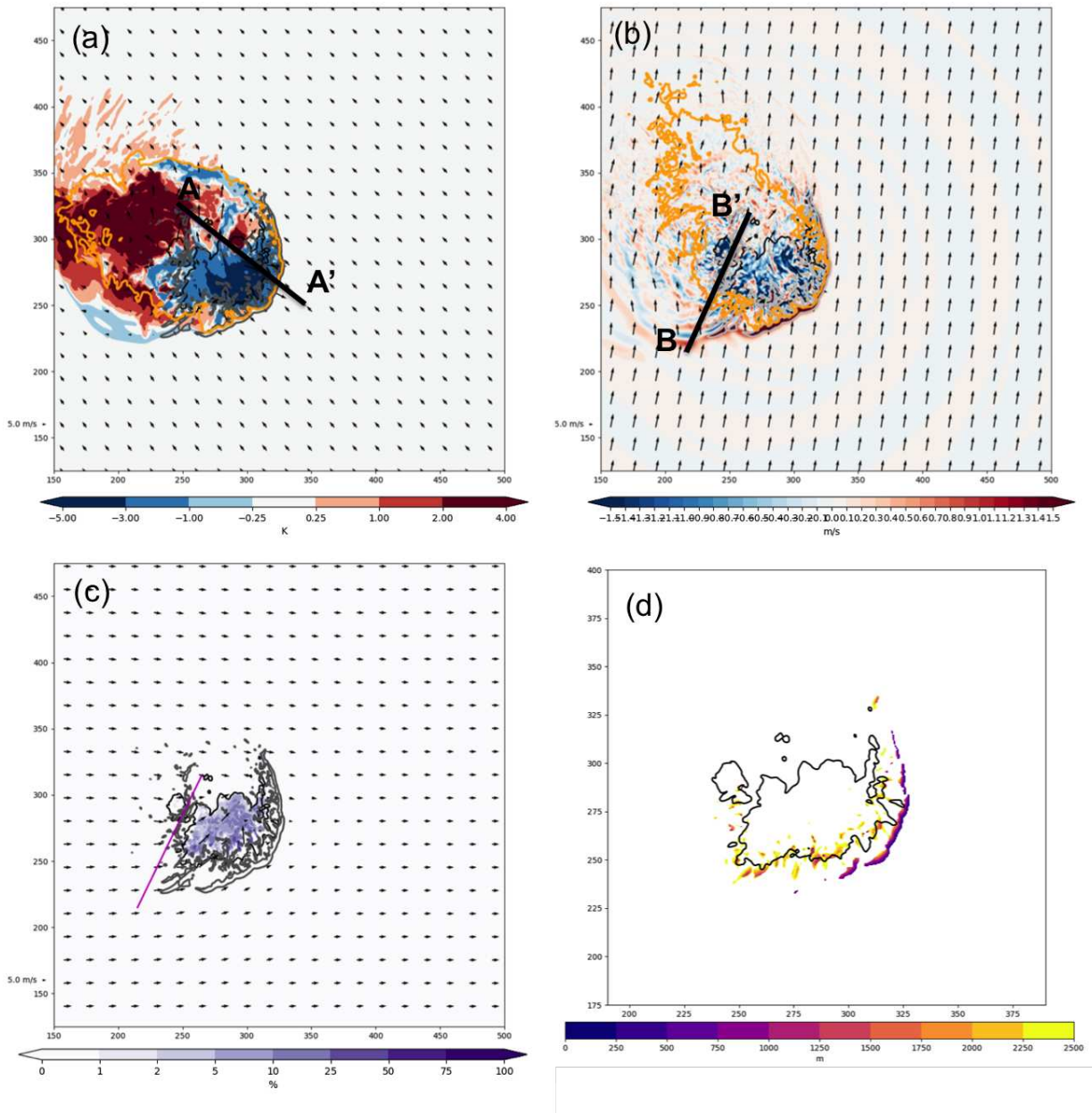


FIG. 4.18. Panels as in Fig. 4.10 but for UhookVLLJ run. Note cross section locations are different due to different MCS motion, but the labeling of cross section direction/orientation is identical to Fig. 4.10.

As in the control run, the southwestern portion of the gust front has a number of oscillations associated with the leading edge of a bore (Fig. 4.18b). In fact, despite being the run with the strongest cold pool, the MCS appears to be supported primarily by a density-current-driven bore. Along the leading line, there are oscillations and a semi-permanent increase in the isentropes heights up to 2 km. The

main updraft is not lifted immediately at the leading edge, but rather by the second wave crest (Fig. 4.19a,b). This combined with the displacement of  $5 \text{ m s}^{-1}$  updrafts associated with the gust front from the precipitation suggests that this is true along other parts of the leading line (without taking dozens of cross sections). It is worth mentioning, that in Coniglio et al. (2006) and Weisman and Trapp (2003) that cells were displaced further behind the gust front in bowing MCS simulations with weaker shear, but in stronger shear environments like the one here cells were closer to the gust front. Passive tracer is removed at the leading edge of the gust front below 1.5 km, and appears to be lifted by and through the wave.

Updrafts are tilted strongly upshear (of deep layer shear), the large buoyancy gradient to the rear of the storm leads to a relative low pressure, and results in the generation of a RIJ which is brought to the surface by convective downdrafts. There is also relatively strong FTRF that actually changes the direction of the winds in the outflow region aloft. The thermodynamic and wind structure of the leading line closely resembles that of a classic bowing MCS like described in Weisman (1993).

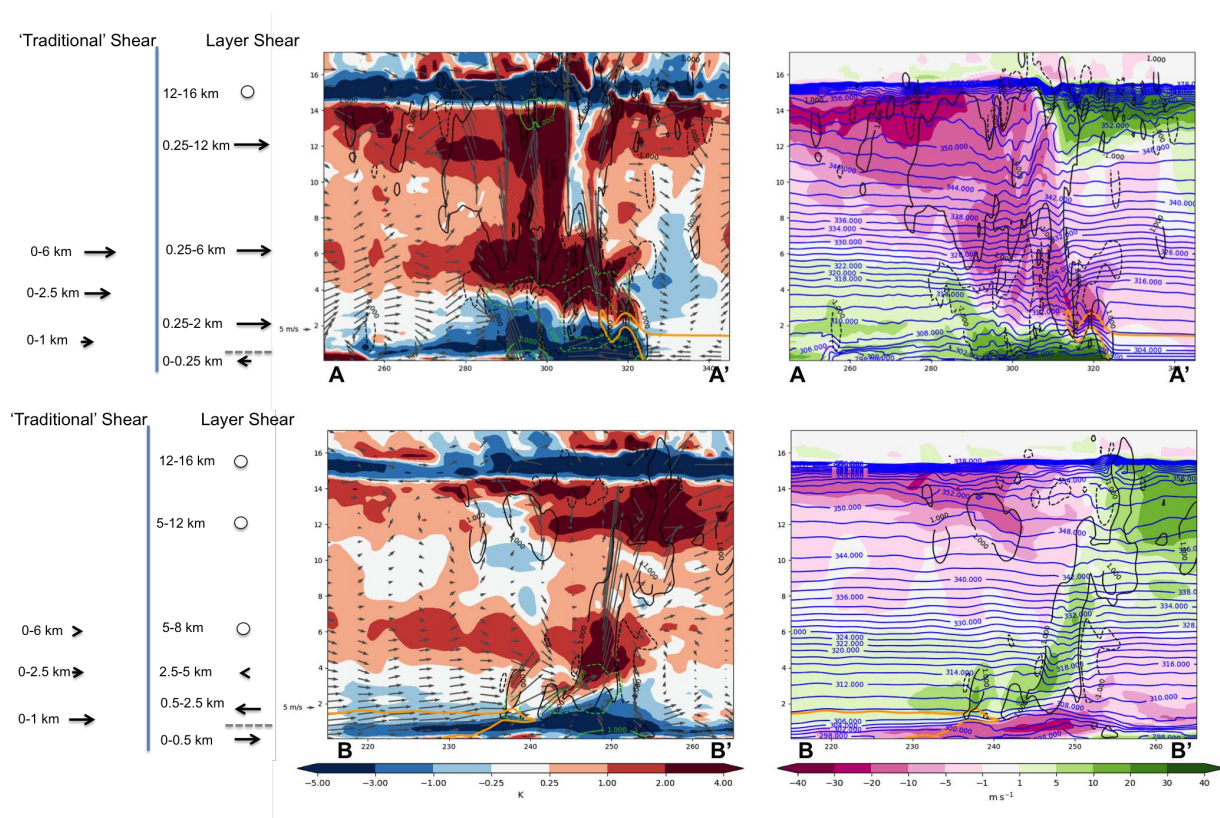


FIG. 4.19. Cross section through Fig. 4.18 for UhookVLLJXC run. Panels as in Fig. 4.11.

In the cross section through the ROD, the same elevated  $\theta_\rho$  decrease is observed below 1 km associated with the leading bore, and a deeper, more dramatic elevated  $\theta_\rho$  deficit is located some distance behind the leading edge. Unlike the CTRL run, trajectories suggest that parcels do not experience significant descent before entering the ROD updraft. Instead, parcels here appear to be lifted slightly at the leading edge of the bore, lifted further by a wave-like perturbation in the lowest 0.25 km (couplet in  $\theta'$ /temporary upward perturbation of near-surface isentropes between  $x=235$  and  $x=240$ ), and finally lifted into the updraft by a much stronger perturbation, much like that in the CTRL run (Fig. 4.20). However, also unlike the CTRL run, at 4 hours, the location of the most dramatic lifting is also the location of the surface density current, evidenced by  $\theta_\rho$  deficits at the surface and positive pressure perturbation in figure 4.20h around  $x=245$ . So in this run, there may be more gradual ascent analogous to that described in Peters and Schumacher (2015b) and Blake et al. (2017), but the steepest ascent still occurs with the final perturbation, which in this case is generated by upward displacement of isentropes below about 2.5 km in association with the presence of a surface density current. As in the CTRL run, the vast majority of parcels come from the south and west of the convection, but some parcels do come from the southeast, and all parcels have a more northwestward trajectory until they interact with the bore at the leading line and turn to the east.

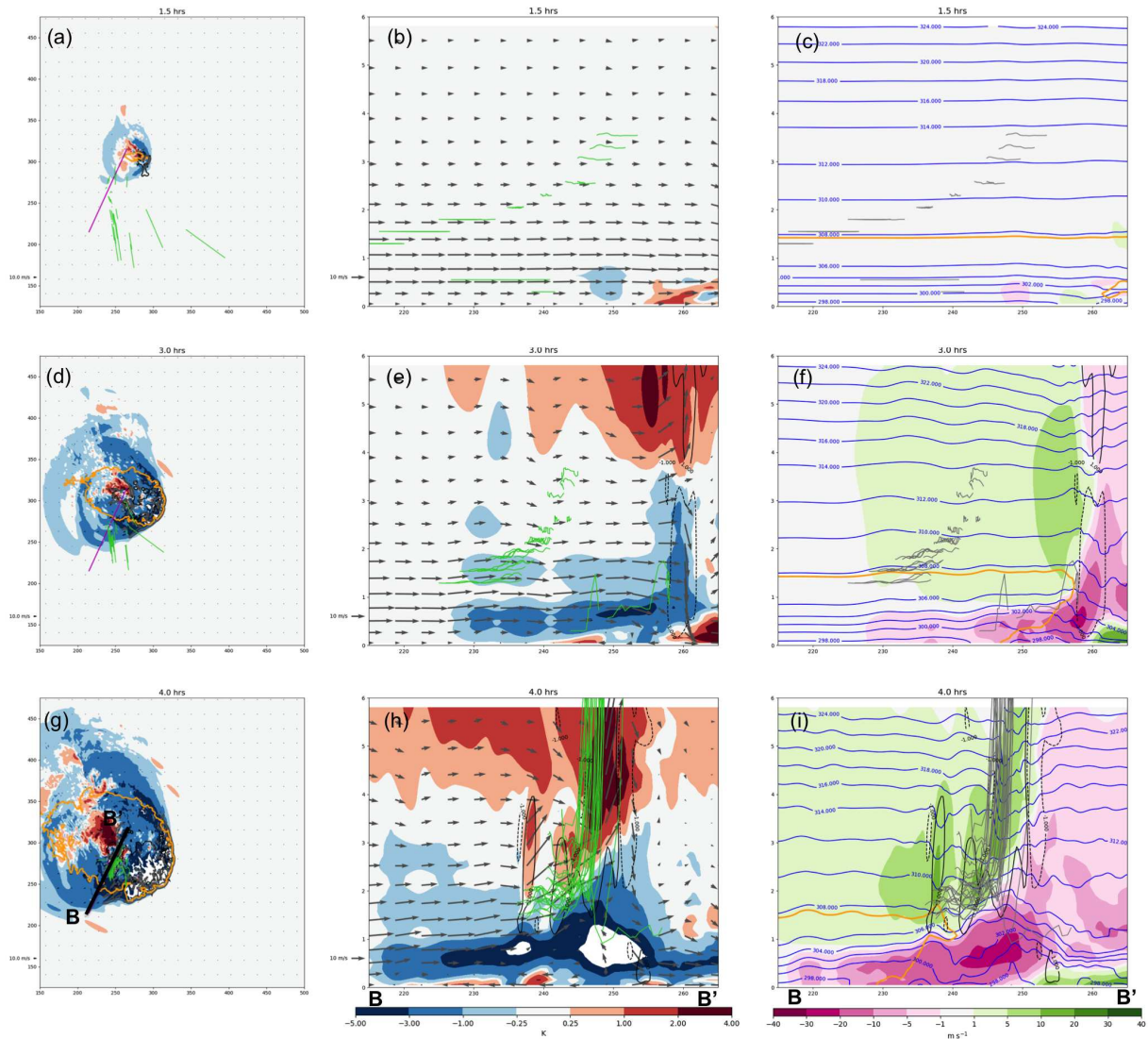


FIG. 4.20. Parcel trajectories for ROD updrafts in the UhookVLLJ run. Panels as in Fig. 4.12. Cross sections at location B-B' consistent with cross section B-B' in figure 4.19

While the forward-propagating portion of the leading line resembles a more classic bowing MCS, an exploration of other regions of the MCS suggests that in this thermodynamic environment, the low-level jet itself is conducive to ROD. One explanation for this is the favorable bore environment provided by a combination of the strong boundary layer stability and curvature in the wind profile provided by the LLJ (Haghi et al. 2017). A trapped bore can move away from convection and the density current that generates it, and as it does the associated semi-permanent lifting in the isentropes can help bring parcels closer to their LFCs (if they do not immediately reach them), much like the cold pool described

in Peters and Schumacher (2015b). Some distance behind the leading edge of the bore, a surface density current generates a deeper perturbation in the isentropes, able to lift parcels the final distance needed to reach their LFCs. This run and mechanism is very similar to the case detailed in Blake et al. (2017). However, the presence of a surface cold pool and its role in lifting of parcels is notably different from the CTRL run, where after an initial ascent, parcels actually descended some distance behind the leading edge of the bore but ahead of ROD updrafts. Additionally, in the CTRL run there was little-to-no evidence of a cold pool in the region of strong ascent where parcels were lifted to their LFCs.

#### 4.3.2.4 LLJ AND 5 KM WIND MAX (UHOOKVJET2)

One of the features of the 0428 UTC 25 June 2015 wind profile used in Chapter 3 that really stood out as a departure from the composite profile of elevated instability cases created in Chapter 2 is the presence of a second strong southerly wind maximum in the  $v$  profile that begins around 5 km (Fig. 4.2). The UhookVjet2 experiment was designed to explore the effects of just the 5 km wind maximum by adding it to the LLJ profile, but continuing to exclude the upper-level jet. This can also be thought of as an experiment that withholds the upper-level jet from the UujVjet3 (analytical version of the full profile) experiment. The resulting MCS develops much like the CTRL and UhookVLLJ runs at earlier times, though early cells associated with the northern wave ( $-0.5$  K  $\theta$ 's to the north in Fig. 4.13f) quickly race north. The northwestern most cells around 2 hours continue to grow and eventually become the ROD convection as the southwestern gust front continues to propagate away from them. After 3 hours, new convection is initiated some distance behind the leading edge of the surface cold pool ( $-0.5$   $\theta'$  contour) but separate from the existing ROD, and remains offset from the leading SW gust front throughout the duration of the run. Convection along the eastern portion of the line is closely tied to the surface cold pool and remains so throughout the run (Fig. 4.14f). As evidenced by the precipitation totals, this simulation had a more northeastward trajectory throughout the simulation compared to the CTRL and UhookVLLJ runs. Precipitation totals in this run were also generally lower than both previously described runs, with a maximum of 81.76 mm, over 40 mm less than the UhookVLLJ experiment.

Like the UhookVLLJ run, this run produced a surface cold pool with  $\theta_\rho$  deficits larger than 3 K in the bowing portion of the line. The largest  $\theta_\rho$  deficits are primarily confined to the regions of heaviest precipitation, but a region of negative surface perturbations extend some distance behind the southwest gust front boundary (Fig. 4.21a). Passive tracer is removed at the surface nearly everywhere cooling is observed, but also extends into the region of positive  $\theta$ 's (Fig. 4.21a). As in UhookVLLJ, vertical velocities oscillate along the southwest gust front boundary. The largest concentrations of passive tracer

lofted from the layer below 500 m to 5 km is in the northern portion of the convective line, predominantly downstream from the 5 km wind maximum. The most coherent region of  $5 \text{ m s}^{-1}$  updrafts is primarily to the east at 4 hours, and remain primarily to the east throughout the duration of the run. These  $5 \text{ m s}^{-1}$  updrafts are observed below at least 500 m along this leading gust front. In the region of ROD,  $5 \text{ m s}^{-1}$  updrafts are well above 1 km, and actually appear in almost a wave-like pattern oriented NW-SE, but it is not clear why.

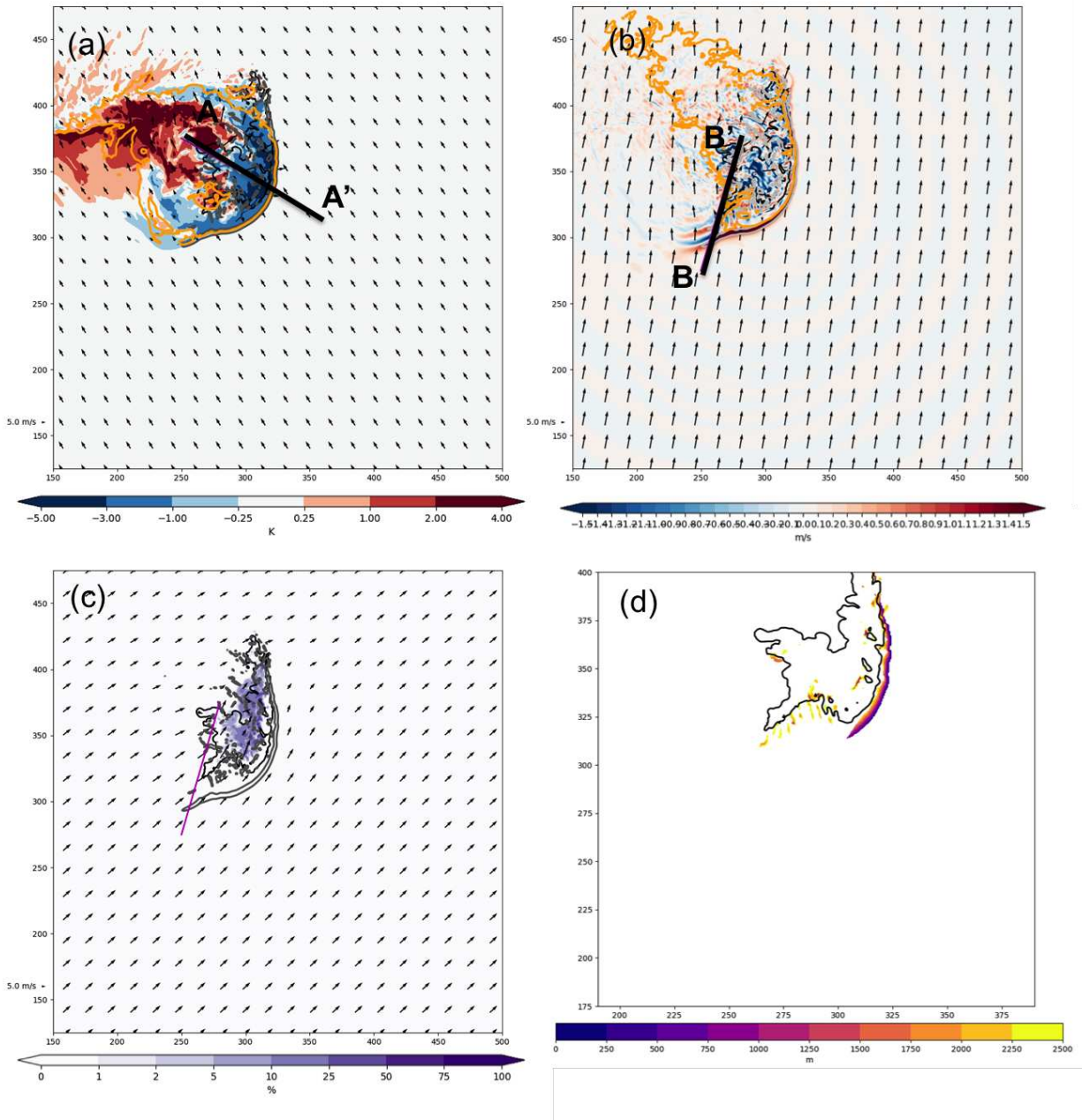


FIG. 4.21. Panels as in Fig. 4.10 but for UhookVjet2 run. Note cross section locations are different due to different MCS motion, but the labeling of cross section direction/orientation is identical to Fig. 4.10.

In the cross section through the leading line, the density current is clear, where  $\theta_p$  deficits larger than 3 K extend to the surface (Fig. 4.22a). Updrafts are tilted over the density current and the deepest penetrating updraft actually begins behind the initial gust front boundary. In this run, portions of the leading line in the region of the cross section take on characteristics of a trailing stratiform (TS) MCS

(e.g. Houze et al. 1990) with some bowing, where the balance that leads to strong updrafts is maintained by the development of a RIJ much like in the UhookVLLJ run. The RIJ is clear in both the full field wind vectors between 2 and 6 km in the west (closer to A), descending towards the east, and in the positive wind perturbations (Fig. 4.22). In this run, front to rear flow has also developed in the region up ascent ( $w > 1 \text{ m s}^{-1}$  contours)

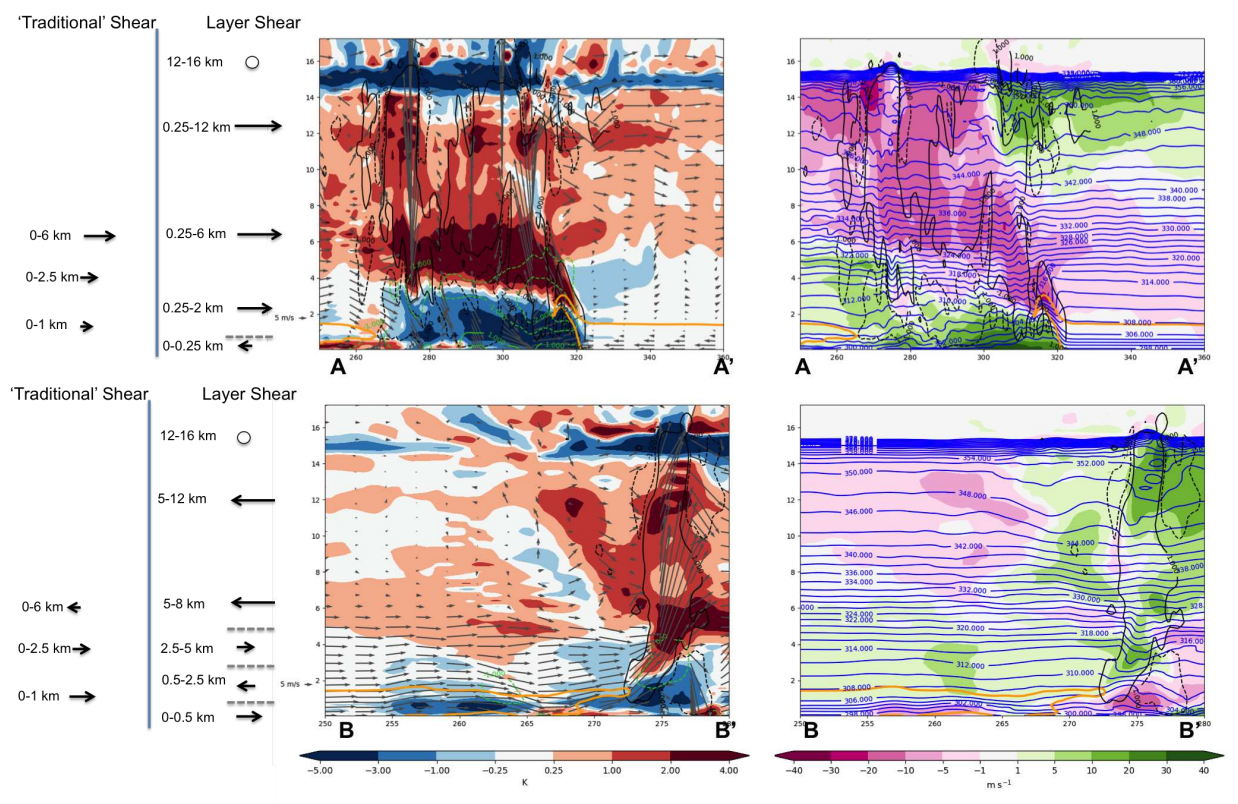


FIG. 4.22. Cross section through Fig. 4.21 for UhookVjet2 run. Panels as in Fig. 4.11.

There are two different regions of ROD in this particular run. The ROD convection that forms only slightly offset from the leading SW gust front is still tied to the surface cold pool, and parcels are lifted as in Peters and Schumacher (2015b) (not shown). In the cross section through the region of ROD that is well offset from the leading gust front boundary, cooling is predominately elevated, and oscillations below about 1km at the leading edge are associated with the bore at the southwest boundary like in the UhookVLLJ and CTRL runs (Fig. 4.22). Similar to the CTRL run, there is actually a gap and a region of descent behind the leading edge of the bore but ahead of the ROD updraft. More similar to the UhookVLLJ run, there is evidence that a cold pool has reached the surface just below the ROD updrafts. ROD updrafts appear to still be supported by a wave feature between 1 and 2 km. In this case, upward

isentropes perturbations extend to the surface, suggesting that similar to UhookVLLJ this wave is tied to the density current at the surface.

Compared to runs discussed thus-far, an especially large number of parcels reach updrafts in the ROD region (Fig. 4.23). Most of these parcels come from south of the convective line with a northwestward trajectory, and as in previous runs, turn towards more northeastward after interacting with the leading bore. The vast majority of parcels also begin above 1 km, but in this run, there are also several parcels from 0.5 and 0.8 km that reach ROD updrafts in the identified region. These parcels experience a much stronger ascent over the leading bore, are still not lifted to their LFCs, but generally remain above 1 km until they are lifted into the ROD updrafts. The parcels above 1 km generally have the same experience as parcels in the CTRL run.

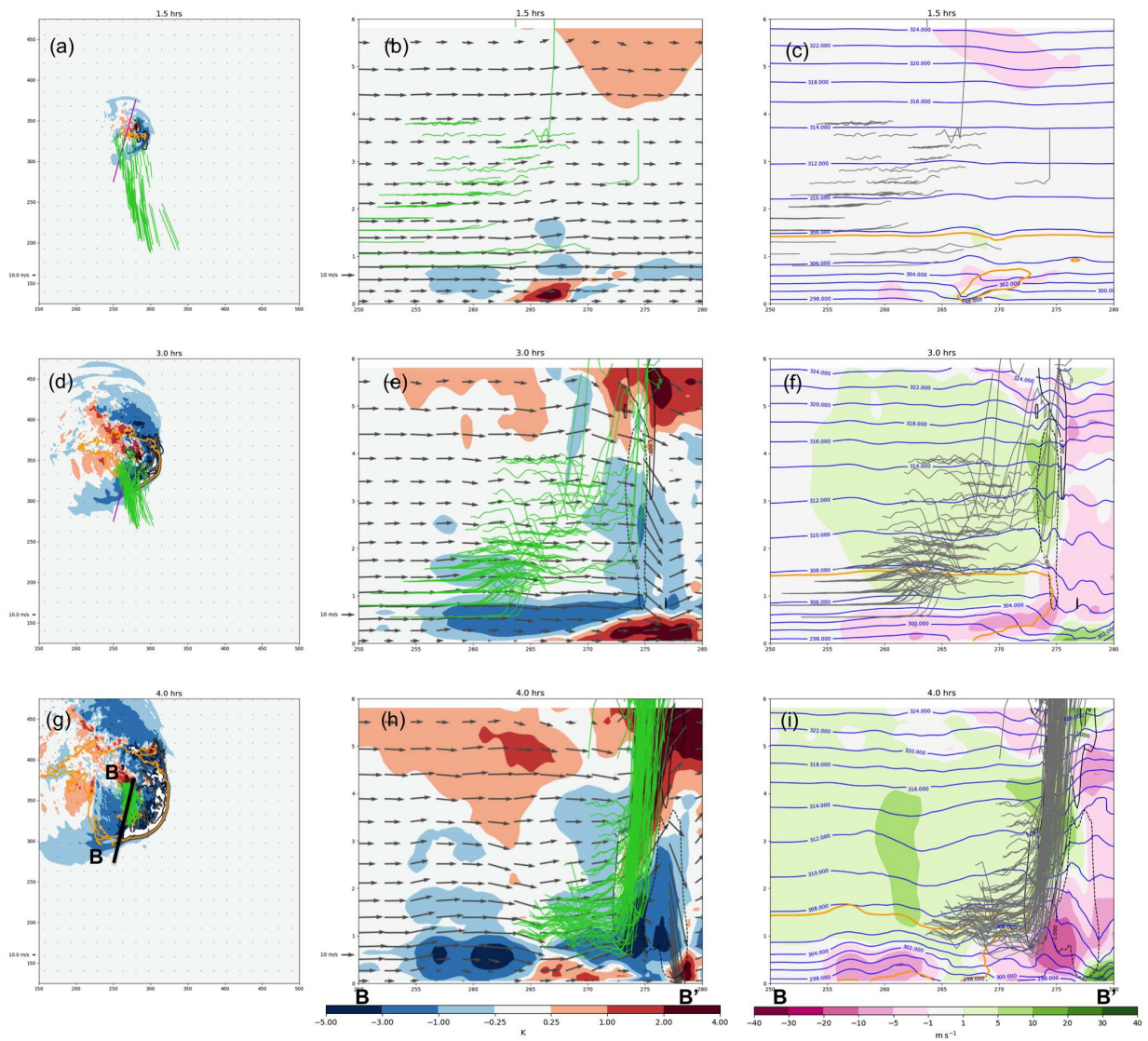


FIG. 4.23. Parcel trajectories for ROD updrafts in UhookVjet2 run. Panels as in Fig. 4.12. Cross sections at location B-B' consistent with cross section B-B' in figure 4.22

In summary, much like the CTRL and UhookVLLJ experiments, there is a bore along the southwest gust front, near surface parcels are lifted by the leading line and end up downstream, and the region of stratiform precipitation is behind the leading line. The addition of a 5 km wind maximum shifts the convection towards a more N-S orientation, with  $5 \text{ m s}^{-1}$  updrafts observed consistently and nearest to the ground along the eastern gust front boundary, which suggests it is the location of strongest near surface lifting. In this run, the development of a RIJ and front to rear flow likely aid in generating balance needed to maintain convection along the leading line. This run shares some characteristics that

are more similar to the CTRL run and others that are more similar to the UhookVLLJ run. The lifting of parcels into the ROD updrafts closest to the SW gust front and presence of a surface cold pool are more like the UhookVLLJ run, while the descent of parcels after the passage of the bore but ahead of the ROD updraft far behind the leading gust front is more similar observations of the ROD in the CTRL run. In the absence of an upper-level jet, the combination of the LLJ and a 5 km southerly wind maximum led to the development in of two different regions of ROD, that appear to be supported by different lifting mechanisms. However, in both cases, the presence of a surface density current may create the perturbations aloft necessary for the final lifting needed to get parcels to their LFCs.

#### 4.3.2.5 MOST LIKE CTRL (UujVJET3)

The winds used in this simulation are meant to be the closest analytical representation of the winds observed in the 0428 UTC sounding used to initialize the base state of the CTRL simulation. The resulting MCS has arguably one of the most similar structures to the CTRL run (UujVjet2, not discussed here, also had a very similar structure), but the maximum precipitation total is actually 40 mm higher (Figs. 4.14k,l and 4.15k,l). Early on, convection generally resembles other simulations with an upper-level jet, and similar to UhookVjet2, an early cell rapidly propagates north and continues to do so throughout much of the run. Initiation of what eventually becomes ROD begins shortly after 2 hours, but ROD convection takes longer to organize than in the CTRL run and is consequently less organized at 4 hours than ROD in the CTRL run (Fig. 4.14k,l). Only just before the end of the simulation does ROD convection become less discrete (not shown).

In this run, a surface cold pool is only present in the far southernmost portion of the leading line. Other weak regions of  $\theta_p$  deficits do exist in various other places, but in much of the northern line, surface  $\theta$  deficits are less than 1 K (Fig. 4.24a). Passive tracer at the surface is predominately reduced in the wake region immediately behind the surface cold pool (Fig. 4.24a). As in other runs, waves are present along the southwestern portion of the gust front (Fig. 4.24b). Unlike UhookVjet2, passive tracer lofted from below 500 m is found mostly in the southern portion of the convective line (Fig. 4.24c). Like the CTRL run,  $5 \text{ m s}^{-1}$  updrafts are only observed along the gust front in the southern portion of the leading line (where the cold pool reaches the surface), but the region where this occurs is smaller in the UujVjet3 run (Fig. 4.24a). Rather, most of the  $5 \text{ m s}^{-1}$  are associated with individual cells. A wider portion of the leading line is associated with  $2 \text{ m s}^{-1}$  updrafts below 2.5 km, but this region still does not extend far to the north (not shown).

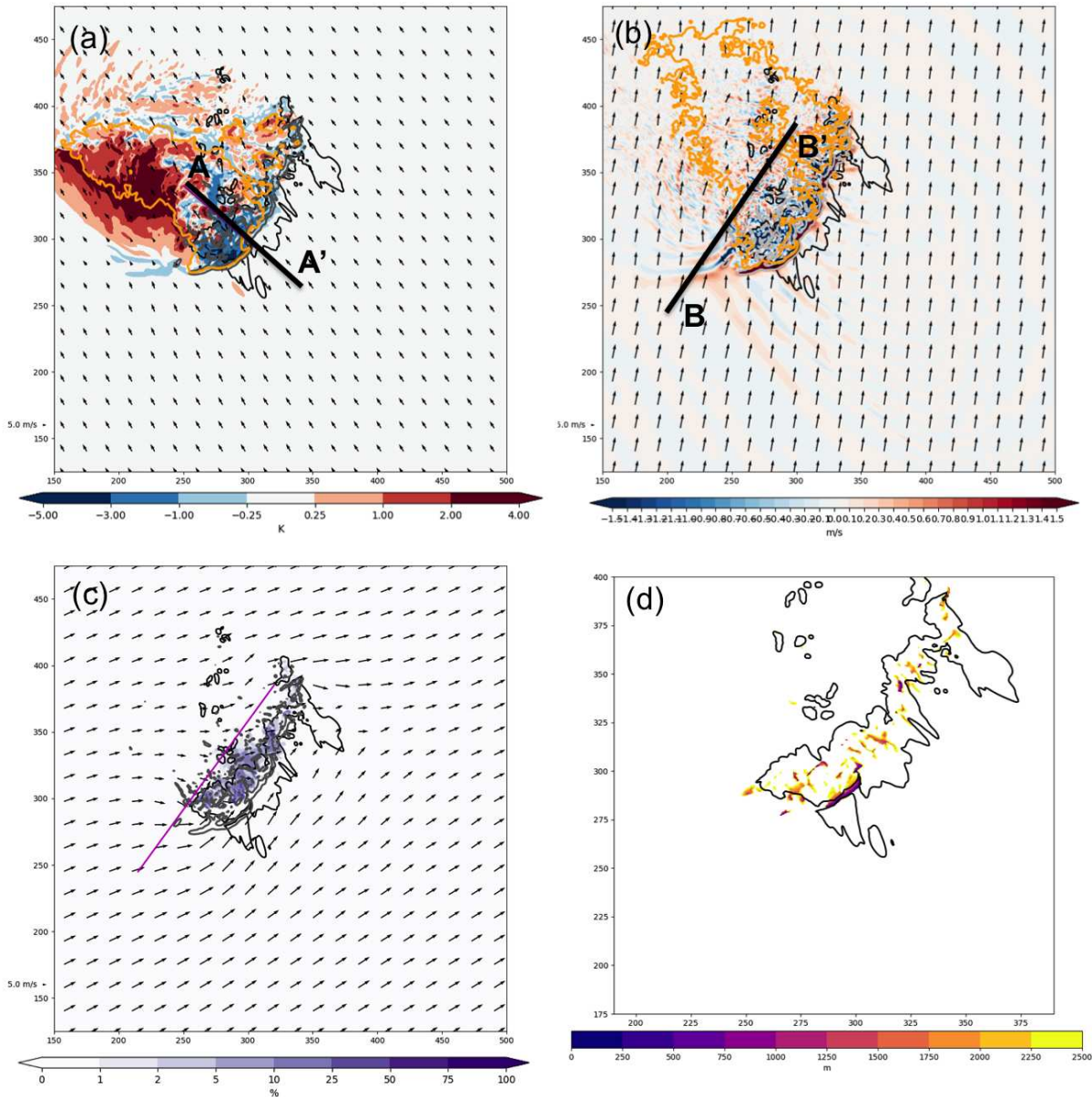


FIG. 4.24. Panels as in Fig. 4.10 but for UujVjet3 run. Note cross section locations are different due to different MCS motion, but the labeling of cross section direction/orientation is identical to Fig. 4.10.

The leading line cross section was taken through a portion of the MCS with a stronger cold pool in the UujVjet3 simulation than in the CTRL simulation, so they are not exactly comparable. Still, the greatest cooling was observed in an elevated layer (despite a cold pool actually reaching the surface),

there is some evidence of weak rear inflow, but leading line convection generally takes on LS characteristics and does resemble the CTRL run.

Cross sections through the region of ROD pass through the same features, but are closer to the leading line in the UujVjet3 cross section, since ROD convection is less organized and closer to the leading line. However, both cross sections are taken through the bore along the southwest gust front in comparable locations and are roughly oriented tangent to the parcel paths. At 4 hours, while precipitation has not yet begun at the location of the cross section in UujVjet 3, updrafts have begun to form at the leading edge of the bore. The leading edge of the bore is accompanied by larger elevated  $\theta_p$  deficits than in the CTRL run, and is followed by several similarly stronger oscillations (Fig. 4.25c). In UujVjet3, the elevated layer of  $\theta$  deficits is consistently deeper noisier than in the CTRL simulation, which could be a function of its closer location to the leading line, and could explain the numerous more discrete updrafts in the wake region until later in this run. Closer to the surface (below  $\sim 0.5$  km), several  $\theta'$  and  $U'$  couplets suggest the presence of waves. The curvature of the wind is supportive of wave trapping in this layer, and it is possible to identify some coherent wave structures in the 0.5 km updrafts. Trapped low-level waves might also lead to perturbations aloft, but its less clear why this would also not occur in the CTRL run then.

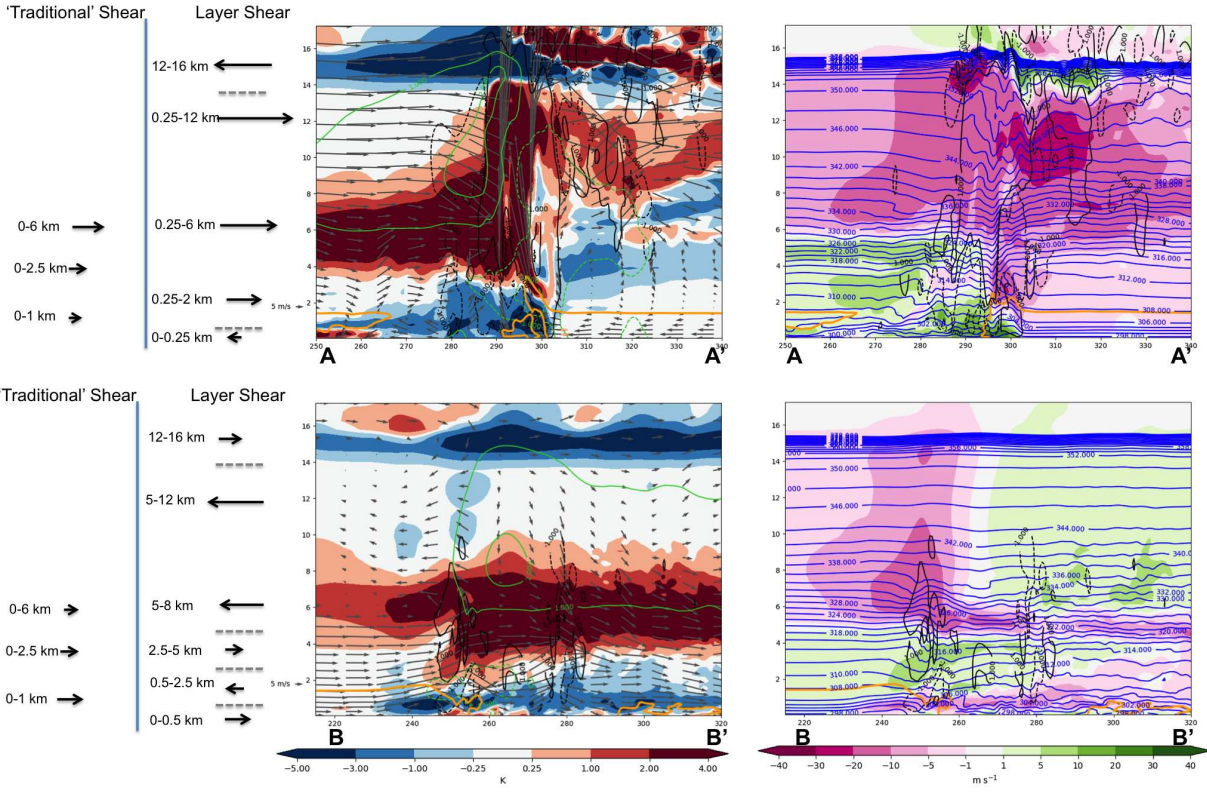


FIG. 4.25. Cross section through Fig. 4.24 for UujVjet3 run. Panels as in Fig. 4.11.

While fewer in number, parcels that reach one of these updrafts still follow the same approximate trajectory as CTRL and UhookVjet2 parcels that reach ROD updrafts well removed from the leading gust front (Fig. 4.26). Parcels approach from the southwest, ascend slightly over the leading edge of the bore at a time where it is still not sufficient to generate an updraft, and descend before reaching a wave between 1 and 2.5 km in this case that lifts them the rest of the way to their LFCs. More like the UhookVjet2 run than the CTRL run, the upper-level wave is co-located with a shallow negative  $\theta'$  at the surface.

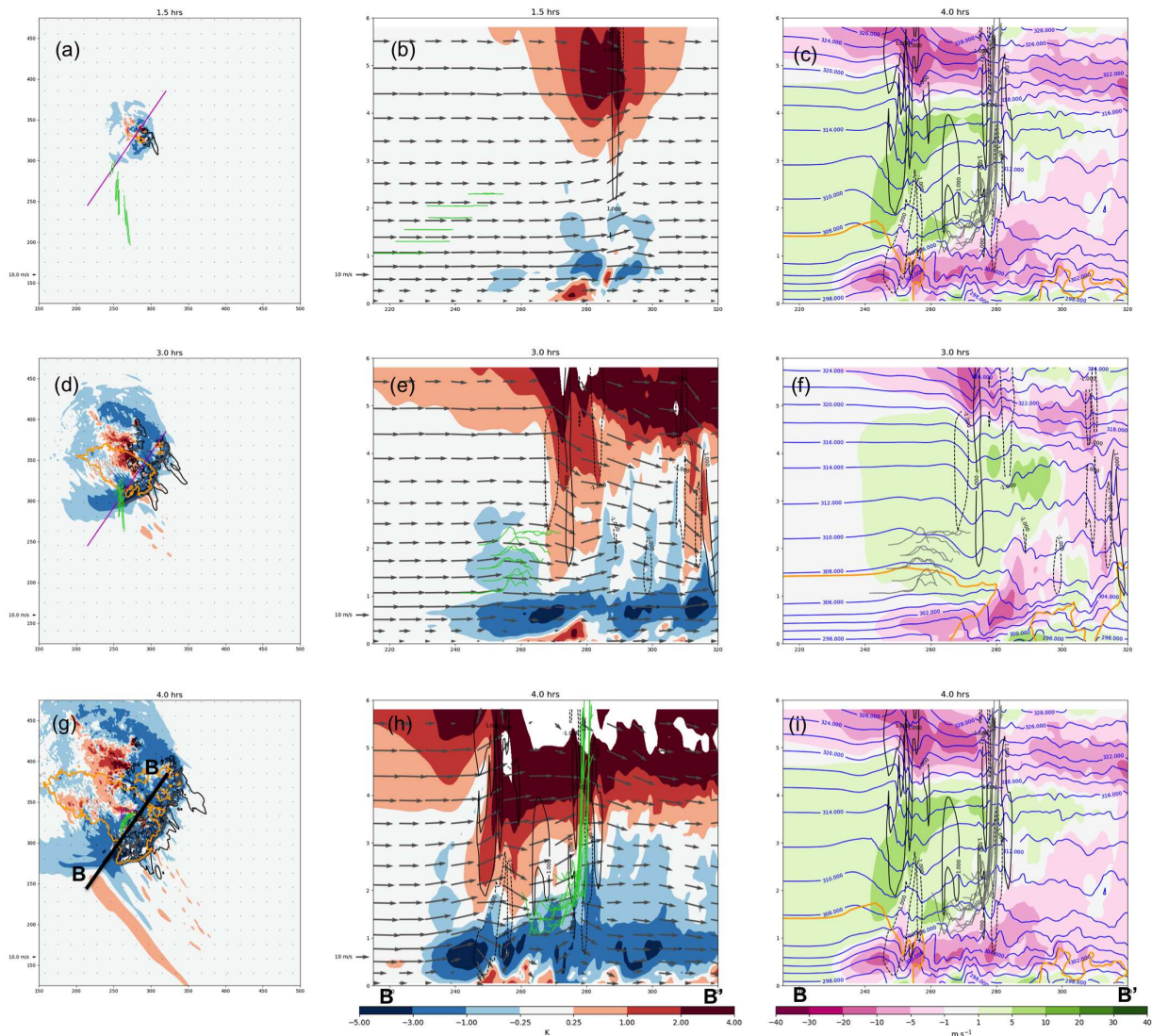


FIG. 4.26. Parcel trajectories for ROD updrafts in the UujVjet3 run. Panels as in Fig. 4.12. Cross sections at location B-B' consistent with cross section B-B' in figure 4.25

In summary, the UujVjet3 simulation resembled the CTRL run in many ways. One of the largest differences, the more discrete ROD convection, may be tied to a number of waves near the surface that generate perturbations aloft. It is possible that 'lucky' parcels in some locations are lifted just enough to reach their LFCs, and the resulting convection eventually self-organizes. It is also possible that something like this happens in the CTRL and other runs. However, the consistent presence of a deep wave between 1 and 2 km in other runs suggests that it is a more coherent feature. An alternative explanation for ROD in this run is that the more discrete convection early on is what generates the noisier wave structures at low levels and results in slower organization. Finally, despite representing

the general structures of the observed profile, the resulting ROD and low-level  $\theta$  structures were notably different. This shows just how sensitive MCSs can be to even small changes in the vertical wind profile. One major difference between observed profiles and the analytical profile used here is in the overly simplified representation of the upper-level jet, and in particular the sharp decrease in wind around and above 15 km. It may be worthwhile to consider a closer representation of upper-level winds in the future.

#### 4.3.2.6 NO 5 KM WIND MAXIMUM (UujVuj)

As an counterpart to the UhookVjet2 run, the UujVuj run includes the full 3D LLJ and upper-level jet, but excludes the 5 km wind maximum. Since the addition of a 5 km wind maximum led to development of ROD similar to that observed in the CTRL and UujVjet3 runs in addition to the ROD observed in the UhookVLLJ run, this test essentially explores what happens if the 5 km jet is removed from the UujVjet3 run to see if the upper-level jet alone can create an environment conducive to the development of ROD. The short answer is that with this upper-level jet profile, it can not.

The MCS in this run begins much like the MCSs in the other runs with the 3D upper-level jet (Fig. 4.13i). As it matures, the leading line develops a much more SW-NE orientation than any of the runs discussed thus far, and propagates towards the southeast (Fig. 4.14i). At various times throughout the simulation, a few discrete cells form behind the leading line in the far northern portion of the MCS, but these cells never organize. The precipitation maximum is over 100 mm along the far southwestern edge of the convection, but moderate totals are more widespread than most other simulations. The forward propagating portion of this simulation also moves quite rapidly compared to other runs (all domains translate the same), putting the MCS in further south and east portion of the domain shown in (Fig. 4.14i; the zoomed in domain displayed is the same for all runs).

In this run, the strongest surface cold pool is still observed to in the far southwestern portion of the MCS, but covers an even smaller region than any of the other runs described (Fig. 4.27a). Regions of surface  $\theta$  deficits greater than 1 K do exist throughout the MCS convective region. Passive tracer removal at the surface basically highlights the wake region of the MCS and exists nearly everywhere downstream of the convective line both at the surface and at 0.5 km (Fig. 4.27a,b). Oscillations along the far southwest gust front are noticeably weaker than in any of the runs described so far, but various wave structures can still be see in the wake region (Fig. 4.27b). Passive tracer from the layer below 500 m is lofted to 5 km nearly everywhere along the convective line, but to a lesser extent than some of the other simulations suggesting that near-surface updrafts may be weaker (Fig. 4.27c). The only region

of  $5 \text{ m s}^{-1}$  updrafts that appear to be connected to the leading gust front at 4 hours (and throughout the simulation), are in the far southwestern region consistent with the location of the surface cold pool (Fig. 4.27a,c). Despite this, in analysis of the average starting height of  $5 \text{ m s}^{-1}$  updrafts (below 3 km) over the entire domain presented earlier,  $5 \text{ m s}^{-1}$  updraft bases were lower than in most other runs until about 3 hours into the simulation (Fig. 4.16b). This may just mean that stronger updrafts reached lower altitudes earlier as the MCS matured faster; as other MCSs matured, most runs with a 3D jet developed  $5 \text{ m s}^{-1}$  at similar heights on average.

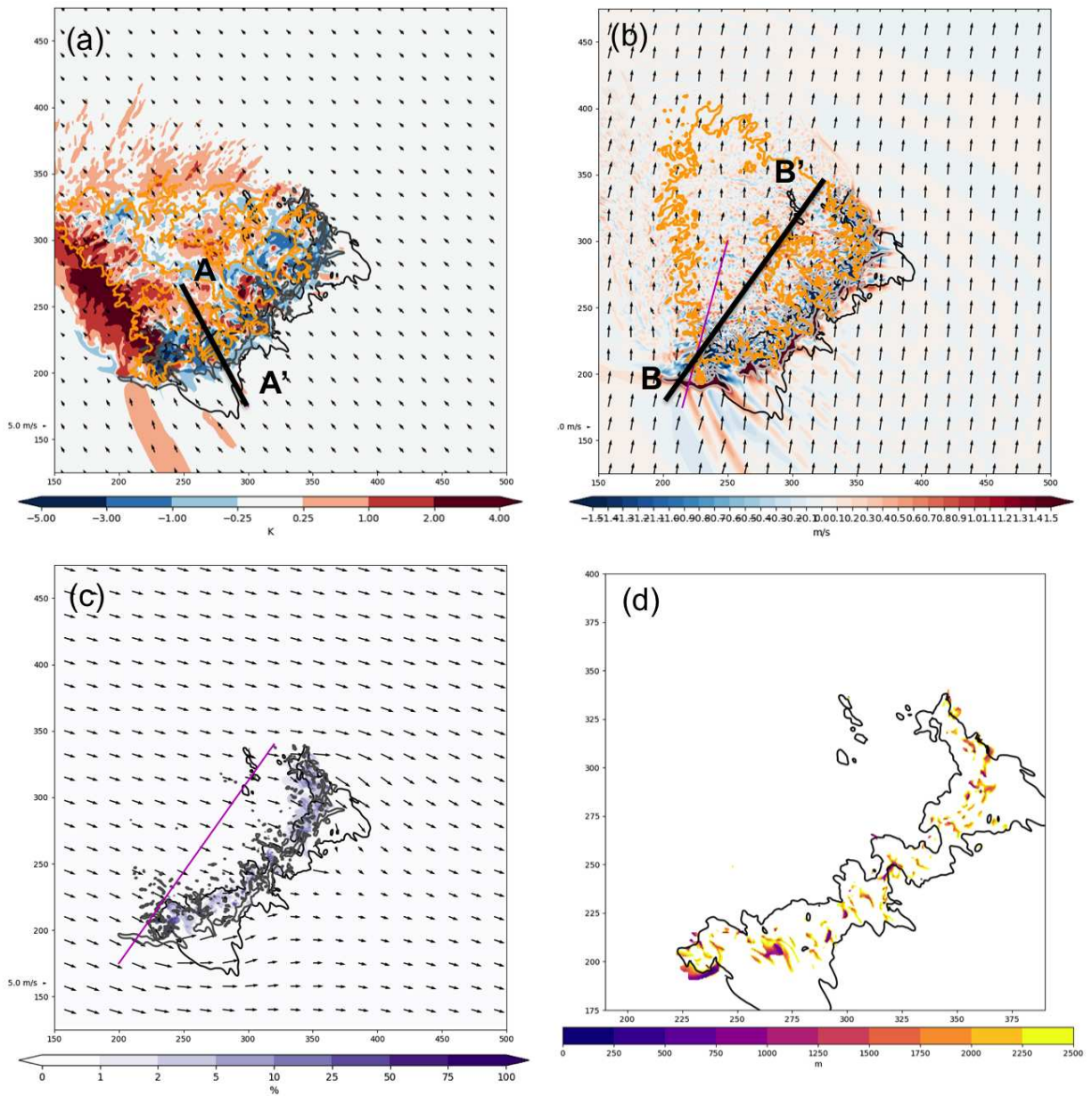


FIG. 4.27. Panels as in Fig. 4.10 but for UujVuj run. Note cross section locations are different due to different MCS motion, but the labeling of cross section direction/orientation is identical to Fig. 4.10.

Cross sections through the leading line after 4 hours suggest that inflow actually comes from both the east and the west (Fig. 4.28a). Updrafts are nearer to the surface to the east, while those to the west draw inflow from the 2-4 km layer at this time (Fig. 4.28a). Structure like this exists at different times, and in different places along the leading line. At many points during the MCS evolution, updrafts

appear to tilt strongly downshear (visible in Fig. 4.28a, but stronger at other times). The elevated  $\theta$  deficit is also deeper in the convective region than in any of the other runs. LS MCSs, are generally considered to draw their inflow from the front or from the rear, but this MCS draws inflow from one or the other at various points in its lifetime, and sometimes both. This said, updrafts that draw their inflow from the front are generally tapping into the inflow air with the most CAPE (not shown). The vertical buoyancy gradient induced by the structure of  $\theta$ 's behind the leading line,  $U'$  below 5 km, and reversal of wind direction to the rear of the convective line are consistent with the development of a RIJ, but a comparison to UhookVLLJ and UhookVjet2 runs suggest that it is not as strong in this run.

Cross sections through the convective wake region are very similar to those through ROD convection in other experiments. The leading edge of the bore is accompanied by a semi-permanent increase in the height of isentropes between 0.5 and 1 km in this case, with several oscillations (Fig. 4.28c). Here, the leading edge was accompanied by the largest perturbations and a shallow updraft. The second oscillation was co-located with very shallow surface cooling and also generated a shallow updraft, but was located almost immediately following the first oscillation. None of the oscillations that followed was apparently large enough to generate deep enough updrafts to initiate new convection behind the leading line.

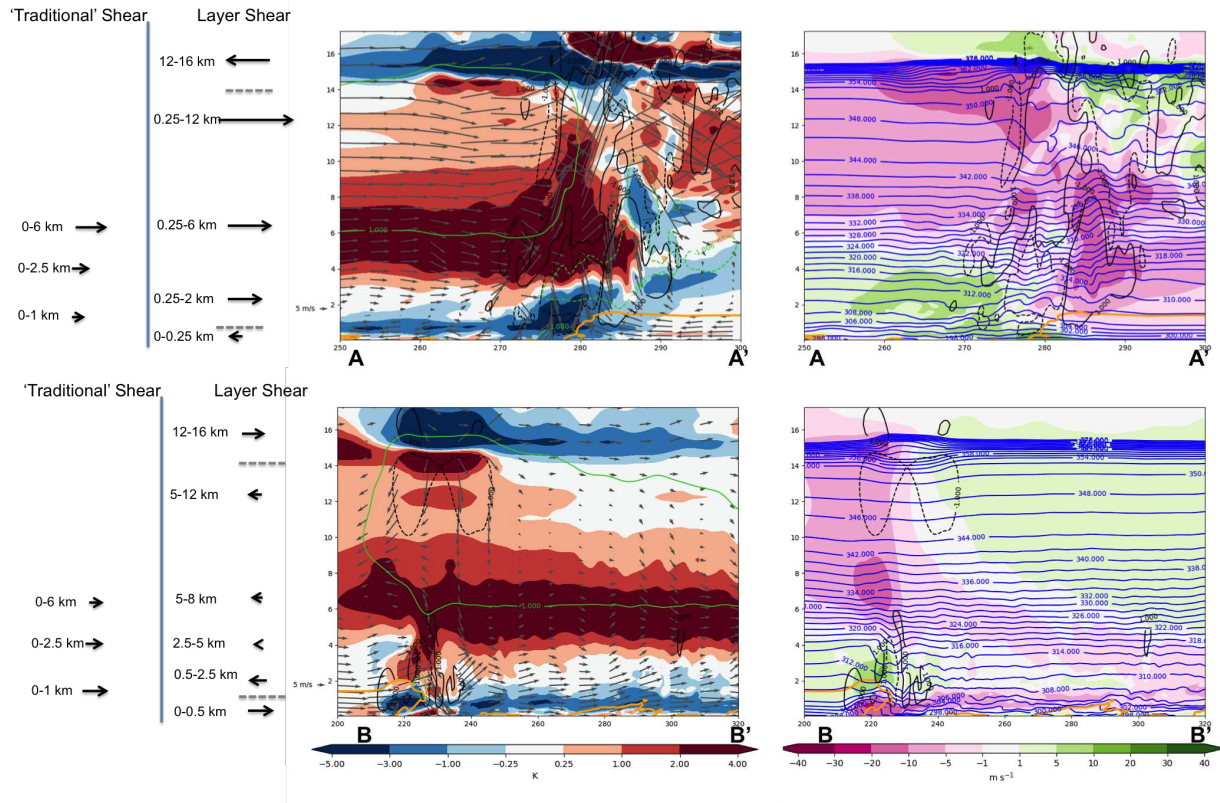


FIG. 4.28. Cross section through Fig. 4.27 for UujVuj run. Panels as in Fig. 4.11.

Since no organized region of ROD actually developed in this run, parcel trajectories were looked at in two different ways in order to try to understand why. In the first, a box was used to identify a small region surrounding an updraft that did form in the wake region in the northern portion of the MCS. The parcel trajectories displayed represent a sample of all parcels that start in the lowest 4 km and pass through the selected box at 4 hours (Fig. 4.29).

The parcels that reach this region all either interact with the leading line or approach from the northwest. What weak updrafts are captured by the cross section in figure 4.29 are very elevated. Based on the profile in figure 4.3 without the 5 km wind maximum, and taking into account the domain translation of  $4.5 \text{ m s}^{-1}$  to the north, parcels above about 2 km will have a northwesterly trajectory. Parcels below 2 km are those that interact with the leading line, and CAPE above 2 km is exceptionally low, so parcels that are lucky enough to reach their LFCs in this region do not have much available energy to begin with, and convection is not sustained.

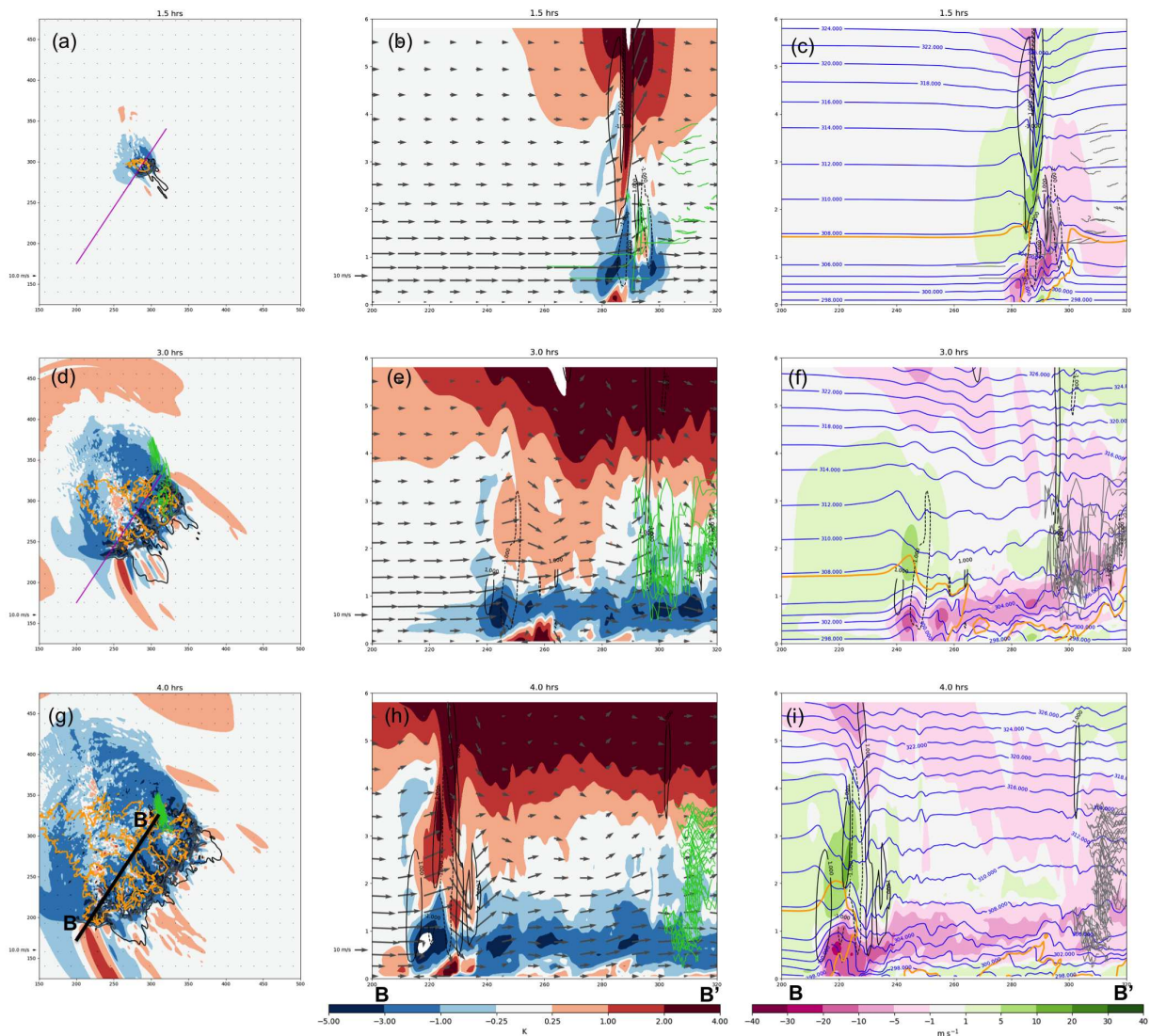


FIG. 4.29. Parcel trajectories for box in wake region where discrete cells develop in the UujVuj run. Panels as in Fig. 4.12. Cross sections at location B-B' consistent with cross section B-B' in figure 4.28

In order to identify parcels that pass through the region where ROD forms in other runs but not this one, ROD updraft parcels were first identified in the run with the most similar orientation (ULLJVuj, described briefly in the following section). The general region where those parcels passed at 1.5 hours was subjectively identified and the paths of parcels in the UujVuj run that pass through a 15x15 km box in that region were explored (Fig. 4.30). The identified region was adjusted to ensure that parcels that reached wave-like  $\theta$  perturbations in the wake region were included. Only parcels that begin between 1 and 2 km were included here for clarity, since these parcels constitute the primary inflow layer for

ROD in the other runs. Parcels with nearly due southerly trajectories are at low levels, and the increase in westerly winds with height leads to more southwesterly trajectories for parcels that begin at higher altitudes. Some of the parcels encounter only a very weak region of the leading bore and more or less continue to the north unaffected. Some of the parcels are ingested by updrafts in the southwest portion of the leading line. Finally, some of the parcels experience the same turn towards the northeast observed in ROD updraft parcels in other runs. Those parcels that get directed into the wake region encounter the numerous wave structures including one extending to 1.5 km in the vertical, but none is sufficient to lift parcels in this region to their LFC.

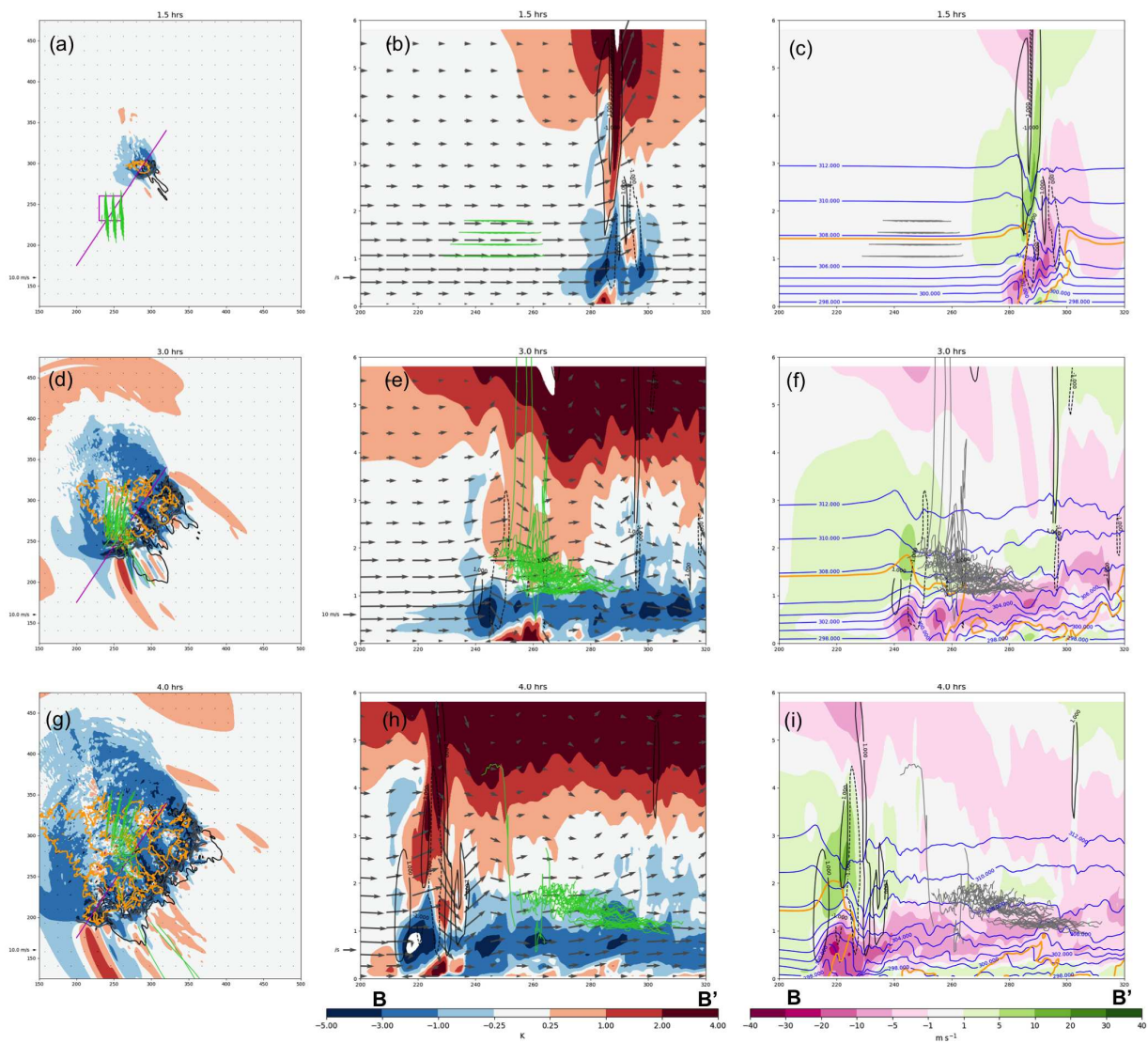


FIG. 4.30. Parcel trajectories for box in wake region where discrete cells develop. Panels as in Fig. 4.12. Cross sections at location B-B' consistent with cross section B-B' in figure 4.28

While the UujVuj run had many similar characteristics to other runs that do have ROD, convection that formed in the wake region in this run was spurious, discrete, and short-lived. Instead, parcels that entered the region where discrete cells did form, approached from the northwest, or through the leading line. Parcels that enter the wake region from the southwest, like ROD updraft parcels in other runs, ascend and descend over various oscillations, but no wave is deep enough to lift parcels to their LFC. This may be related to the orientation of the leading line, the strength and location of the surface cold pool, the lack of wave production along the southwest gust front, or any number of other factors. It is clear however, that with this particular 3D upper-level jet, the absence of the 5 km wind maximum, or perhaps just southerly winds through a deeper layer, leads to an MCS structure with no ROD.

#### 4.3.2.7 DISCUSSION OF RESULTS THUS FAR

The results presented above suggest that in an environment with the LLJ and upper-level jet characteristics of the CTRL wind profile, the 5 km wind maximum is critical for ROD to occur for reasons that are still not completely clear; this emphasizes the importance of 3D effects of vertical wind shear. As discussed in section 4.3.2.2, the addition of the 5 km wind maximum to the  $v$  wind profile leads to weaker updrafts and downdrafts as well as more elevated  $5 \text{ m s}^{-1}$  updraft and downdraft bases on average. This combined with results of the previous section could indicate MCSs that are more elevated and/or weaker are more likely to have ROD. A less efficient leading line may not realize all of the available energy, so parcels that reach the wake region still have enough energy to generate new convection if they are lifted sufficiently. At the same time, a density current of varying strengths was apparent in all runs, including UujVuj, but its expanse and MCS relative location varied from case to case. Cases with both strong and weak density currents on both southern and eastern portions of the leading line developed ROD. The resulting bores did have notably stronger oscillations in the cases with ROD, and the leading lines generally had a more N-S orientation, without much development of convection along the southernmost outflow boundary and a stronger eastward propagation component.

One consideration is that the addition of the 5 km wind maximum counteracted the strong upper-level jet to reduce deep-layer shear and cloud mean-layer wind speeds. Coniglio et al. (2006) found that the addition of weak-to-moderate deep-layer shear led to an overturning circulation and consequently stronger and more upright updrafts. They found that stronger deep layer shear led to the development of LS MCSs and more isolated cell structures. The strong deep-layer shear in UujVuj led to LS and the downshear tilt of leading line updrafts in UujVuj, while runs with the 5 km wind maximum and an upper-level jet had more upright deep updrafts and those with no upper-level winds had updrafts

that tilted over the strong cold pool. It is not clear if the characteristics of the leading line updrafts has a relationship to the lack of ROD, since ROD developed in simulations with and without an upper-level jet. However, the presence of (or lack of) the 5 km wind maximum certainly played a role in the orientation and direction of MCS motion. Coniglio et al. (2006) and Moncrieff and Liu (1999) discuss the importance of a 'steering level' flow (defined in the level where the cold pool and environmental wind speeds are approximately the same) from an MCS maintenance point of view, and Corfidi et al. (1996); Corfidi (2003) expands the idea of a steering flow to an theory for forecasting the MCS motion. It is proposed that the mean cloud layer wind and LLJ may be used to estimate the MCS propagation. In this application, the addition of the 5 km wind maximum modifies the mean cloud layer wind, which may help explain the more southerly MCS propagation in the UujVuj, where the strong northerly winds appear to dominate. The stronger southerly propagation and consequently greater lifting along the southern gust front lifts some parcels to their LFCs before they have had a chance to reach the wake region.

Another consideration is that the 5 km wind maximum creates an additional layer of positive curvature aloft below a weak layer of negative curvature due to the upper-level jet that extends nearly to the top of the troposphere. This layer is much more elevated than the low-level curvature layer produced by the LLJ, and could potentially aid in trapping deeper tropospheric waves, such as those responsible for lifting ROD parcels, below it. While this idea breaks the two layer assumption of linear wave theory, its plausible that if a shear reversal at low levels is capable of trapping waves that a strong shear reversal in another layer may do the same. As a reminder, a layer of positive curvature capped by a layer of negative curvature is conducive to wave trapping (Haghi et al. 2017). In figure 4.31, this layer exists for waves propagating between 200 and 300 degrees (between southwest and northwest) at low levels in both UujVuj and UujVjet3 runs, but a second layer of positive curvature capped by negative curvature exists for waves propagating from around 300 to 50 degrees (from the northwest to northeast) in the UujVjet3 run, consistent with the orientation of waves observed in the ROD region.

At the same time, the change in orientation of the convective line modifies the direction of the waves generated by the bore. Those generated along the southern gust front propagate from the east-northeast rather than the north-northwest. Based on 4.31, this direction is less favorable for wave trapping, which explains the fewer waves along this boundary. For those parcels in UujVuj that take similar trajectories as ROD updraft parcels, this lack of wave trapping could also explain the reduction in the amplitude of waves in the convective wake region.

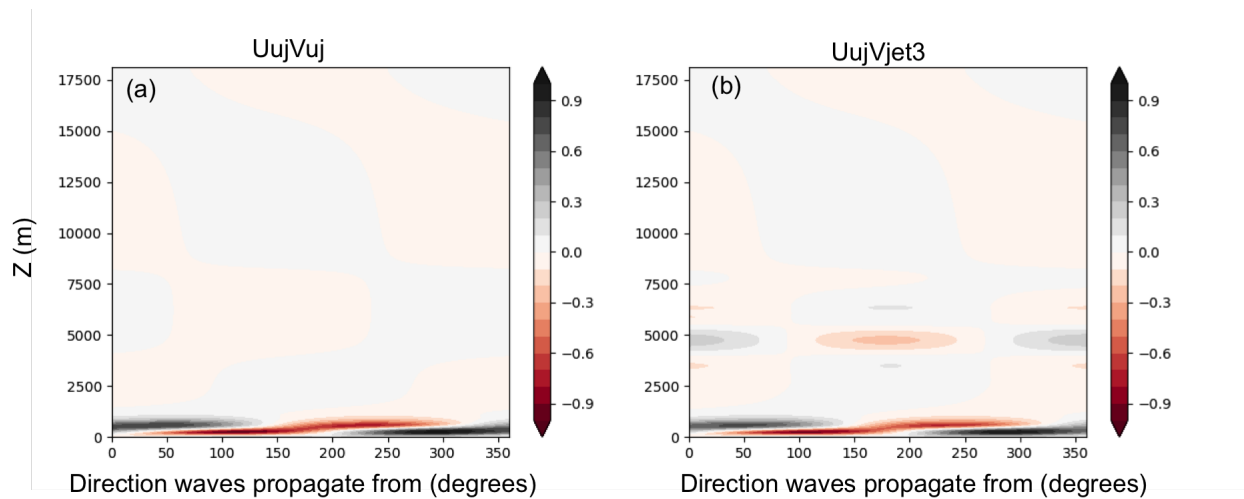


FIG. 4.31. Curvature of the wind profile as a function of height (m) for waves approaching from a direction specified along the x-axis for (a) UujVuj run and (b) UujVjet3 run.

Missing from the discussion of results presented in this section are experiments that test the sensitivity of the 3D simulation to modifications to individual components of either the upper or lower jet profiles. The UujVLLJ, ULLJVuj, UujVjet2 as well as the experiments where either u or v wind profiles are constant listed in Table 4.2 test individual components of upper and lower jets with and without the 5 km wind maximum. The additional experiments were motivated by the goal to make the above results more robust, but gave surprising results. Those results are described generally in the following section, but a more detailed analysis of these runs is required in the future.

#### 4.3.3 Additional Sensitivities

In both variations on the upper-level jet where only one of the components was included (UujVLLJ and ULLJVuj), but where the 5 km wind maximum was excluded, ROD developed and organized by 4 hours into the simulation (Fig. 4.14g,h). The UujVLLJ run produced an MCS that was organized much like the CTRL run but had a more eastward motion, likely due to the lack of strong upper-level northerly winds. The majority of the ROD updraft parcels took similar paths to those in the CTRL run, but some did have more western/northwestern origins. As in the CTRL run parcels encountered a deep upward perturbation of the isentropes in the 1-2 km layer some distance behind the leading edge of the gust front (not shown). More similar to the runs with no upper-level jet, cooling at the surface was observed co-located with the deeper elevated isentropes at this location and may actually represent the southern boundary of the density current in this case (not shown). In other words, in this run, the density current reached the surface but generated a strong bore that propagated more quickly and

initiated convection along its southern and eastern boundary. Parcels approaching from the southwest were not lifted sufficiently by the bore where trapping is less favorable (trapping most favorable for waves propagating from the west, similar to cases shown in Fig. 4.31), but upon reaching the density current are finally lifted to their LFCs, much like runs described earlier. It seems that in the absence of the strong northerly upper-level jet, a 5 km wind maximum was not necessary for convection to organize in a favorable way for ROD to develop. Based on the structure of the surface cold pool and its role in lifting of ROD parcels, it seems feedbacks between density current, LLJ and upper-level jet are important here.

In the ULLJVuj run, the strong northerly jet and absence of 5 km wind maximum led to an MCS orientation and propagation much more similar to UujVuj than any of the other runs. Yet, despite this, strong, organized ROD still developed, but is displaced further west of the leading line than in any other case. ROD updraft parcels come from the southwest and northwest, and a few even passed through the leading line, but were ultimately lifted by a deep wave whose perturbations extended to the surface much like the CTRL run. This run had a strong northerly jet and excluded the 5 km wind maximum, which indicates that the feedbacks and mechanisms proposed in the previous discussion related to the 5 km wind maximum do not represent the only possible processes which may contribute to ROD.

A final variation on upper-level winds included just the upper-level jet in  $u$ , and just the 5 km wind maximum in  $v$  (UujVjet2), but the MCS structure and organization closely resembles a combination of the UujVLLJ and UujVjet3 runs and so will not be discussed further.

Based on the runs explored in detail and the ones summarized here, there must be some balanced feedbacks between the low-level windshear, convective downdrafts, and upper-level windshear that determine the ability of cold pools to reach the surface, their extent, structure, and depth. These factors, plus the properties of the bores/waves they generate in the stable layer and their interaction with wind shear all appear to be important factors in the development of ROD. Additional work is still needed in order to understand all of the intricacies of the feedbacks that the above simulations bring to light.

Three tests of individual components of the LLJ were also included in the initial set of experiments, but the resulting MCSs were unsurprisingly quite different from the CTRL simulation. At the same time, early tests of the UujVjet3 run (meant to most closely resemble the CTRL simulation) also included several simulations that failed to produce sustained convection. This sparked renewed interest in questions that resulted from Chapter 3 about what it was that allowed an MCS to grow upscale from

a single warm bubble in this particular thermodynamic environment. For this reason, the initial single component wind experiments were expanded, and results will be detailed in the following subsection.

#### 4.3.3.1 SENSITIVITY OF MCS INITIATION TO THE LOW-LEVEL WIND PROFILE

In the endeavor to generate sustained convection in the fully 3D analytical wind profiles, it became clear that upscale growth from the initial warm bubble was very sensitive to low-level  $u$  profile. Additional sensitivity experiments detailed in Table 4.3 were used to investigate the initial support structures of MCSs under different low-level wind shear conditions. While experiments do not immediately appear to directly relate to the success of ROD development, processes that support MCS development from earlier cells may shed light on why convection does/does not form along the southwest gust front, and processes that support sustained convection at the leading edge may be applicable to other regions of the MCS. In the name U15V0, 15 refers to the parameter ( $U_s$ ) that determines the strength of the wind shear, so U15V0 and U35V0 are weak and strong shear cases compared to ‘moderate’ shear U25V0 case which has the most similar profile to UhookV0 (but without the strong curvature or ‘hook’). Figure 4.32 shows low-level winds for experiments that vary only  $u$ .

TABLE 4.3

Run	Description	Equations	Parameters	Figure
U15V0	Weak unidirectional	$u = u_{WK82}$	Us=15, Zs=0.85, C=5	
	wind shear below 850 m			
U35V0	Strong unidirectional	$u = u_{WK82}$	Us=35, Zs=0.85, C=25	
	wind shear below 850 m			

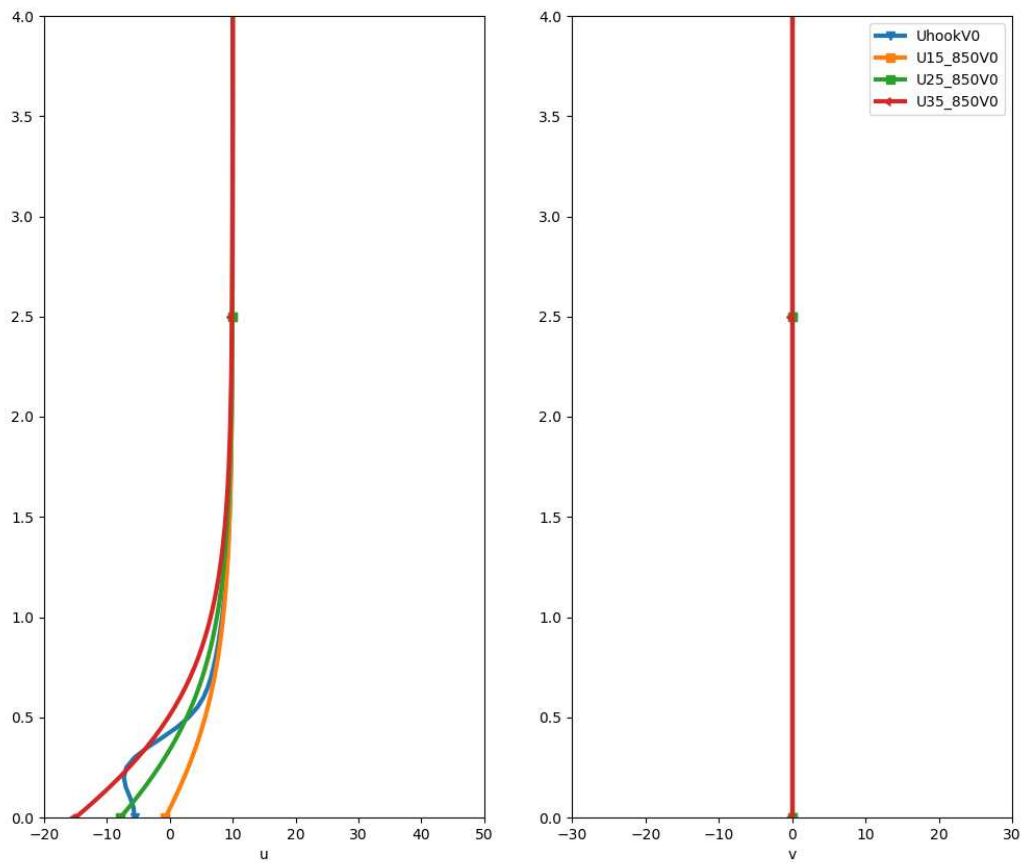


FIG. 4.32. Wind profiles for u modification experiments.

After 4 hours, the two simulations with the strongest unidirectional wind shear (U25V0 and U35V0), and the simulation with a shear reversal at  $\sim 250$  m have grown upscale into a bowing (albeit with a

slightly unusual tail) MCS (Fig. 4.33). Convection in the run with the weakest unidirectional wind shear (U15V0) has essentially died.

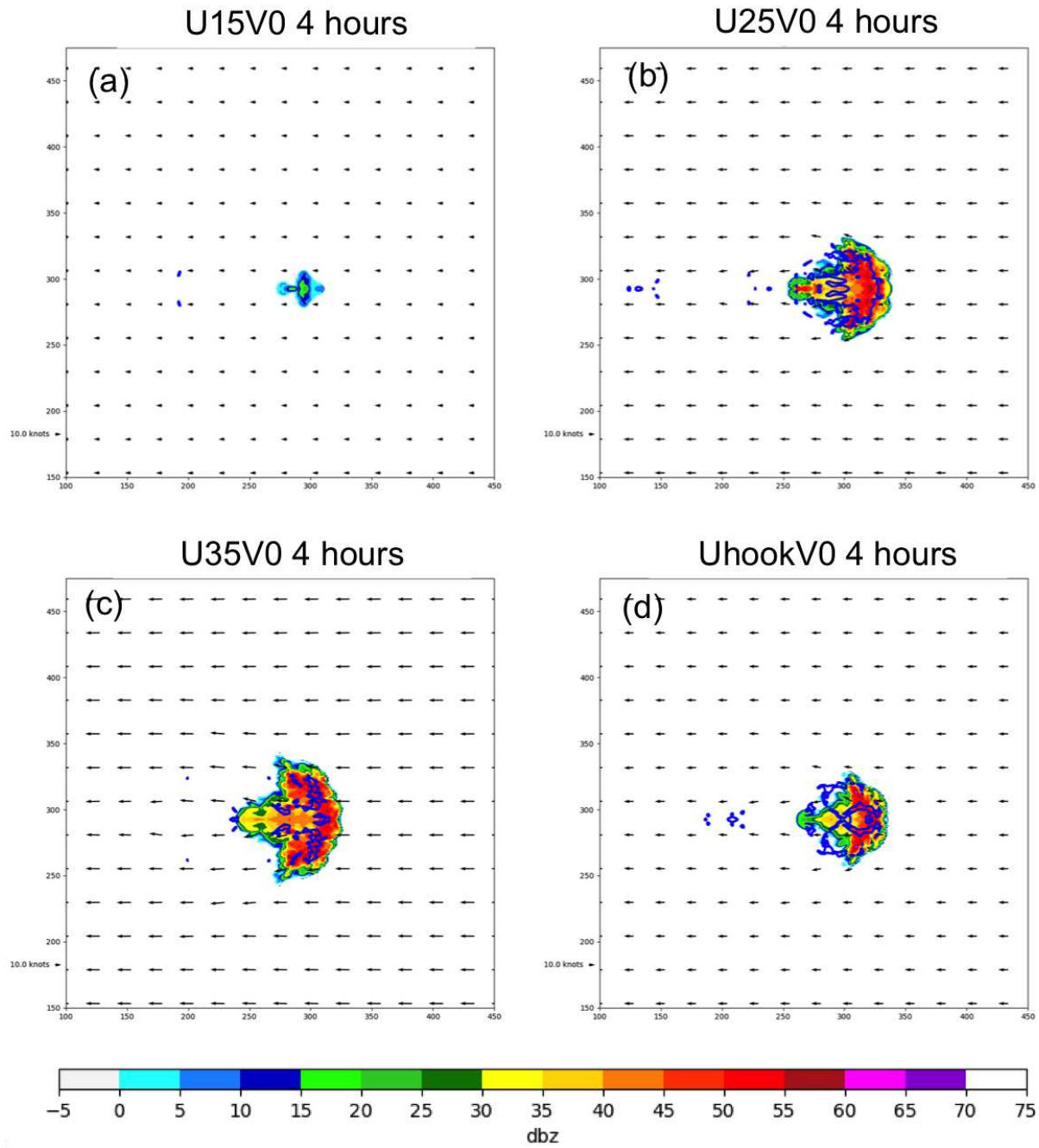


FIG. 4.33. Simulated reflectivity and  $-0.5$  surface  $\theta'$  after 4 hours for (a) U15V0, (b) U25V0, (c) U35V0, and (d) UhookV0 runs.

In U25V0, the region of  $-0.5 \text{ K } \theta_\rho$  deficits have relatively coherent coverage after 3.5 hours which suggests the beginning of a weak cold pool. This does not occur in U35V0 and UhookV0 runs until after 4 hours (Fig. 4.33). By the end of the simulation (after 5 hours), the  $\theta$  deficits in the UhookV0 simulation align well with the leading edge of the precipitation over much of the MCS (not shown). Cross sections confirm that while UhookV0 remains driven by a wave-like bore after 4 hours (Fig. 4.34g,h), it transitions to a density current driven bore by the end of the simulation (not shown) where the speed of the density current is the same as the speed of the bore ('Type C'; Rottman and Simpson 1989). At the end of U25V0 and U35V0 runs, the  $-0.5 \text{ K } \theta$  deficit is some distance behind the leading edge of the precipitation. This strongly suggests convection is maintained by a bore propagating ahead of the density current in these cases. Further evidence of this is seen in horizontal cross sections through the leading line after 4 hours (Fig. 4.34c-f) and 5 hours (not shown). In U35V0, the bore is more wave-like, and a density current is only produced to the north and south of the MCS center (but never in the region of the strongest bow). After 5 hours, when all three stronger shear simulations have a cold pool U25V0 has a cold pool intensity (C) computed within CM1 averages  $30 \text{ m s}^{-1}$  at the leading edge and has a depth of 2.5-3.5 km but is very non-uniform. In the U35 simulation, C averages about  $25 \text{ m s}^{-1}$  at the leading edge, and has a more uniform depth of 3 km. In the UhookV0 simulation, C averages more than  $30 \text{ m s}^{-1}$  at the center of the bow, but decreases to the north and south, and has a depth of about 2.5 km that is less uniform than the depth in U35V0 but more uniform than the depth in U25V0 (not shown). Where the density current likely generated a bore, this calculation may also be capturing the bore.

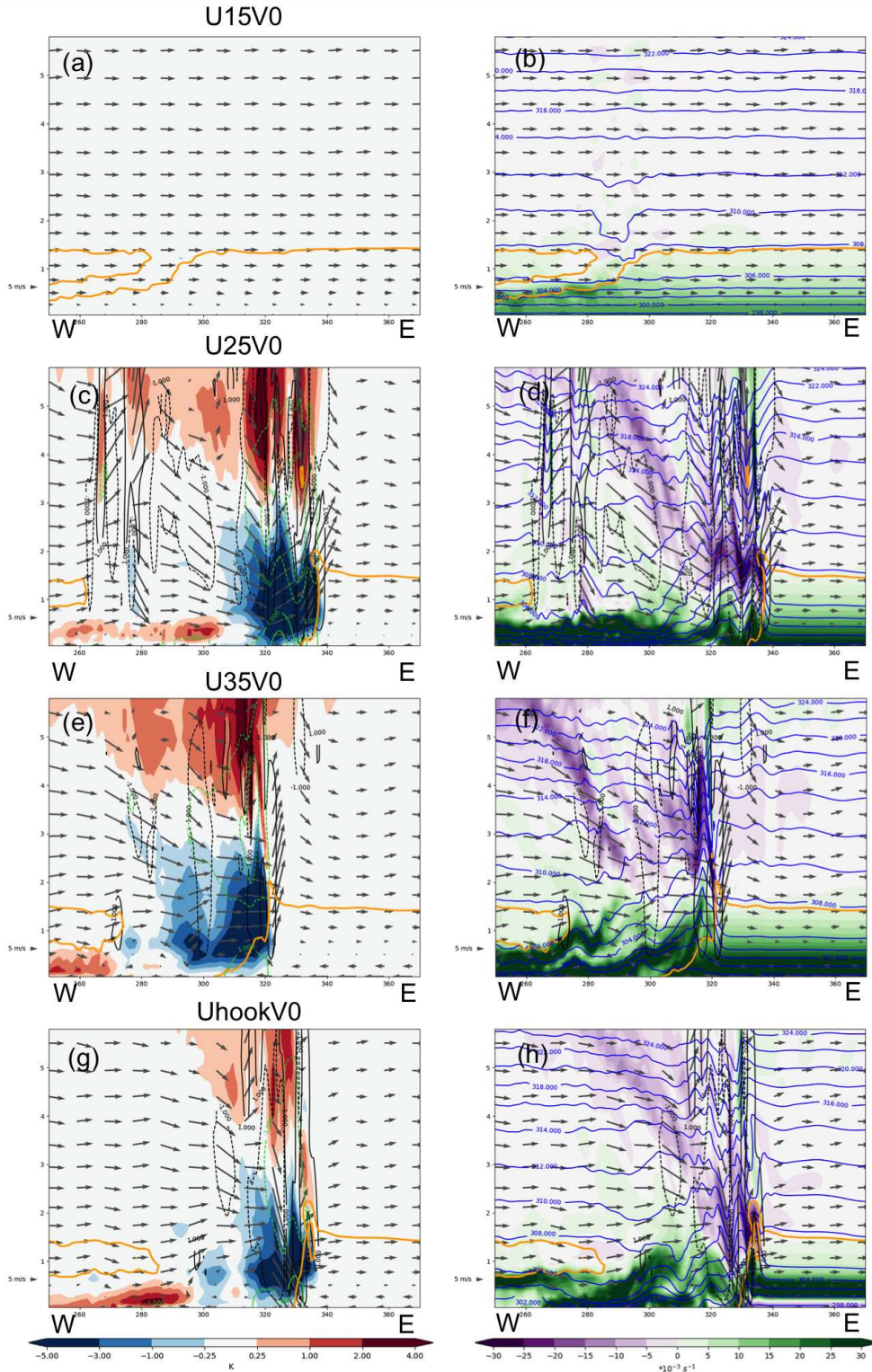


FIG. 4.34. W-E cross sections through convective cell at 1 hour. (a,c,e,g)  $\theta'_\rho$  (K; filled). (b,d,f,h) horizontal vorticity ( $\times 10^{-3} \text{ s}^{-1}$ ; filled),  $\theta$  (blue unfilled). All plots show  $w = \pm 1$  ( $\text{m s}^{-1}$ ; black unfilled), passive tracer = 80% (orange unfilled), and wind vectors for reference.

Considering that wind shear only exists in one direction, and only at low levels (basically confined below 1.5 km), its rather remarkable that a single warm bubble was able to grow upscale into an MCS. Since there is no cold pool present at the time of this upscale growth, based on existing research, the things most likely to contribute to sustained convection in these simulations are 1) A trapped large amplitude wave or bore (e.g. Wilson and Roberts 2006; Haghi et al. 2017) 2) Down-shear wave amplification (Schmidt and Cotton 1989) of deep tropospheric gravity waves, and 3) Some sort of vorticity balance in the style of RKW (Rotunno et al. 1988) suggested by Schmidt and Cotton (1989); French and Parker (2010) and others.

Let's consider the possibility of a bore or trapped wave, where a bore by definition consists of a spectrum of gravity waves. Linear wave theory assumes the atmosphere is well represented by a two layer system where a layer of constant positive Scorer parameter ( $l^2$ ) is capped by an infinitely deep layer with a negative Scorer parameter. A trapped wave mode exists if the horizontal wave number lies between the square root of the Scorer parameters of the layers (e.g.  $l_1 < k < l_2$ ). The Scorer parameter is defined as part of the Taylor-Goldstein equation:

$$\bar{w}'' - m^2(z)\bar{w} = 0 \quad (4.4)$$

$$m^2 = l^2 - k^2 = \frac{N^2}{(U - C_b)^2} - \frac{\frac{d^2U}{dz^2}}{U - C_b} - k^2 \quad (4.5)$$

,

where  $\bar{w}$  is the vertical velocity,  $m$  is the vertical wave number,  $l^2$  is the Scorer parameter,  $k$  is the horizontal wave number,  $C_b$  is the ground relative bore speed,  $U$  is the horizontal wind normal to the bore orientation, and  $N$  is the Brunt Vaisala frequency.  $N$  is defined as

$$N = \sqrt{\frac{g}{\theta_v} \frac{d\theta_v}{dz}} \quad (4.6)$$

where  $\theta_v$  is the virtual potential temperature. The Scorer parameter has two terms, the stability term ( $\frac{N^2}{(U - C_b)^2}$ ) and the curvature term ( $\frac{\frac{d^2U}{dz^2}}{U - C_b}$ ). While the stability term does contribute to wave trapping, (Haghi et al. 2017) show that in IHOP cases, the curvature term was consistently the dominant term. Here, curvature is very small in the simulations with unidirectional shear, and only in UhookV0 is a layer of positive curvature capped by a layer of negative curvature, considered favorable for wave trapping. Even then, the layer of negative curvature is exceptionally shallow. The full Scorer parameter was calculated for a theoretical bore propagating at  $10 \text{ m s}^{-1}$  every 10 degrees from the range possible

directions, and only in the UhookV0 experiment does a positive Scorer layer below a negative Scorer layer exist. Despite this, 3 of the 4 experiments developed an MCS. So from this standpoint, even if wave trapping did occur in the UhookV0 experiment, it is likely not the dominant factor in the upscale growth into an MCS.

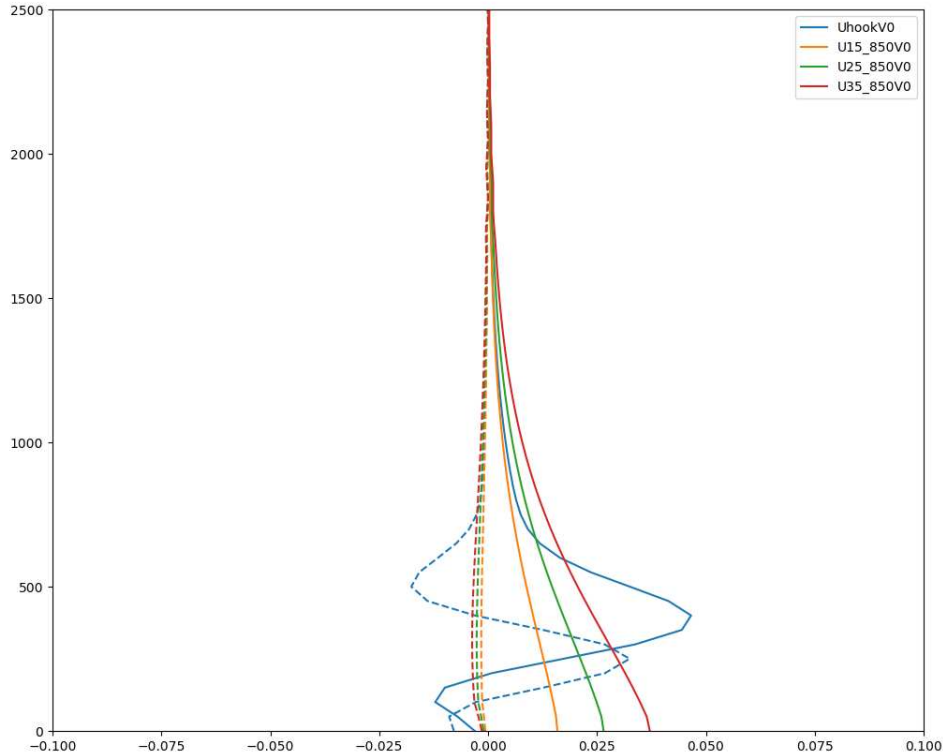


FIG. 4.35. Horizontal vorticity ( $\frac{du}{dz}$ ;  $s^{-1}$ ) and curvature ( $\frac{d^2u}{dz^2}$ ;  $s^{-2}$ ) in solid and dashed lines respectively for the four u modification experiments. Vorticity is computed for the environment orthogonal to the direction of motion. Curvature is computed for the same orthogonal plane, but \*in the same direction as the direction of motion\* and is multiplied by 100 to scale.)

In the balance presented by RKW for the interaction of cold pools with low-level environmental wind shear, the negative horizontal vorticity produced by baroclinically by the cold pool is balanced by the positive vorticity flux produced by the environmental wind shear leads to more intense, vertically erect updrafts (Rotunno et al. 1988). Gravity waves are essentially traveling packets of vorticity, associated with a perturbation in isentropes (e.g. a  $\theta$  gradient or baroclinic zone) and vertical wind shear is a

component of horizontal vorticity (In 2D:  $\eta = \frac{du}{dz} - \frac{dw}{dx}$ ), so it is reasonable to consider an expansion of downshear amplification waves into a vorticity framework as suggested by Schmidt and Cotton (1989).

In order to examine the outflow - stable layer interactions that led to upscale growth, W-E cross sections were through the initial convective cell after an hour (Fig. 4.36). Around this time, initial downdrafts had reached their greatest strength (and penetration depth). In the 3D simulations,  $\hat{i}$  and  $\hat{j}$  components of horizontal vorticity were computed and then projected on to the cross section. In these zonal cross sections,  $\eta$  is just  $\frac{du}{dz} - \frac{dw}{dx}$ .

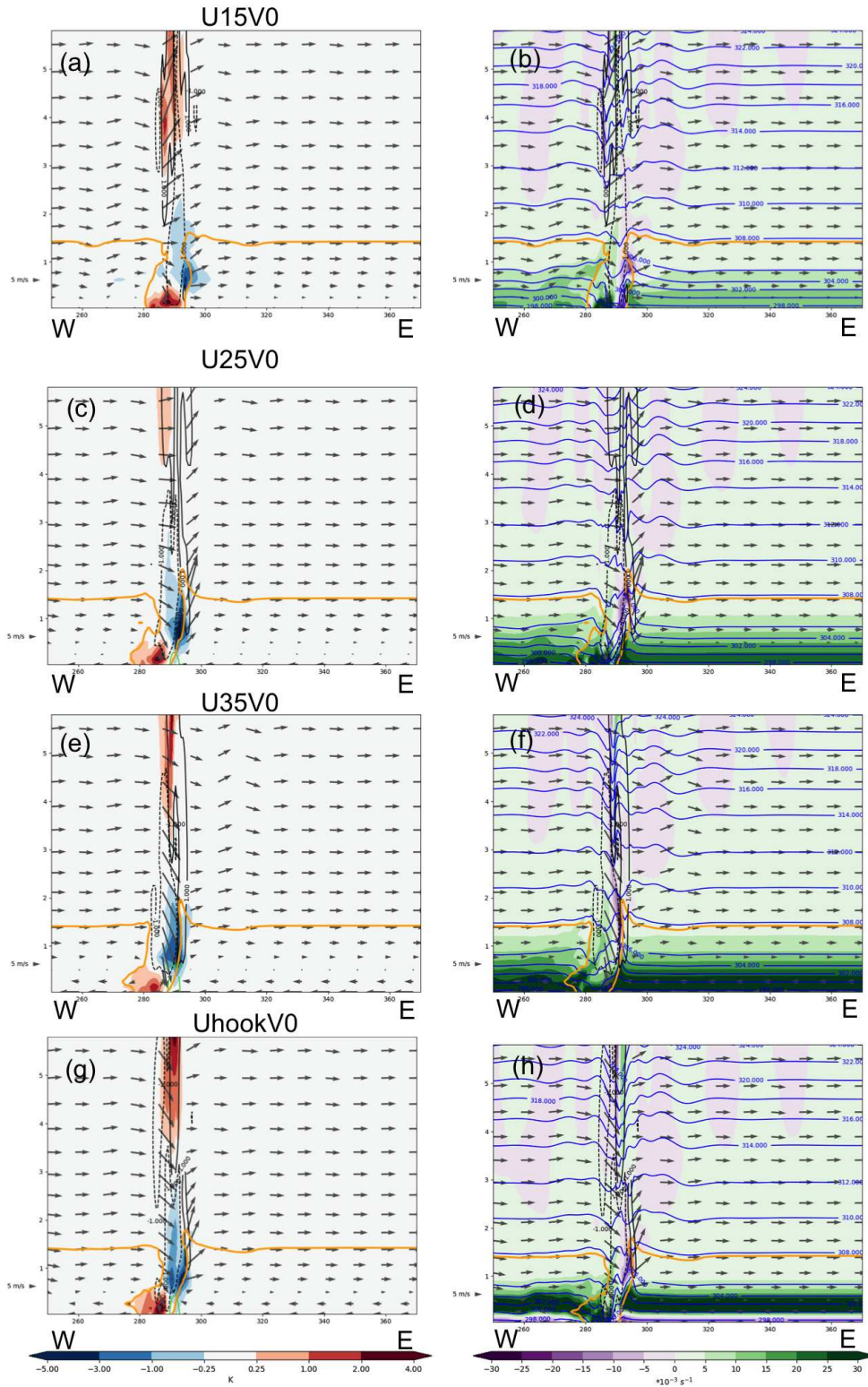


FIG. 4.36. As in Fig. 4.34 but after 1 hour.

In all four simulations, downdrafts extend well below 1 km, into the stable layer (Fig. 4.36). As discussed in Chapter 3 and the 2D experiments earlier in this chapter, downdrafts generate a warm perturbation at the surface, which is likely a result of mixing of warmer inversion air down and downdrafts that are warmer than the surface at this time. To the west, the downdrafts impact on the stable layer have generated a low amplitude gravity wave below 1 km that quickly moves west. Passive tracer concentrations are reduced in a region consistent with the downdraft, and downstream advection of initial outflow. Negative  $\theta$  perturbations associated with waves are generated in the 0.25-2 km layer. The initial downdraft is produced nearly on top of the initial updraft location, and acts to split the initial wave response below the updraft into two waves, one on either side of the downdraft.

In all four simulations, the downshear wave is amplified, but the extent of the amplification and horizontal vorticity is differ between runs. At this time, U25V0 has the largest negative  $\theta'_\rho$  (indicative of upward perturbation in isentropes), and greater  $-\theta'_\rho$ s extend over a deeper layer than in other runs. U35V0 does not have a region of -4 K  $\theta'_\rho$  like other simulations, but -2 K perturbations extend from 500 m to 2 km, and at all later times, a deep region of perturbations with magnitudes of -4 K or larger. U15V0 has a -1 K perturbation that extends between 500 m and 2 km, but larger perturbations are confined to a much narrower depth than in U25V0 or U35V0. The positive surface perturbation and negative elevated perturbation are also more vertically stacked in the U15V0 simulation, which is a reflection of the weaker shear. UhookV0 has 2  $\theta$  perturbation minima, the -2 K perturbation extends from below 500 m to 2 km.

In U15V0, the downdraft reaches the surface (consistent with the largest positive  $\theta$ ), and generates large positive vorticity to the west and a narrow region of  $-15$  to  $-20 * 10^{-3} \text{ s}^{-1}$  to the east (Fig. 4.36b). Very near the surface, the vorticity due to wind shear is slightly modified and also has a magnitude of 15 to  $20 * 10^{-3} \text{ s}^{-1}$ . Between these two regions, a  $1 \text{ m s}^{-1}$  updraft does form, but is perhaps not strong enough to break through the top of the stable layer. Around 1 km, the amplified eastern wave is associated with a region of negative vorticity with a maximum magnitude of  $-10$  to  $-15 * 10^{-3} \text{ s}^{-1}$ . The corresponding positive vorticity due to wind shear in the layer is  $< 5 * 10^{-3} \text{ s}^{-1}$ . New deep updrafts never initiate in this simulation, and the downshear wave ends up propagating away from its generation location as a return flow (like that described in the 2D simulations) propagates rapidly from east to west at low levels, and associated isentropes actually take on characteristics that resemble a cold pool.

In the two simulations with stronger unidirectional wind shear, downdrafts do not extend as close to the surface, and downshear waves are more strongly amplified than in U15V0. In U25V0, a narrow

strip of negative vorticity ( $\sim -10$  to  $-15 * 10^{-3} \text{ s}^{-1}$ ) extends to about 500 m along the on the western branch of the downshear wave (Fig. 4.36d). In the same layer, the positive shear-generated vorticity increases from around 5 to  $15 * 10^{-3} \text{ s}^{-1}$  towards the surface. At low levels, there is actually an increase in positive vorticity everywhere except immediately below the downdraft, where there is a slight decrease in positive vorticity. The largest concentration of negative vorticity (magnitude  $\sim -15 * 10^{-3} \text{ s}^{-1}$ ) is between 1 and 1.5 km, where positive vorticity is  $< 5 * 10^{-3} \text{ s}^{-1}$ . At this time, a deep updraft is on the eastern branch of the wave with a  $1 \text{ m s}^{-1}$  base around the top of the stable layer. A second shallower layer of  $1 \text{ m s}^{-1}$  updrafts is located on the western branch of the same wave between 500 m and 1 km.

In U35V0, the band of negative vorticity is even more elongated, but there is a decrease in positive vorticity in the outflow/downdraft region between just above the surface and 1 km. In this run, waves below 1 km are still associated with strong positive vorticity (and even a positive vorticity perturbation w.r.t. the vorticity at a given height). Waves above 1 km are tilted toward the west, and associated with vorticity of  $-10$  to  $-15 * 10^{-3} \text{ s}^{-1}$ . The updraft base is around 500 m, on the east branch of 500m-1km waves. It is curious that in vorticity at the locations of waves responsible for lifting is so closely tied to the layer lifted. Perhaps, in the case of strong vorticity/wind shear the amplification of the waves was sufficient that isentropic ascent alone could lift parcels to their LFCs. This may also speak to the contribution of the updraft to wave amplification. It's also particularly interesting, that with another increase in low-level wind shear, downdrafts once again do not reach as close to the surface - here  $1 \text{ m s}^{-1}$  contours extend to around 500 m.

While vorticity balance could potentially explain why waves with strong negative vorticity quickly propagated away from their source in the U15V0 experiment, and contribute to vertical motion in the 500 m - 1km layer of the U25V0 experiment, the  $\theta'_p$ 's differences between simulations and the persistent strong positive vorticity in the the U35V0 run suggests perhaps the Doppler effect amplification by shear, and the layer it occurs in, is more important than the vorticity relationships in these simulations.

The UhookV0 run is unique, because the wind shear profile reverses with height. It's also unique because the strongest vorticity (which is much stronger than the strongest vorticity in any of the other experiments) is located above the surface. In early experiments, this profile was the only one that consistently produced an MCS, regardless of what modifications were made to upper levels or the v profile. An immediately noticeable difference between this simulation and the unidirectional experiments is that strong positive vorticitythe surface by the downdraft (Fig. 4.36h). This creates a favorable vorticity balance right near the surface, but vertical velocities generated are not strong enough to penetrate the

stable layer (not shown). Waves extend from near the surface deep into the troposphere on the eastern side of the downdraft, but are most amplified in the region of positive shear/vorticity (i.e. downshear). Negative vorticity is present above 1 km, similar to the U25V0 run, but is larger in magnitude than the shear-generated vorticity in the same layer. At later times, more complex structures with multiple wave crests develop, and it is not clear why (Fig. 4.34). Unlike other runs, near surface waves remain tied to the elevated waves. This may actually be a function of the favorable environment for wave trapping, and may help bring updrafts closer to the surface.

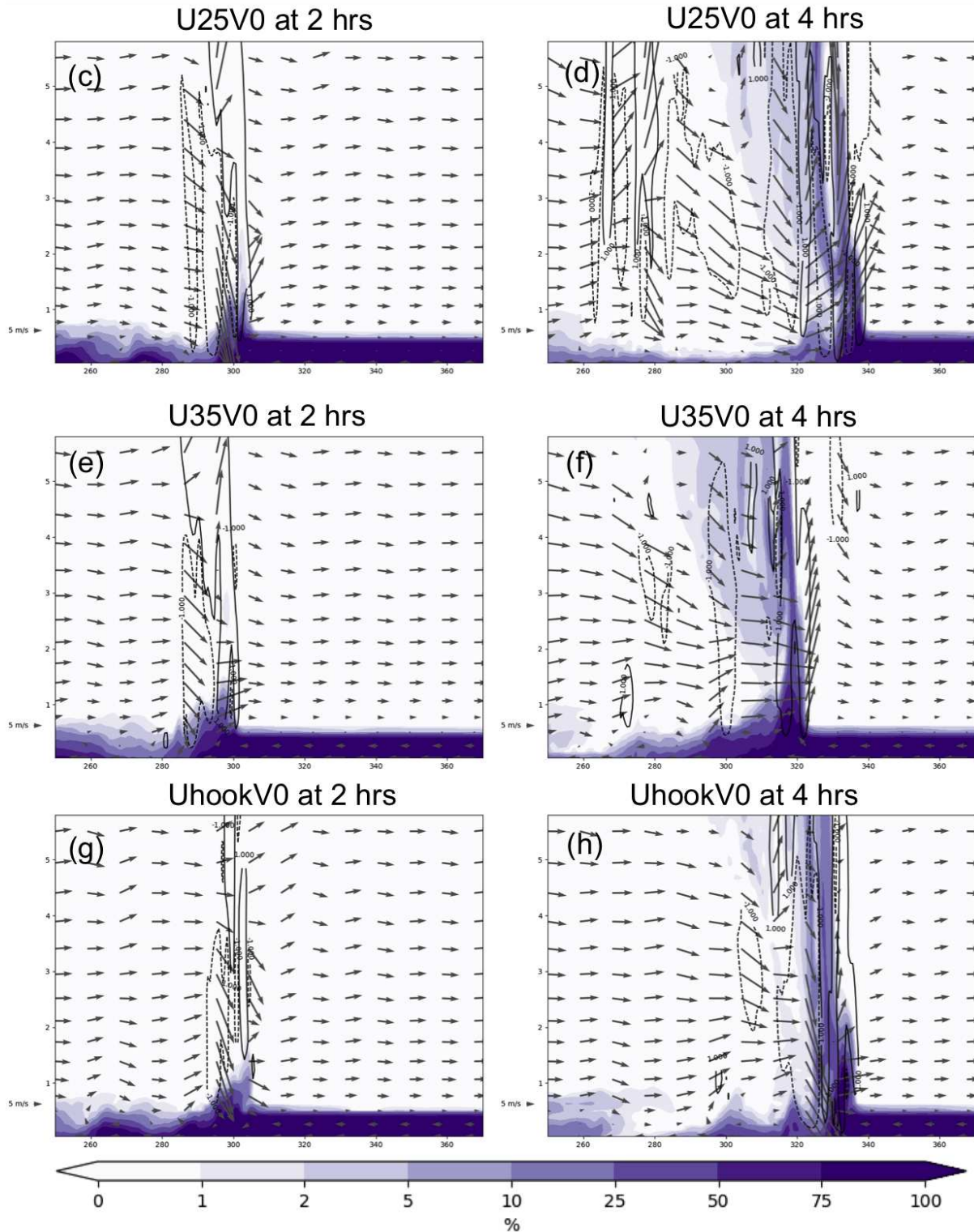


FIG. 4.37. Passive tracer % of initial concentration after (a,c,e) 2 hours and (b,d,f) 4 hours for (a,b) U25V0, (c,d) U35V0, and (e,f) UhookV0 runs.

Early in the three MCS-producing simulations, W-E cross sections of passive tracer concentration show that very little of the passive tracer initiated below 500 m is lofted into updrafts (Fig. 4.37a,c,e). After 4 hours, passive tracer concentrations in updrafts exceed 25% of the concentration initialized in the lowest 500 m. This occurs even though two of the three runs had not yet produced a cold pool (Fig 4.37b,d,f) at this time. This along with the discussion above suggest that storms are initially elevated, but as they mature, are able to draw inflow from the stable layer. This may be possible because even when they are not strong enough to reach the surface, downdrafts help to deepen supporting wave structures/generate waves at lower levels. In an *effective* layer framework, generation of waves at lower levels modifies the relevant shear layer and the resulting effective inflow layer. This may help updrafts tap into an additional source of CAPE, resulting in more intense convection, and consequently stronger downdrafts. Some form of gradual transition like the one described may help to explain why all three simulations eventually produce surface cold pools, and the lofting of tracer at later times. This said, at 4 hours, large concentrations of tracer behind updrafts make it clear that not all of the near surface air is lifted.

#### 4.4 SUMMARY OF RESULTS

In this work, a number of simulations were run to explore the interaction of downdrafts and a strong stable layer under sheared and unsheared conditions in 2 and 3 dimensions. In the first series of experiments, the goal was to understand the behavior of a simple cold bubble dropped from above a stable boundary layer in a dry 2D environment. Sensitivity to the strength of the  $-\theta'$  was used as a proxy to modifying the stable layer itself, since the stable layer can not be modified without also modifying moisture and winds in this case. Sensitivity of the representation of this interaction to horizontal and vertical grid spacing was also explored. In the second series of experiments, individual components of a control wind profile were isolated, starting with the LLJ, and increasing in complexity, until the full 3D wind profile was represented. The control wind profile was a smoothed version of the sounding used in detailed analysis presented in Chapter 3 from 0428 UTC 25 June 2015. On that day, the observed MCS had both forward-propagating convection and ROD, and simulations produce an MCS with ROD nearly identical to the one analyzed in Chapter 3 initialized with a less idealized sounding. The goal for the set of experiments presented in Table 4.2 was to isolate the specific wind characteristics in the control profile that were different from the composite elevated insatiability environment from Chapter 2, to better understand what led to ROD development in this thermodynamic environment. Results of

these runs highlighted that feedbacks between both low-level and deep-layer wind shear and MCS outflow are important. These feedbacks impact MCS organization, motion, and ultimately the processes that support ROD development. Finally, based on results early tests that indicated a strong dependence of convection sustenance on the low-level wind profile, an additional subset of these experiments was designed. Careful modifications to just the low-level u wind profile were made in order to gain deeper understanding of the processes that allowed an MCS to grow upscale from a single warm bubble in this idealized environment.

A combination of experiments presented here, the results of Chapter 3, and existing literature, suggest 4 primary scenarios for ROD development. 1) The gradual lifting of parcels by a cold pool for some distance behind the southwest gust front boundary when they are unable to reach their LFCs at its leading edge (Peters and Schumacher 2015b). 2) A similar process to that described above, but rather than a cold pool, initially a bore is responsible for the gradual lifting. In this case, parcels are lifted the final distance to their LFCs when they reach the density current (Blake et al. 2017). Here, the density current itself might lift parcels, or generate perturbations in isentropes in the 1-2 km layer above it (if it is shallow). 3) Similar to the previous process, parcels encounter a bore (or wave) at the southwest gust front and are lifted. However, parcels descend a great distance before being lifted to their LFCs by either a density current itself, or by perturbations in isentropes between 1 and 2 km generated by the density current. This might occur in cases where the bore moves much more rapidly than the density current; parcels have the time to descend after the passage of the bore and before they reach the density current. 4) In the absence of a density current at the surface, the intrusion of convective outflow into the stable layer generates deep waves (much like a density current) capable of sustaining convection. Waves may experience additional support through amplification in favorable shear layers (discussed in Chapter 3).

A summary of additional major findings from all three sets of experiments is as follows:

- Dry cold bubble experiments produce very similar structures to downdrafts generated in moist warm bubble experiments. This result reduces concern about the strong ties between convection maintenance by wave and the wave generated by the initial warm bubble discussed in (Schmidt and Cotton 1990)
- A  $-24\text{ K } \theta'$  was necessary to generate a density current in this thermodynamic environment.
- The general wave structures between 2D runs with lower and higher horizontal and vertical resolution are consistent, but a reduction in downshear wave amplification is noted.

- On average, updraft bases become closer to the surface and maximum updraft speeds become stronger on average during the first three hours and then approach a quasi-steady state.
- On average, downdrafts rapidly reach closer to the surface during the first hour, and the strongest downdrafts become stronger over time in experiments with upper-level winds.
- Cases with only low-level winds take on characteristics of TS MCSs and bow-echos, while cases with upper-level winds take on characteristics of LS MCSs.
- Both the LLJ and mid-upper-level winds impact the MCS propagation and organization.
- ROD develops in the case with only a 3D LLJ, but is supported by mechanisms more like Peters and Schumacher (2015b) and Blake et al. (2017) than the CTRL run.
- The simulation with strong upper-level jet in the absence of the 5 km wind maximum was the only run with a 3D wind profile in the original set of experiments unable to produce ROD. This suggests that the 5 km wind maximum may somehow act to balance or oppose the effects of the strong upper-level jet, but its unclear how.
- In cases with sustained ROD, parcels come primarily from south-southwest of the MCS.
- In the UujVuj case without ROD, parcels with similar trajectories encounter a number of oscillations in the wake region at the top of the elevated layer of  $\theta$  deficits, but none is sufficient to lift parcels to their LFCs.
- Other simulations with only one component of the upper-level jet were able to develop ROD in the absence of the 5 km wind maximum.
- The success of upscale growth from a single cell to an MCS in an idealized homogeneous environment with a strong stable layer is dependent on the magnitude of the low-level wind shear. When shear is too weak, waves are not amplified sufficiently to generate new convection. This is likely also dependent on the shear in the layer where waves are generated.
- It may be possible to make an RKW-like vorticity balance argument for waves, but is conceptually less elegant, at least in the manner presented here.

The successful development of ROD is determined by a combination of factors including: density current- stable layer interactions, the effects of both low-level and deep-layer shear on density current dynamics, the effects of vertical wind shear on wave trapping, amplification, and motion, as well as a other potential factors not yet considered. A significant amount of research on each of these individual processes is still necessary in order to better understand nocturnal MCSs.

## CHAPTER 5

### SUMMARY OF FINDINGS

This work represents the summary of three studies that ultimately aim to improve the understanding of nocturnal MCS environments, and the complex interactions between convective outflow, a stable boundary layer, and wind shear that govern the motion, support, and organization of MCSs in this environment. This improved understanding will eventually lead to better human and model forecasts for these types of events. The research presented was motivated by a combination of past research on the subject, the poor forecast skill and number of remaining unanswered questions about nocturnal convection, and experiences and observations made during the Plains Elevated Convection at Night field campaign.

In chapter 2, analysis of radiosonde observations in pre-convective environments found that only about half of the PECAN MCS cases had the classic profile elevated layer of high  $\theta_e$  air associated with moisture advection by the nocturnal LLJ. Instead, a large number of soundings had a potentially neutral environment below 2-3 km, even well after dark. In cases with an elevated  $\theta_e$  maximum, advection of warm, moist air by the LLJ rapidly lead to a more favorable environment, while in potentially neutral cases that also had a strong low-level jet, lower elevated moisture levels and a weak gradient lead to minimal advection and almost no observable thermodynamic change in time. Nearly all pre-convective soundings had near surface stable layers, but the strength and depth were highly variable not just between cases, but also within individual cases. In every case, differences between pre- and post-convective soundings suggest the presence of a cold pool at the surface regardless of the boundary layer stability. However, the degree and depth of observed  $-\theta'_s$  is highly variable, and in several cases the largest magnitude  $\theta'_s$  were observed in an elevated layer. Despite the large variations in both stable layer characteristics and post-convective thermodynamic profiles, there is an apparent relationship between the stable layer characteristics and the depth at which cooling is maximized. Stronger, deeper stable layers lead to larger  $-\theta'_s$  in an elevated layer. This could be simply that the warm air at the top of the stable layer is the first thing the downdraft will interact with, and so cools it rapidly, but experiences a reduction in its relative negative buoyancy (both through mixing, and the decrease in  $\theta$  towards the surface) as it descends further. It could also be evidence of layer lifting by a density-current-driven bore (since their is still cooling at the surface) where the density current moves at the same speed as the bore.

Interpretation of results from this chapter are generally limited by the where and when we had observations of MCSs, the timing of those events, and the regions where MCSs formed. Additional work to connect observed environment clusters to measures of MCS intensity, organization, or other properties as well as the larger environment would be worthwhile. This work could also be expanded to use other types of observations from PECAN, observations from other field campaigns, or in a comparison to operational model environments. There is still much that can be learned from these as well as the numerous other observations gathered during PECAN, but this analysis presents a number of insights about nocturnal MCS environments before and after the passage of convection based on radiosonde observations.

In chapter 3, a simulation with horizontally homogeneous initial conditions based on an environmental sounding from shortly before the passage of an MCS observed during PECAN, and initialized by a warm bubble developed into a ‘bow-and-arrow’ MCS with a forward-propagating leading line and ROD. Much of the leading line was associated with some form of bore, and the largest  $\theta$  deficits were observed in an elevated layer, much like post-convective observations in some PECAN cases discussed in Chapter 2. As they impact the stable layer, downdrafts generate a variety of wave structures that are amplified downshear as shown in (Schmidt and Cotton 1989). The amplification may have some layer dependency (in the same fashion as the layered approach to RKW discussed in (French and Parker 2010), where relevant layers are determined by the sign of the shear. In an environment where downdrafts are more buoyant than air near the surface, they may continue past their equilibrium level (like an over shooting top), and have a warming effect at the surface. The ubiquitousness and magnitude of warming is not observed real environments, likely due to other processes that have a simultaneous cooling effect in real environments. Where downdraft air settles in a layer of similar density in the form of an intrusion, it moves downstream. Analysis of updraft base heights and lofting of parcels below 500 m showed that even in a homogeneous simulation along the same outflow boundary, updrafts may draw inflow from different layers depending on the interaction of the outflow generated and environmental wind shear. Updrafts were nearest to the surface along convection to the south, and became progressively more elevated to the north along the leading line. Finally, ROD updrafts were nearly completely elevated, drawing inflow from a layer above 1 km. Updrafts appear to be supported by an amplified wave structure that remains tied to the convection by wind shear the inflow layer.

In chapter 4, 2D experiments explored the interactions of a dry cold bubble with a stable layer, and 3D experiments explored both the generation of ROD and the sensitivity of MCS development in

a stable environment to low-level shear under a variety of shear conditions. In 2D experiments, cold bubbles needed very large  $\theta'$ s to generate anything that resembled a density current at the surface. This departure from realistic  $\theta'$ s highlights the importance of moist processes in cold pool production. In 3D experiments, ROD develops in runs with only low-level shear and with various configurations of mid-to-upper-level winds, and associated with TS MCSs that have expansive cold pools and RIJs and LS MCSs that have weak cold pools confined to only a portion of the leading line. Despite this, a common theme emerges for parcels that reach ROD updrafts. Parcels begin to the southwest of the MCS and encounter a bore (in these runs) at the southwest gust front boundary that is not deep enough to lift parcels to their LFCs. Then some distance behind the leading edge of the bore, parcels encounter perturbations in the isentropes between 1 and 2 km (or deeper) and are lifted to their LFCs. The primary differences that arise are tied to the existence (or lack thereof) of cold pool air at the surface below perturbations aloft at the location where parcels experience their final ascent, and whether or not parcels are permanently lifted by the bore ahead of the ROD updrafts. Based on the results of Chapter 2, in the former, in instances with no cold pool, waves may be supported by favorable wind shear, and the convective outflow itself in the form of an intrusion even when a cold pool does not reach the surface. The latter depends on the relative locations of early convective outflow and the bore that it generates, and is probably dependent on their relative strengths, speeds, and direction of motion. Both differences appear to be closely tied to 3D vertical windshear profile. In the run with no ROD, a strong northwesterly jet and no opposing 5 km wind maximum lead to stronger updrafts along the southern edge of the leading line, and an orientation less conducive to long-lived waves along the southwest boundary. Wake region waves encountered by parcels approaching from the south were largest along the outflow boundary but weaker behind, so parcels that reached this region without encountering leading convection did not encounter waves deep enough to help them reach their LFCs. Finally, convective cells initiated in an environment with moderate and strong unidirectional low-level shear are able to grow upscale into MCSs through shear amplification of the supporting elevated wave. An environment with a shear reversal with height (hook) and strong shear in the 0.5 to 1 km layer was also able to generate an MCS. Even though the thermodynamic environment used in the experiments presented in this chapter had the strongest observed stability during PECAN, the leading convective lines all lifted parcels from a layer below 500 m, well below the top of the stable layer in this case, to upper levels. The extent of this, and observed height of  $5 \text{ m s}^{-1}$  updraft bases varied widely along the leading line indicating along-line

heterogeneity in the layer lifted despite the homogeneous initial conditions. In the region of ROD, updrafts were consistently elevated, drawing inflow from above 1 km. These differences in updraft base and surface parcel lifting also coincide with observations of different lifting mechanisms in different regions of the convection. So not only are MCSs maintained by different processes in different environments depending on the interaction of low-level stability and shear that impact the effective inflow layer and energy available to convective updrafts, but in environments with strong turning of the winds with height, a single MCS may be maintained by different processes that effectively tap into the available energy in different layers in different regions of the MCS. Furthermore, 3D simulations of MCSs presented here all begin elevated, but as they mature, are able to lift more stable boundary layer air. The rate at which they mature appears dependent on the vertical wind shear, but in all runs, measures of intensity and updraft base indicate that MCSs eventually reach a steady state after 1-3 hours.

Analysis of observations of pre-convective nocturnal MCS environments showed that in some cases, the most unstable parcel is not necessarily elevated, even when the boundary layer is stable. At the same time, even MCSs simulated with the most stable boundary layer observed were able to lift parcels from the stable layer in some portions of the storm in a variety of shear environments. Furthermore, in observations of post-convective MCS environments every case had some near surface cooling, and while this was variable, many MCSs still had strong, deep cold pools despite their nocturnal nature. This evidence all provides strong support for more recent proposals that nocturnal convection is often not decoupled from the boundary layer as previously thought. While simulations here were performed in homogeneous environments that ignore many time and space dependent processes, the degree to which convection is elevated depends not only on the environment, but mesoscale feedbacks in different regions within an individual MCS. In chapters 3 and 4, convection was more elevated along northern portions of the leading line in several simulations. In an environment with a quasi-stationary frontal zone where temperatures decrease to the north, this could become even more pronounced if convection remains tied to the frontal zone. While not discussed in this work, moisture gradients have also been shown to impact MCS placement and propagation Peters et al. (2017), and could further enhance along line heterogeneities and impact processes that affect ROD development.

While observed post-convective environments all had near surface cooling, in several cases with stronger, deeper stable layers the largest decrease in  $\theta_v$  behind the leading line was observed in an elevated layer. In simulations with the strongest, deepest stable layer post gust front cooling in an elevated layer was attributed to both the semi-permanent increase in the height of isentropes associated with

bore passage, and the presence of outflow air in an elevated layer in the form of an intrusion in different regions of the MCS. Dry 2D soundings with rather unrealistic cold pool strengths were able to reproduce the same structures observed in the 3D environment, and pseudo-soundings taken through those features look much like observed post-convective soundings.

Analysis of ROD in a strongly stable environment based on a specific PECAN case, and with a variety of vertical wind shear profiles lead to an expansion of the theory developed in Peters and Schumacher (2015b). In a stable boundary layer, with strong low-level wind shear and a layer of shear reversal, early convective outflow generates a bore that propagates more quickly to the south than the outflow itself. In the case where a density current does reach the ground, it remains well north of the leading bore edge (likely due to its relatively weak strength and strong southerly shear), but generates perturbations in the isentropes in the 1-2 km layer that aid in lifting parcels to their LFCs. In the case where a density current does not reach the ground, based on 2D and 3D simulations, the bulk of the convective outflow propagates to the north in an elevated layer, but a combination of convective outflow and waves generated as it penetrates the stable layer appear to generate a similar wave feature in the 1-2 km layer, that again helps lift parcels to their LFCs. Whether or not parcels descend after the passage of the bore is dependent on how permanent the increase in isentropes heights are, and how far offset from the leading edge of the bore ROD is. Expansion of this analysis to more realistic runs, and identification and analysis of cases where these processes might occur would provide further support for this theory. Further analyses of wave processes could also help to more concretely identify the structure responsible for lifting ROD parcels as a wave (particularly where a cold pool is absent). Additionally, only a selection of sensitivities to the existence or absence of larger features was explored, but controlled studies of the direction/magnitude of individual features could prove worthwhile.

While not included here, studies that explore the impact of the strength and depth of the stable layer on the resulting MCS will also still be worthwhile. Some of this work is still on-going in collaboration with a post-doctoral researcher at the University of Washington. Given the sensitivity of MCSs to stable layer characteristics, and the large variability in observed stable layers even with single case, there would be significant value in future studies that aim to map the spatial and temporal heterogeneities of low-level stability on a larger scale, and to better understand the abundance of processes that lead to its development. At the same time, the on-going work by other researchers using the PECAN data set to better understand the spatial and temporal variabilities and dynamics of the LLJ, is important. Finally, it's clear that MCSs are sensitive to 3-dimensional shear over a deep layer, but there is still much

to be learned to this end. Fundamentally, MCSs are impacted by everything from the larger scale circulation to representation of precipitation in microphysics schemes, but nocturnal MCSs have the added factor of the nocturnal boundary layer, where not only is the relationship of the low-level wind shear to convective outflow important, but feedbacks exist between these processes and the larger scale environment throughout the depth of the troposphere and are highly 3 dimensional. The scope of the nocturnal MCS problem is enormous, and while there is much work to be done, this dissertation both provides new insights and identifies new challenges to understanding nocturnal MCSs.

## REFERENCES

- Alfaro, D. A., and M. C. Coniglio, 2018: Discrimination of mature and dissipating severe-wind-producing MCSs with layer-lifting indices. *Wea. Forecasting*, **33**, 3–21, doi: <https://doi.org/10.1175/WAF-D-17-0088.1>.
- Augustine, J. A., and F. Caracena, 1994: Lower-tropospheric precursors to nocturnal MCS development over the central United States. *Wea. Forecasting*, **9**, 116–135, doi: [https://doi.org/10.1175/1520-0434\(1994\)009<0116:LTPTNM>2.0.CO;2](https://doi.org/10.1175/1520-0434(1994)009<0116:LTPTNM>2.0.CO;2).
- Benjamin, S. G., and Coauthors, 2016: A North American hourly assimilation and model forecast cycle: the Rapid Refresh. *Mon. Wea. Rev.*, **144**, 1669–1694, doi: [10.1175/MWR-D-15-0242.1](https://doi.org/10.1175/MWR-D-15-0242.1).
- Billings, J. M., and M. D. Parker, 2012: Evolution and maintenance of the 22–23 June 2003 nocturnal convection during BAMEX. *Wea. Forecasting*, **27**, 279–300, doi: [10.1175/WAF-D-11-00056.1](https://doi.org/10.1175/WAF-D-11-00056.1).
- Blake, B. T., D. B. Parsons, K. R. Haghi, and S. G. Castleberry, 2017: The structure, evolution, and dynamics of a nocturnal convective system simulated using the wrf-arw model. *Mon. Wea. Rev.*, **145**, 3179–3201.
- Bosart, L. E., and J. P. Cussen Jr, 1973: Gravity wave phenomena accompanying east coast cyclogenesis. *Mon. Wea. Rev.*, **101**, 446–454.
- Bryan, G. H., and J. M. Fritsch, 2000: Moist absolute instability: The sixth static stability state. *Bull. Amer. Meteor. Soc.*, **81**, 1207–1230, doi: [https://doi.org/10.1175/1520-0477\(2000\)081<1287:MAITSS>2.3.CO;2](https://doi.org/10.1175/1520-0477(2000)081<1287:MAITSS>2.3.CO;2).
- Bryan, G. H., and J. M. Fritsch, 2002: A benchmark simulation for moist nonhydrostatic numerical models. *Mon. Wea. Rev.*, **130**, 2917–2928.
- Carbone, R. E., J. W. Conway, N. A. Crook, and M. W. Moncrieff, 1990: The generation and propagation of a nocturnal squall line. Part I: Observations and implications for mesoscale predictability. *Mon. Wea. Rev.*, **118**, 26–49, doi: [https://doi.org/10.1175/1520-0493\(1990\)118<0026:TGAPOA>2.0.CO;2](https://doi.org/10.1175/1520-0493(1990)118<0026:TGAPOA>2.0.CO;2).
- Carbone, R. E., J. D. Tuttle, D. A. Ahijevych, and S. B. Trier, 2002: Inferences of predictability associated with warm season precipitation episodes. *J. Atmos. Sci.*, **59**, 2033–2056, doi: [https://doi.org/10.1175/1520-0469\(2002\)059<2033:IOPAWW>2.0.CO;2](https://doi.org/10.1175/1520-0469(2002)059<2033:IOPAWW>2.0.CO;2).
- Chappell, C. F., 1986: Quasi-stationary convective events. *Mesoscale Meteorology and Forecasting*, P. S. Ray, Ed., Amer. Meteor. Soc., 289–309.
- Clark, A. J., W. A. Gallus, Jr, and T.-C. Chen, 2007: Comparison of the diurnal precipitation cycle in convection-resolving and non-convection-resolving mesoscale models. *Mon. Wea. Rev.*, **135**, 3456–3473, doi: <https://doi.org/10.1175/MWR3467.1>.
- Clark, R., 2016: FP3 Ellis, KS Radiosonde Data. Version 2.0. UCAR/NCAR - Earth Observing Laboratory. Accessed: 22 Sept 2016, <https://doi.org/10.5065/D6GM85DZ>.
- Coffer, B. E., and M. D. Parker, 2015: Impacts of increasing low-level shear on supercells during the early evening transition. *Mon. Wea. Rev.*, **143**, 1945–1969.
- Coniglio, M. C., D. J. Stensrud, and L. J. Wicker, 2006: Effects of upper-level shear on the structure and maintenance of strong quasi-linear mesoscale convective systems. *J. Atmos. Sci.*, **63**, 1231–1252.

- Corfidi, S. E., 2003: Cold pools and MCS propagation: Forecasting the motion of downwind-developing MCSs. *Wea. Forecasting*, **18**, 997–1017, doi: [https://doi.org/10.1175/1520-0434\(2003\)018<0997:CPAMPF>2.0.CO;2](https://doi.org/10.1175/1520-0434(2003)018<0997:CPAMPF>2.0.CO;2).
- Corfidi, S. E., S. J. Corfidi, and D. M. Schultz, 2008: Elevated convection and castellanus: Ambiguities, significance, and questions. *Wea. Forecasting*, **23**, 1280–1303, doi: <https://doi.org/10.1175/2008WAF2222118.1>.
- Corfidi, S. E., J. H. Merritt, and J. M. Fritsch, 1996: Predicting the movement of mesoscale convective complexes. *Wea. Forecasting*, **11**, 41–46, doi: [https://doi.org/10.1175/1520-0434\(1996\)011<0041:PTMOMC>2.0.CO;2](https://doi.org/10.1175/1520-0434(1996)011<0041:PTMOMC>2.0.CO;2).
- Correia, J., J., and R. W. Arritt, 2008: Thermodynamic properties of mesoscale convective systems observed during BAMEX. *Mon. Wea. Rev.*, **136**, 4242–4271, doi: <https://doi.org/10.1175/2008MWR2284.1>.
- Crook, N. A., 1988: Trapping of low-level gravity waves. *J. Atmos. Sci.*, **45**, 1533–1541, doi: [https://doi.org/10.1175/1520-0469\(1988\)045<1533:TOLLIG>2.0.CO;2](https://doi.org/10.1175/1520-0469(1988)045<1533:TOLLIG>2.0.CO;2).
- Crook, N. A., and M. W. Moncrieff, 1988: The effect of large-scale convergence on the generation and maintenance of deep moist convection. *J. Atmos. Sci.*, **45**, 3606–3624, doi: [https://doi.org/10.1175/1520-0469\(1988\)045<3606:TEOLSC>2.0.CO;2](https://doi.org/10.1175/1520-0469(1988)045<3606:TEOLSC>2.0.CO;2).
- Cunning, J. B., 1986: The Oklahoma-Kansas. Preliminary Regional Experiment for STORM-Central. *Bull. Amer. Meteor. Soc.*, **67**, 1478–1486, doi: [https://doi.org/10.1175/1520-0477\(1986\)067<1478:TOKPRE>2.0.CO;2](https://doi.org/10.1175/1520-0477(1986)067<1478:TOKPRE>2.0.CO;2).
- Davis, C., and Coauthors, 2004: The Bow Echo and MCV Experiment: Observations and opportunities. *Bull. Amer. Meteor. Soc.*, **85**, 1075–1093, doi: <https://doi.org/10.1175/BAMS-85-8-1075>.
- Davis, C. A., K. W. Manning, R. E. Carbone, S. B. Trier, and J. D. Tuttle, 2003: Coherence of warm-season continental rainfall in numerical weather prediction models. *Mon. Wea. Rev.*, **131**, 2667–2679, doi: [https://doi.org/10.1175/1520-0493\(2003\)131<2667:COWCRI>2.0.CO;2](https://doi.org/10.1175/1520-0493(2003)131<2667:COWCRI>2.0.CO;2).
- Deardorff, J. W., 1980: Stratocumulus-capped mixed layers derived from a three-dimensional model. *Bound.-Layer Meteor.*, **18**, 495–527.
- Done, J., C. A. Davis, and M. Weisman, 2004: The next generation of NWP: Explicit forecasts of convection using the Weather Research and Forecasting (WRF) model. *Atmos. Sci. Lett.*, **5**, 110–117.
- Doswell, C. A., III, H. E. Brooks, and R. A. Maddox, 1996: Flash flood forecasting: An ingredients-based methodology. *Wea. Forecasting*, **11**, 560–581.
- Ertoz, L., M. Steinbach, and V. Kumar, 2002: A new shared nearest neighbor clustering algorithm and its applications. *Workshop on clustering high dimensional data and its applications at 2nd SIAM international conference on data mining*, 105–115.
- Flynn, M., and P. Linden, 2006: Intrusive gravity currents. *J. Fluid Mech.*, **568**, 193–202.
- Flynn, M. R., and B. R. Sutherland, 2004: Intrusive gravity currents and internal gravity wave generation in stratified fluid. *J. Fluid Mech.*, **514**, 355–383.

- French, A. J., and M. D. Parker, 2008: The initiation and evolution of multiple modes of convection within a meso-alpha-scale region. *Wea. Forecasting*, **23**, 1221–1252, doi: <https://doi.org/10.1175/2008WAF2222136.1>.
- French, A. J., and M. D. Parker, 2010: The response of simulated nocturnal convective systems to a developing low-level jet. *J. Atmos. Sci.*, **67**, 3384–3408, doi: <https://doi.org/10.1175/2010JAS3329.1>.
- Fritsch, J. M., and G. S. Forbes, 2001: Mesoscale convective systems. *Severe Convective Storms*, 50, Amer. Meteor. Soc., Boston, MA, 323–357.
- Fritsch, J. M., R. J. Kane, and C. R. Chelius, 1986: The contribution of mesoscale convective weather systems to the warm-season precipitation in the United States. *J. Appl. Meteor.*, **25**, 1333–1345.
- Geerts, B., and Coauthors, 2017: The 2015 Plains Elevated Convection At Night (PECAN) field project. *Bull. Amer. Meteor. Soc.*, **98**, 767–786, doi: [10.1175/BAMS-D-15-00257.1](https://doi.org/10.1175/BAMS-D-15-00257.1).
- Haertel, P. T., R. H. Johnson, and S. N. Tulich, 2001: Some simple simulations of thunderstorm outflows. *J. Atmos. Sci.*, **58**, 504–516, doi: [https://doi.org/10.1175/1520-0469\(2001\)058<0504:SSSOTO>2.0.CO;2](https://doi.org/10.1175/1520-0469(2001)058<0504:SSSOTO>2.0.CO;2).
- Haghi, K. R., D. B. Parsons, and A. Shapiro, 2017: Bores observed during IHOP\_2002: The relationship of bores to the nocturnal environment. *Mon. Wea. Rev.*, **145**, 3929–3946, doi: <https://doi.org/10.1175/MWR-D-16-0415.1>.
- Herman, G. R., and R. S. Schumacher, 2018: Money doesn't grow on trees, but forecasts do: Forecasting extreme precipitation with random forests. *Mon. Wea. Rev.*, **146**, 1571–1600, doi: [10.1175/MWR-D-17-0250.1](https://doi.org/10.1175/MWR-D-17-0250.1).
- Hewson, E., 1937: The application of wet-bulb potential temperature to air mass analysis. III rainfall in depressions. *Quart. J. Roy. Meteor. Soc.*, **63**, 323–338, doi: <https://doi.org/10.1002/qj.49706327105>.
- Holdridge, D., and D. Turner, 2016: FP6 Hesston, KS Radiosonde Data. Version 1.0. UCAR/NCAR - Earth Observing Laboratory. Accessed: 22 Sept 2016, <https://doi.org/10.5065/D6765CD0>.
- Houze, R. A., Jr., 2004: Mesoscale convective systems. *Rev. Geophys.*, **42**, RG4003, doi: [10.1029/2004RG000150](https://doi.org/10.1029/2004RG000150).
- Houze, R. A., Jr., B. F. Smull, and P. Dodge, 1990: Mesoscale organization of springtime rainstorms in Oklahoma. *Mon. Wea. Rev.*, **118**, 613–654.
- Jirak, I. L., W. R. Cotton, and R. L. McAnelly, 2003: Satellite and radar survey of mesoscale convective system development. *Mon. Wea. Rev.*, **131**, 2428–2449, doi: [https://doi.org/10.1175/1520-0493\(2003\)131<2428:SARSOM>2.0.CO;2](https://doi.org/10.1175/1520-0493(2003)131<2428:SARSOM>2.0.CO;2).
- Johnson, A., and X. Wang, 2012: Object-based evaluation of a storm-scale ensemble during the 2009 NOAA Hazardous Weather Testbed Spring Experiment. *Mon. Wea. Rev.*, **141**, 1079–1098, doi: <https://doi.org/10.1175/MWR-D-12-00140.1>.
- Johnson, A., X. Wang, F. Kong, and M. Xue, 2013: Object-based evaluation of the impact of horizontal grid spacing on convection-allowing forecasts. *Mon. Wea. Rev.*, **141**, 3413–3425, doi: <https://doi.org/10.1175/MWR-D-13-00027.1>.

- Kain, J. S., and Coauthors, 2013: A feasibility study for probabilistic convection initiation forecasts based on explicit numerical guidance. *Bull. Amer. Meteor. Soc.*, **94**, 1213–1225.
- Keene, K. M., and R. S. Schumacher, 2013: The bow and arrow mesoscale convective structure. *Mon. Wea. Rev.*, **141**, 1648–1672, doi: 10.1175/MWR-D-12-00172.1.
- Kincer, J. B., 1916: Daytime and nighttime precipitation and their economic significance. *Mon. Wea. Rev.*, **44**, 628–633.
- Klein, P. M., D. D. Turner, E. N. Smith, and J. Gebauer, 2016: Mobile PISA 1 OU/NSSL CLAMPS Radiosonde Data. Version 1.0. UCAR/NCAR - Earth Observing Laboratory. Accessed: 22 Sept 2016, <https://doi.org/10.5065/D6416VDH>.
- Klemp, J. B., and R. B. Wilhelmson, 1978: The simulation of three-dimensional convective storm dynamics. *J. Atmos. Sci.*, **35**, 1070–1096.
- Knupp, K., 2015: Mobile PISA 2 UAH MIPS Radiosonde Data. Version 1.0. UCAR/NCAR - Earth Observing Laboratory. Accessed: 22 Sept 2016, <https://doi.org/10.5065/D6MC8X3V>.
- Koch, S. E., C. Flamant, J. W. Wilson, B. M. Gentry, and B. D. Jamison, 2008: An atmospheric soliton observed with doppler radar, differential absorption lidar, and a molecular doppler lidar. *J. Atmos. Oceanic Technol.*, **25**, 1267–1287.
- Koch, S. E., and R. E. Golus, 1988: A mesoscale gravity wave event observed during CCOPE. Part I: Multiscale statistical analysis of wave characteristics. *Mon. Wea. Rev.*, **116**, 2527–2544.
- Laing, A. G., and J. M. Fritsch, 2000: The large scale environments of the global populations of mesoscale convective complexes. *Mon. Wea. Rev.*, **128**, 2756–2776, doi: [https://doi.org/10.1175/1520-0493\(2000\)128<2756:TLSEOT>2.0.CO;2](https://doi.org/10.1175/1520-0493(2000)128<2756:TLSEOT>2.0.CO;2).
- Loftus, A. M., D. B. Weber, and C. A. Doswell, III, 2008: Parameterized mesoscale forcing mechanisms for initiating numerically simulated isolated multicellular convection. *Mon. Wea. Rev.*, **136**, 2408–2421.
- Lombardo, K., and T. Kading, 2018: The behavior of squall lines in horizontally heterogeneous coastal environments. *J. Atmos. Sci.*, **75**, 1243–1269.
- Maddox, R. A., 1980: Mesoscale convective complexes. *Bull. Amer. Meteor. Soc.*, **61**, 1374–1387, doi: [https://doi.org/10.1175/1520-0477\(1980\)061<1374:MCC>2.0.CO;2](https://doi.org/10.1175/1520-0477(1980)061<1374:MCC>2.0.CO;2).
- Maddox, R. A., 1983: Large scale meteorological conditions associated with midlatitude mesoscale convective complexes. *Mon. Wea. Rev.*, **111**, 1475–1493.
- Maddox, R. A., F. Canova, and L. R. Hoxit, 1980: Meteorological characteristics of flash flood events over the western United States. *Mon. Wea. Rev.*, **108**, 1866–1877.
- Maddox, R. A., C. F. Chappell, and L. R. Hoxit, 1979: Synoptic and meso- $\alpha$  scale aspects of flash flood events. *Bull. Amer. Meteor. Soc.*, **60**, 115–123.
- Maddox, R. A., L. R. Hoxit, C. F. Chappell, and F. Caracena, 1978: Comparison of meteorological aspects of the Big Thompson and Rapid City flash floods. *Mon. Wea. Rev.*, **106**, 375–389, doi: [https://doi.org/10.1175/1520-0493\(1978\)106<0375:COMAOT>2.0.CO;2](https://doi.org/10.1175/1520-0493(1978)106<0375:COMAOT>2.0.CO;2).

- Markowski, P., and Y. Richardson, 2010: *Mesoscale Meteorology in Midlatitudes*. Wiley-Blackwell, 142 pp.
- Marshall, J. H., K. A. Browning, J. C. Nicol, D. J. Parker, E. G. Norton, A. M. Blyth, U. Corsmeier, and F. M. Perry, 2010: Multi-sensor observations of a wave beneath an impacting rear-inflow jet in an elevated mesoscale convective system. *Quart. J. Roy. Meteor. Soc.*, **136**, 1788–1812, doi: <https://doi.org/10.1002/qj.669>.
- Moncrieff, M. W., 1992: Organized convective systems: Archetypal dynamical models, mass and momentum flux theory, and parameterization. *Quart. J. Roy. Meteor. Soc.*, **118**, 819–850, doi: <https://doi.org/10.1002/qj.49711850703>.
- Moncrieff, M. W., and C. Liu, 1999: Convective initiation by density currents: Role of convergence, shear, and dynamical organization. *Mon. Wea. Rev.*, **127**, 2455–2464.
- Moore, J. T., F. H. Glass, C. E. Graves, S. M. Rochette, and M. J. Singer, 2003: The environment of warm-season elevated thunderstorms associated with heavy rainfall over the central United States. *Wea. Forecasting*, **18**, 861–878, doi: [https://doi.org/10.1175/1520-0434\(2003\)018<0861:TEOWET>2.0.CO;2](https://doi.org/10.1175/1520-0434(2003)018<0861:TEOWET>2.0.CO;2).
- Morrison, H., J. A. Curry, and V. I. Khvorostyanov, 2005: A new double-moment microphysics parameterization for application in cloud and climate models. Part I: Description. *J. Atmos. Sci.*, **62**, 1665–1677.
- Naylor, J., M. S. Gilmore, R. L. Thompson, R. Edwards, and R. B. Wilhelmson, 2012: Comparison of objective supercell identification techniques using an idealized cloud model. *Mon. Wea. Rev.*, **140**, 2090–2102.
- North, G. R., T. L. Bell, R. F. Cahalan, and F. J. Moeng, 1982: Sampling errors in the estimation of empirical orthogonal functions. *Mon. Wea. Rev.*, **110**, 699–706.
- Parker, M. D., 2008: Response of simulated squall lines to low-level cooling. *J. Atmos. Sci.*, **65**, 1323–1341, doi: [10.1175/2007JAS2507.1](https://doi.org/10.1175/2007JAS2507.1).
- Parker, M. D., and R. H. Johnson, 2000: Organizational modes of midlatitude mesoscale convective systems. *Mon. Wea. Rev.*, **128**, 3413–3436, doi: [https://doi.org/10.1175/1520-0493\(2001\)129<3413:OMOMMC>2.0.CO;2](https://doi.org/10.1175/1520-0493(2001)129<3413:OMOMMC>2.0.CO;2).
- Parker, M. D., and R. H. Johnson, 2004a: Simulated convective lines with leading precipitation. Part I: Governing dynamics. *J. Atmos. Sci.*, **61**, 1637–1655.
- Parker, M. D., and R. H. Johnson, 2004b: Simulated convective lines with leading precipitation. Part II: Evolution and maintenance. *J. Atmos. Sci.*, **61**, 1656–1673.
- Parker, M. D., and R. H. Johnson, 2004c: Structures and dynamics of quasi-2D mesoscale convective systems. *J. Atmos. Sci.*, **61**, 545–567.
- Parsons, D. B., K. R. Haghi, K. T. Halbert, B. Elmer, and J. Wang, 2018: The potential role of atmospheric bores and gravity waves in the initiation and maintenance of nocturnal convection over the southern great plains. *J. Atmos. Sci.*
- Peters, J. M., E. R. Nielsen, M. D. Parker, S. M. Hitchcock, and R. S. Schumacher, 2017: The impact of low-level moisture errors on model forecasts of an MCS observed during PECAN. *Mon. Wea. Rev.*,

- 145**, 3599–3624, doi: 10.1175/MWR-D-16-0296.1.
- Peters, J. M., and R. S. Schumacher, 2014: Objective categorization of heavy-rain-producing MCS synoptic types by rotated principal component analysis. *Mon. Wea. Rev.*, **142**, 1716–1737, doi: 10.1175/MWR-D-13-00295.1.
- Peters, J. M., and R. S. Schumacher, 2015a: Mechanisms for organization and echo training in a flash-flood-producing mesoscale convective system. *Mon. Wea. Rev.*, **143**, 1058–1085, doi: 10.1175/MWR-D-14-00070.1.
- Peters, J. M., and R. S. Schumacher, 2015b: The simulated structure and evolution of a quasi-idealized warm season convective system with a training convective line. *J. Atmos. Sci.*, **72**, 1987–2010, doi: 10.1175/JAS-D-14-0215.1.
- Peters, J. M., and R. S. Schumacher, 2016: Dynamics governing a simulated mesoscale convective system with a training convective line. *J. Atmos. Sci.*, **73**, 2643–2664, doi: 10.1175/JAS-D-15-0199.1.
- Pinto, J. O., J. A. Grim, and M. Steiner, 2015: Assessment of the high-resolution rapid refresh model's ability to predict mesoscale convective systems using object-based evaluation. *Wea. Forecasting*, **30**, 892–913.
- Raymond, D. J., and R. Rotunno, 1989: Response of a stably stratified flow to cooling. *J. Atmos. Sci.*, **46**, 2830–2837, doi: [https://doi.org/10.1175/1520-0469\(1989\)046<2830:ROASSF>2.0.CO;2](https://doi.org/10.1175/1520-0469(1989)046<2830:ROASSF>2.0.CO;2).
- Rodwell, M. J., and Coauthors, 2013: Characteristics of occasional poor medium-range weather forecasts for Europe. *Bull. Amer. Meteor. Soc.*, **94**, 1393–1405.
- Rossby, C.-G., 1932: *Thermodynamics applied to air mass analysis*. Massachusetts Institute of Technology.
- Rottman, J. W., and J. E. Simpson, 1989: The formation of internal bores in the atmosphere: A laboratory model. *Quart. J. Roy. Meteor. Soc.*, **115**, 941–963.
- Rotunno, R., J. B. Klemp, and M. L. Weisman, 1988: A theory for strong, long-lived squall lines. *J. Atmos. Sci.*, **45**, 463–485.
- Schmidt, J. M., and W. R. Cotton, 1989: A High Plains squall line associated with severe surface winds. *J. Atmos. Sci.*, **46**, 281–302.
- Schmidt, J. M., and W. R. Cotton, 1990: Interactions between upper and lower tropospheric gravity waves on squall line structure and maintenance. *J. Atmos. Sci.*, **47**, 1205–1222.
- Schultz, D. M., P. N. Schumacher, and C. A. Doswell, III, 2000: The intricacies of instabilities. *Mon. Wea. Rev.*, **128**, 4143–4148, doi: [https://doi.org/10.1175/1520-0493\(2000\)129<4143:TIOI>2.0.CO;2](https://doi.org/10.1175/1520-0493(2000)129<4143:TIOI>2.0.CO;2).
- Schumacher, A. B., M. DeMaria, and J. A. Knaff, 2009: Objective estimation of the 24-h probability of tropical cyclone formation. *Wea. Forecasting*, **24**, 456–471.
- Schumacher, R. S., 2009: Mechanisms for quasi-stationary behavior in simulated heavy-rain-producing convective systems. *J. Atmos. Sci.*, **66**, 1543–1568, doi: 10.1175/2008JAS2856.1.
- Schumacher, R. S., 2015: Sensitivity of precipitation accumulation in elevated convective systems to small changes in low-level moisture. *J. Atmos. Sci.*, **72**, 2507–2524, doi: 10.1175/JAS-D-14-0389.1.

- Schumacher, R. S., 2017: Heavy rainfall and flash flooding. Oxford University Press.
- Schumacher, R. S., A. J. Clark, M. Xue, and F. Kong, 2013: Factors influencing the development and maintenance of nocturnal heavy-rain-producing convective systems in a storm-scale ensemble. *Mon. Wea. Rev.*, **141**, 2778–2801, doi: 10.1175/MWR-D-12-00239.1.
- Schumacher, R. S., and R. H. Johnson, 2005: Organization and environmental properties of extreme-rain-producing mesoscale convective systems. *Mon. Wea. Rev.*, **133**, 961–976, doi: 10.1175/MWR2899.1.
- Schumacher, R. S., and R. H. Johnson, 2008: Mesoscale processes contributing to extreme rainfall in a midlatitude warm-season flash flood. *Mon. Wea. Rev.*, **136**, 3964–3986, doi: 10.1175/2008MWR2471.1.
- Schumacher, R. S., and R. H. Johnson, 2009: Quasi-stationary, extreme-rain-producing convective systems associated with midlevel cyclonic circulations. *Wea. Forecasting*, **24**, 555–574, doi: <https://doi.org/10.1175/2008WAF2222173.1>.
- Surcel, M., M. Berenguer, and I. Zawadzki, 2004: The diurnal cycle of precipitation from continental radar mosaics and numerical weather prediction models. part i: Methodology and seasonal comparison. *Mon. Wea. Rev.*, **138**, 3084.
- Sutherland, B. R., P. J. Kyba, and M. R. Flynn, 2004: Intrusive gravity currents in two-layer fluids. *J. Fluid Mech.*, **514**, 327–353.
- Sutherland, B. R., and J. R. Munroe, 2014: Intrusions in stratified fluids.
- Trenberth, K. E., A. Dai, R. M. Rasmussen, and D. B. Parsons, 2003: The changing character of precipitation. *Bull. Amer. Meteor. Soc.*, **84**, 1205–1218.
- Trier, S. B., C. A. Davis, D. A. Ahijevych, M. L. Weisman, and G. H. Bryan, 2006: Mechanisms supporting long-lived episodes of propagating nocturnal convection within a 7-day WRF model simulation. *J. Atmos. Sci.*, **63**, 2437–2461, doi: <https://doi.org/10.1175/JAS3768.1>.
- Trier, S. B., C. A. Davis, and J. D. Tuttle, 2000: Long-lived mesoconvective vortices and their environment. Part I: Observations from the central United States during the 1998 warm season. *Mon. Wea. Rev.*, **128**, 3376–3395, doi: 10.1175/1520-0493(2000)128<3376:LLMVAT>2.0.CO;2.
- Trier, S. B., J. H. Marsham, C. A. Davis, and D. A. Ahijevych, 2011: Numerical simulations of the postsunrise reorganization of a nocturnal mesoscale convective system during 13 June IHOP\_2002. *J. Atmos. Sci.*, **68**, 2988–3011, doi: 10.1175/JAS-D-11-0112.1.
- Trier, S. B., and D. B. Parsons, 1993: Evolution of environmental conditions preceding the development of a nocturnal mesoscale convective complex. *Mon. Wea. Rev.*, **121**, 1078–1098, doi: [https://doi.org/10.1175/1520-0493\(1993\)121<1078:EOECPT>2.0.CO;2](https://doi.org/10.1175/1520-0493(1993)121<1078:EOECPT>2.0.CO;2).
- Tuttle, J. D., and C. A. Davis, 2006: Corridors of warm season precipitation in the central United States. *Mon. Wea. Rev.*, **134**, 2297–2317, doi: <https://doi.org/10.1175/MWR3188.1>.
- UCAR/NCAR - Earth Observing Laboratory., 2015a: FPI ARM Central Facility Radiosonde Data, Version 1.0. UCAR/NCAR - Earth Observing Laboratory. Accessed: 22 Sept 2016, <http://data.eol.ucar.edu/dataset/485.021>.

- UCAR/NCAR - Earth Observing Laboratory., 2015b: National Weather Service High Resolution Radiosonde Data (ESC Format). Version 1.0. UCAR/NCAR - Earth Observing Laboratory. Accessed: 22 Sept 2016, <https://doi.org/10.5065/D6R20Zfv>.
- UCAR/NCAR - Earth Observing Laboratory., 2016a: FP4 NCAR/EOL QC Soundings. Version 2.0. UCAR/NCAR - Earth Observing Laboratory. Accessed: 22 Sept 2016, <https://doi.org/10.5065/D63776XH>.
- UCAR/NCAR - Earth Observing Laboratory., 2016b: FP5 NCAR/EOL QC Soundings. Version 2.0. UCAR/NCAR - Earth Observing Laboratory. Accessed: 22 Sept 2016, <https://doi.org/10.5065/D6ZG6QF7>.
- UCAR/NCAR - Earth Observing Laboratory., 2016c: MP4 NCAR/EOL QC Soundings. Version 2.0. UCAR/NCAR - Earth Observing Laboratory. Accessed: 22 Sept 2016, <https://doi.org/10.5065/D6707ZNV>.
- Vermeesch, K., 2016: FP2 Greensburg, KS Radiosonde Data. Version 1.0. UCAR/NCAR - Earth Observing Laboratory. Accessed: 22 Sept 2016, <https://doi.org/10.5065/D6FQ9TPH>.
- Wagner, T. J., E. Olsen, N. Smith, and W. Feltz, 2016: Mobile PISA 3 UW/SSEC SPARC Radiosonde Data. Version 2.0. UCAR/NCAR - Earth Observing Laboratory. Accessed: 22 Sept 2016, <https://doi.org/10.5065/D6VH5M7B>.
- Wallace, J. M., 1975: Diurnal variations in precipitation and thunderstorm frequency over the conterminous United States. *Mon. Wea. Rev.*, **103**, 406–419, doi: [https://doi.org/10.1175/1520-0493\(1975\)103<0406:DVIPAT>2.0.CO;2](https://doi.org/10.1175/1520-0493(1975)103<0406:DVIPAT>2.0.CO;2).
- Weckwerth, T. M., and Coauthors, 2004: An overview of the international h2o project (ihop\_2002) and some preliminary highlights. *Bull. Amer. Meteor. Soc.*, **85**, 253–278.
- Weisman, M. L., 1993: The genesis of severe, long-lived bow echoes. *J. Atmos. Sci.*, **50**, 645–670.
- Weisman, M. L., and J. B. Klemp, 1982: The dependence of numerically simulated convective storms on vertical wind shear and buoyancy. *Mon. Wea. Rev.*, **110**, 504–520.
- Weisman, M. L., and R. J. Trapp, 2003: Low-level mesovortices within squall lines and bow echoes. part i: Overview and dependence on environmental shear. *Mon. Wea. Rev.*, **131**, 2779–2803.
- Weisman, M. L., and Coauthors, 2015: The Mesoscale Predictability Experiment (MPEX). *Bull. Amer. Meteor. Soc.*, **96**, 2127–2149, doi: [10.1175/BAMS-D-13-00281.1](https://doi.org/10.1175/BAMS-D-13-00281.1).
- Wilson, J. W., and R. D. Roberts, 2006: Summary of convective storm initiation and evolution during IHOP: Observational and modeling perspective. *Mon. Wea. Rev.*, **134**, 23–47, doi: <https://doi.org/10.1175/MWR3069.1>.
- Wurman, J., D. Dowell, Y. Richardson, P. Markowski, E. Rasmussen, D. Burgess, L. Wicker, and H. B. Bluestein, 2012: The second verification of the origins of rotation in tornadoes experiment: VORTEX2. *Bull. Amer. Meteor. Soc.*, **93** (8), 1147–1170.
- Zhang, F., C. Snyder, and R. Rotunno, 2003: Effects of moist convection on mesoscale predictability. *J. Atmos. Sci.*, **60**, 1173–1185.

Zhang, J., and Coauthors, 2016: Multi-Radar Multi-Sensor (MRMS) quantitative precipitation estimation: Initial operating capabilities. *Bull. Amer. Meteor. Soc.*, **97**, 621–638.

Ziegler, C. L., M. C. Coniglio, M. D. Parker, and R. S. Schumacher, 2016: CSU/NCSU/NSSL MGAUS Radiosonde Data. Version 3.0. UCAR/NCAR - Earth Observing Laboratory. Accessed: 22 Sept 2016, <http://doi.org/10.5065/D6W66HXN>.

## APPENDIX

### A1 PECAN RADIOSONDE OBSERVATIONS OF MCS ENVIRONMENTS

Soundings launched by fixed and mobile teams documented the target MCS environments and their changes over time. Figures A1 and A2 show all of the observed thermodynamic (here represented as equivalent potential temperature or  $\theta_e$ ) and meridional wind profiles from soundings launched by just the highly mobile MGs during June and July cases respectively. These teams were often placed at the same location for high frequency ( $\sim 15$  minute) launches as convection approached, but in a few cases teams were spread out for less frequent launches with greater spatial coverage (Figs. A1a,f, A2a,f,i). On 25-26 June, differences between the low-level  $\theta_e$  at different MG locations are quite clear (Fig. A1f). In many cases, soundings documented a low-level southerly wind maximum that increased in magnitude with time, but the initial strength of this wind maximum and the change with time varied from case to case (Figs A1, A2). In some cases  $\theta_e$  changes substantially in the hours before the passage of convection (Figs. A1e, A2g). In other cases, almost no change is observed prior to the passage of the convective line (Figs. A1d, A2d). Similarly, in some cases the most unstable parcel (here, defined as the parcel with largest  $\theta_e$  in the lowest 500 hPa) lies well above the surface (Figs. A1e, A2g), while in others the most unstable parcel appears surface based, even in soundings launched well after dark (Fig. A2b,d). These differences motivated much of the analysis in the first part of this paper.

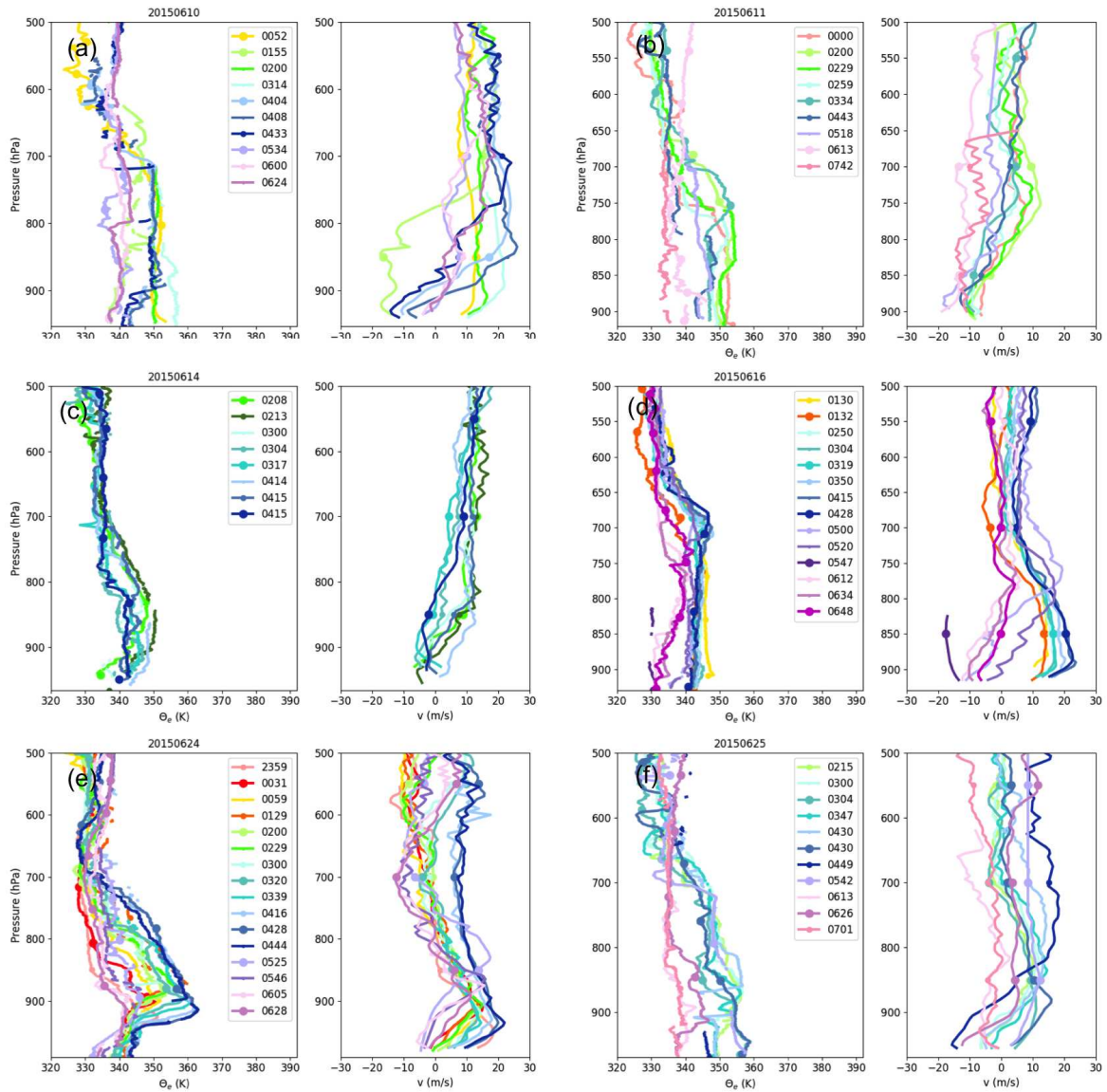


FIG. A1. All pre- and post-convective  $\theta_e$  (K) and meridional wind ( $\text{m s}^{-1}$ ) profiles from MG teams for (a) 10-11 June (b) 11-12 June (c) 14-15 June (d) 16-17 June (e) 24-25 June (f) 25-26 June. Each hour is represented by a color family with 00xx UTC profiles in reds and 04xx UTC profiles in blues. \*All MG profiles on 14-15 June observed post-convective regions.

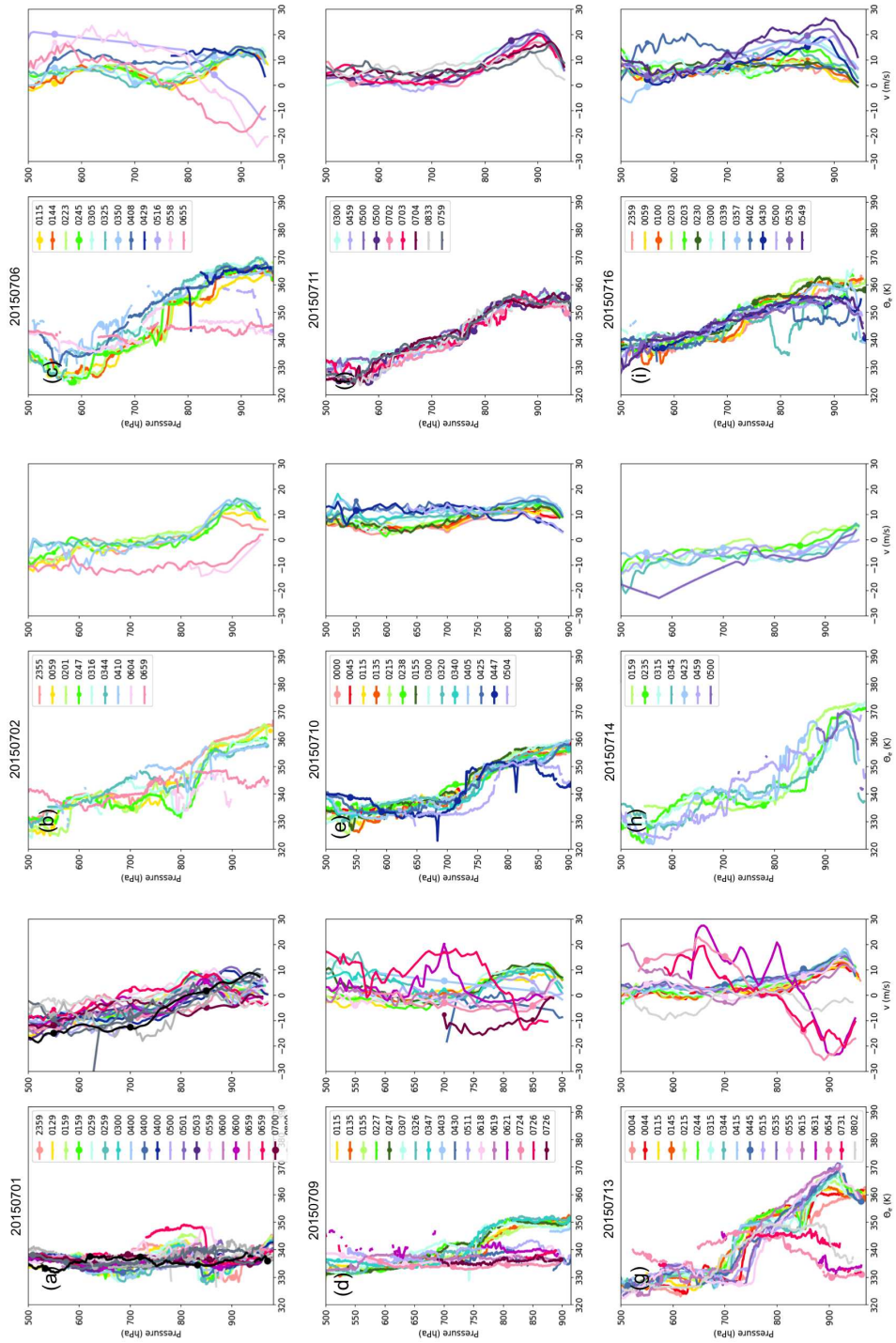


FIG. A2. All pre- and post- convective  $\theta_e$  (K) and meridional wind ( $\text{m s}^{-1}$ ) profiles from MG teams for (a) 30 June – 1 July (b) 1-2 July (c) 5-6 July (d) 8-9 July (e) 9-10 July (f) 10-11 July (g) 12-13 July (h) 13-14 July (i) 15-16 July. Each hour is represented by a color family with 00xx UTC profiles in reds and 04xx UTC profiles in blues. \*All MG profiles on 10-11 July observed pre-convective environments.

There are also notable differences between  $\theta_e$  profiles of observed post-convective environments not discussed elsewhere in this work. In some cases, the post-convective environment is potentially neutral through a large depth of the troposphere, and essentially all instability has been removed (Fig. A2d). In other cases, some potential instability remains, even a few hours after the passage of the leading line. Additionally, in some cases, MGs actually sampled the environment after the passage of a gust front, but before the arrival of the precipitation. This can usually be distinguished by profiles of  $\theta_e$  that are similar to pre-convective profiles everywhere but at the lowest levels where they tend to have a sharp increase with height (e.g. Fig. A2e). This is often accompanied by a decrease in the low-level meridional winds, even becoming negative in some cases (e.g. Fig. A2c). At least two soundings launched by MG teams into this region made it into the storm's updraft, and have unique thermodynamic profiles (Fig. A2c 0516 UTC and g 0654 UTC).

## A2 PRINCIPAL COMPONENT ANALYSIS

North et al. (1982) argues that the degree of confidence in a principal component or PC is related to the degree of separation between the eigenvalues (or variance explained). The equation

$$\Delta\lambda = \lambda \sqrt{\frac{2}{N^*}} \quad (\text{A1})$$

where  $\lambda$  is the eigenvalue  $\Delta\lambda$  and  $N^*$  is the degrees of freedom can be used to identify the 95% confidence interval bounds of the eigenvalues. In this dataset, the selection of  $N^*$  was determined to be between 180 and 360 using 3 variables, 15 cases, approximately 8 hours of launches per case, and assuming that the environment changes enough every 1-2 hours to be independent (which may be a big assumption in some cases). Calculations of  $\Delta\lambda$  were not very sensitive to  $N^*$  values in this range. Two breaks between eigenvalue confidence intervals appear between the first and second and the third and fourth eigenvalues. Because the first PC only explained about 18% of the variance, and based on differences in the PC loadings (Fig. B3), the first 3 PCs were retained.

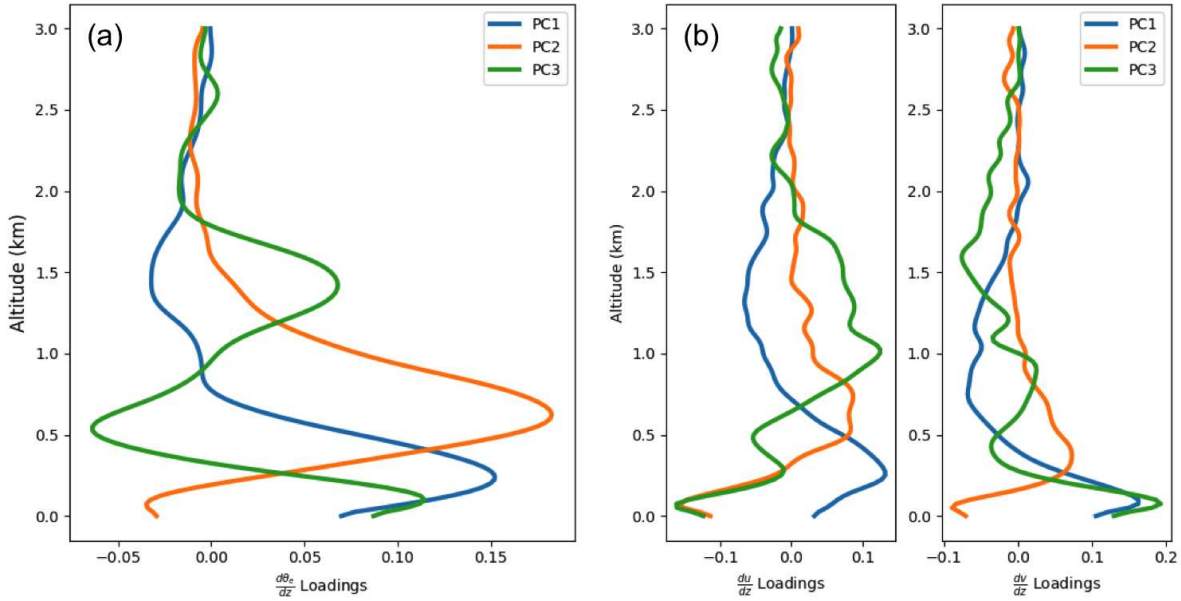


FIG. A3. PC Loadings for (a)  $\frac{d\theta_e}{dz}$ , (b)  $\frac{du}{dz}$ , (c)  $\frac{dv}{dz}$

Plotted PCs show  $\frac{d\theta_e}{dz}$ ,  $\frac{du}{dz}$ , and  $\frac{dv}{dz}$  since those were the input variables to the PCA (Fig. B3). The absolute sign of the PC loadings can be either positive or negative (i.e. the profile can be reflected about the  $x = 0$ ), but the relative signs of the loadings for each PC are important. PC1 and 3 have been flipped to make relative loadings most relevant to this dataset.  $\frac{d\theta_e}{dz}$  of PC1 is positive near the surface, increases to a maximum near 250 m, decreases to a slightly negative value and then becomes nearly constant. This is like having an increase in  $\theta_e$  in the layer below around 500 m, and a shift to a fairly constant negative slope, just like many profiles in the ‘elevated instability’ cluster. Similarly, the wind loadings for PC1 fit the elevated instability cluster.  $\frac{du}{dz}$  is positive until just above 500 m and becomes weakly negative thereafter, capturing the increase in westerly winds to about 500 m.  $\frac{dv}{dz}$  is also positive until just below 500 m, similar to the positive slope seen in  $v$  for both elevated instability and potentially neutral + jet winds. In PC2,  $\frac{d\theta_e}{dz}$  is positive from just above the surface to around 1.5 km where it becomes weakly negative with an decrease in both  $u$  and  $v$  very near the surface, most closely resembling profiles from 11-12 June. In PC3,  $\frac{d\theta_e}{dz}$  describes  $\theta_e$  profiles that have slight potential stability near the surface, and then oscillate slightly between potentially unstable and potentially stable below 2 km. Winds in this PC fit most closely with the potential neutral cluster where near surface slopes of  $u$  and  $v$  have opposite signs. The two potentially neutral clusters seem to be made up of a combination

of PC2 and PC3 where  $\frac{d\theta_e}{dz}$  in the two PCs has opposite signs, zonal winds have an easterly surface component and meridional winds are different between clusters.

### A3 SHARED NEAREST NEIGHBORS (SNN) CLUSTERING

The Shared Nearest Neighbors (SSN) method was selected for this application because unlike other methods, it handles variable density clusters, does not require the number of clusters to be specified in advance, and does not force every point into a cluster (i.e. outliers are not forced into ill-fitting clusters). Scatter plots of PCs against each other showed that the pre-convective environmental sounding dataset has both variable densities, and a number of outliers. Clusters produced by the SSN method were broadly similar to clusters produced by DBSCAN and K-means methods, but without the same limitations.

SNN defines similarity between a pair of points based on their shared nearest neighbors. If two points have the same neighbor, they are closer/more similar (Ertoz et al. 2002). To apply this, nearest neighbors were first identified. Unlike other methods where this distance is retained, if the points were identified as a neighbor, they were given a value of one, so that density is redefined based on the number of shared neighbors. In this way, points that have many other points in common become the core of the clusters. Once density is redefined, DBSCAN will filter out points that do not have many shared neighbors, and will cluster groups based on how many neighbors they share. DBSCAN has two parameters: one is related to the acceptable multi-dimensional physical distance of points in a cluster ( $\epsilon$ ), the other is the minimum number of neighbors a point must have to be included in a cluster (minPts). In this method, a rather large number of minimum points, 34, can be used to create physically sensible clusters for this dataset. The Manhattan distance metric was chosen so that if two points are both neighbors or are not both neighbors with the same third point, they don't contribute to the distance of the cluster. If one of the points is a neighbor but the other is not, then they do not share the neighbor and the distance of the cluster increases. Since  $\epsilon$  is the physical distance of points permitted in the cluster, here, it means that the maximum number of unshared nearest neighbors is also 34. In other words, half of the nearest neighbors between any two soundings in a cluster must be shared.